Thesis manuscript

for the degree of Doctor of Philosophy

in physics

Single Diffraction in proton-proton scattering with TOTEM at The Large Hadron Collider

Fredrik Oljemark

2020

Doctoral Dissertation, to be presented for public discussion with the permission of the Faculty of Science for the University of Helsinki, in Hall E204, Physicum, on the 27th of November, 2020, at 12 o'clock.

Supervisor: Prof. Kenneth Österberg

HELSINKI INSTITUTE OF PHYSICS, and
UNIVERSITY OF HELSINKI
FACULTY OF SCIENCE
DEPARTMENT OF PHYSICS
PB 64
FIN-00014 University of Helsinki

HIP-Internal Report Series HIP-2020-04
ISSN 1455-0563
ISBN (print) 978-951-51-1295-8
ISBN (pdf) 978-951-51-1296-5

Contents

List of Figures

List of Tables

Nomenclature

β^*	The beta-function $\beta(s=0)$ at the IP, for the magnetic optics
ϵ	Beam emittance, the phase space of the beam, proportional to beam width and beam angular spread
η	Pseudo-rapidity $\eta = -\ln(\tan(\theta/2))$, where θ is the scattering angle with respect to the beam direction. η is approximately equal to true rapidity when the rest mass is negligible compared to the momentum of the particle ($p \gg m$) and the scattering angle is much bigger than $1/\gamma$ ($\theta \gg 1/\gamma \approx 270\,\mu$rad for 3.5 TeV beam protons)
γ	Gamma = $1/\sqrt{1-v^2/c^2}$ is the ratio between relativistic energy and rest mass (in energy units)
$\hbar$	Smallest unit of quantized angular momentum, the reduced Planck's constant $= \frac{h}{2\pi} \approx 1.055 * 10^{-34}$ Js $\approx 6.58 * 10^{-22}$ MeV s
μb	Microbarn, unit of area for particle interaction cross sections = $10^{-34}\,m^2$
μm	Micrometer, 10^{-6} m
ϕ	Angle around the beam in the perpendicular plane to the beam direction
$\underline{p}$	Four-momentum in special relativity
$\vec{p}$	Momentum
ξ	Fractional momentum loss, of a proton with respect to unscattered beam protons
c	Speed of light, constant = 299 792 458 m/s
E	Energy

p_T Transverse momentum, the component of particle momentum perpendicular to the beam direction

s Mandelstam variable equalling the centre-of-mass energy squared, always positive in this thesis. In magnetic optics, like the proton transport around the LHC, s is also used for the distance travelled around the ring.

t Mandelstam variable, showing the four-momentum exchanged, always negative in this thesis (positive values shown are absolute values)

y Rapidity $y = \frac{1}{2} \ln \frac{E+p_z c}{E-p_z c}$, a momentum variable that transforms additively between different frames in special relativity

0T2 SD event with one proton and no tracks in T2; very low mass SD event not measured in this thesis

1T2 SD event with one proton, and tracks only in the opposite arm of T2, divided into 3 classes in Table 5.2

2T2 SD event with one proton, and tracks in both arms of T2

ASIC Application-specific integrated circuits - a generic name for specialized silicon chips

Baryon Heavier hadron consisting of three quarks

BD Beam divergence, the small angular spread of beam protons due to the emittance, implying that the protons don't collide perfectly head-on at the IP but with a small angle that varies from collision to collision. This spread is also propagated to the final state particles and is mainly of relevance for leading protons.

BH Beam Halo, background protons outside the main beam, whose displacement transverse to the beam makes them look like scattered protons

Bunch A group of billions of protons accelerated together, and brought together at the IP with a counter-rotating bunch to produce collisions

BX Bunch Crossing, occasion when two particle bunches cross each other at the interaction point. Also used for data collected during BX without looking at

detector information. In this thesis used for modelling the effect of several simultaneous proton-proton interactions during one bunch crossing.

CD Central Diffraction, a diffractive interaction between protons giving two protons, two gaps, and a central system

CERN The largest particle physics centre in Europe, situated in Geneva and neighbouring France

CMSSW The CMS simulation software, also used to simulate the TOTEM detectors

CoM Centre of mass, the frame co-moving with the particle, or – in case of decays – with the decayed parent particle

Coupling constant A parameter of a quantum theory describing the strength of particle interactions. It is unitless, but not truly constant, since due to renormalisation it will in general depend on the particle interaction energy scale.

DAQ Data acquisition system, used to read out data from the TOTEM detectors

DD Double Diffraction, where two protons interact diffractively, and both fragment into hadronic systems, but with a rapidity gap between them

Dead time An inefficiency of the data readout system; the period during the read-out or trigger event cycle, when further data cannot be read out or triggered, and will be lost.

Dip Minimum in the differential elastic cross section, beyond which the cross section has a secondary maximum.

Elastic scattering A collision with no energy loss and no transformation of the colliding particles, only an exchange of momentum and change of direction

EM Electro-magnetism, the force occurring between electrically charged particles and mediated by the photon. All charged particles are affected by electromagnetism.

EPOS EPOS is Regge-theory-based inclusive cosmic ray, heavy-ion and hadron collision Monte Carlo event generator, without ability for the user to select specific processes. It is used as a reference event generator along with Pythia 8 in this thesis.

eV Electron volt, unit of energy = $1.602 * 10^{-19}$ J. Defined as the amount of energy an electron would gain or lose when traversing a potential difference of 1 V

Filling scheme The actual number of bunches and co-rotating (relative) positions of all bunches circulating in a particle accelerator, during a particular run

GEM Gas Electron Multiplier, a detector technology that multiplies the signal in successive gas-filled, metallized and electrically charged micro-perforated foils

GeV Giga-electron volt = 10^9 eV

Hadron Composite particle of quarks and gluons

IP Interaction point, where counter-rotating proton bunches in the LHC are brought to collide, leading to proton-proton interactions

keV kilo-electron volt = 1000 eV

LEP Large electron-positron collider, the previous flagship accelerator at CERN

LHC Large Hadron Collider, the largest proton-proton collider at CERN

mb Millibarn, unit of area for particle interaction cross sections = 10^{-31} m^2

Meson Particle consisting of two quarks (one quark and an antiquark).

MeV Mega-electron volt = 10^6 eV

MeV/c Unit of momentum = $5.36 * 10^{-22}$ kg*m/s

MeV/c^2 Unit of mass = $1.79 * 10^{-30}$ kg

Minimum bias Inelastic events in general, named for the bias introduced by trigger selections, like high p_T selection cuts

MJ Megajoule, unit of energy =10^6 J

Momentum fraction For composite particles, the fraction of the particle momentum that can be attributed to an individual constituent, like a quark or gluon in a proton. Called the Bjorken x, x_{Bj}.

mrad Milliradian, angular unit = 0.001 rad

ns Nanosecond, 10^{-9} s

Overlap region Overlapping part of vertical and horizontal RPs used for RP alignment. For the LHC optics used in the special TOTEM run analyzed in this thesis, it contains mainly protons with high ξ.

Parton Collective name for quarks and gluons

Pileup Several overlapping simultaneous proton-proton interactions during the same bunch crossing

PU Pileup is a background where several, for the analysis of this thesis most commonly two, proton interactions happen simultaneously, during the same bunch crossing. The overall topology may look like an SD signal event

Pythia 8 Pythia is a general Monte Carlo particle physics event generator, with individual processes configurable and selectable. Pythia 8 is the latest version, rewritten and tuned for LHC data.

QGSJet QGSJet is a Regge-theory-based inclusive cosmic ray, heavy ion and hadron collision Monte Carlo event generator, without ability for the user to select specific processes. We did not find the momentum conservation of the implementation in CMSSW of this event generator satisfactory and therefore did not use it in the analysis. The author provided us with predictions from the event generator for comparison with the measurements in this thesis.

Quantum number Quantized value characteristic for a particle, for example the sign change under discrete symmetry transformations like parity

Quark Main constituent of protons, never free as individual quark below an energy scale $\mathcal{O}(1)$ GeV

rad Radian, angular unit, $360^\circ = 2\pi$ rad

ROOT A particle physics analysis framework program, for C++ and Python code.

RooUnfold A program for doing numerical unfolding, to try to undo resolution smearing effects in a detector.

RP Roman Pot, a moveable beam device that can be inserted into the beampipe vacuum to within a few mm of the out-going beam and retracted during beam injection, ramp, and collision setup.

RP-V Vertical roman pots, i.e. top and bottom RPs

SD Single Diffraction, where two protons collide, but only one of them fragments into a hadronic system, while the other one stays intact and can be observed in the Roman Pots

SI Système international, the international metric system of units

SM Standard model of particle physics, explains all known particle interactions except gravity

SPS Super Proton Synchrotron, the penultimate stage in the LHC proton acceleration, which was the CERN flagship proton and antiproton accelerator during the 1980s

SR Special Relativity, a theory important for particles moving at a significant fraction of the speed of light

Strong force The force between the constituents of the proton, affects only quarks and gluons

T Tesla, unit of magnetic field strength

T1 The TOTEM T1 telescope is a charged-particle cathode strip chamber detector

T2 The TOTEM T2 is a charged-particle GEM detector that can trigger on inelastic events

TeV Tera-electron volt = 10^{12} eV

Topology Classification that is invariant to scaling of subcomponents, as long as their relative position is the same. In mathematics, used also for invariance under arbitrary continuous deformations. Used in this thesis to talk about SD event classification.

TOTEM An LHC experiment to measure the total cross section, elastic scattering and diffraction dissociation. This thesis analyses data taken by TOTEM.

VFAT Data readout electronics used by TOTEM detectors

Weak force The force that is responsible for radioactive decays and mediated by $W^{\pm}$ and Z bosons. All Standard Model particles are affected by the weak force.

Zero bias Data collected during bunch crossings without looking into detector information, equivalent to BX-triggered data.

Abstract

The understanding of the strong interaction with low-momentum transfer is of primary importance for our understanding of the behaviour of nuclear matter. Suitable processes to study such low-momentum transfers are soft diffractive high energy physics processes. In this thesis, soft Single Diffraction (SD) in proton-proton scattering was studied at 7 TeV centre-of-mass energy with the TOTEM experiment at CERN's Large Hadron Collider (LHC), in Geneva, Switzerland.

SD is a significant part of the total inelastic proton-proton scattering but despite that not so well known, nor much studied. SD events are characterized by an intact proton opposite a diffractive system with a large rapidity region without primary particles, a so-called rapidity gap, in between. In these studies, the out-going intact protons are measured at 5-30 mm from the out-going beam using the TOTEM Roman Pots (RP), movable beam-insertion detectors located about 220 m from the collision point. The proton track in the RP is used to reconstruct the scattering angle and proton longitudinal momentum loss. The diffractive system and the rapidity gap are both tagged and measured using the TOTEM T1 and T2 charged particle telescopes. The data used for the studies was taken in a special run at the LHC in 2011 with β^* = 90 m optics that optimized the proton acceptance for low scattering angles at any proton longitudinal momentum loss value below 20%.

Results are presented for the total SD cross section and differential cross section versus $|t|$ – the absolute momentum transfer squared – in four ranges of the proton longitudinal momentum loss ξ, inferred from the size of the rapidity gap measured by T1 and T2. The results are compared to expectations from various event generators as well as earlier SD measurements at the LHC. The total SD cross section obtained is 11.10 ± 1.66 mb for the range $2.7 * 10^{-7} < \xi < 20$ %. Compared to earlier studies, these studies cover a significantly larger ξ range. They also show, for the first time at the LHC, the expected dependence of the exponential slope of the $|t|$ distribution as function of ξ, i.e. that the $|t|$ distribution becomes less steep with increasing ξ. The

results provide relevant information regarding the proton structure, as well as valuable input to the modelling of cosmic-ray air showers and inelastic collisions.

Acknowledgements

I would like to thank professor Kenneth Österberg for supporting me during the making of this thesis and the analysis it is based on. I also thank Mirko Berretti, Jan Kaspar and Hubert Niewiadomski for helping me to better understand the TOTEM simulation code, and Valentina Avati, Mario Deile and Simone Giani for guiding me how to take part in the TOTEM collaboration.

The author acknowledges support from the Magnus Ehrnrooth foundation, the Waldemar von Frenckell foundation, Nylands Nation vid Helsingfors Universitet, the University of Helsinki and Helsinki Institute of Physics.

Author's contributions to TOTEM publications

The research for this thesis was carried out within the TOTEM project at the Helsinki Institute of Physics during the years 2007-2020. During this time, the author first did feasibility studies on the potential of common CMS and TOTEM data taking at the LHC, then developed software for TOTEM's T2 telescope and studied the RP inefficiency for the first TOTEM elastic papers. Since 2012, the focus of the author has been on studies of single diffractive processes with TOTEM, which is the main topic of this thesis, including also studies of low mass diffraction in generators for the inelastic rate measurement. The publications listed below are a result of a wider group effort, where the author's contribution is outlined in detail for each publication. The Author presented TOTEM results at various international and national conferences and events during the years.

List of publications

1. **Proton-proton elastic scattering at the LHC energy of $\sqrt{s}$ = 7 TeV** [2]

   G. Antchev et al. (TOTEM collaboration) with F. Oljemark, Europhysics Letters 95 (2011) 41001

   Abstract: Proton-proton elastic scattering has been measured by the TOTEM experiment at the CERN Large Hadron Collider at $\sqrt{s}$ = 7 TeV in dedicated runs with the Roman Pot detectors placed as close as seven times the transverse beam size (σ_{beam}) from the outgoing beams. After careful study of the accelerator optics and the detector alignment, $|t|$, the square of four-momentum transferred in the elastic scattering process, has been determined with an uncertainty of δt = 0.1 GeV $\sqrt{|t|}$. In this letter, first results of the differential cross-section are

presented covering a $|t|$-range from 0.36 to 2.5 GeV^2. The differential cross-section in the range $0.36 < |t| < 0.47$ GeV^2 is described by an exponential with a slope parameter B = $(23.6 \pm 0.5(stat) \pm 0.4(syst))$ GeV^2, followed by a significant diffractive minimum at $|t|$ = $(0.53 \pm 0.01(stat) \pm 0.01(syst))$ GeV^2. For $|t|$-values larger than $\sim$ 1.5 GeV^2, the cross-section exhibits a power law behaviour with an exponent of $-7.8 \pm 0.3(stat) \pm 0.1(syst)$. When compared to predictions based on the different available models, the data show a strong discriminative power despite the small t-range covered.

Author's contribution: The author studied the trigger efficiency of the "double-arm RP near-far or" trigger for elastic scattering in detail as well as the RP inefficiency in elastic events due to secondary interactions in the material in front and in the RPs using offline RP data. The final outcome of the studies are quoted as two numbers in the table 2 of the published paper. A writeup of the studies can be found in Appendix A of this manuscript. These studies were crucial for the publication since this was the first publication by TOTEM and all the efficiencies were completely unknown. It was also mandatory to ensure that there was no hidden inefficiency that had not been taken into account so these studies also included various cross-checks.

2. **Double diffractive cross-section measurement in the forward region at LHC** [3]

   G. Antchev et al. (TOTEM collaboration) with F. Oljemark, Physical Review Letters 111 (2013) 262001

   Abstract: The first double diffractive cross-section measurement in the very forward region has been carried out by the TOTEM experiment at the LHC with a center-of-mass energy of $\sqrt{s}$ = 7 TeV. By utilizing the very forward TOTEM tracking detectors T1 and T2, which extend up to $|\eta|$ = 6.5, a clean sample of double diffractive pp events was extracted. From these events, we determined the cross section σ_{DD} = (116 ± 25) μb for events where both diffractive systems have $4.7 < |\eta|_{min} < 6.5$.

   Author's contribution: The author estimated the single diffractive backgrounds for the double diffractive signal in this paper using a preliminary version of the analysis described in this manuscript.

3. **Measurement of pseudorapidity distributions of charged particles in proton-**

proton collisions at $\sqrt{s}$ = 8 TeV by the CMS and TOTEM experiments [4]
S. Chatrchyan et al. (CMS and TOTEM collaborations) with F. Oljemark, European Physical Journal C 74 (2014) 3053

Abstract: Pseudorapidity (η) distributions of charged particles produced in proton–proton collisions at a centre-of-mass energy of 8 TeV are measured in the ranges $|\eta| < 2.2$ and $5.3 < |\eta| < 6.4$ covered by the CMS and TOTEM detectors, respectively. The data correspond to an integrated luminosity of L = $45\,\mu b^{-1}$. Measurements are presented for three event categories. The most inclusive category is sensitive to 91–96 % of the total inelastic proton–proton cross section. The other two categories are disjoint subsets of the inclusive sample that are either enhanced or depleted in single diffractive dissociation events. The data are compared to models used to describe high-energy hadronic interactions. None of the models considered provide a consistent description of the measured distributions.

Author's contribution: The author estimated the SD cross section for events with tracks in one arm of T2 only as a fraction of the cross section for events with the same T2 topology, but no demand for a proton, for 7 TeV data. This was used to validate the MC proton selection criteria for classifying inclusively generated MC events as SD.

4. **First measurement of elastic, inelastic and total cross-section at $\sqrt{s}$ = 13 TeV by TOTEM and overview of cross-section data at LHC energies** [5]

   G. Antchev et al. (TOTEM collaboration) with F. Oljemark, European Physical Journal C 79 (2019) 103

   Abstract: The TOTEM collaboration has measured the proton–proton total cross section at $\sqrt{s}$ = 13 TeV with a luminosity-independent method. Using dedicated β^* = 90 m beam optics, the Roman Pots were inserted very close to the beam. The inelastic scattering rate has been measured by the T1 and T2 telescopes during the same LHC fill. After applying the optical theorem the total proton–proton cross section is σ_{tot} = (110.6 ± 3.4) mb, well in agreement with the extrapolation from lower energies. This method also allows one to derive the luminosity-independent elastic and inelastic cross sections: σ_{el} = (31.0 ± 1.7) mb and σ_{inel} = (79.5 ± 1.8) mb.

   Author's contribution: The author studied the rate of diffractive events resulting

in no tracks in the TOTEM T1 and T2 telescopes as well as the ratio between inelastic events with tracks in only one T2 arm and those with tracks in both T2 arms in various Monte Carlo event generators as function of different LHC energies. These studies were used to estimate the low mass diffraction correction and its uncertainty to the inelastic rate, which is the dominant uncertainty source in the determination of the total cross section using the luminosity independent method by TOTEM. The author also made Figure 5 of the published paper showing the "zoomed" comparison of the different 7 and 8 TeV total cross section measurements of ATLAS and TOTEM experiments.

Chapter 1

Introduction

At the Large Hadron Collider in CERN, Geneva, protons are accelerated to large values of momentum and collided to produce high-energy particle physics interactions. In general, these interactions destroy the individual protons, since the centre-of-mass collision energy is much larger than the binding energy of the proton constituents to each other. However, when momentum transfer in the collision is lower, it may lead to elastic or diffractive scattering. These processes are a significant fraction of the total proton-proton "cross section", i.e. their interaction probability.

In elastic scattering, both protons emerge intact from the scattering interaction without momentum loss and only a slight change of direction corresponding to the so-called scattering angle, while in diffractive scattering the protons may emerge intact with both a small momentum loss and scattering angle, or be excited into a low-mass system of fragments separated by a large distance in phase space from the other proton. This void of particles in rapidity space, a so-called rapidity gap, is diagnostic for diffractive events, since in standard inelastic non-diffractive proton-proton scattering the central region between the proton remnants is usually filled, with large gaps being exponentially suppressed.

In the quantum field theory of strong interaction, diffractive interactions are mediated by colour neutral objects composed of gluons, the simplest being described by two gluons that is conventionally called the "Pomeron". Diffractive processes can be subdivided into elastic scattering, where both protons stay intact, Single Diffraction (SD), where one proton fragments and the other stays intact – the topic of this thesis – and Double Diffraction (DD), where both protons fragment.

In this thesis, the intact proton was measured in the TOTEM Roman Pot silicon

strip detectors, placed very near the circulating proton beam, at about 220 m from the interaction point (IP). The charged particles produced from the other fragmenting proton were measured in the TOTEM T1 and T2 charged particle telescopes that were also used to find the rapidity gap in these events. The T2 was also used for triggering the SD events, which gives access to all SD events with a diffractive mass M_X of the fragmentating system above 3.1 GeV. The proton track in the RP was used to reconstruct the scattering angle and proton momentum loss, the latter being in direct relation with the diffractive mass M_X seen on the other side.

The data used for the measurements was taken in a special TOTEM run at the LHC in 2011 with β^* = 90 m optics that optimized the proton acceptance for low scattering angles at any proton longitudinal momentum loss value below 20 %.

The measurements of the total and differential SD cross sections versus $|t|$ in four ranges of M_X are presented, where $|t|$ is the absolute value of the momentum transfer squared. The M_X ranges were inferred from the rapidity gap detected by the T1 and T2 telescopes. The measurements are compared with predictions from various Monte Carlo event generators as well as with published SD measurements at the LHC.

The outline of the thesis is as follows. In the second chapter, the theoretical background is provided both in terms of relativistic kinematics, concepts as well as models for hadron-hadron interactions. The third chapter describes the experimental apparatus and the fourth the software tools used including the Monte Carlo event generators. In the fifth chapter, the SD analysis is presented in general terms, whereas the sixth chapter goes into the analysis details and the systematics. The results as well as the conclusions and outlook are given in chapter 7, wrapping up with a short summary in chapter 8.

Chapter 2

Theory

2.1 Relativistic kinematics

2.1.1 Units

Particle physicists use the electron-volt as the basic unit of energy. This unit for energy is also used for masses and momenta. See Nomenclature section for values in SI units.

2.1.2 Special Relativity

The protons circulating in the LHC have an energy of up to 6.5 TeV, while their mass is only 938 MeV/c^2. The protons we study in this thesis are therefore moving at ultra-relativistic speed very near the speed of light, so it is necessary to use Special Relativity (SR) to know their movements in the various frames of reference used, like the $p+p$ centre of mass (CoM) frame, and the lab frame where a detector makes measurements.

2.1.3 Four-vectors

In SR, momentum and energy is conserved, but the Newtonian momentum vector ($\vec{p}_N = m\vec{v}$) has to be generalized to account for the limiting speed of light

$$\lim_{v\to c} |\vec{p}_{SR}| = \infty, \text{ not } = mc, \text{ if } m \neq 0 \tag{2.1}$$

This can be expressed as

$$\vec{p}_{SR} = \gamma m_0 \vec{v} \tag{2.2}$$

where $\gamma = 1/\sqrt{1 - v^2/c^2}$, and m_0 is the invariant rest mass. However, these formulas are calculated in a particular frame, and to be able find the corresponding values in another frame we need rules for transforming from one coordinate system to another one, moving at some velocity $\vec{v}_{\text{frame}}$. We can write down a 4-dimensional Lorentz vector combining the energy E and the three-dimensional momentum $\vec{p}$ into a momentum four-vector $\underline{p} = (E, \vec{p}c)$, which is isomorphic with a position four-vector $\underline{r} = (ct, x, y, z)$. Lorentz vectors do not transform like Euclidean four-dimensional vectors; instead, the position or momentum vector component along the boost direction (parallel to $\vec{v}_b$) mixes with the time- or energy-component

$$E' = \gamma_b E - p_{||}\gamma_b v_b \tag{2.3}$$

$$p'_{||} = p_{||}\gamma_b - E\gamma_b v_b/c^2 \tag{2.4}$$

Lorentz vectors have a Minkowski space norm for calculating the vector "length"

$$\eta^{\mu\nu} = \begin{pmatrix} 1 & 0 & 0 & 0 \\ 0 & -1 & 0 & 0 \\ 0 & 0 & -1 & 0 \\ 0 & 0 & 0 & -1 \end{pmatrix} \tag{2.5}$$

$$\underline{p} \cdot \underline{p} = \sum_{\mu,\nu} \eta^{\mu\nu} p_\mu p_\nu = E^2 - \vec{p}^2 c^2 \tag{2.6}$$

For photons this norm is always zero, while for massive particles the norm equals the rest mass squared $(m_0 c^2)^2$. See Fig. 2.1 for a schematic representation of the Lorentz vectors and their norms.

2.1.4 Rapidity and pseudorapidity

Since we saw above that velocities don't transform additively in SR, it would be useful to find some variable that does have a simple constant offset between frames moving at $\vec{v}_b$ with respect to each other. This generalisation of velocity is called rapidity (y), and is defined as

$$y = \operatorname{artanh}(v/c) = \operatorname{artanh}(\frac{|\vec{p}c|}{E}) = \frac{1}{2}\ln\frac{E + |p|}{E - |p|} \tag{2.7}$$

$$y_z = \frac{1}{2}\ln\frac{E + p_z c}{E - p_z c}, \tag{2.8}$$

The latter is convenient to use for boosts along the beam axis, where asymmetric parton momentum fractions in an interaction give $p_{CM,z} \gg p_{CM,x,y}$. $p_z = 0$ corresponds to

Figure 2.1: Lightcone representation of Lorentz vectors, plotted in 2D (1D space+1D time). The thick red arrow represents a massive particle with $|v| < c$; addition of any number of such slower-than-light vectors will always give another vector inside the $v = c$ cone. The dashed line shows a spacelike vector representing a virtual particle with negative M^2, or $|v| > c$

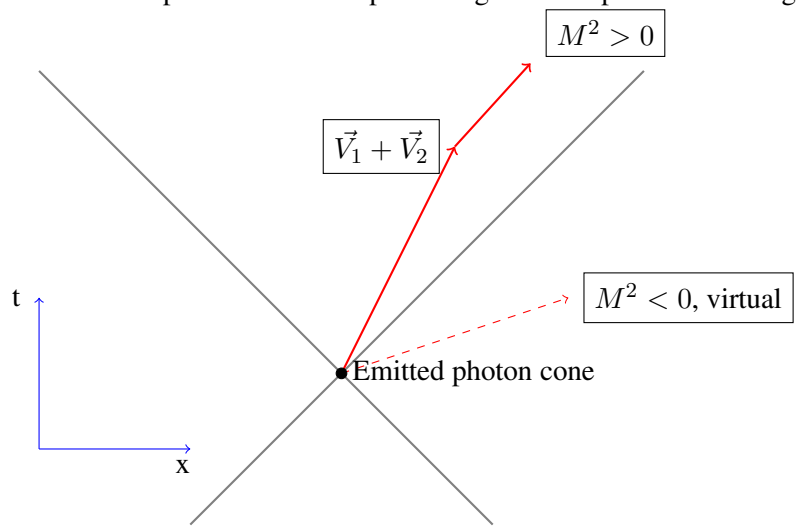

$y = 0$, and y varies between

$$\pm\, y_{\text{max}} = \pm \ln(\frac{E+p}{m}) \approx \pm \ln(2E/m) = \pm \ln(\sqrt{s}/m) \tag{2.9}$$

To measure y, we must be able to measure the mass of the particle, which experimentally gets harder for very relativistic particles ($\gamma \gg 1$). Therefore we can make the approximation $m \approx 0$, defining the pseudorapidity η

$$\eta = -\ln(\tan(\theta/2)), \tag{2.10}$$

where θ is the polar angle. The rapidity $y \approx \eta$ is a good approximation when $mc \ll |\vec{p}|$ and $\theta^2 \gg \gamma^{-2}$; at the limit of validity, where $\theta = 1/\gamma$, $|\eta_{lim.}| = y_{max} = \ln(2\gamma) = y_{real} + \frac{1}{2}\ln(2)$.

2.1.5 Mandelstam variables

Since Lorentz vectors may be encountered in multiple frames of reference, the transformation properties of Lorentz vectors and their combinations is of interest. The easiest transformation is for Lorentz scalars, which are invariant under boost. All dot products of two Lorentz vectors are invariant, and some especially interesting ones were presented by Mandelstam [6] for the case of two-particle collisions invariants

that are the same in all frames. Defining the collision as $p_{i,1} + p_{i,2} \rightarrow p_{f,1} + p_{f,2}$, where i stands for initial and f for final state particles, these are the three Mandelstam variables :

$$s = (p_{i,1} + p_{i,2})^2 = (p_{f,1} + p_{f,2})^2 \tag{2.11}$$

$$t = (p_{i,1} - p_{f,1})^2 = (p_{i,2} - p_{f,2})^2 \tag{2.12}$$

$$u = (p_{i,1} - p_{f,2})^2 = (p_{i,2} - p_{f,1})^2 \tag{2.13}$$

$$s + t + u = 4m_p^2 \tag{2.14}$$

The first one, s, is the centre-of-mass energy squared. The last two, t and u, measure the momentum change in the process, $t, u \leqslant 0$. Because of the final constraint 2.14, only two of the three variables are independent. Comparing t and u, we see that the particle labels are simply exchanged between identical protons, so in this thesis I will use s and t only.

If the momenta in these formulas are negative; for example, if $p_{f,1\&2} < 0$, then we have what is called t-channel scattering with $t = E_{CM}$, and s and u corresponding to the two momentum transfer variables.

2.2 Rate, cross-section and luminosity

The colliding protons in the LHC are grouped into bunches of $N_{p/b} \approx 10^{10...11}$ protons, with a chance of a collision every time the proton has circulated around the 27 km accelerator at a speed very near the speed of light. The number of bunches N_b can be many thousands, but in the special run analysed in this thesis the filling scheme had two big bunches, one colliding and one non-colliding, and 13 small ones. Therefore we only use the big colliding one, since the per-bunch event rate is

$$R_b \propto N_{bunches} N_{p/bunch}^2 \tag{2.15}$$

The other bunches were used to check the calibration of the luminosity measurement provided by CMS. The rate of proton-proton interactions between colliding proton bunches depends on N_b, N_p, $f_{LHC} = c/2\pi r_{LHC}$ – where the latter is the circulation frequency around the LHC – and on the beam cross-sectional area A at the collision point ($\propto 1/A$). These variables can be grouped into a quantity called luminosity, with units rate per area, that does not depend on the physics of the proton and its

interactions,

$$L = \frac{N_b * f * N_{p/b}^2}{A} \tag{2.16}$$

The interaction rate is then

$$R_b = L_{LHC} * \sigma_p \tag{2.17}$$

where σ_p encodes the physics of the proton, and can to first order be considered the "classical" cross section of the proton times the probability of the specific proton interaction sought. The unit used for cross sections in this thesis is the barn, equal to 10^{-28} m^2. This can be inverted to go from the measured event rate and integrated luminosity to a measurement of the process cross section,

$$\sigma_{process} = \frac{R_{process}}{\ell_{CMS}} \tag{2.18}$$

$$= \frac{\mathcal{A}N_{process}}{\int \ell_{CMS} dt} \tag{2.19}$$

$$= \frac{\mathcal{A}N_{process}}{\mathcal{L}_{CMS}} \tag{2.20}$$

where $\mathcal{A}$ contains the acceptance corrections to go from the measured rate to the total signal, and we integrate both the rate (to a corrected total number of events) and the instantaneous luminosity ℓ to the integrated luminosity $\mathcal{L}$.

2.3 The Standard Model

The Standard Model (SM) of particle physics consists of 24 elementary particles in three generations of increasing mass, plus 12 force carriers, and one scalar boson. All have already been discovered, and are shown in Table 2.2. Ordinary matter consists of the first generation quarks and lepton only; atoms are built from electrons and triple-quark nucleons, called protons (uud) and neutrons (udd), that interact dominantly with gluons (within each nucleon), and photons (at larger scales than the nucleus). The SM contains three forces, schematically described in Table 2.1. The strong force has a self-interaction strength that grows at lower energies, causing the particles that are affected by the strong force (called quarks) to always be bound into groups of 2 or 3 quarks (called mesons in the first case, baryons in the second ; a common term for all particles bound by the strong force is hadron) with no naked strong force charges remaining free, at low energies (below the hadronisation scale around $\mathcal{O}(1)$ GeV). In contrast, electromagnetism (EM) and the weak force can be combined into one force

that asymptotically looks like EM at low energies, but that is symmetric between both above a symmetry-breaking energy scale. That symmetry breaking is created by the so-called Higgs mechanism, and the corresponding Higgs field is responsible for the mass of all the other elementary particles – but not for the binding energy of composite particles like the proton, the mass of which comes from the strong force binding, and consequently is much larger than the sum of masses for its three constituent quarks.

The last of these SM particles to be experimentally discovered was the Higgs boson, found at the Large Hadron Collider (LHC) in 2012 [7, 8].

2.3.1 Quantum numbers

In the SM, particles carry some conserved quantities; angular momentum, charges with respect to the various forces, and discrete transformation symmetries like parity. Composite particles like the proton can have angular momentum both from the spin of the individual partons and from the orbital angular momentum between them; quantum numbers are usually given in the shorthand form $J^{PC} = 1^{++}$, or $J^P = \frac{1}{2}^+$ for the proton; here $\vec{J} = \vec{L} + \vec{S}$ is the sum of spin and orbital angular momentum, in units of $\hbar$, the reduced Planck's constant, while $P = \pm$ is the sign change under parity transformation, and $C = \pm$ under matter-antimatter-exchange, that is, when changing the sign of all charges. The latter transformation is not trivial for neutral particles since they may have a distinct antiparticle or be their own antiparticle, like the neutron and photon, respectively.

2.4 Hadron-hadron interaction processes

Hadrons consist of partons: constituent quarks, with momentum fraction x_{cq} (defined as $\vec{p}_{cq} \equiv x_{cq} * \vec{p}_{hadron}$) peaked near $x_{cq} \approx \frac{1}{5} \ldots \frac{1}{3}$ [13], sea quarks – "virtual" particles with $x_{sq} \ll 1$) – and gluons, with lower momentum fraction than constituent quarks. Hadrons can interact through all four known forces, but the relevant ones for proton interactions in this thesis are the strong force and electromagnetism, the latter dominating beyond the range of the former. Because protons are charged, below a momentum transfer $|t| \approx 10^{-4}$ GeV^2 the interaction is elastic and dominated by collective Coulomb repulsion. At higher t the strong force takes over, but elastic scattering is still a large fraction of the overall total interaction cross section – we find 25 mb elastic interactions out of a total cross section of 98 mb at 7 TeV [14]; the other part of the total

Table 2.1: The fundamental forces in nature and those in the Standard Model

Name	Explanation	Range of validity (m)	Charges	In SM
Electromagnetic	Theory for electric charges and electric+magnetic fields, combined by Maxwell [9]	$10^{-17} < r < \infty$	pos.,neg.	yes
Weak	Radioactive decays, combined with EM by Weinberg [10]	10^{-18} $\propto 1/M_W$	Flavour-changing	yes
Electroweak	Combination valid up to and beyond M_Z	$10^{-19} < r < \infty$		yes
Strong	Binding force for hadrons, residual force between hadrons	10^{-15} $\propto 1/m_\pi$	3 colours SU(3)	yes
Gravity	Non-quantum theory by Einstein (GR [11])	∞	pos.	no

cross section consists of inelastic interactions, which can be further subdivided into parton-level inelastic high-energy collisions and collective proton-proton diffractive interactions.

2.4.1 Diffractive processes

Diffraction is a particle interaction where the two colliding protons exchange a multi-gluon system with vacuum quantum numbers ($J^{PC} = 0^{++}$), and the protons either survive intact or the momentum transferred excites the proton to a low-lying nucleonic state ($p + p \to N^* + X$); there are many such N^*-states, starting with the $N^*(1440)$. It was named diffraction because of some analogies with optical scattering – the "diffractive excitation model" [15] and "Fireball model" [16] were first proposed as complete models of soft hadron-hadron interactions, before it was found that they only describe a fraction of the total. Because the interaction has no net colour charge, there will be a gap with no final-state particles between the two protons; this gap may be filled in by re-radiation during the late hadronisation stages in the same event [17], and this survival factor S^2 has been found to be smaller at the LHC than at the TeVatron, and was larger yet at HERA, so it shrinks with collision energy. However, the survival factor is

Table 2.2: The particles and force carriers in the Standard Model, according to [12]

Name	Symbol	Mass	Charge	Spin	Num.
Quarks		$[\frac{\text{GeV}}{\text{c}^2}]$		$\frac{1}{2}$	
up	u	1.8-2.7$*10^{-3}$	2/3		3
down	d	4.4-5.2$*10^{-3}$	-1/3		3
charm	c	1.24-1.30	2/3		3
strange	s	0.092-0.104	-1/3		3
top	t	173.0 ± 0.4	2/3		3
bottom	b	4.15-4.22	-1/3		3
Leptons				$\frac{1}{2}$	
electron	e	5.11$*10^{-4}$	-1		1
electron neutrino	ν_e	$< 2 * 10^{-6}$ (*)	0		1
muon	μ	0.106	-1		1
muon neutrino	ν_μ	$< 1.9 * 10^{-4}$ (*)	0		1
tau lepton	τ	1.78	-1		1
tau neutrino	ν_τ	< 0.0182 (*)	0		1
Electroweak vector bosons				1	
photon	γ	0 ($< 1 * 10^{-27}$)	0		1
W-boson	W^-/W^+	80.38	± 1		2
Z-boson	Z	91.19	0		1
gluons (SU(3) colour octet)	g	$0 * 10^{-3}$	0	1	8 3*3-1
SM scalar boson				0	
Higgs	H	125.2 ± 0.2	0		1
(*)	Neutrino $m_\nu > 0$ oscillations	$> 8 * 10^{-12}$			

process- and impact-parameter dependent, not a constant.

The diffractive process can have different topologies:

- When two protons exchange a single "Pomeron" – which is older terminology for the gluonic system exchanged – and one proton survives intact, separated by a rapidity gap from the remnants of the other proton, that is called Single

Diffraction (SD: $p+p \rightarrow p+\text{gap}+X$). SD has a diffractive mass $M_X \approx \sqrt{s \cdot \xi}$, where ξ is the fractional proton momentum loss, but also $gap = \delta y \approx -\ln(\xi)$. The expected cross section is $\mathcal{O}(10\text{ mb})$, approximately 20% of the total inelastic cross section.

- If both protons fragment, but are still separated by a gap, we call it Double Diffraction (DD), where we now have two masses M_X, M_Y and one gap $\delta y_{X,Y}$. The DD cross section is a smaller contribution, but still sizeable at 10% of the total inelastic one (< 10 mb [18]).

- Central Diffraction (CD) is obtained if both protons emit a Pomeron and those Pomerons form a central system, separated by gaps from both protons. The cross section for CD is smaller than for SD or DD, of the order 1 mb or less.

These processes are compared with nondiffractive and elastic interactions in Figure 2.2 and plotted schematically versus pseudorapidity η (along the beam axis) and ϕ, the azimuthal angle in the plane transverse to the beam.

Figure 2.2: Diagram of proton interactions used in this thesis. The red points represent surviving protons, while the dotted region is the remnants of the fragmented proton.

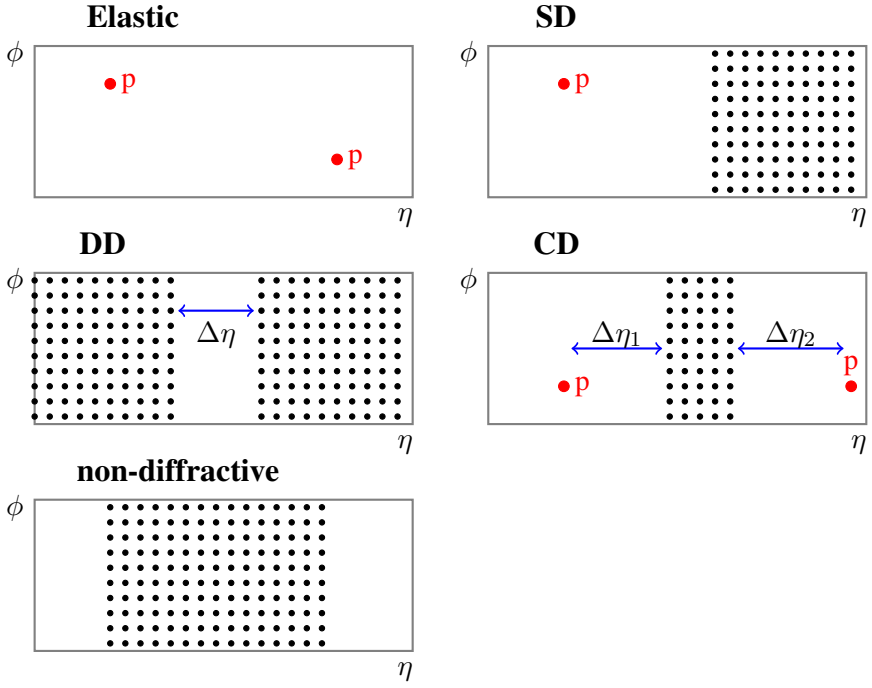

2.5 Strong interaction theory

2.5.1 Regge theory

Before the Standard Model of particle physics was formulated, several models for the strong interaction between nucleons and other hadrons were presented, among them the S-matrix theory [19–22]; it was named for the transition matrix S for all states from time $t = -\infty$ to $+\infty$. This theory sought to use constraints from known symmetries, analyticity assumptions (requirements from complex analysis on the continuity of complex functions for their total derivatives to exist, and their integrals on the complex plane (Here the Mandelstam variables were treated as complex, at the end taking the limit $\to 0^+$ for the imaginary part) and dispersion relations (complex integral equations from analyticity constraints) to find a unique matrix for evolving states from time t_a to t_b without needing a classical spacetime definition during the intervening timespan; based on this S-Matrix theory, Regge [23] reformulated quantum-mechanical potential scattering problems by generalizing the quantized angular momentum from integer to complex values, and assuming analyticity everywhere except for isolated poles and cuts, for easy integrability.

Reggeons

In [24], this Regge formulation was applied to hadronic scattering, where the very strong short-range nuclear force has many possible s-channel hadronic resonances as intermediaries, some of them having the same quantum numbers but differing amounts of quantized angular momentum $\ell = (0, 1, 2\ldots) \cdot \hbar$, or $J = \hbar\cdot$(half-)integer values, when the scattering particles have spins. For each such sequence R of resonances in the t-channel $t = m_i^2$, $\ell = \alpha_R(t)$, where $\alpha_R(m_i^2) = i$ are integer points on a t-channel Regge trajectory which can be approximated as $\alpha_i(t) = \alpha_i(0) + \alpha_i' \cdot t$. By extracting a prediction [24] for the transition matrix amplitudes T from this, it can be shown that the elastic scattering cross section

$$\frac{d\sigma_{el}}{dt} \approx |T(s,t)|^2 \cdot 1/s^2 \propto s^{2\alpha(t)-2}, \text{ where } S_{i,f} = \delta i, i + T_{i,f} \tag{2.21}$$

$$\sigma_{tot} \approx \Im(T(s, t = 0)) \cdot 1/s \propto s^{\alpha(0)-1} \tag{2.22}$$

From the known hadronic resonances, one can extract the corresponding Reggeon trajectories; for the meson (f, ρ, ω, etc) and baryon families (p,n,Δ,Λ,Σ) these turn

out to be substantially below 1 ($-0.8 < \alpha(0) < 0.5$), meaning the total cross section should go down with energy. This is not experimentally observed; TOTEM finds a total p-p cross section around 100 mb at 10^4 GeV, compared to ≈ 40 mb at $\sqrt{s} \approx 10$ GeV.

Pomeron

The Pomeron emerged as an ad-hoc Regge trajectory with linear intercept $\alpha(0) \approx 1$ to explain this high-energy cross section. This did not correspond to any known resonance, and being the t-channel process of elastic scattering, it had to have vacuum quantum numbers; as you can see in the sketch 2.3, s-channel $1 + 2 \to 1 + 2$ corresponds to $1 + \overline{1} \to 2 + \overline{2}$ in the t-channel. The self-interaction triple Pomeron vertex coupling is weak but nonzero, and it is challenging to making a self-consistent model of the Pomeron for this reason and because asymptotically, we expect $\alpha(0) < 1$ due to the Froissart bound [25, 26] on the total cross section, $\sigma_{tot} \propto \ln^2(s)$ [1]. The Froissart bound is due to the effective hadron interaction radius growing, at most, proportionately to the logarithm of s.

In the SM quantum theory of quarks and gluons (QCD, described below), the Pomeron corresponds to a ladder of several gluons constrained to have zero overall colour charge by a long-range (low-energy) "screening" gluon.

Pomeron interactions

Self-interaction The Pomeron has a self-interaction (three-Pomeron) vertex weaker than that for interaction with nucleons [28], so single-Pomeron exchange is a fair first approximation to Single Diffraction dissociation. To zeroth order in $\alpha(t)$, the double differential SD cross section in this Triple Regge model, with coupling constant $\mathcal{G}_{PPP}$, is

$$\frac{d^2\sigma_{SD}}{dt\, d\xi} \propto \mathcal{G}_{PPP} M_X^{-2} \exp(B(t,\xi)t) \tag{2.23}$$

$$\frac{d\sigma}{d\xi} \propto\approx \mathcal{G}_{PPP} (B(\xi)\xi)^{-1} \exp(B(\xi)t_{min}) \tag{2.24}$$

$$\frac{d\sigma}{d\log\xi} \propto\approx \mathcal{G}_{PPP} B(\xi)^{-1} \tag{2.25}$$

[1] the so-called Critical Pomeron [27] was proposed as a bare Pomeron pole with $\alpha(0) = 1 + \epsilon$, $\epsilon = 10^{-2}$ that would saturate the Froissart bound and have $\alpha(0) = 1$ after renormalisation, but was not able to give a consistent fit to all data

Figure 2.3: Schematic representation of elastic scattering as an s-channel process, and the corresponding (particle annihilation) t-channel diagram, obtained by rotating the left plot by 90°.

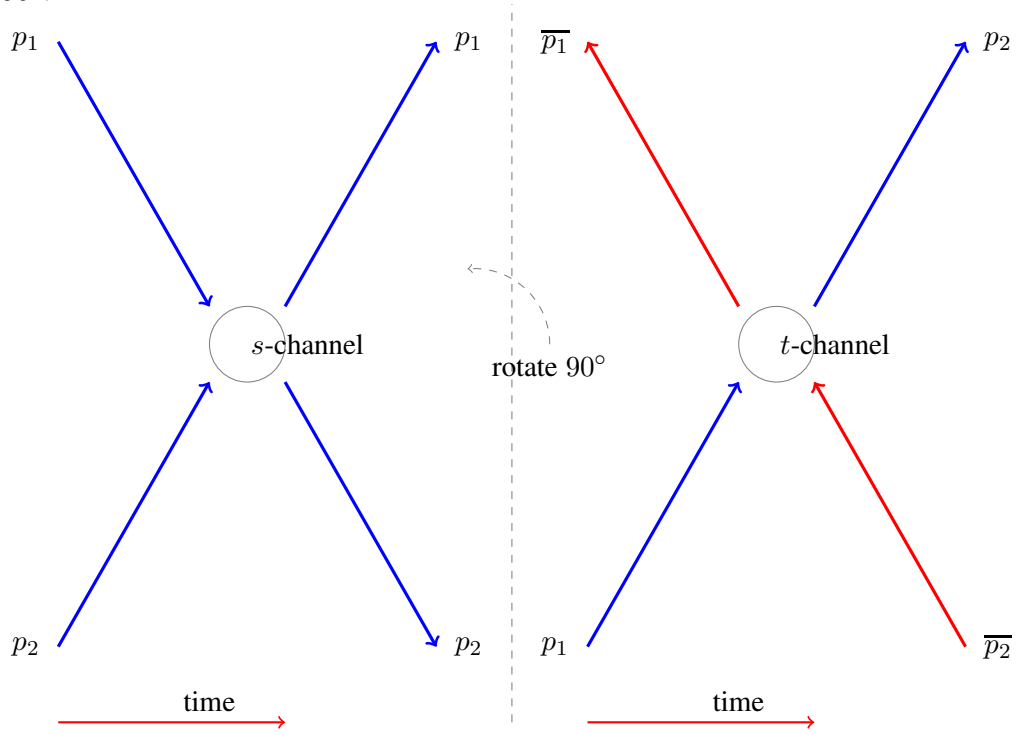

Taking into account $\alpha(t)$, [28] gives

$$\frac{d^2\sigma}{dt\, d\log\xi} \propto\approx \mathcal{G}_{PPP}\xi^{1+\alpha(0)-2\alpha(t)} \exp(B(\xi)t) \tag{2.26}$$

Since we assumed previously that $\alpha(t)$ can be approximated as a linear trajectory in t, we can move the t-dependence into the exponential slope by a redefinition of the exponential slope parameter $B(\xi, t)$ to $B'(\xi)$.

$$\alpha(t) = \alpha(0) + \alpha' \cdot t \tag{2.27}$$

$$\frac{d^2\sigma}{dt\, d\log\xi} \propto\approx \mathcal{G}_{PPP}\xi^{1-\alpha(0)} \exp(B(\xi)t - 2\alpha' \cdot \ln\xi \cdot t) \tag{2.28}$$

$$B'(\xi) = B(\xi) - 2\alpha' \cdot \ln\xi \tag{2.29}$$

$$\frac{d^2\sigma}{dt\, d\log\xi} \propto\approx \mathcal{G}_{PPP}\xi^{1-\alpha(0)} \exp(B'(\xi)t) \tag{2.30}$$

After this redefinition, the parameter $\alpha(0)$ can be extracted from the measured differential spectrum $d\sigma/d\log\xi$ for SD, assuming we have also measured the t-slope. This measurement was done by ATLAS [29] at 8 TeV, where they found a value of $\alpha(0) = 1.07 \pm 0.09$(tot.).

Fitting parameters Regge theory can contain multi-Reggeon and Pomeron interactions, some of which may be unitarity-violating at tree level and need some renormalisation, so there are many parameters that one can fit. However, many of the signatures of each, like the scaling with s, are hard to disentangle from data that does not span a very large range in collision energy [30]; for example, HERA and TeVatron results were explained in the 1990s by a single soft Pomeron with $\alpha(0) \approx 1.08$ [31], which alone would not violate the unitarity bound of Froissart before energies many orders of magnitude above the LHC, whereas later a combination of a hard ($\alpha(0) \approx 1.3$) "BFKL" Pomeron and soft ($\alpha(0) \approx 1$) Pomeron was also found to give a good fit over the range ISR to LHC [32, 33].

2.5.2 Quantum Chromo-Dynamics

Based on symmetries and degeneracies seen in the masses of light hadrons, among others, it was proposed in 1963 that hadrons could be understood as consisting of two or three fractionally charged constituents (called quarks by Murray Gell-Mann [34]). The quarks have charges of $\pm e/3$ or $\pm 2e/3$, and are fermions, with e being the fundamental electric charge. At first three quarks were known (u, d, s), with the strange quark known to be heavier. To satisfy the Pauli exclusion principle, baryons having three equivalent quarks, like the $\Omega(sss)$ must have some quantum number that differs for all three s-quarks. This strong force charge has been analogized to the additive RGB colours, in the sense that we can obtain a sum of "no colour" either by summing a colour and the same anti-colour (quark-antiquark pairs, like known mesons), or by summing together three colours into "white" (3 quarks, like known baryons). The quantum theory of the strong force has been named Quantum Chromodynamics following this analogy.

At the end of the decade deep inelastic scattering experiments [35] showed these partons to physically exist and to be quasi-free at high energy, but that they were always imprisoned within hadrons. This was understood as due to the strong coupling constant α_s running with energy to higher values at low energy; or equivalently, due to the colour exchange particle, the gluon, having a colour charge, unlike the electromagnetic photon, and therefore the strength of gluon exchange between coloured particles diverging as α_s grows. This self-coupling comes about because of the non-Abelian nature of the SU(3) symmetry group of QCD.

The discovery of the pointlike nature of hadron constituent partons in the 1960s

and the new heavy quarks found in the 1970s (c-quarks in J/Ψ [36, 37] and b-quarks in $\Upsilon(1S)$ [38, 39]) eventually validated QCD as a good description of the strong force at high energies, where perturbative expansions could be calculated in the so called perturbative QCD (pQCD).

2.5.3 Non-perturbative models

Below a (renormalisation-scheme-dependent) hadronisation scale $\Lambda_{QCD} < 1$ GeV, perturbation theory diverges and cannot be used to generated adequate predictions by summing the first few terms of a perturbative expansion in powers of the coupling constant, but QCD still applies. One way to obtain results on particle masses and decay widths is to perform numerical QCD calculations on a small lattice of points in space and time [40]. This is theoretically rigorous, but very numerically taxing, and must still be extrapolated to infinite box size and continuum spacetime, which gives an unavoidable systematic uncertainty. The strong force may also be phenomenologically modelled through fits to the nuclear and scattering data, which are more ad hoc, or making various simplifications of the QCD strong-coupling in various limits of low energy scale, zero temperature and so on. A simplified form of the confining QCD potential for the quarks has also been used to evaluate hadron masses and mass splittings [41].

For interactions with some momentum scale $p_X > \Lambda_{QCD}$ one can calculate the high energy part in pQCD and may be able to factorize out the nonperturbative part to a multiplicative prefactor, to be determined from the data for some analogous process. For proton interactions, these can be parametrised as structure functions $F_p(x, Q^2)$; here x is the parton momentum fraction, and Q^2 the momentum transfer squared. Depending on what variables (spin, etc.) are measured there may be multiple structure functions, and they may depend on additional variables.

2.6 Single Diffraction and the structure of the proton

2.6.1 Single diffraction

Single diffraction (SD) was first studied at fixed-target experiments in the 1960's and 70's[2] (for a presentation of previous results, see Appendix C).

[2] at Fermilab [42] and IHEP [43] (in Protvino, Russia), among others

SD was found to be lower-multiplicity than inelastic collisions in general, and quasi-exponential beyond a few initial resonance-like peaks at $M_X < 1.5$ GeV and therefore the first σ_{SD} integral cross sections reported are based on fitting a constant exponential slope in t, assuming a power law differential distribution in M_X [3], and integrating over both t and s, in a region $0 < -t < \infty$, $2 < M_X^2 < 0.05s$[4]. Later, it was intensively studied at the ISR [44, 45] [5], which as the first pp collider, could produce collisions approximately in the CoM and therefore allow easy tagging of all three components of SD: the proton (with special forward proton detectors [46]), the gap, and the remnants on the opposite side. This allowed good coverage at small and medium t, where the largest $d\sigma/dt$ contribution arises, and a measurement of the M_X spectrum both from the diffractive system and from a measurement of ξ for the surviving proton.

Single diffraction and elastic scattering, measured as a function of momentum exchange t and proton momentum loss ξ, gave information about the proton [47], and about the mediating gluonic state [48, 49].

At low ξ the SD interaction is expected to be mostly "Pomeron", but at higher $\xi > 10\%$, a Reggeon contribution also arises. Since the Reggeon trajectories have $\alpha(0) < 1$, they also contribute relatively more at lower s, thereby confounding expectations of scaling according to the simple triple-Pomeron vertex.

The differential cross section as a function of t is quasi-exponential $d\sigma/dt \approx a_0 \cdot \exp(-B_0 t)$, like the elastic p-p scattering below the dip (the minimum in the elastic cross section, beyond which the cross section has a maximum, followed by a powerlaw spectrum at very high $|t|$); the slope is different, and varies with SD-mass M_X. The differential M_X dependence had initially been parametrised as $\propto M_X^{-2}$, since this dependence was seen at low M_X on top of an inelastic continuum, if rapidity gaps were not selected in the analysis.

2.6.2 Diffraction and proton structure

Diffractive processes like SD give information about the transverse distribution of the proton. This distribution can be extracted from the differential spectra of SD (and elastic) measurements, by transforming from momentum space ($t = q^2$, where q is

[3] if triple-Pomeron coupling is dominant we expect $d\sigma/dM_X^2 \propto M_X^{-2}$ and at most logarithmic change vs. s, $\propto \ln^{0/1/2}(s)$

[4] The conventional upper limit to exclude the Reggeon-dominated high-ξ mass range.

[5] the latter SD analysis was never published

the virtual momentum transfer) to impact parameter space (b is the transverse distance between the colliding protons).

Other diffractive and elastic processes also give constraints to the proton structure; for example, [50] argues CD would violate the Froissart bound on the total cross section, unless the proton is maximally opaque in central elastic scattering. On the other hand, a maximally opaque "Black disc" approximation for proton scattering is known to give $\sigma_{el} = \sigma_{inel} = \frac{1}{2}\sigma_{tot}$, while TOTEM measures the elastic-to-total ratio as still only around 26% at 7 TeV [14], with equality reachable only many orders of magnitudes above the present LHC energies. However, models containing diffraction may have a stricter limit: Pumplin [51] found a limit of $\frac{1}{2}\sigma_{tot}$ for the sum of diffractive and elastic cross sections.

Chapter 3

Experiment

3.1 Large Hadron Collider

CERN (Conseil Européen pour la Recherche Nucléaire) is a large European particle physics centre at the French-Swiss border in Geneva, whose flagship particle accelerator during the last decade has been the Large Hadron Collider (LHC), an underground proton-proton collider in a 27 km-circumference tunnel. The LHC started collecting data in 2009, and has plans to continue running for the next two decades, at least. The maximum collision energy was raised from 7 TeV in 2011, to 8 TeV in 2012, and to the present value of 13 TeV in the latest data run (2015-2018). Right now the LHC is in the Long Shutdown 2 (from 2019-2021), and work is ongoing to upgrade all the detectors and collider infrastructure to reach the planned maximum energy of 14 TeV with a very high luminosity of $\mathcal{L} > 2 \cdot 10^{34} cm^{-2} s^{-1}$ at the beginning of 2022.

3.1.1 LHC parameters

The protons in the LHC are first accelerated in the Super Proton Synchrotron (SPS) to 450 GeV and then injected into the main ring in the form of bunches containing $\sim 10^{11}$ protons each, the bunch separation being 25 ns at present – at the time of the 2011 run, it was 50 ns, corresponding to an inter-bunch distance of 15 m. They are then accelerated symmetrically to half the maximum design collision energy quoted above (3.5 – 7 TeV); that maximum is reached when they collide head-on, but the crossing angle is not precisely zero so that the beams separate after the designated interaction point (IP). In ordinary high-luminosity data taking the beams are compressed to their minimum cross section of $\mathcal{O}(10)\,\mu m$, leading to tens of protons per bunch crossing

experiencing high-energy mutual scattering[1], since the effective proton radius is much smaller, at ≈ 1 fm. Beam emittance ϵ (proportional to the beam size and beam angular dispersion) is approximately a constant, so if we want to measure small-angle proton scattering, we must use a very wide beam (high β^* at the interaction point), which results in a lower interaction probability (cross section).

The beam size in the x or y plane at any point s ($\approx z$) along the circular trajectory around the LHC is given by

$$\epsilon = \text{constant, or growing}$$
$$\sigma_{x/y}(s) = \sqrt{\epsilon\beta_{x/y}(s)},$$

where $\beta_x(s)$ is the beta function, whose value at $s = 0$ is β^*.

For an overview of the main LHC parameters, see table 3.1.

Table 3.1: Parameters of the Large Hadron Collider [52] at CERN as of 2011 [53]

	Special TOTEM run	Regular (2011)
Parameter (unit)	(2011)	Data Taking
Luminosity ($cm^{-2}s^{-1}$)	$1 * 10^{28}$	$3.6 * 10^{33}$
Bunch spacing (ns)	-	50
Number of bunches	1+1(non)+13(small)	1380
Circulating beam current (A)	-	0.362
Protons per bunch	$6 * 10^{10}$	$1.45 * 10^{11}$
Interactions per crossing	0.03	-
β^* at IP (m)	90	1
Proton energy (TeV)	3.5	3.5
Proton rapidity y (1)	± 8.92	± 8.92

3.1.2 LHC optics

Magnets are used to "trap" the protons in a circular orbit around the LHC [52]. Dipole bending magnets deviate the whole proton bunch into a circle, whereas quadrupole magnets focus and defocus the beam alternatively in the vertical and horizontal plane,

[1] Most are pileup, a background to collisions of interest.

on net confining the proton bunch in both. The optics are further fine-tuned with higher-order magnets, like octupoles. The magnets are superconductive electromagnets with a maximum bending field of 8.3T, and a maximum current of 11 kA, in 13 TeV operation in 2018. Since quadrupole magnets can focus charged particles (with the focal length depending on the field gradient in the magnet and the magnet length), the proton transport around the collider is called "magnetic optics", in analogy with classical geometric optics.

The proton position and momentum vector at any point along the circular orbit depends on the collider optics and the proton position at the IP $(x, y)|_{IP}$, the angle at the IP $(\theta_x, \theta_y)|_{IP}$ and the fractional momentum loss with respect to beam protons ξ. This function can be expressed in a linear approximation as a matrix equation, whose elements have been measured by TOTEM [54],

$$\begin{pmatrix} x(s) \\ \theta_x(s) \\ y(s) \\ \theta_y(s) \\ \xi \end{pmatrix} = \begin{pmatrix} v_x(s,\xi) & L_x(s,\xi) & 0 & 0 & D_x(s,\xi) \\ \frac{dv_x}{ds}(s,\xi) & \frac{dL_x}{ds}(s,\xi) & 0 & 0 & \frac{dD_x}{ds}(s,\xi) \\ 0 & 0 & v_y(s,\xi) & L_y(s,\xi) & D_y(s,\xi) \\ 0 & 0 & \frac{dv_y}{ds}(s,\xi) & \frac{dL_y}{ds}(s,\xi) & \frac{dD_y}{ds}(s,\xi) \\ 0 & 0 & 0 & 0 & 1 \end{pmatrix} * \begin{pmatrix} x(0) \\ \theta_x(0) \\ y(0) \\ \theta_y(0) \\ \xi \end{pmatrix} \tag{3.1}$$

Here s is the position parameter along the LHC ring, as defined previously. The optical functions are the individual nonzero elements of the transport matrix; $v_{x,y}$ is the magnification function, $L_{x,y}$ the effective length, and $D_{x,y}$ is the dispersion. The data used for this thesis were taken with a special β^* = 90 m optics allowing the measurement of smaller vertical scattering angles by the RPs. For elastic and low-mass SD protons in the β^* = 90 m optics, these functions are approximately constant at a given s, and in particular $L_x \approx 0$ near the vertical far RPs, while $D_y \approx 0$ and $v_y \approx 0$ for small ξ, simplifying the reconstruction of low-ξ protons. Some representative values for the optical functions of the β^* = 90 m optics are given in Table 3.2, and shown as a function of ξ in Figures 3.1 - 3.6.

3.1.3 LHC Predecessor : electron-positron collisions

The predecessor of the LHC was the Large Electron-Positron collider (LEP), for which the present LHC tunnel was built (in 1985-1988). LEP ran from 1989 to 2000, at energies ranging from 90 GeV to 209 GeV, limited by the very high synchrotron loss

Table 3.2: Values for the optical functions at proton momentum loss $\xi = 0$, -2.7%, and -20%, at the edges between the two SD classes 1T2 and 2T2, see Table 5.2, in near and far RPs, for the β^* = 90 m optics.

Function	Value ($\xi = 0\%$)	Value (-2.7%)	Value (-20%)
Name [unit]	(near/far)	(near/far)	(near/far)
L_x [m]	2.9/0.001	-1.2/-3.6	-34/-30
L_y [m]	238/263	236/261	171/191
D_x [mm]	-57/-43	-57/-42	-56/-23
D_y [mm]	7/6	14/14	120/140
v_x [1]	-2.16/-1.87	-2.18/-1.86	-2.11/-1.62
v_y [1]	0.02/0.00	-0.27/-0.33	-3.48/-3.93

from electrons under continuous circular acceleration. This limit does not affect protons in the same tunnel, since to a first approximation, charged particles lose energy proportional to m^{-4}, so $dE_p^{(sync.)}/dz \propto (m_e/m_p)^4 \approx 8.8 * 10^{-14}$ for protons.

3.1.4 LHC history

The Large Hadron Collider (LHC) was proposed as a hadron collider that would reuse the LEP tunnel. it was decided to maximize the luminosity of the LHC to compensate for the lower energy of the LHC compared to the U.S. Superconducting Supercollider (SSC), which was due to the LHC having a shorter tunnel. By using proton-proton collisions, the constraints and inefficiencies from antiproton production, deceleration, storage, and reacceleration that had affected the Tevatron and the CERN SPS would be bypassed.

See Appendix B for a discussion why the LHC collision energy was 7 TeV in the 2011 special run, only half the design value of 14 TeV.

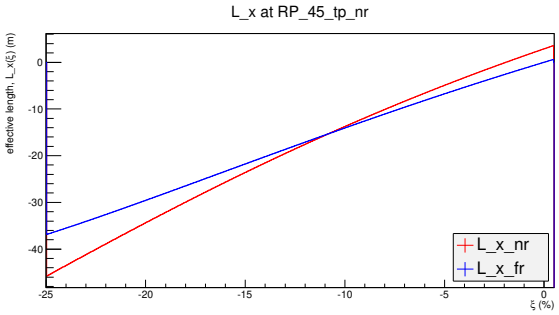

Figure 3.1: Effective length in x, for near and far RPs, for the β^* = 90 m optics.

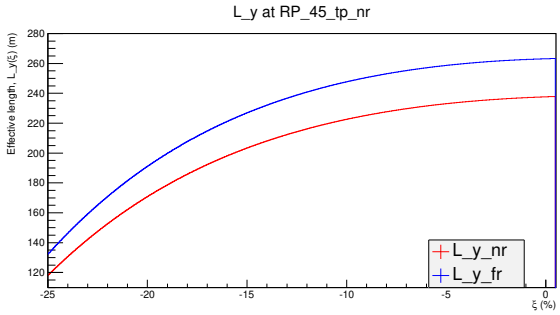

Figure 3.2: Effective length in y, for near and far RPs, for the β^* = 90 m optics.

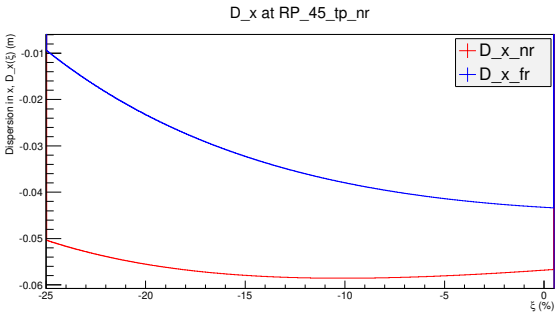

Figure 3.3: Dispersion in x, for near and far RPs, for the β^* = 90 m optics.

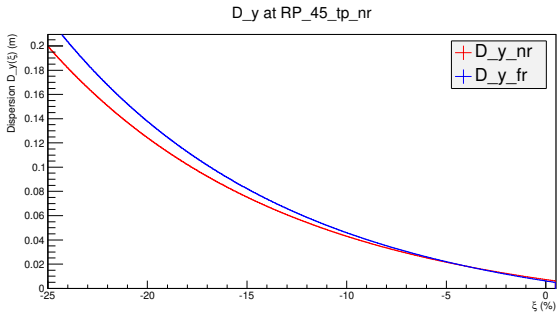

Figure 3.4: Dispersion in y, for near and far RPs, for the β^* = 90 m optics.

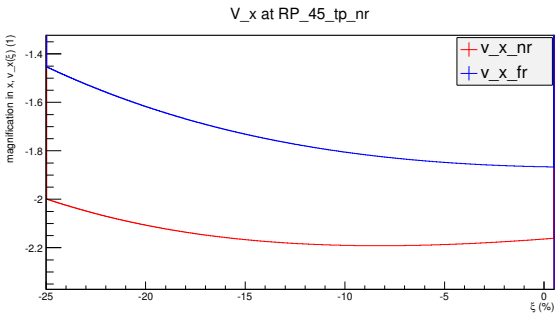

Figure 3.5: Magnification in x, for near and far RPs, for the β^* = 90 m optics.

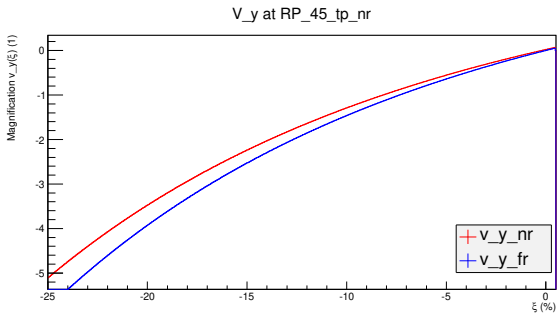

Figure 3.6: Magnification in y, for near and far RPs, for the β^* = 90 m optics.

3.2 TOTEM experiment

3.2.1 Physics programme

The TOTEM experiment [55] is a dedicated collaboration to study diffraction, elastic scattering and the total cross-section at the LHC. TOTEM has measured elastic scattering at many energies between 2.76 TeV and 13 TeV [2,5,14,56–62]. The total cross section has also been studied, with multiple independent methods, in [5, 14, 56, 57]. Finally, different topologies of diffraction have been measured, too; double diffraction [3], where two protons collide and both decay to low-mass baryon resonances, separated by a large rapidity gap, and single diffraction [63], where one proton survives intact.

3.2.2 Experimental apparatus

TOTEM has three subdetectors placed symmetrically on both sides of the interaction point: Roman Pot detectors to identify leading protons at 220 m from the IP, and the T1 and T2 telescopes (at 9 m and 14 m from the IP, respectively) to detect charged particles in the forward region. The data is read out by VFAT[2] cards [64] at each detector and sent to the Data AcQuisition (DAQ) system for storage. The short form names of the TOTEM detectors used in this thesis are given in Table 3.3.

T1 telescope

The T1 telescope in each arm consists of 30 cathode strip chambers distributed in 5 planes that measure charged particles with p_T >100 MeV/c at pseudo-rapidities[3] of 3.1< $|\eta|$ <4.7, with full 2π coverage in the azimuthal angle, and a spatial resolution of 1 mm. This detector has a trigger capability, but was not used for triggering in the Oct 2011 special run analysed in this thesis. For this detector only, there was also a gradual desynchronization of the VFAT output from the corresponding event data for T2 and RP, during some runs. This lead us to only analyse the run segments until the first desynchronized event appears; for example, we use $2.3 * 10^6$ out of $8 * 10^6$ events taken with the RP's positioned at 6.5 times the transverse beam size (σ_{beam}); see Table 3.5 for all the data subsamples. See Figures 3.7 and 3.8 for pre-installation pictures.

[2]TOTEM-specific ASIC cards

[3]η=-ln[tan(θ/2)] where θ is the polar angle.

Figure 3.7: One half-arm of T1, assembled before installation (trusses not shown)

Figure 3.8: One T1 plane shown before final assembly

T2 telescope

In each arm, T2 [4] consists of 20 half-planes of triple-GEM (Gas Electron Multiplier [65], chosen for excellent radiation hardness) chambers that detect charged particles with p_T >40 MeV/c at 5.3 < $|\eta|$ < 6.5, and also has full coverage in ϕ, the azimuthal angle (each half-arm telescope covers $192°$, giving a small overlap region). The GEM-foils are made from 50 μm thick kapton foil with a conductive film of 5 μm copper on both sides, with $\approx 70\mu m$ wide holes in the foil every 140 μm. By applying a voltage of ≈ 500 V between the upper and lower copper film, the electric field in any hole will give electrons entering enough energy to ionize more electrons. This multiplication is done in three stages (3 GEM foils) to allow operation at lower voltages, where the degradation of the foil is much smaller; the voltage applied to the latter foils is also somewhat smaller to minimize the probability of uncontrolled discharges or sparks. The foils are separated by a 2 mm drift space from each other and from the readout electronics board, for isolation and to allow the signal to spread out to more holes in the latter stages of multiplication. The detector readout is segmented into 2*256 radial strips with 0.1 mm resolution ($\delta\phi = 96°$) and 24*65 (η, ϕ) pads with a size $(\delta\eta, \delta\phi) = (0.06, 2.7°)$, meaning the linear size of the pads is smaller nearest to the beam. The trigger signal is based on groups of 3*5 pads (superpads) that need to have signal in 5 out of 10 planes, corresponding to a linear track with allowance for tracks near the edge between superpads.

This detector can trigger $> 95\%$ [5] of inelastic events, missing only very low mass

[4] The T2 planes were assembled and tested in the HIP Detector Laboratory here in Helsinki.

[5] Value at 7 TeV, checked for multiple MC with differing diffraction cross sections

SD events with M_X < 3.1 GeV/c^2. This detector was used for triggering SD events and finding events with rapidity gaps covering one arm of T2 in the 2011 special run. See Figures 3.9 to 3.11 for pre-installation pictures.

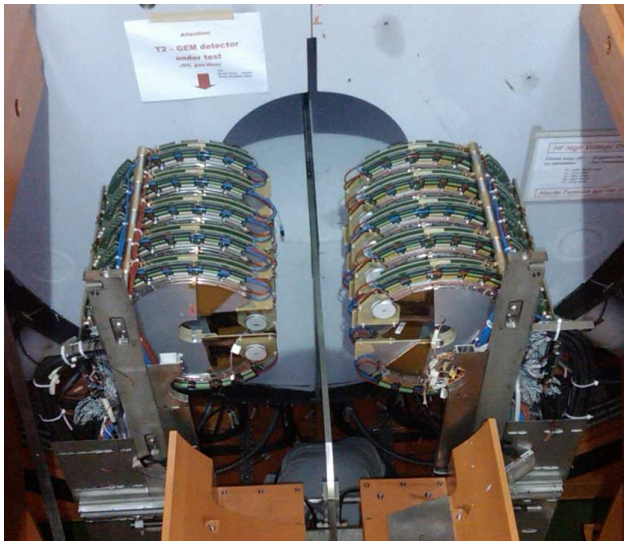

Figure 3.9: One arm of T2, assembled before installation for a test run

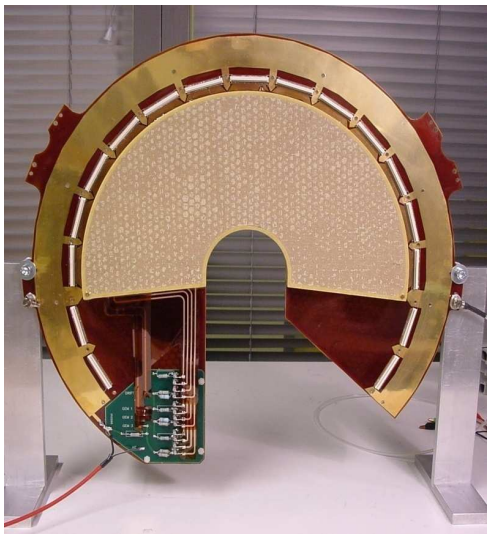

Figure 3.10: One T2 plane shown before final assembly

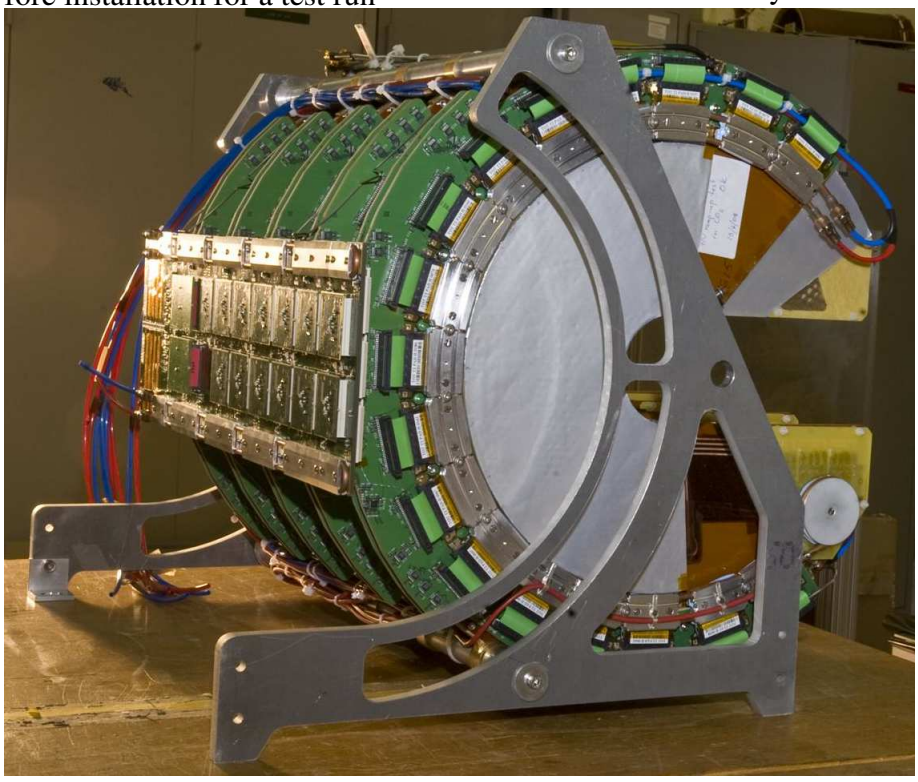

Figure 3.11: Five T2 half-planes assembled

Roman Pots

The Roman Pots (RP) are silicon strip detectors at 220 m from the interaction point with a very thin insensitive edge, housed in a moveable pressurised "pot" (with a thin window separating the detector from the beampipe vacuum) that can approach the beam very closely. The RPs measure scattered protons: with the high-β^* special LHC optics (β^* = 90 m) they can detect a proton with any amount of momentum loss for vertical momentum transfers larger than $|t_y| > 0.005$ GeV^2.

An RP consists of 10 planes, 5 planes oriented at $+45^\circ$ in the (x, y) plane, the other 5 being at -45°; they are called u- and v-planes, respectively, and have 512 strips and a strip pitch of 66 μm each. Because each plane only measures the proton position in one dimension, the reconstruction of multiple protons would be ambiguous (2 hits in both coordinates would give 4 possible positions for 2 protons). Since our signal has only one proton and the data set has low pileup, we use a single-track reconstruction module, treating events with signal and background protons in the same pot as an inefficiency that we correct for in the final result. The first level of the RP trigger looks for a single linear track in at least 3 out of 5 u or v planes, within a track road 32 strips wide (equal to 2 mm).

There are 12 RPs in all, 6 in one arm of the LHC, positioned as pairs at distance of 5m to measure both the local proton position and local track angle. These 3 pairs approach the beam from the top and bottom (four vertical pots that see all protons in the RP acceptance including elastic, used for SD topology RP tracks), and from the side (two horizontal pots, not used for SD topology estimation, only for reconstructing high-ξ protons ($|\xi| > 10\%$) that hit four overlapping pots instead of only two neighbours, useful for alignment corrections).

The elastic protons and low-mass SD protons are detected in the vertical RPs only, because the displacement from x = 0 is proportional to the momentum loss ξ, while the horizontal pots cover only x > 10 mm.

See Figures 3.12 to 3.14 for pictures of RP planes, installed view of an RP station, and the Roman Pots themselves that the detector type is named for[6].

[6]They were first used by the Rome-CERN group at the ISR [26]

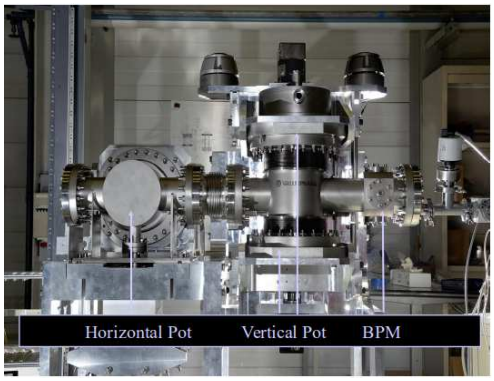

Figure 3.12: A Roman Pot station

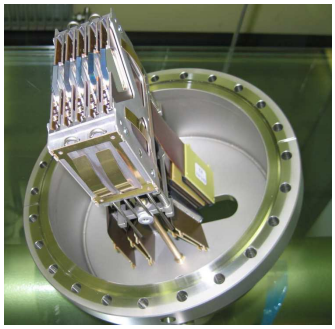

Figure 3.13: Five RP planes before assembly

Figure 3.14: Roman Pots shown without beam tubing

Trigger

The TOTEM data readout is initialised by the level-one hardware programmable trigger, which can trigger on activity in T1 or T2, on combinations of the two arms of the RPs (including all RPs or only the vertical or horizontal), and on zero bias (bunch-crossings BX).The trigger bits used in the data taking that this analysis is based on are shown in Table 3.4. The data are read out by VFAT cards from each detector, and sent to the DAQ for storage.

3.2.3 Calibrations

RP alignment and LHC optics

The RP detectors are aligned in three stages. First, the edge of the beam is scraped by LHC collimators to a known multiple of the beam size σ, and the RPs are allowed

Table 3.3: TOTEM and LHC naming conventions

Name	Description
IP5	The IP where TOTEM and CMS are
Arm 4-5	The beam direction to IP4
Arm 5-6	The beam direction to IP6
T2-	T2 negative arm, in arm 5-6
T2+	T2 positive arm, in arm 4-5
RP_V	Some or all vertical RP's
45_tp	2 vertical top RP's in arm 4-5
45_bt	2 vertical bottom RP's in arm 4-5
45_hr	2 horizontal RP's in arm 4-5
56_tp	2 vertical top RP's in arm 5-6
56_bt	2 vertical bottom RP's in arm 5-6
56_hr	2 horizontal RP's in arm 5-6
45_tp_nr	vertical top near RP in 4-5, ≈ 215 m from IP5
45_tp_fr	vertical top far RP in 4-5, ≈ 220 m from IP5
. . . _nr & _fr	12 RP's in total

Table 3.4: Trigger bits used in the special TOTEM Oct 2011 run

Trigger bit	Description
T2	T2- "or" T2+
RP-2arm	in each arm, near "or" far + two arms: arm 4-5 "and" 5-6
RP-1arm	in both arms, near "or" far and arm 4-5 "or" 5-6
RP-V-2arm	Vertical RP's only: two arms 4-5 "and" 5-6, each arm near "or" far
BX	Bunch crossing events, taken at fixed time intervals. Not dependent on contents of the event.

to approach the beam in steps of $5\mu m$ [2] and retracted $0.8 \ldots 2 * \sigma$ when they hit the rapidly increasing rate at the scraped edge of the beam envelope. This defines an

approximate beam-based alignment position for each individual pot. Second, tracks detected in both near and far RPs, and in the overlapping area of horizontal and vertical RPs are used to find the inter-RP track-based misalignment. Finally, elastic proton tracks (that are exactly 180° apart in the centre-of-mass frame, which is to a good approximation equal to the LHC rest frame) are selected from the data and used for finding misalignments between diametrically opposite pots in tilt and shifts.

The measured final elastic alignment correction extracted from the analysed data set is applied to both simulated and real data in this analysis.

Luminosity

To convert measured rates to cross sections with equation 2.17, we use the luminosity measured (as a function of time) simultaneously by CMS [66], with a quoted uncertainty of 4%. On average, the instantaneous luminosity for the one colliding bunch (out of 15 total) was 6 $mb^{-1}s^{-1}$.

3.3 Data sets and published results

This analysis uses proton-proton collision data that TOTEM collected in October 2011 at 7 TeV, with $\beta^* = 90$m; the RPs approached the beam to within 4.8/5.5/6.5σ_{beam}. The data was taken with triggers on bunch crossings ("BX", ca 200 Hz), on vertical RPs ("RP-V-2arm") or all RPs ("RP-2arm") in two-arm coincidence or on the T2 ("T2"), where the combined rate of the RP and T2 triggers was ca 500 Hz. The detailed conditions for the triggers can be found in Table 3.4. The pileup probability per collision in this run was $\approx 3\%$, and the minimum proton $|t|$ observed before applying any selection cuts was $|t| \approx 0.005 \ldots 0.008$ GeV^2. The luminosity and pileup slowly fell from the beginning of the data taking to the end as protons were continuously scattered out of the main bunch, but the effect is not large, and in this analysis we assume constant pileup and use a random selection from the whole BX sample to estimate what synthetic pileup events would look like, for pileup subtraction (described later in chapters 4.5.1 and 5.2). The Beam Halo background – that is, displaced beam protons reconstructed in the RPs as scattered protons coming from the IP – was studied using events selected with a single-arm RP trigger ("RP-1arm") in data from an initial run called segment 0. In segment 0 data was taken with triggers BX (ca 80 Hz), T2 (small rate) and single-arm RP-1arm (ca 570 Hz). The data taken and that used in this analysis are

shown in Table 3.5.

Table 3.5: Data samples from the special Oct 2011 run, and those used for this analysis, with correctly sync'ed T1 readout. Segment ("Seg.") is the label used for data segments with given settings for RP and trigger.

Seg.	RP position (σ_b)	Total events (10^6)	Selected events (10^6)	Comments
0	5.0	0.74	-	RP-1arm
1a	6.5	0.58	0.58	RP-V-2arm trigger
1b	6.5	8.64	2.29	RP-2arm trigger (main sample)
2	5.5	1.18	0.28	RP-2arm
3	4.8	1.03	0.42	RP-2arm

See Tables 3.6 – 3.7 for a short description of articles we have published based on data taken in and after 2011. Based on these data, we have published elastic, inelastic and total cross sections [2, 14, 56, 67], and double diffraction [3] measurements.

Lately, TOTEM has shown two pieces of experimental evidence for a C-odd (antisymmetric under exchange of particle for antiparticle) t-channel exchange, mediated by a three-gluon system, which has previously been argued to be the QCD "Odderon" [68]. Firstly, a precise measurement of ρ, the ratio of the real and imaginary part of the elastic nuclear amplitude at t = 0, done at 13 TeV, which in combination with all previous TOTEM total proton-proton cross section measurements from 2.76 to 13 TeV does not seem to allow a good description using only C-even t-channel exchange [60]. Secondly, a measurement of the proton-proton differential elastic cross section versus t at 2.76 TeV [62], which is characterized by a clear diffractive minimum, contrary to the corresponding D0 measurement in proton-antiproton collisions at the nearby energy 1.96 TeV, which only exhibits a "kink" in the differential elastic cross section t-spectrum. This apparent difference in elastic scattering of proton on proton and proton on antiproton in the TeV energy range would be a sign of C-odd t-channel exchange.

Table 3.6: Articles and PhD theses published based on TOTEM special runs

Date	Detector configuration	$\sqrt{s}$ (TeV)	β^* (m)	integr. lumi.	selected articles
Oct 2010	RP $7\sigma_b$	7	3.5	6.1/nb	elastic, $0.36 < \|t\| < 2.5$ GeV^2 [2]
May 2011	T1, T2	7	1.5	$(\frac{8}{mb \cdot s})$	charged particle multiplicity [69, 70] $dN_{ch}/d\eta$, for $5.3 < \|\eta\| < 6.4$
Jun 2011	RP $10\sigma_b$ T1, T2	7	90	1.7/μb	elastic $0.02 < \|t\| < 0.33$ GeV^2 [71] and total cross section [14]
Oct 2011	RP 4.8-6.5σ_b T1, T2	7	90	83/μb	elastic $5 * 10^{-3} < \|t\| < 0.37$ GeV^2, total and inelastic [14, 56, 67], also Double Diffractive (DD) [3] and SD (this thesis)
Jul 2012	RP 6-9.5σ_b T1, T2, CMS	8	90	45/μb	elastic $10^{-2} < \|t\| < 1.2$ GeV^2 [57] total and inelastic (lumi. indep.), elastic $0.027 < \|t\| < 0.2$ GeV^2 [58] $dN_{ch}/d\eta$, for $5.3 < \|\eta\| < 6.4$ and $\|\eta\| < 2.2$ [4], inelastic classification [63]
Sep 2012	T2	8	90	-	$dN_{ch}/d\eta$, for $3.9 < \eta < 4.7$, and $-6.95 < \eta < -6.9$ [72] (displaced interaction point by 11.25m from nominal IP5)
Oct 2012	RP 3-10σ_b T1, T2	8	1000	20/μb	elastic $6 * 10^{-4} < \|t\| < 0.2$ GeV^2, Coulomb-nuclear interference (CNI) and total [59]
Feb 2013	RP $13\sigma_b$ T1, T2	2.76	11	$(\frac{0.1}{nb \cdot s})$	elastic $0.36 < \|t\| < 0.74$ GeV^2 [62]
Oct 2015	RP 5-10σ_b T2 CMS	13	90	0.4/pb	elastic, total, and inelastic (lumi.indep.) [5], differential elastic [61]

Table 3.7: Articles and PhD theses published based on TOTEM special runs, cont.

Date	Detector configuration	$\sqrt{s}$ (TeV)	β^* (m)	integr. lumi.	selected articles
Sep 2016	RP $3\sigma_b$	13	2500	0.4/nb	elastic $\|t\| > 8 * 10^{-4}$ GeV^2 , CNI [60]
Jul 2018	RP CMS	13	90	5/pb	
Oct 2018	RP	0.9	90		

Chapter 4

Software tools

To analyse the data taken with the TOTEM detectors described in the last chapter, we need to be able to simulate both the production of particles, and their detection as they traverse the volume of the detectors. For the first part, we use the general-purpose Monte Carlo particle simulator Pythia, but also the specifically diffraction-focused MCs EPOS and QGSJet. The detector simulation is a TOTEM-specific version of the CMSSW software framework used by the CMS experiment.

4.1 Event generators

4.1.1 Pythia 8

PYTHIA 8 is a general-purpose Monte Carlo particle simulation framework [73], which has been tuned with successive LHC data releases, but still underestimates the high ξ diffractive proton in comparison to QGSJet II, described below. PYTHIA 8 has an SD implementation that is a little steeper than its predecessor PYTHIA 6 at low masses, $\propto M_X^{-1-2*\delta}$ ($\delta = 0.085$), based on the Donnachie-Landshoff triple-Pomeron model [74], whereas PYTHIA 6 [75] had a triple-Pomeron process with $\delta = 0$ ($\propto M_X^{-1}$) [18].

4.1.2 QGSJet II

QGSJet II.04 [76] was planned to be used as reference for the analysis of the real data since it has the most complete implementation of soft Reggeon theory [17, 77] and is more consistent with the low mass diffraction estimate of TOTEM at 7 TeV [67]

than e.g. Pythia 8. In addition, QGSJet II gives more high-mass diffraction than PYTHIA. However, the momentum conservation in the CMSSW implementation of QGSJet II.04 was not found to be satisfactory and was therefore not used in the analysis.

This version of QGSJet had been benchmarked [78] against CMS and TOTEM SD and DD data including a very preliminary version [79] of the measurement presented here. This very preliminary measurement contained a rough estimate of the systematic uncertainties ($\pm$ 20%), no class migration and only within-class unfolding, and a T2 track-based trigger efficiency correction bug. The largest change will occur for the 1T2-2T1 class, where the important class migration to the 2T2 class was neglected.

The author provided us with predictions from the II.04 version of the event generator for comparison with the measurements in this thesis. These predictions are presented in Appendix N.

4.1.3 EPOS

EPOS [80, 81] is a cosmic ray air shower and heavy-ion particle simulator first created in 2005 [82]; the version used in this thesis (called EPOS LHC) was based on EPOS 1.99 [83], tuned with LHC data. EPOS is based on a parton-level Regge formulation [84] where parton ladders (QCD flux tubes) interact with nuclear matter and other flux tubes to give a simulation of jets and in-medium modifications of jets and hadrons [85, 86]. The parton ladders contain both hard (QCD) and soft scattering, the latter being parametrised Regge poles. The retuned EPOS LHC version does not use a full 3D hydrodynamic simulation in the interest of speed, which makes it less suited for precise predictions for heavy-ion collisions, but the MC authors propose [80] it as a good model for few-nucleon collisions like $p + p$ or $p + A$.

EPOS is used as one of the references along with PYTHIA 8 for MC-dependent measures, namely class migration from SD class based on particle topology to reconstructed detector track topology, and unfolding of integral and differential cross section spectra, see Section 4.4 below.

4.1.4 MC data sets

The MC generators EPOS and Pythia (and QGSJet, too) were used to produce samples of 150 000 to 1 000 000 events that were fully reconstructed in TOTEM software, as

MC Data samples	Events	SD-like events
EPOS, general inelastic	1 000 000	175 000 (particle level)
Pythia 8 SD only	210 000	203 000 (particle level)
Real data:		after all selection cuts
Seg 1b main sample	1 439 000	54 000 (SD classes 1T2 and 2T2, track level)
Seg 1b systematic comparison	900 000	35 000

Table 4.1: MC data set size, comparison with real data

described below. This was done separately for all parameter values whose impact on the results were studied. These samples were used for unfolding and doing the full chain of reconstruction and analysis code validation. The various simulated data sets are shown in Table 4.1, and compared with the main real data samples.

In order to avoid various over-learning biases in the unfolding process, we wanted to have approximately equal number of SD events in the various data sets, both MC and real data. This was enforced more strictly for the MC samples, since we want to evaluate the MC bias by unfolding one sample with the other as learning sample, and vice versa. Therefore the latest results presented in this thesis use an EPOS sample with around 175 000 events matching one of the five SD signal classes in generator-level particle topology, defined in Table 5.1. The Pythia 8 SD sample contains around 203 000 matching events out of 210 000 total, and the main real data sample contains around 54 000 SD-class after all cuts, counting only the four SD classes with tracks in T2.

4.2 CMS Offline Software

The TOTEM detector is simulated with CMSSW, a Geant4 [87] and OSCAR-based [88] simulation software that was written in C++ for the general-purpose CMS (Common Muon Solenoid) experiment at the same interaction point (IP5). Geant4 is used for simulation of the interactions between the long-lived particles produced in the (user-selected) MC with the physical material in the detectors. CMSSW contains a (simplified) mapping of all the detectors, their components and the materials they are built from. Each detector then has one or more module that simulates the data produced, possibly in multiple hierarchical layers, like hits forming a track candidate, track candidates forming a track, and finally, beyond the detector level, there are modules combining detector outputs to create physics-level reconstructed particle objects.

4.2.1 TOTEM software in CMSSW

The TOTEM code consists of CMSSW modules for the various subdetectors and readout systems of TOTEM, and can be run both as an online data monitor, and as offline reconstruction software. This data analysis uses the validated TOTEM offline software built on top of CMSSW versions 4.2.4 and 7.0.4.RunI, and the experimental version 6.2.0. To speed up the analysis, both the one in this thesis and previous published results, TOTEM created a so-called Ntuple[1] of just the trigger and track information for the three TOTEM detectors in as small a representation as possible, extracting the necessary parts from the full reconstructed data.

T1+T2

The inelastic telescopes T1 and T2 use a common class for reconstructed tracks (*T1T2Track*), produced by four levels of reconstruction modules: hit finding, hit clusterization (T2 only), cluster road-finding, and track selection from cluster roads. These were written by Mirko Berretti (T2) and Fabrizio Ferro (T1) [67, 89]. The T1 detector layout is not orthogonal to the x, y, and z-vector of the LHC coordinate system that we want to measure hits in. However, after finding the individual T1 hits, a pattern recognition road-finding module produces "roads" in (η, ϕ) that can be projected to linear tracks in

[1] A flat information tree

the (x, z) and (y, z) planes. Similarly, the T2 detector is segmented in cylindrical coordinates (R, ϕ), and the half-planes are at constant z, so after the hits are clusterized, they can be fitted as linear track candidates by the road-finder module.

In this thesis, reconstructed T1 and T2 tracks are accepted with no cut (both primaries and secondaries), since the SD categorization does not use the parameters of the reconstructed tracks, only their presence or absence in each arm of the T1 or T2. Whenever the track η is used, for T2 we assume straight-line propagation from the IP (zero vertex) to the measured T2 track entry point, while for T1 tracks we use the reconstructed track η, since the η resolution is better for T1 than T2, and there are fewer secondaries in T1, due to smaller amounts of material between T1 and the IP.

RP

For the RP, individual strip hits are clusterized [1], and transformed into geometrical points using the measured detector geometry, which changes between runs if the RPs are moved. A pattern recognition module rejects noise hits, and then a road finder algorithm selects track candidates that are approximately collinear with the beam, and have hits in at least 3 out of 5 RP u- and v-planes. The track candidates in the near and far RP pair are then fitted with a linear track over the 5 m distance between the RPs, and this fit is further processed by the proton reconstruction modules described in the next paragraphs.

Elastic reconstruction

Elastic proton reconstruction (ξ = 0) is the most used and best-validated proton reconstruction method [90], but cannot be used here because of the bias from non-zero ξ it would introduce even for low-mass SD protons, due both to the diffraction term directly proportional to ξ, but also to the optical functions not being constants but variables depending on ξ.

Inelastic reconstruction

This proton reconstruction module by [91] for inelastic protons is less used, with more parameters and therefore higher systematic uncertainty; also, the optics functions change nonlinearly with ξ, and in the case of SD we only have one proton, not two. This means we must take the Beam Divergence (BD) correction from the elastic anal-

ysis [56] of this same data run, where it could be extracted from the non-collinearity of the two detected protons. Beam divergence is the difference from totally head-on proton-proton collisions due to all the protons not having exactly the same momentum, and in the above-mentioned analysis the BD spread in y was measured to be $\theta_{y,BD} = (2.47 \pm 0.07) * 10^{-6}$ rad. Here we apply a constraint on the full inelastic reconstruction, that the IP vertex $x^{IP} = 0$, since there is some degeneracy going from two variables measured in the RP, (x_{RP}, θ_x^{RP}), to three reconstructed ones, $(\xi, x^{IP}, \theta_x^{IP})$, at the IP.

Table 4.2: TOTEM track-finding parameters

Name	Description
T1 roads	
$\delta\eta$	0.1
$\delta\phi$	0.2
Hits	4 . . . 30
Planes	3 of 5
T2 tracks	
Hits	> 4
Planes	3 of 10
RP roads	
δx,y	200 μm
$\delta\theta_{RP}$	7 mrad
Planes	3 of 5 + 3 of 5 (U and V)
Hits	1 – 5 per plane
RP Tracks	
Number of tracks	1 per RP

4.3 ROOT

The data, produced with CMSSW, based either on MC simulation or raw detector data, is analysed with code run inside CERN's ROOT software framework [92].

ROOT files can contain compiled C++ class objects in a directory structure, all

data being serialized and compressed; the same file may contain different, incompatible versions of the same class as long as they are saved with different class version numbers. This was used to combine MC data with real pileup.

ROOT can scale from very small to very big analysis types; large data sets can be processed with compiled C++ analysis module code Large datasets at CERN were accessed from the CASTOR service (tape-based and HDD-cached) and from EOS (HDD-based) [93, 94].

TOTEM code and data have been validated for use with CMSSW 4.2.4 and CMSSW 7.0.4(RunI), and we have used the versions of ROOT included in these CMSSW versions: $5.27/06b$ (CMSSW424), $5.34/38$ (CMSSW704) and $5.34/07$ (TOTEM-unstable CMSSW620).

4.4 RooUnfold

Bayesian unfolding can be used to mitigate resolution smearing effects, and in this thesis, I used the RooUnfold package written for use in ROOT in 2011 by Tim Adye [95]. This package can do iterative Bayesian unfolding, singular value decomposition (SVD), bin-by-bin correction and unregularized matrix inversion. The treatment of the uncertainties can be selected, from full variance matrix propagation based on input histogram error bars and unfolding uncertainty propagation, to simply assuming Poisson-distributed uncertainties, just on the input. Bayesian unfolding is the only method in RooUnfold that can also be used to multidimensional unfolding (2D to 2D, with a 4D correlation matrix). Because ξ and θ_x are both correlated with the local x_{RP} we studied 2D unfolding of (ξ, θ_x), but we could not get it to converge well enough for us to use it instead of doing the unfolding separately for each variable. As explained in Section 6.4.3, this may have been due to wrongly weighted learning histograms, when training the unfolding.

4.5 Analysis framework

The data analysis algorithm used in this thesis was originally implemented as a producer module in CMSSW, run on both the full real reconstructed data and simulated, then reconstructed MC data. The C++ class and its member functions were extracted and minimally modified to be able to run them over the smaller TOTEM Ntuples in-

stead of the full reconstructed data, which speeded up processing by a factor > 10.

4.5.1 Algorithm

The module reads in the data event-by-event three times: first reading the real data and saving all Bunch Crossing (BX) events (for pileup(PU) mixing and subtraction), second reading the event timestamps and segmenting the data into piecewise constant luminosity segments divided after each 10 000 events, or any events with timestamp jumps over than 3s, whichever is smaller; for MC data, luminosity per event is set to 1.

Finally, each event of the MC data is read and mixed with a randomly selected real-data BX pileup event, forming a synthetic event SD event with pileup, for validation of the pileup subtraction. The pileup background is subtracted per category using the same kind of combination of signal and background events with random real BX PU events having complementary TOTEM detector topologies, like the proton occupancy fraction in the BX PU sample combined with appropriately weighted and corrected no-proton T1 and T2 only events. For each event, all signal and background histograms are filled with a weight proportional to the track and trigger efficiency corrections, and to the proton geometrical acceptance correction. After all the data are read, the cross section histograms are divided by the integrated luminosity of the big bunch for all events with T1 read out correctly by the DAQ, or by the number of processed events in the case of MC data.

Chapter 5

Single Diffraction

5.1 Signal

Single diffraction (SD) is the process in which two colliding hadrons interact inelastically, one proton staying intact while the other dissociates to a hadronic system, usually denoted "diffractive". The interaction is mediated by an "object" with the quantum numbers of the vacuum, i.e. the Pomeron that was introduced in Chapter 2.4.1, which in QCD can be described by a colourless pair or "ladder" of gluons. Experimentally, SD has a signature of a final state proton opposite a diffractive system, with a rapidity gap in between that is large compared to any random multiplicity fluctuations. The rapidity gap size is defined as $\delta y = ln(s/M_X^2)$, approximately the same as the gap in pseudorapidity η: $\delta y \approx \delta\eta \approx ln(s/M_X^2)$, where M_X is the mass of the diffractive system, and the expected proton fractional momentum loss is $\xi = M_X^2/s = (M_X/E_{CoM})^2$.

5.1.1 Signal topologies

In this measurement SD events are selected using the RPs and T2. Since SD events should have only one proton, we require exactly one reconstructed proton, i.e. exactly one near and far vertical RP with a track, with T2 tracks on the opposite side coming from the diffractive system, and a rapidity gap in the T2 on the same side as the proton. The horizontal RPs were not used in this analysis since essentially all diffractive protons in the horizontal RPs were in the overlap region with the vertical RPs due to the large magnification and dispersion in y at large values of ξ, and an effective length only a little smaller than at $\xi = 0$, see Figures 3.2 to 3.6.

The SD candidate events are classified into different SD classes based on the activity in the two T1 arms as given in Table 5.1, where each SD class corresponds to a certain diffractive mass range. These ξ ranges are calculated from the rapidity gap expected between the rapidity of a beam proton[1] and the edges for the T2 and T1 detectors in pseudorapidity η, see Sections 3.2.2 – 3.2.2. The class labels that occur in histograms are explained in Table 5.2.

For the highest SD masses, where the rapidity gap is too small to reach even the T2 nearest to the proton, tracks are demanded in both T2 arms and the signal is classified based on the measured proton momentum loss, ξ. For these high diffractive masses, the ξ resolution is good enough for the diffractive mass to be estimated from the ξ measurement. For these events, no requirement for T1 tracks is used.

The T2 trigger is used to select the events and RP-V[2] double-arm trigger is used as a veto, to remove events with activity in both RP arms that can be due to incompletely reconstructed elastic or central diffractive events, or events with secondary interactions in the beampipe causing activity in the RPs. See Table 3.4 for an overview of all trigger bits used. In this data taking, T1 was not used for triggering. Unfolding is used to correct for T1 and T2 track inefficiencies and secondaries that cause the SD candidate event to be classified in the wrong SD class.

5.1.2 Signal losses

- **DAQ inefficiency:** to correct for events lost due to dead time in the Data Acquisition (DAQ) system. This inefficiency is computed by comparing the number of triggered and recorded events, since all events triggered increase the trigger event counter irrespective of whether they are recorded or not.

- **T2 trigger inefficiency:** to correct for events lost if not fulfilling the T2 trigger pattern requirements, despite having activity in the T2 that was reconstructed offline as tracks. This inefficiency is extracted from zero-bias BX[3] data as a function both of the reconstructed T2 track topology – i.e. tracks in left or right arm only, or in both arms – and of the number of T2 tracks.

- **RP ϕ-acceptance correction:** To correct for events lost due to the limited az-

[1] see Table 3.1

[2] The vertical Roman Pots, having acceptance for all $|\xi| < 20\%$

[3] Bunch crossing

imuthal (ϕ) acceptance of the RPs in the scattering angle θ^{IP}. Done by weighting each reconstructed SD candidate event with the geometrical acceptance in ϕ for protons at the same scattering angle θ by sampling a circle of constant θ^{IP}, and checking using a MADX parametrisation whether the proton would be in the acceptance of the RPs and pass all beam aperture and proton selection cuts.

- **RP t-acceptance correction:** to correct for the events lost due to scattering angles below the minimum RP acceptance in the scattering angle θ (or t-value). Done by fitting the reconstructed differential $|t|$ cross section of each SD class by a constant exponential, $dN/d|t| = A * e^{-B*|t|}$, in the range $|t(peak+1)| < |t| < 0.3$ GeV^2. Here $|t(peak+1)|$ is the next t-bin to the right of the bin with the highest $d\sigma/dt$, $|t(peak)|$, as shown in Figure 5.1. The cross section below $|t(peak+1)|$ is calculated by integrating the fitted exponential over the range $0 \leq |t| < |t(peak+1)|$. Using the highest bin $|t(peak)|$ in the fit turned out to give less stable results due to possible RP edge acceptance effects than restricting the fit to start from the next bin to the right, $|t(peak+1)|$. Adding data at high $|t|$ lead to bad convergence of the constant exponential fit, therefore we decided to restrict the fits to below 0.3 GeV^2. So as not to double-count events seen below $|t(peak+1)|$, we subtract the integral of the reconstructed differential $|t|$ cross section over the same region, $0 \leq |t| < |t(peak+1)|$.

- **RP track and reconstruction inefficiency:** to correct for the events lost due to RP reconstruction inefficiency, secondary interactions, or pileup that don't allow a clean track reconstruction in the RP. Three inefficiencies are taken into account that are determined from elastic scattering candidate events: uncorrelated near and far RP track inefficiency due to proton interactions with the material of an RP, correlated far RP inefficiency due to nuclear interaction of the proton in the near RP producing a shower in the far RP, and pileup background that doesn't allow a unique track reconstruction in the RPs due to the presence of multiple tracks in the RPs. The latter inefficiency is caused by the RPs being equipped with silicon microstrip detectors with one-dimensional reconstruction that is not able resolve multitrack configurations. In addition, two specific SD inefficiencies are determined from single proton data: non-converging ξ and t-reconstruction from the local RP coordinates, and simultaneous reconstruction of protons in both top and bottom RPs in the same arm due to pileup. All these correction factors are constant as function of ξ, t and SD class; they differ be-

tween the data segments due to the different RP approach distances being subject to differing amounts of beam background and pileup.

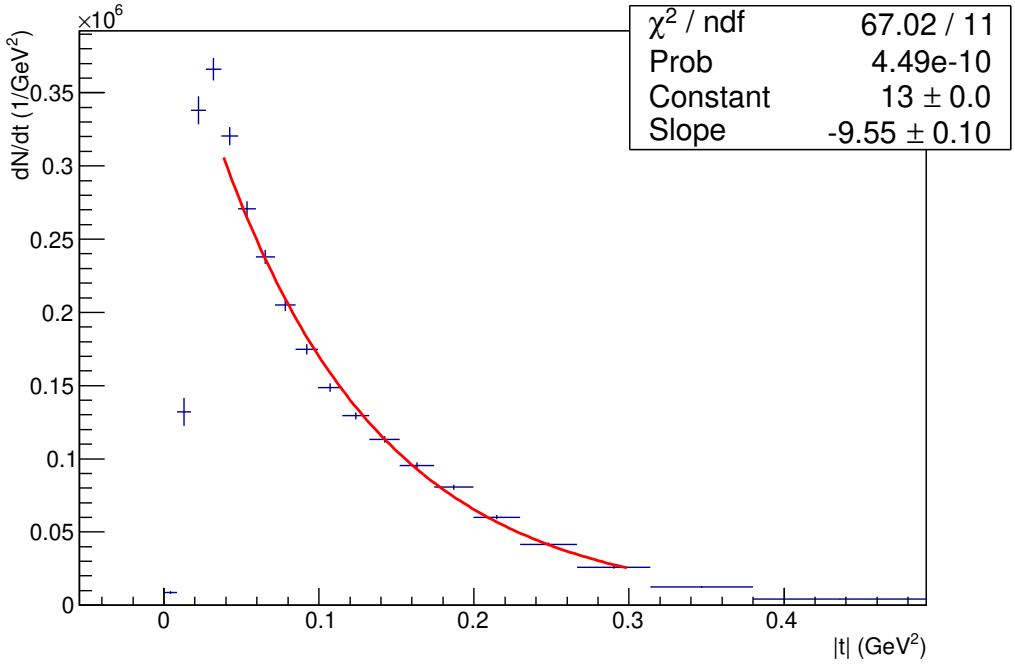

Figure 5.1: Example of fit to |t| distribution used for estimating the RP t-acceptance correction, see Section 5.1.2. The sample used is 540 000 Pythia SD events, with mixed real PU, for the 1T2-1T1 class reconstructed with the 56 bottom RP.

5.2 Backgrounds

- **Collision event pileup (PU):** background from two simultaneous pp collisions summing up to a valid SD topology. This background is estimated by mixing real or simulated collision events with random bunch crossing (BX) triggered events and checking whether the topology corresponds to a valid SD topology.

- **Pileup with beam halo (BH):** background from the coincidence of a standard pp collision with a laterally offset beam proton not originating from pp collisions during the same bunch crossing, and corresponding to a valid SD topology. This background is automatically included in the mixed events used to estimate the

PU background. BH proton can be separated from diffractive protons by examining the RP horizontal coordinate x_{RP}, and the corresponding horizontal angle at the RP, θ_x^{RP}, as long as the ξ of the proton is significantly different from $\xi = 0$. For the 2T2 SD class, i.e. very high mass SD events with significant ξ, the BH background is large simply because the majority of minimum bias[4] events have a 2T2 topology. Therefore, for this SD class we explicitly subtract the BH background using the x_{RP} and θ_x^{RP} correlation of the proton; for details see Section 6.2.2.

- **RP ϕ-acceptance two-proton background:** background from pp collision events with two protons, where one proton is undetected due to the limited ϕ-acceptance of the RP. Done by weighting each reconstructed non-elastic two-proton event with the geometrical acceptance in ϕ for both protons at their scattering angle $\theta_{1,2}^{IP}$ by sampling two circles of constant θ_1^{IP} or θ_2^{IP} and checking, using a MADX parametrisation whether only one of the two protons would be in the acceptance of the RPs and pass all beam aperture and proton selection cuts.

- **RP t-acceptance two-proton background:** background from pp collision events with two protons, where one proton is undetected due to the limited RP t-acceptance. Done by estimating from the $|t|$-distribution of reconstructed non-elastic two-proton events – via an extrapolation to $|t| = 0$, in a similar manner as in Figure 5.1 – the probability to have a non-elastic two-proton event where one proton is lost due to the limited RP t-acceptance.

- **One proton missed elastic two-proton background:** background from the coincidence of an elastic event, where one proton is lost either due to beam divergence (BD) induced change in the vertical scattering angle θ_y^{IP} or differences in the approach distance for the vertical RPs in opposite arms, and a standard pp collision event. This background is mitigated by demanding the vertical RP position, y_{RP}, to be sufficiently far from the active y-edge of the RP in terms of the vertical beam divergence spread, σ_y^{BD}.

Note that backgrounds due to standard elastic events with two protons within the RP acceptance and non-elastic events with two reconstructed protons are removed by the RP-V double-arm trigger veto, discussed in Section 5.1.1 above.

[4] generic inelastic event

SD class	Inelastic telescope configuration	Diffractive mass range (values for 7TeV)	Momentum loss (ξ)
Very low mass	nothing in T2 (unseen)	<3.1 GeV	$< 2 * 10^{-7}$
Low mass	T2 opposite p only (no T1)	3.1 – 7.7 GeV	$2 * 10^{-7}$ – $1.2 * 10^{-6}$
Medium mass	T2 opposite p + T1 opposite p	7.7 – 380 GeV	$1.2 * 10^{-6}$ – 0.30%
High mass	T2 opposite p + T1 same side as p	0.38 – 1.15 TeV	0.30% – 2.7%
Very high mass 1	T2 both sides	1.15 – 2.0 TeV	2.7% – 8%
Very high mass 2	T2 both sides	2.0 – 2.5 TeV	8% – 13%
Very high mass 3	T2 both sides	2.5 – 3.1 TeV	13% – 20%
or:			
Very high mass	T2 both sides	1.15 – 3.1 TeV	2.7% – 20%

Table 5.1: SD classes used for the 7 TeV data analysis

5.3 Theoretical expectations

The total cross section was found to grow at the ISR, as did the diffractive one; in Regge theory Pomeron models with $\alpha(0) > 1$ the diffractive cross section would grow large enough to dominate the total one at the TeV-scale, in contradiction with CDF and $Sp\overline{p}S$ measurements, so some kind of saturation has to occur before the TeV-scale [96]. In Table 5.3 we give some post-saturation model predictions for the SD cross sections at the LHC.

SD class	Label (text)	Label (numbers)
Signal classes		
RP p+nothing in T2	kRpOnly	0T2
RP p+T2 opposite p only (no T1)	kT2OppNoT1	1T2-0T1
RP p+T2 opposite p + T1 opposite p	kT1T2Opp	1T2-1T1
RP p+T2 opposite p + T1 same side as p	kT1SameT2Opp	1T2-2T1
alternatively:		
RP p + T2 both sides ($2.7\% < \xi < 8\%$)	kT2BothLow	2T2(a)
RP p + T2 both sides ($8\% < \xi < 13\%$)	kT2BothMid	2T2(b)
RP p + T2 both sides ($13\% < \xi < 20\%$)	kT2BothHigh	2T2(c)
or		
RP p + T2 both sides ($2.7\% < \xi < 20\%$)	kT2BothLow	2T2
Background classes		
RP p+T2 same side as p only (no T1)	kT2SameOnlyNoT1	(1T2-0T1-bkg) (not subtracted as background, PU and 2-proton backgrounds used instead
RP p+T2 and T1 same side as p only	kT1T2Same	(likewise, 1T2-1T1-bkg)
RP p+T2 same as p only and T1 opposite side	kT2SameT1Oppo	(likewise, 1T2-2T1-bkg)
Two-proton backgrounds:		
RP 2 p+T2 one side (no T1)	k2p0T1	
RP 2 p+T2 one side + T1 on T2 side only	k2p1T1	
RP 2 p+T2 one side + T1 on opposite side as T2	k2p2T1	
RP 2 p+T2 both sides	k2p2T2	

Table 5.2: SD class labels and abbreviations

Table 5.3: Predictions for the SD cross section at LHC energies. Durham: δy_F = rapidity gap filled by fragments. MBR: δy= rapidity gap size. GW=Good-Walker, soft N^* excitation. MP=Multi-Pomeron model. PFR=Pomeron Flux Renormalisation

Group (ref.)	Year	$\sqrt{s}$ (TeV)	Type	Range	Value (mb)
Durham [97]	2000	14	pre-LHC		9.4 – 15.4
		7	(from graph)		9 – 13
Durham [98]	2008	14	pre-LHC	low: $\delta y_F < 1.5$	4.9
				high: $\delta y_F > 1.5$	14.1
		7	(from graph)	high	13
		7		total	17
Durham [99]	2011	7	pre-LHC	$M_{SD} > 2.5$ GeV	9.9 – 10.2
				$M < 2.5$ GeV	5.5 – 6.7
Tel Aviv [100]	2008	14	pre-LHC	total	11.8
				low mass (GW)	10.52
				high mass (MP)	1.28
Tel Aviv [101]	2010	7	pre-LHC		10.2
		14			10.8
Tel Aviv [102]	2012	7	LHC tuned	$\xi < 5\%$	10.7+4.18
		8			10.9+4.3
Ostapchenko [76]	2010	7	LHC tuned	$\xi < 15\%$	13.4
				$M_X > 5GeV$	9.6
Kaidalov [103]	2009	7	pre-LHC	$\xi < 5\%$	11.6
		14			13
[104]	2010	7	LHC tuned		10.95
		14			11.89
Blois conf. [105, 106]	2009	14	PFR	$\xi < 5\%$	10.0 ± 1.0
(Goulianos [96])	1995	7	(fit quoted	above)	9.6 ± 1.0
MBR [107]	2012	7	LHC tuned	$\delta y > 2 \pm 0.5$	10.91
		14		$(\xi \lessapprox 13.5\%)$	11.26
Schuler [108]	1993	16	pre-LHC		14.41
				$\xi < 5\%$	12.64

Chapter 6

Analysis

6.1 Signal selection

The SD signal category is extracted from the reconstructed tracks in the T2 and RPs that are all combined and checked for an SD-like topology. We select SD candidates with exactly one proton in one of the arms, i.e. exactly one near and far vertical RP with a track, and T2 tracks in the other coming from the diffractive system, with a rapidity gap in the T2 in the same arm as the proton. These track-based signal candidates don't yet have any background removed, or demands on the proton reconstruction applied. For SD events with very high diffractive mass, the rapidity gap is so small that it does not reach the T2 on the same side as the proton. For this class, tracks in both T2 arms are required.

6.1.1 T2 and T1 tracks

We do not determine the rapidity gap size based on the nearest T1 or T2 track to the proton, due to the lack of η acceptance at central rapidities ($0 < |\eta| < 3.1$) and significant production of secondaries from interaction with material in the experiment that affects the measurements in T1 and T2. Instead, we classify events according to the track topology in T2 and T1. Since low-mass SD events have low multiplicity, this means we can increase our efficiency by using all T1 and T2 tracks; both primaries, produced in the pp collision, as well as secondaries, from interaction with material in the experiment. Because of a higher material budget between the IP and the detector above the T1 $|\eta|$ acceptance, there are more secondaries in T2 than T1. Above $p_T = 40$ MeV/c for T2 and $p_T = 100$ MeV/c in T1, particle tracks are essentially straight, since

the small CMS dipole magnetic field inside T1 and T2 only bends the charged-particle tracks a negligible amount, and therefore the tracks can be reconstructed efficiently [70] as straight lines.

To show the MC samples simulate both primary and secondary T1 and T2 tracks in SD events adequately, we compared the multiplicity in each arm with tracks for each SD class. Figures can be found in the Appendix L.

Based on studies for the forward charged particle multiplicity measurement [4], the material in front of T2 in the MC has an uncertainty of about 40%.

The effect on the present analysis will be studied looking at the fraction of T1 only events in the BX triggered data and fraction of "wrong-side" T2 events – i.e. events with T2 activity only on the same side as the proton, which does not correspond to a valid SD topology – both in data and MC samples.

6.1.2 RP tracks

Using both the near and far RP in one arm, one is able to measure both the local position (x_{RP}, y_{RP}) and the local track angles $(\theta_x^{RP}, \theta_y^{RP})$. This allows the reconstruction of all variables $(x_{IP}, y_{IP}, \theta_x^{IP}, \theta_y^{IP}, \xi)$ for the scattered proton. In the horizontal plane, the reconstruction is ambiguous, since three IP variables are to be determined from two measured RP ones.

To select SD events, we demand exactly one track in a pair of vertical RPs – either an RP-bottom or an RP-top pair – with all other vertical RPs empty;there may be tracks in the horizontal RPs in the overlap region, as explained in Section 5.1.1.

The proton reconstruction uses both horizontal and vertical RPs, but all the fiducial cuts described in the following paragraph do not use any tracks in the horizontal RPs, since the vertical RPs have adequate acceptance from $\xi = 0$ up to $\xi = 20\%$.

RP fiducial selection cuts

Because of residual insertion misalignments, the inner edge of the geometric acceptance in y_{RP} differs between pots, so we apply a conservative upper and lower limit in y_{nr}^{RP}: $y_0 < |y_{nr}^{RP}| < 30$ mm, where y_0 depends on the RP approach distance to the beam. From the Beam Divergence (BD) plots in Appendix D.2, we see that elastic sample has a small bias due to the beam divergence loss up to $|y_{RP}| \approx 7 - 7.5$ mm, so we set the lower limit about 0.5 mm further away from the beam. Therefore the limit is

$y_0 = 8$ mm for the largest data set, segment 1b, and $y_0 = 7.4$ mm and $y_0 = 6.6$ mm for segments 2 and 3. This lower limit works as a beam divergence veto for elastic events, because the location of the selection cut is $\sim 4 * \sigma_y^{BD}$ away from the active edge seen in elastic two-proton events, when we demand all four RPs in a diagonal configuration have tracks. Here σ_y^{BD} is the spread in the y position in the RP due to the beam divergence, equal to $L_y(\xi = 0) * \sigma_{BD}(\theta_y^{IP}) \approx 0.59$ mm, with $\sigma_{BD}(\theta_y^{IP}) = 2.47\mu$rad being the beam divergence angular spread and $L_y(\xi)$ the effective length, see Section 3.1.2.

This $|y|$ requirement implies that we still veto elastic two-proton events even when one proton is displaced by beam divergence up to $4 * \sigma_{BD}(\theta_y^{IP})$.

Because elastic protons center around $x_{RP} = 0$ in the RP, while higher ξ moves the proton to positive x_{RP}-values, the proton reconstruction will be biased at negative x_{RP}. Looking at Figure 6.1, we find a ξ bias of more than $3\sigma_\xi$ in half the events at $x_{RP} \approx -1.5$ mm when using the vertex constrained fit ($x_{IP} = 0$, see Section 6.1.4), so we apply a fiducial selection cut $x_{RP} > -1.44$ mm. For the very high-mass SD category we also apply a one-sided linear Beam Halo (BH) veto, see Section 6.2.2.

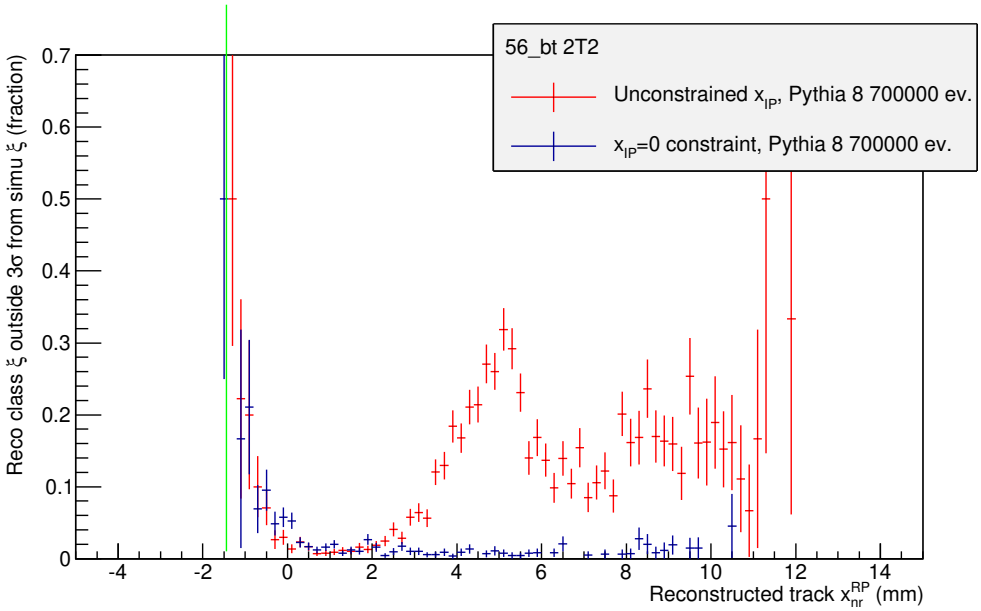

Figure 6.1: Proton momentum loss ξ misreconstruction rate (fraction having $|\xi_{RECO} - \xi_{gen.}| > 3 * \sigma_\xi$) vs reconstructed RP track x_{RP}. The misreconstruction rate is shown for two ξ and t reconstruction algorithms, unconstrained x_{IP} and constrained $x_{IP} = 0$. The sample used is 700 000 Pythia SD events, for 2T2 class. Green line shows position of fiducial selection cut in x_{RP}.

We also veto protons with an anomalously high reconstructed ξ in a small acceptance window around $-35 < \xi < -30\%$, with the fiducial $y_{RP} < 30$ mm requirement. These are not real high ξ protons but tracks from secondaries produced in front of the RP.

6.1.3 Reconstruction of proton kinematics

The proton kinematics are reconstructed from the RP tracks with a two-stage solver by Hubert Niewiadomski [91]. The local RP (y_{RP}, θ_y^{RP}) position depends on the position and angle at the origin, (y_{IP}, θ_y^{IP}), and should thus be unambiguously solvable.

In the horizontal plane the situation is ambiguous, since the local position (x_{RP}, θ_x^{RP}) depends on three parameters at the origin, $(x_{IP}, \theta_x^{IP}, \xi)$. As you can see in Figure 6.2, the ξ distribution for the real data is found to have a spread of 0.8% for events from the 1T2-0T1 SD class, with a rapidity gap between the proton in the RP and tracks only in the T2 arm on the other side from the proton. Since the ξ of the events in this class is expected to be negligible ($|\xi| < 10^{-6}$) compared to the resolution, the spread of the ξ distribution reflects the true ξ resolution, and was found to be similar to the resolution seen for elastic protons ($\xi = 0$) with the well-validated elastic proton reconstruction module[1].

The resolution depends on the optics and is therefore a function of ξ, reaching 0.2% at $\xi = 20\%$, as you can see in the Figure 6.3 [1]. The large correlation between the reconstructed ξ and θ_x with the standard proton reconstruction is shown in the same figure. A systematic scale uncertainty of $\mathcal{O}(10\%)$ on ξ is assumed, based on our knowledge of the optical functions, especially D_x.

6.1.4 Improvements in proton reconstruction

To improve the proton reconstruction efficiency at high ξ, we apply a constraint on the horizontal position of the proton at the IP ($x_{IP} = 0$) in the proton reconstruction. MC simulation shows that this improves the reconstruction efficiency for obtaining a correct ξ substantially at $|\xi| > 10\%$; without the constraint on x_{IP} many of these protons converge to the wrong ξ value, while some do not converge at all. See Figure 6.4 for a comparison of the fraction of events with a ξ reconstruction bias larger than 3σ, where

[1] Tested as an alternative to the constrained $x_{IP} = 0$ inelastic reconstruction presented in Section 6.1.4, but found to be biased already at small ξ.

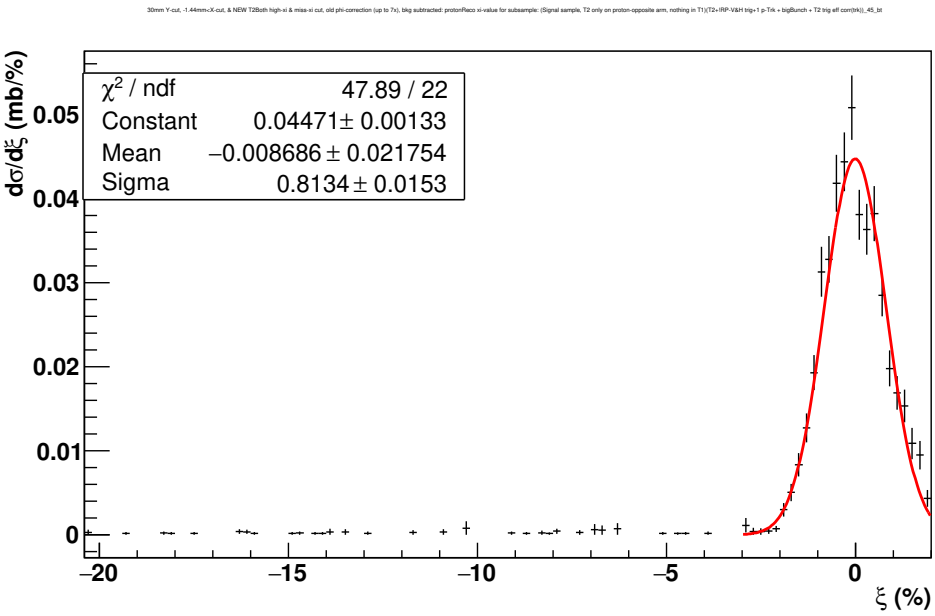

Figure 6.2: A Gaussian fit of the differential reconstructed ξ-spectrum for the SD class 1T2-0T1, in pot 45_tp. Data sample used is 1 140 000 events from Segment 1b.

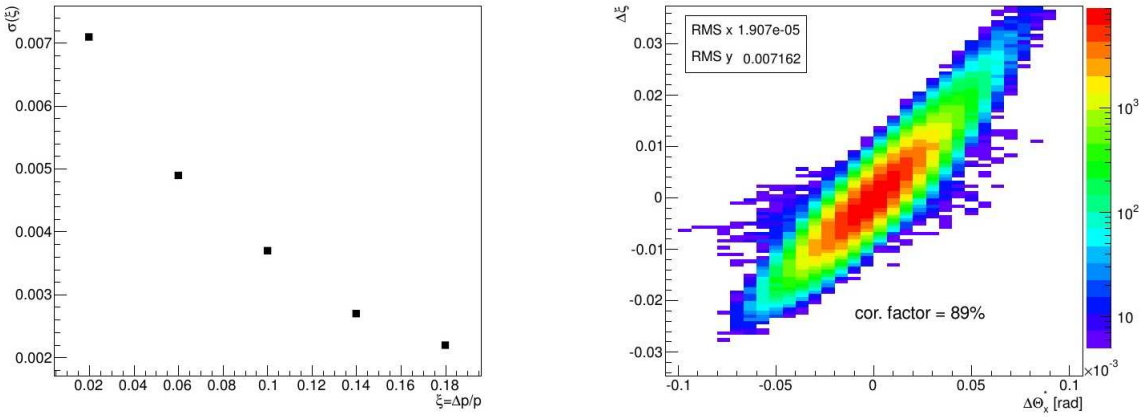

Figure 6.3: The ξ resolution in the standard proton reconstruction on the left, and the correlation between ξ and θ_x in the standard proton reconstruction, on the right. Taken from [1]

σ is the resolution given in the previous section, from 0.2% to 0.8%. As you can see, the standard method was biased in 20 – 50% of events at all values of $|\xi| > 8\%$, while the constrained reconstruction is biased in less than 5% of events for all values of ξ that are within the acceptance of the RPs.

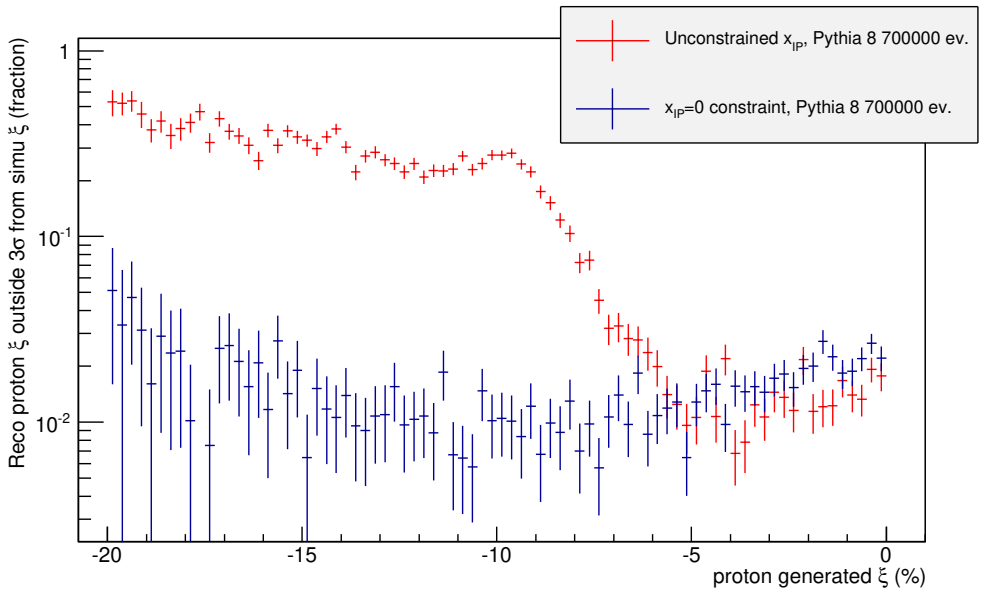

Figure 6.4: Proton momentum loss ξ misreconstruction rate (fraction having $|\xi_{RECO} - \xi_{gen.}| > 3 * \sigma_\xi$) vs generated ξ. Plotted for events in SD class 2T2 based on generated particles. The sample used was 700 000 Pythia 8 events.

6.1.5 Luminosity

After all backgrounds are subtracted and rate corrections applied, the integral event counts and the differential counting spectra dN/dX_i (where X_i is some variable) are transformed to (integral or differential) cross sections using the integral of the calibrated instantaneous luminosity measured by CMS at the interaction point IP5. The instantaneous luminosity was provided in the form of a CSV text file table[2], with time-stamped measurements for each bunch. The calibrated luminosity for the colliding big bunch was

$$L = L_{BB} - 0.4 * L_{NC1} - 0.4 * L_{NC2} \tag{6.1}$$

Here BB is the measurement for the big bunch, and NC1 and NC2 are two non-colliding bunches used for calibration, whose luminosity would be zero if the measurement was ideal. This luminosity measurement has been validated by TOTEM, combining the variables used for the luminosity-independent total cross section measurement [14] to obtain the luminosity from the measured elastic and inelastic rates.

$$\mathcal{L}_{int} = \frac{1+\rho^2}{16\pi\hbar^2 c^2} \frac{(N_{el} + N_{inel})^2}{dN_{el}/dt|_{t=0}} \tag{6.2}$$

[2]for LHC/CMS fill 2232, in units μb/s

Here ρ, the real-to-imaginary ratio of the nuclear elastic amplitude is taken to be 0.141 ± 0.007, from the COMPETE extrapolation [109], and N_{el} and N_{inel} are the elastic and inelastic rates, with $dN/dt|_{t=0}$ being the differential elastic rate as a function of $|t|$, extrapolated to t = 0. By using 6.2, we found an integral luminosity that is compatible[3] with the one measured by CMS; the difference was 1%, well within the quoted uncertainties of 4% on each luminosity.

6.2 Background estimation

6.2.1 Collision event pileup

Signal pileup (PU) is any two simultaneous collision topologies summing to a valid SD topology, but only one having an RP proton. The main contribution comes from very low mass SD ($M_X < 3.1$ GeV/c^2) with only one proton visible in RP, and no tracks in T1 and T2.

In case a signal SD event with a proton in the vertical RPs occurs in coincidence with another collision, it might be reconstructed in another SD class due to the additional tracks in T1 and T2 that is taken into account by the signal unfolding described in Section 6.4.5.

The pileup background is estimated by mixing real or simulated collision events with random bunch crossing (BX) triggered events and checking whether the topology corresponds to a valid SD topology. In the case of real data, the underlying events chosen are those with T2 tracks but no tracks in the RP, mixing with BX events having proton tracks in the RPs a few percent of the time. This selection is done since valid SD topologies have one proton and are triggered by T2 tracks. Therefore we must not have two protons either in different arms –vetoed by RP 2-arm trigger – or in top and bottom RPs of the same arm – in which case proton reconstruction fails because of multiple tracks, as can be seen in Appendix D.4 – or multitracks in the same RP, which likewise fails to reconstruct a proton. These latter one-arm RP selections for PU are corrected with the same correction factors as the signal, described below in Section 6.3.3.

[3] See Table 2 in [14]

6.2.2 Pileup with beam halo

Beam halo (BH) protons are transversely displaced protons not in the main beam bunch that get wrongly reconstructed parameters due to the proton reconstruction assuming they come from the IP.

The same mixing method used for PU above will also subtract pileup with BH.

In addition, for the highest-mass SD classes (2T2) the BH is removed using the correlation between the horizontal RP position x and the horizontal angle at the RP (θ_x^{RP}). This is also the SD class with the highest BH pileup, since most minimum bias collisions have a 2T2 topology.

The BH proton distribution in RP overlaps that of low-mass SD protons, so the BH selection can only be used to separate high-mass SD protons from beam halo protons.

The BH removal is done in the (x_{RP}, θ_x^{RP})-plane at 7 times the width of the BH line observed for 56_tp, the RP with the highest amount of BH. An example plot of the BH seen in this RP in the RP-OR single-proton triggered run is shown in Figure 6.5, with the other RPs shown in Appendix E. This run was the one just before the runs used for the SD analysis and thus taken under similar conditions. For validation, the small amount of BX-triggered BH in the largest data set was checked for compatibility with the BH line fit from the RP-OR run, and found compatible, see Figure 6.7.

This BH rejection cut will also remove part of the SD signal for the very high mass 2T2 class, especially at lower ξ, as can be seen from the x_{RP} vs. θ_x^{RP} distribution from simulation of this SD class as shown in Figure 6.6. This is not detrimental for the analysis as long as at least some acceptance in ϕ^{IP} is maintained for each ξ and θ^{IP} value so that the rejected signal can be recovered with the RP acceptance ϕ-correction described in Section 6.3.3.

6.2.3 Two proton background evaluated in ϕ

This background consists of events with two independent protons, of which only one is seen in RP. It is measured by demanding an SD-like T2 topology with two RP protons, one per side, while vetoing elastic pairs[4] antisymmetric in $\theta_y^{IP} : \theta_{y,45}^{IP} = -\theta_{y,56}^{IP}$, and then calculating the geometric acceptance for seeing only one of the RP protons, assuming independent azimuthal angles $\phi_{p,45}^{IP}, \phi_{p,56}^{IP}$.

No clear correlation can be seen between $\phi_{p,45}^{IP}$ and $\phi_{p,56}^{IP}$ for the two proton events

[4]We apply a $5*\sigma$ cut on the sum $\theta_y^{IP,45} + \theta_y^{IP,56}$ where $\sigma = \sqrt{2}\sigma_y^{BD}$, as explained in the Appendix D

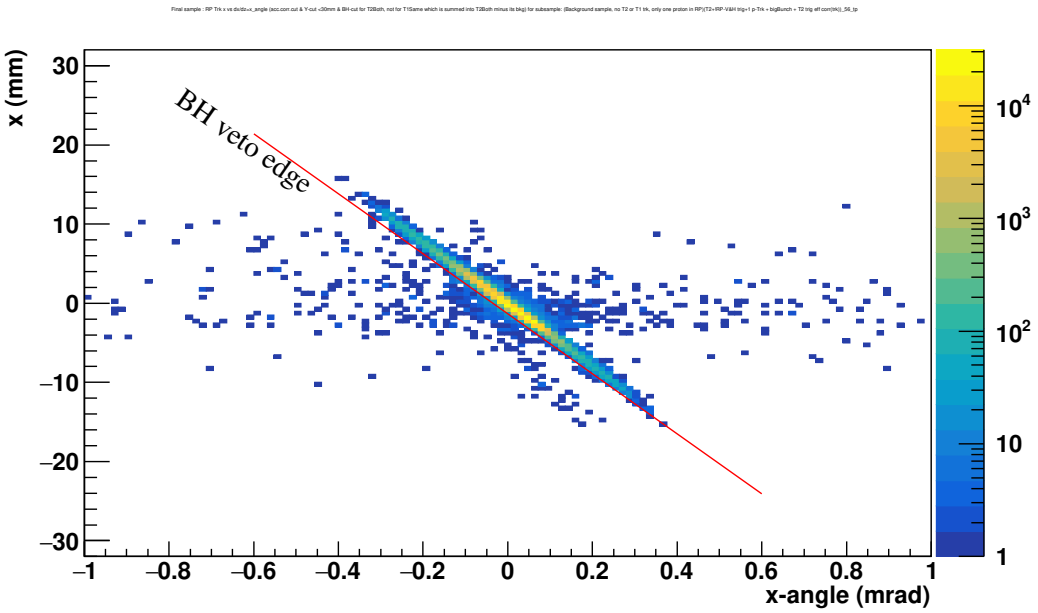

Figure 6.5: The horizontal position in the RP x_{nr}^{RP} as a function of the horizontal angle at the RPs θ_x^{RP} for the RP **56_tp** and category RPOnly, with no T2 tracks, that is expected to be dominated by Beam Halo (BH). BH veto limit at $-7 * \sigma_{BH}$ shown in red; anything above that line is rejected in the analysis. The data sample used is an RP-OR one-proton-triggered run with 721 000 events.

passing the elastic veto for SD class 2T2, as you can see in Figures 6.8 – 6.9. However, in the SD classes 1T2 this 2-proton background estimator may overestimate the background for RP 56_bt, since Figures 6.10 – 6.11 show a top-top, bottom-bottom two-arm correlation for events evaluated as background to SD class 1T2 in arm 5-6, while evaluating the same background for arm 4-5 does not show such a correlation. Each reconstructed non-elastic two-proton event is weighted with the geometrical acceptance in ϕ^{IP} for both protons at their scattering angle $\theta_{45,56}^{IP}$ by sampling two circles of constant θ_{45}^{IP} or θ_{56}^{IP} and checking, using a MADX parametrisation whether only one of the two protons would be in the acceptance of the RPs and pass all beam aperture and proton selection cuts. Of course the selection cuts are only used for the proton designated as seen, since the other one would trigger the RP-V 2-arm veto if it hit anywhere in the opposite arm RP, thus removing the event from the signal candidates.

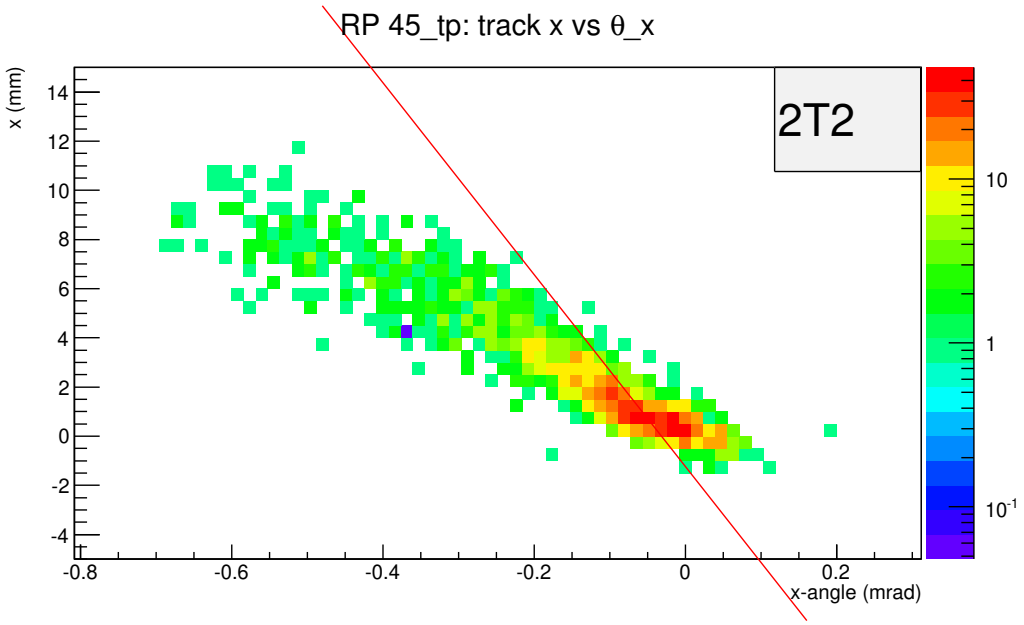

Figure 6.6: The horizontal position in the near RP x_{nr}^{RP} as a function of the horizontal angle at the RPs θ_x^{RP} for the 2T2 SD class in RP **45_tp**. BH veto limit at $-7 * \sigma_{BH}$ shown in red; anything above below that line passes the BH veto. The data used is Pythia 8 SD sample, with 540 000 events.

6.2.4 Exponential t-spectra for two-proton background

The $|t|$-spectra were measured for nonelastic two-proton events, looking for an acceptance cutoff at very low t. If seen, this would give another background from two-proton events for the SD signal. However, for the inelastic two-proton signal we see low-t protons at least down to $|t| = 0.01$ GeV^2. The $|t|$-spectra for the 2p+1T2 and 2p+2T2 SD classes peak at values $d\sigma/dt \approx 0.3$ – 0.8 mb/GeV^2 per category in the lowest-BH RP 45_tp, and $d\sigma/dt \approx 2.5$ mb/GeV^2 per category in 56_tp that has the highest backgrounds.

Since we want to extrapolate down to t-values where the given RP proton is not seen, this means the RP with higher background will give a contribution visible as a one-proton background in the other arm.

Doing a simple exponential extrapolation from the distribution to $t = 0$, as in Figure 5.1, this implies that we can expect at most a two-proton background in the one-proton SD classes of ≈ 0.03 mb/RP in arm 4-5 and ≈ 0.01 mb/RP in arm 5-6.

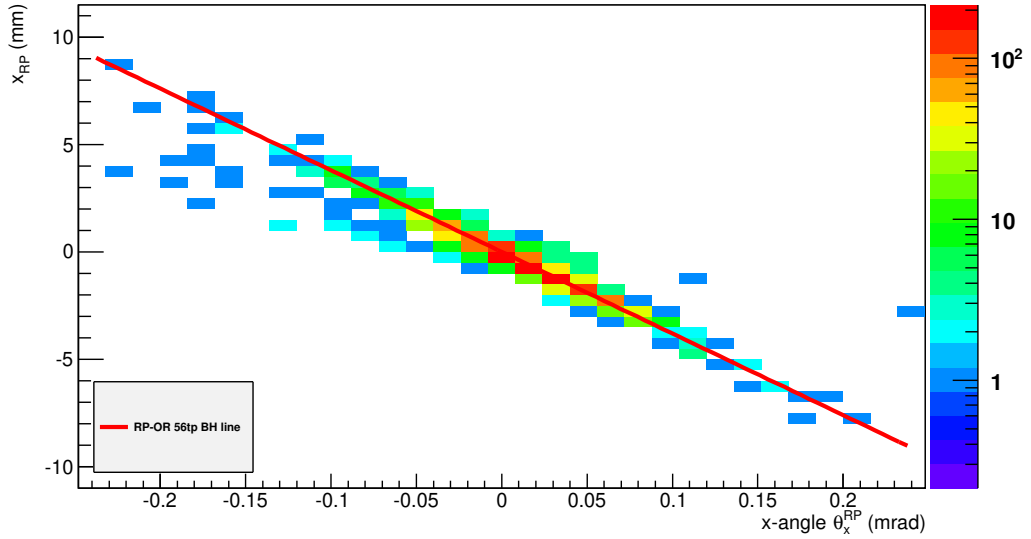

Figure 6.7: The horizontal position in the near RP x_{nr}^{RP} as a function of the horizontal angle at the RPs θ_x^{RP} for SD class 0T2 in RP **56_tp**. The distribution is expected to be dominated by beam halo (BH). The red line shows the BH line fitted from single-proton-triggered data. Data sample used is BX triggered real data, 2 690 000 events – including events with T1 VFAT readout problems.

6.2.5 One missed proton due to elastic beam divergence

There is also a two-proton background that originates from elastic events. The elastic protons are equal and opposite, $\theta_{y,45}^{IP} + \theta_{y,56}^{IP} = 0$, differing only due to beam divergence, a gaussian smearing with width $\sigma_y^{BD} \approx 0.59$ mm. We will see both or neither, not only one, except for the region within a few σ_{BD} of the RP y-edge, which we veto with a selection cut on RP y_{nr}.

The appropriate selection is found by choosing events where we see both elastic protons and looking for the y-value where we start to lose some elastic events, preferentially on one side of the BD peak.

This loss can be diagnosed by calculating the sum of the θ_y^{IP}-angles, which should be near zero with no biased selection cuts; due to RP alignment uncertainties in the $\beta^* = 90$ m data in y_{RP} we find an offset $\pm$ 0.4 μrad, see Appendix D.1. The BD loss is biasing our distribution if $\theta_y^{IP,45} + \theta_y^{IP,56} \neq 0$, or in this case for elastic events, the inequality

$$|y_{45}^{RP} + y_{56}^{RP}| > \epsilon \tag{6.3}$$

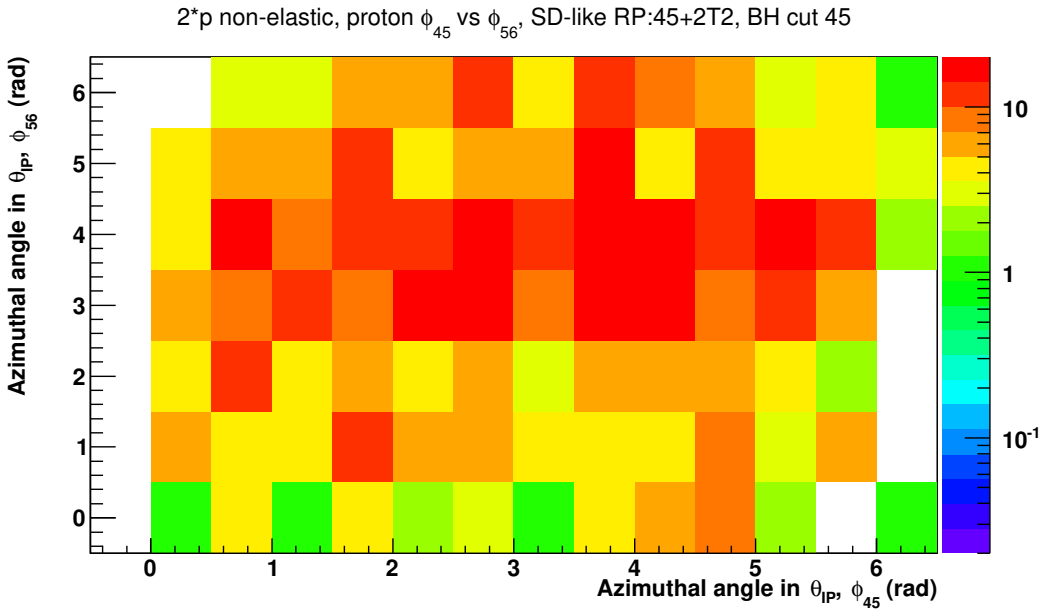

Figure 6.8: For non-elastic two-proton events in real data with T2 tracks in both arms, correlation plot of the azimuthal angle ϕ of the scattering angle θ for each proton. BH selection cut applied to proton in arm 4-5. Based on a data sample of 1 600 000 events from Segment 1b in the real data.

since $\theta_y^{IP,45} + \theta_y^{IP,56} \propto y_{45}^{RP} + y_{56}^{RP}$. Here ϵ is a small constant due to misalignment, of the order 0.1 mm. The BD loss starts around $|y_{RP}| \approx 7 - 7.5$ mm for the main sample Segment 1b, so we set a requirement, $|y_{RP}| > 8$ mm. See Figure 6.12 for an illustration; plots for all four pots are shown in Appendix D.2.

In reconstructed elastic two-proton events, the acceptance starts around $|y_{RP}| \approx 5.5$ mm, so the fiducial selection cut $|y| > 8$ mm corresponds to a 4σ cut on the gaussian beam divergence $\sigma_{BD}(\theta_y^{IP})$, as can be seen in the Figures 6.12 and D.5 – D.16, where we plot two vertical lines, one at the active edge and the other 4σ into the detector in y_{RP}.

Any remaining elastic one-proton background events due to beam divergence are taken into account by the pileup mixing estimation described in Section 6.2.1.

6.2.6 All backgrounds

After subtracting and vetoing the main backgrounds described above, that is, pileup, BH and two-proton non-elastic and elastic backgrounds, we are left with the net signal.

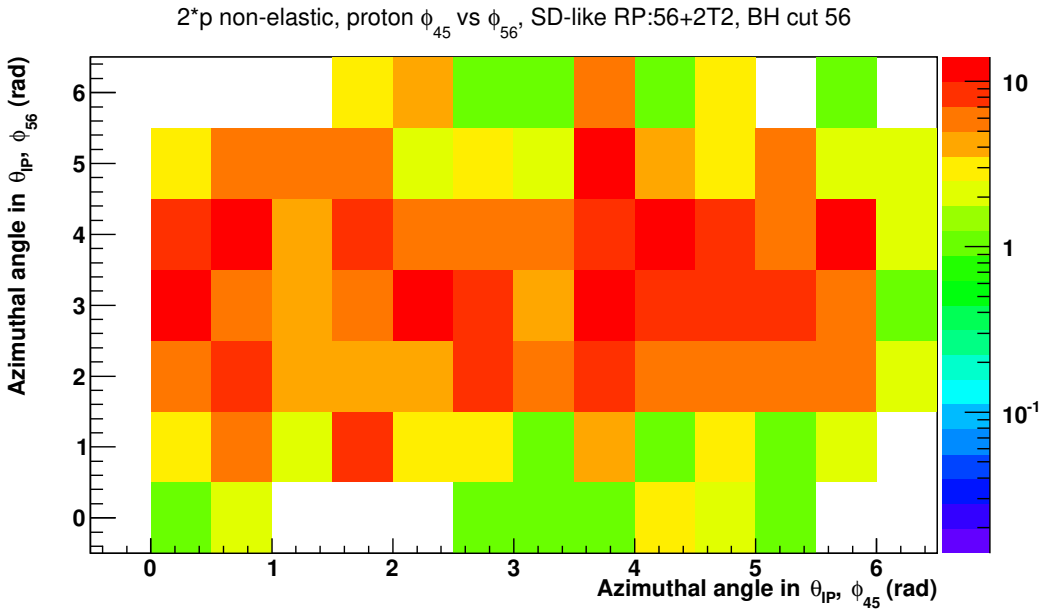

Figure 6.9: For non-elastic two-proton events in real data with T2 tracks in both arms, correlation plot of the azimuthal angle ϕ of the scattering angle θ for each proton. BH selection cut applied to proton in arm 5-6. Based on a data sample of 1 600 000 events from Segment 1b in the real data.

6.3 Rate corrections

In addition to subtracting backgrounds, we also have to correct for various event losses due to inefficiencies , and for the detector coverage, both for T2 and RP.

$$R_{corrected} = (R_{raw} - \sum R_{backgrounds})\epsilon^{-1}_{T2.trigger}\mathcal{A}_{RP,\phi}\epsilon^{-1}_{RP.1trk}\epsilon^{-1}_{p.RECO}\epsilon^{-1}_{DAQ} \quad (6.4)$$

Here $R_{corrected}$ is the final, corrected rate, taking into account all the background rates $R_{backgrounds}$ described above. The other terms are efficiency corrections for T2 trigger $\epsilon_{T2.trigger}$, RP ϕ-acceptance correction $\mathcal{A}_{RP,\phi}$, RP single-track efficiency $\epsilon_{RP.1trk}$, RP proton reconstruction failure rate correction $\epsilon_{p.RECO}$, and DAQ correction for events triggered but not saved.

To estimate the corrected cross section the following formula is used:

$$\sigma_{corrected} = R_{corrected}/\mathcal{L}^{int}_{CMS} + \int_0^{t(peak+1)} dt(d\sigma_{fit}/dt - d\sigma_{data}/dt) \quad (6.5)$$

$$\sigma_{fit} = \int_0^{t(peak+1)} dt a_0 \exp(-a_1 t), \quad (6.6)$$

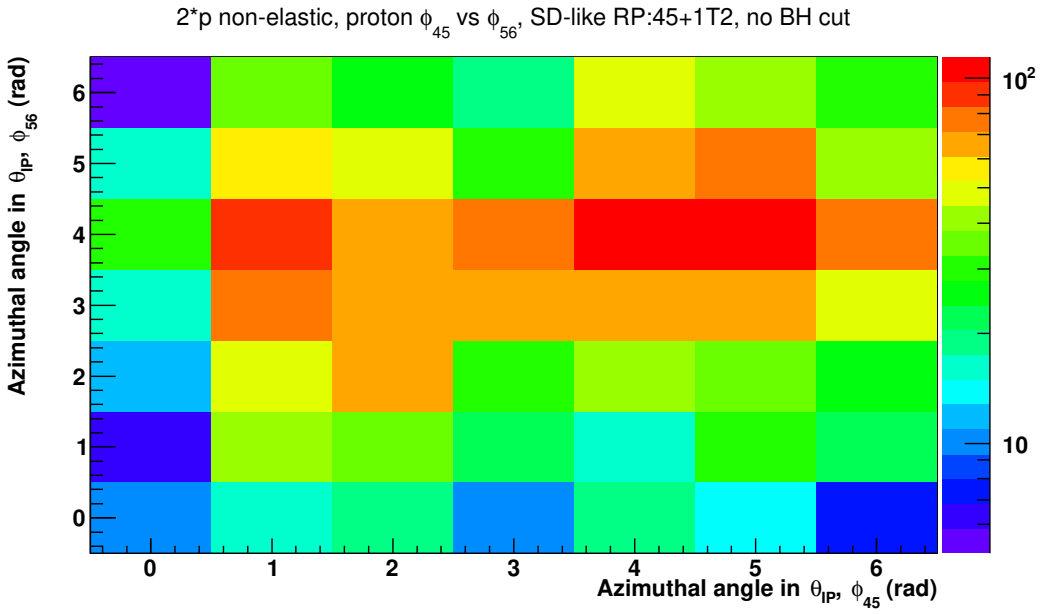

Figure 6.10: For non-elastic two-proton events in real data with T2 tracks in arm 5-6 only, correlation plot of the azimuthal angle $\phi = \arctan(\theta_y^{IP}/\theta_x^{IP})$ of the scattering angle θ^{IP} for the proton in the opposite arm from the T2 tracks, with the azimuthal angle of the proton in the same arm. No BH selection cut used on either proton in this background to SD class 1T2 with a proton in RP arm 4-5. Data sample used is 1 600 000 events from Segment 1b of the real data.

Where a_0 and a_1 are constants obtained by a fit of the data in the range $|t| = [t(peak+1), 0.3]\text{GeV}^2$, $\mathcal{L}_{CMS}^{int}$ is the integrated luminosity as estimated by CMS, and $d\sigma_{data}/dt$ is the cross section visible in the data to the left of the $|t|$-fit range, where acceptance effects start to remove some of the signal seen.

These corrections are described below, in the following subsections.

6.3.1 DAQ inefficiency correction

Some events are lost due to dead time in the DAQ data readout. This inefficiency is computed by comparing the number of triggered events and recorded events, since all events triggered increase the trigger event counter irrespective of whether they are recorded or not. These two counters are extracted from the run metadata and the inefficiency calculated is applied as a correction to the instantaneous luminosity from CMS, to find the luminosity actually read out.

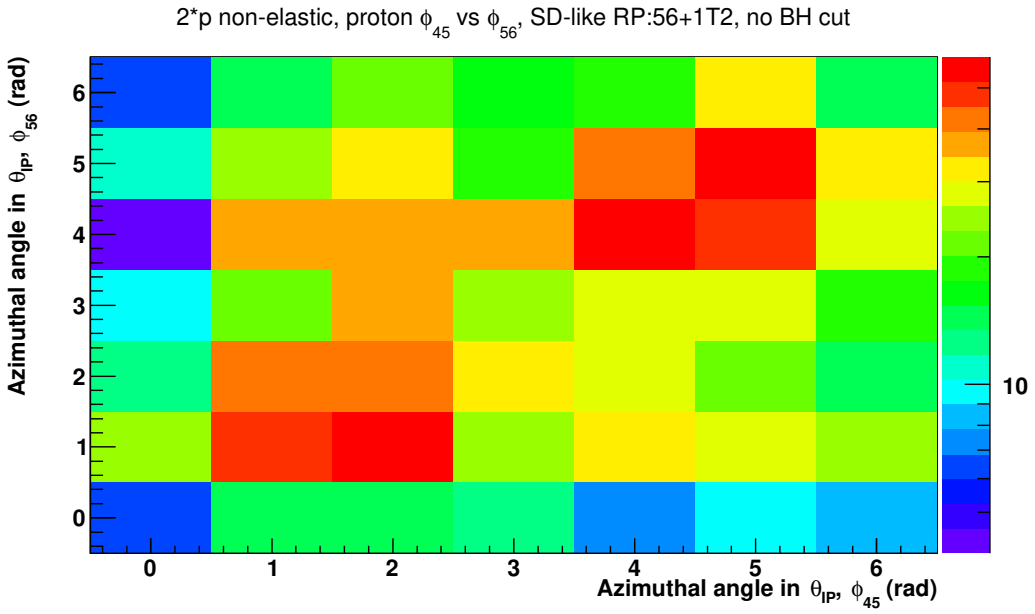

Figure 6.11: For non-elastic two-proton events in real data with T2 tracks in arm 4-5 only, correlation plot of the azimuthal angle $\phi = \arctan(\theta_y^{IP}/\theta_x^{IP})$ of the scattering angle θ^{IP} for the proton in the opposite arm as the T2 tracks, with the angle for the proton in the same arm. No BH selection cut used on either proton in this background to SD class 1T2 with a proton in RP arm 5-6. Data sample used is 1 600 000 events from Segment 1b of the real data.

6.3.2 T2 trigger efficiency correction

From the subsample of zero-bias BX-triggered data, the T2 trigger efficiency $\epsilon_{T2.trig}$ was extracted as a function of number of T2 tracks, separately for events having T2 tracks only in one arm (left and right arm, respectively), and for events having T2 tracks in both arms, see Figures 6.13 to 6.15. The systematic uncertainty from this correction was evaluated by varying one bin in the correction histogram to $+1\sigma$ and -1σ . The correction factor was then applied to a histogram of T2 track multiplicity, bin by bin, and the histogram was integrated. The systematic uncertainty was the largest relative change in the histogram integral, which turned out to be events with only 1 – 3 tracks in T2. Due to T2 having a larger inefficiency in the plus arm (arm 4-5), this uncertainty is larger for SD events with a proton in arm 5-6, opposite T2. These uncertainties and the average correction is given in Table 6.1. Since we will use only SD events with RPs in arm 4-5 for the final cross section determination, the effect is smaller, but we still include this systematic for all SD classes, even though the 2T2

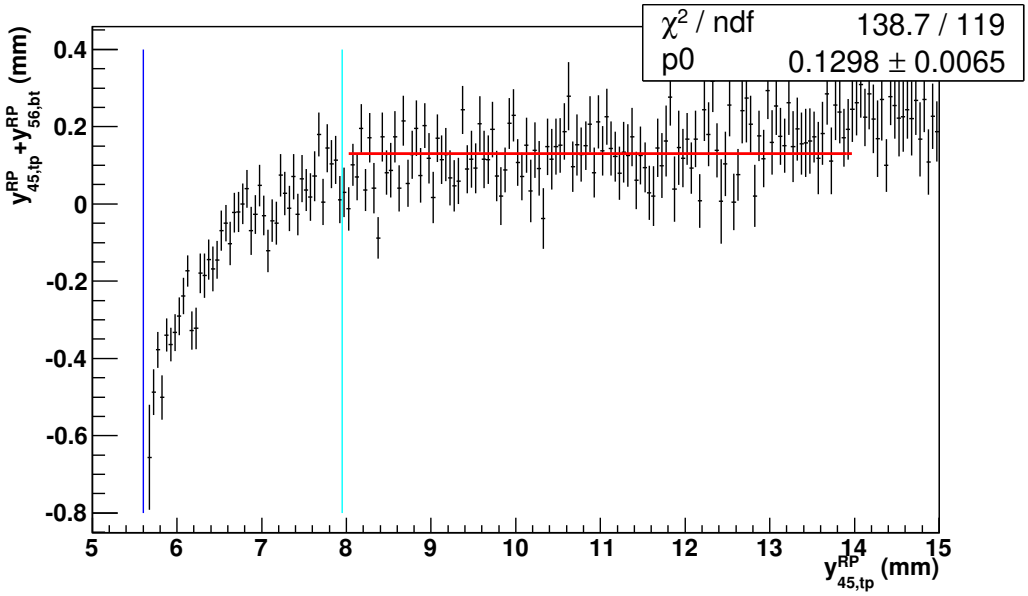

Figure 6.12: The average of the sum of the vertical proton positions, $y_{45}^{RP} + y_{56}^{RP}$, as a function of the vertical proton position in 45, y_{45}^{RP}, for elastic candidate events in one elastic diagonal RP 45_tp-RP 56_bt . The constant line shows a fit to indicate the fully efficient region to determine the near RP y-edge region with possible proton acceptance losses due to beam divergence, for details see Section 6.2.5. The data sample is 800 000 events from Segment 1b.

uncertainty is negligible.

6.3.3 RP acceptance ϕ-correction

The acceptance for a proton with given kinematical parameters is evaluated at the corresponding RP using a MADX [110,111] parametrisation of the LHC optics. Using the same parametrisation, we also checked whether the proton is, or is not, within the LHC apertures at the positions of the main acceptance limiting collimators and beam screens between the IP and the RP.

This allows us to estimate the new (x, y) position in each RP assuming the proton had the same total (θ, ξ), but the (θ_x, θ_y) vector was rotated to another ϕ-angle, using Equation 3.1,

$$x_{RP}(\phi) = x_{RP,0} + L_x(\xi) * (\theta * cos(\phi) - \theta_{x,0}) \tag{6.7}$$

$$y_{RP}(\phi) = y_{RP,0} + L_y(\xi) * (\theta * sin(\phi) - \theta_{y,0}) \tag{6.8}$$

Table 6.1: Integrated T2 trigger efficiency correction per SD class. Determined as the integral of T2 multiplicity spectra normalised to 1, then corrected with the T2 trigger efficiency correction, see Section 6.3.2. T2 multiplicity distribution for 300 000 events of real data from Segment 1b. "Sys." is the relative statistical uncertainty on the integrated correction. Determined as the largest 1σ variation for the corrected number of events, see Section 6.3.2. Number in parentheses is T2 track multiplicity giving largest systematic. 2T2 triggers on either T2- or T2+, so has a very small correction, equal for both arms.

SD class	T2+ (SD RP: 5-6)	Sys.	T2- (SD RP: 4-5)	Sys
1T2-0T1	$121.44^{+2.80}_{-2.32}\%$ (1)	$^{+2.30}_{-1.91}\%$	$109.66^{+1.67}_{-1.49}\%$ (1)	$^{+1.53}_{-1.36}\%$
1T2-1T1	$112.07^{+0.98}_{-0.81}\%$ (1)	$^{+0.87}_{-0.72}\%$	$105.19^{+0.78}_{-0.69}\%$ (1)	$^{+0.74}_{-0.66}\%$
1T2-2T1	$108.96^{+0.58}_{-0.49}\%$ (2)	$^{+0.54}_{-0.45}\%$	$103.75^{+0.53}_{-0.47}\%$ (1)	$^{+0.51}_{-0.45}\%$
2T2	$100.74^{+0.10}_{-0.09}\%$ (3)	$^{+0.10}_{-0.09}\%$	$100.74^{+0.10}_{-0.09}\%$ (3)	$^{+0.10}_{-0.09}\%$

Using this new position we first check if that rotated proton is within the active volume of the vertical top and bottom RPs, then check if such a proton would pass all the fiducial selection cuts and also all parametrised LHC apertures. The total ϕ-correction is the fraction of synthetic protons passing all of these fiducial and aperture tests.

By evaluating this function on $N = 100$ point around a circle of constant θ, we get an estimate for the geometrical acceptance fraction $1/\mathcal{A}_{RP,\phi}$. It was also checked for $N = 500$, but no significant change was found. To limit the systematic uncertainty contribution, we set an upper limit on the RP acceptance correction, $\mathcal{A}_{RP,\phi} < 15$.

With this parametrisation, as a function of ξ, the acceptance reaches 0 around $\xi = -20\%$.

RP inefficiency correction

The RP inefficiency has been measured for the elastic analyses, where it consists of three parts shown in Table 6.2: first, since only one track can be reconstructed in each RP, there is the proton track pileup inefficiency. This varies from RP to RP, and as a function of pileup, between 0.6% and 6.7%. Second, the uncorrelated inefficiency of near and far RPs due to the proton interacting with the RP material was measured to give a contribution of 4.1% to 5.4%. Finally, a proton nuclear interaction in the near

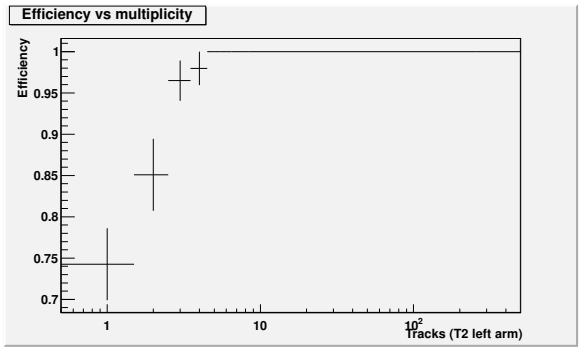

Figure 6.13: T2 trigger efficiency for events having T2 tracks in left arm only, measured from BX-triggered data

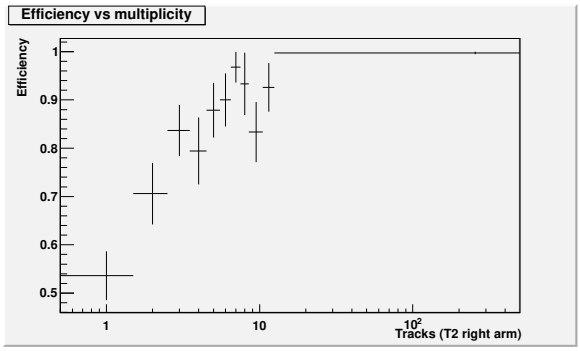

Figure 6.14: T2 trigger efficiency for events having T2 tracks in right arm only, measured from BX-triggered data

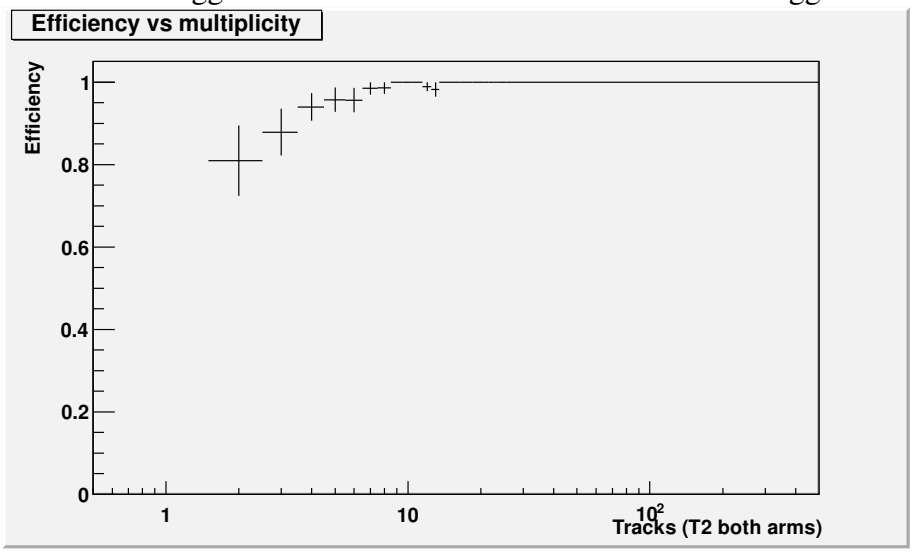

Figure 6.15: T2 trigger efficiency for events having T2 tracks in both arms, measured from BX-triggered data

RP may give rise to a shower of tracks in the far RP, which gives a 1.5% correlated track reconstruction inefficiency.

RP one-arm two-proton pileup correction

SD events with a proton in both the top and bottom RPs of the same arm due to pileup would not trigger the RP-V 2-arm veto, but nor would we select it, with our demand for exactly one track in a near vertical RP and one track in the corresponding far vertical RP. This gives an inefficiency of 0.6% – 7.4% that we correct for. We chose this two-track requirement because the proton reconstruction only produces one proton per arm,

Table 6.2: RP correction factors from the elastic analyses, measured from the real data: here are shown the two varying corrections – the showering correction (1.5%) is the same for all, because it depends on the RP material budget only. PU= Pileup.

	RP near+far inefficiency					
RP	Segment 1		Segment 2		Segment 3	
	PU (%)	2RP ineff. (%)	PU (%)	2RP ineff. (%)	PU (%)	2RP ineff. (%)
45_tp	0.59	4.2	0.77	4.5	1.13	4.6
45_bt	0.64	4.2	0.99	4.7	1.57	5.4
56_tp	3.85	4.3	5.65	4.6	6.7	4.8
56_bt	1.3	4.1	2.07	4.7	2.33	4.5

giving none in the case of three or more vertical RP tracks in the same arm.

The Table 6.3 shows the correction applied per RP and per data segment; these values are obtained from Tables D.2 – D.4 in Appendix D.4.

Table 6.3: Fraction of events with more than two tracks in the vertical RPs in the same arm, for SD-like trigger conditions: T2=on and RP-V 2-arm trigger veto=off. The data samples used for estimating the corrections are 1 600 000 events from segment 1b, and all events from segments 2 and 3

RP	>2 tracks (%) Segment 1b	Segment 2	Segment 3
45_tp	0.87±0.07	0.59±0.13	1.77±0.20
45_bt	0.86±0.07	0.85±0.16	1.52±0.17
56_tp	2.29±0.08	3.13±0.19	3.60±0.17
56_bt	3.98±0.13	5.94±0.37	7.43±0.34

RP inelastic proton reconstruction failure correction

The inelastic proton reconstruction module sometimes fails to converge, in which case it saves a proton with a placeholder value. Any candidate with the proton reconstruction failing will not contribute after applying the (θ_x, θ_y)-dependent acceptance correction.

From a Pythia 8 SD sample we extracted the rate of proton ξ reconstruction failure for events with an SD-like topology of the reconstructed T2 and RP tracks, plotting in Figure 6.16 the fraction of these events vs the ξ of the generated proton with $\xi > -20\%$. This correction is 0.1 – 0.3%.

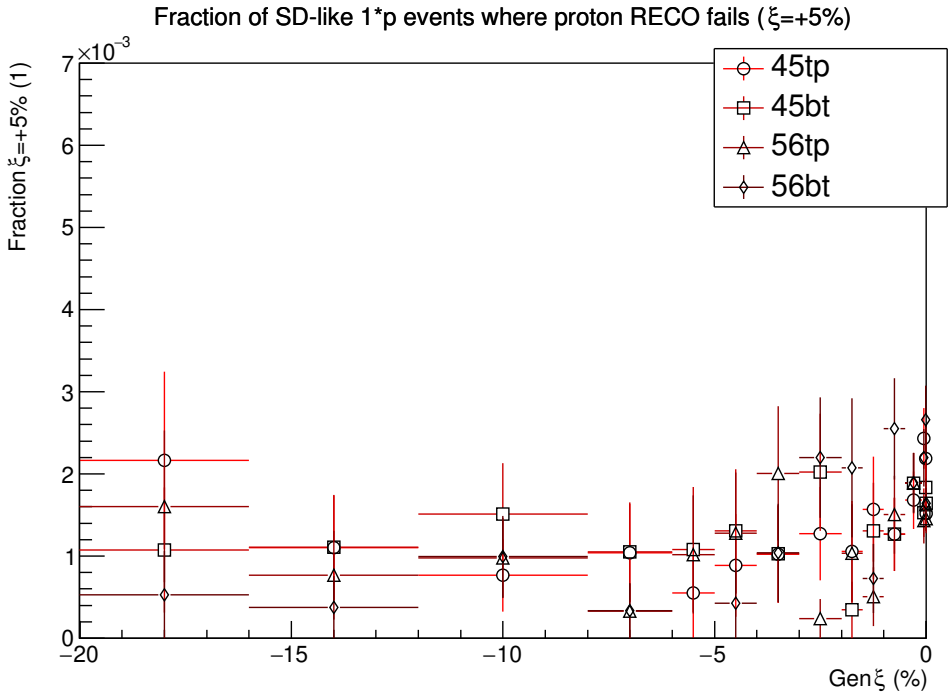

Figure 6.16: Inelastic proton reconstruction failure (obtaining ξ-value + 5% from the proton reconstruction) rate as a function of the generated ξ. The data used is a Pythia 8 SD sample of 539 000 events.

RP t-acceptance correction

The measured differential SD cross section can be approximated as an exponential between at least $|t| \approx 0.4$ GeV^2 and $t_{min} \approx 0.02...0.07$ GeV^2, where t_{min} depends on the proton ξ. Therefore we introduce a correction for the invisible SD below t_{min} by fitting an exponential function to the t-spectra of every class and RP between the first bin to the right of the highest $d\sigma/dt$ bin, $t(peak + 1)$, in the histogram and $-t$ = 0.3 (or 0.4) GeV^2. The latter is used in case the fit to $|t| = 0.3$ GeV^2 gives a bad fit with a positive slope. Then we extrapolate this fit down to $|t| = t_0$. Here $t_0(\xi = 0) = 0$ and

$$t_0(\xi) \approx \frac{m_p^2 * \xi^2}{1 + \xi} \tag{6.9}$$

is the smallest $|t|$-value kinematically allowed. For this t_0, we use representative ξ values for the 2T2 categories: for all 1T2 SD classes t_0 is set to zero, since even at the upper edge of 1T2-2T1 at ξ = 2.7%, t_0 is still only $t_0 \approx 7 * 10^{-4}$ GeV^2.

For the case of one 2T2 class $-20\% < \xi < -2.7\%$ we choose a representative value $\xi = 8\%$ near to but below the midpoint, since the high-ξ acceptance ends just after the upper edge. On the other hand, for the case of three 2T2 classes, with edges $-20\% < \%\xi_3 < -13\%$, $-13\% < \xi_2 < -8\%$ and $-8\% < \xi_1 < -2.7\%$, we use the midpoints for the lower two categories: $\xi_{3,0} = -15\%$, $\xi_{2,0} = -10.5\%$ and $\xi_{1,0} = -5.35\%$, giving respectively t_0 values $t_0(1 * 2T2) \approx 0.0061$ GeV^2 and $t_0(3 * 2T2) \approx 0.0027$ GeV^2 (low ξ), 0.011 GeV^2 (mid-ξ) and 0.023 GeV^2 (high ξ).

6.4 Unfolding

Unfolding refers to mathematical methods that remove the smearing introduced by resolution effects. Because of the smoothing and loss of information in the measurement instrument, inverting this is an ill-posed problem, so straightforward matrix inversion techniques often work very badly. Iterative methods can be used, but in general there will be a tradeoff between convergence and systematic bias when selecting the regularization applied.

6.4.1 Bayesian unfolding methods, and others

RooUnfold [95] is a software tool for unfolding, where we choose to use the Bayesian iterative unfolding method, based on [112], that can unfold both 1-dimensional histograms (with a 2D response matrix), and 2D histograms (4D response matrix). As a systematic, we also choose to use the Singular Value Decomposition (SVD) unfolding method, based on [113]. This method is not iterative in the same way as the Bayesian method, but instead reproduces the learning distribution on scales smaller than N/k, where k is the SVD regularisation parameter, and N is the number of bins in the histogram to be unfolded.

6.4.2 MC sample

The unfolding was done using a reconstructed MC sample based on Pythia 8 SD proton-proton collisions for a learning sample[5], and also with an inclusive inelastic EPOS [80, 81] reconstructed MC sample. The unfolding took the MC generator-level particle topology as training sample Truth and the reconstructed MC track topology as training sample Measured. So as to not introduce an overall rescaling factor unnecessarily, the MC sample events selected were those where any SD topology from Table 5.2 was a match for the topology of the reconstructed tracks.

The effect of mixing pileup from the real data BX-triggered events into the MC sample had an up to 2% effect, as can be seen in Table 6.4.

Table 6.4: Ratio of reconstructed events with and without real pileup mixed in for Pythia 8, for signal SD classes.

Category	Ratio PU / no PU added
0T2	0.984
1T2-0T1	0.980
1T2-1T1	0.977
1T2-2T1	0.989
2T2	1.002

6.4.3 Improving our unfolding methods

The concern to not introduce some scaling factor was later alleviated by filling the response matrix and the reconstructed learning histograms with the same acceptance correction weights as the histograms to be unfolded, filled for the same SD-topology reconstructed events, and filling the unfolding simu truth for all events with a topology of the generated particles matching any of the SD topologies, independent of the reconstructed track topology. This was found to converge much better, as explained in

[5] to determine the 2D response matrix, and the one-dimensional simu truth and resolution-smeared reconstructed distributions

the Appendix O on MC self-unfolding and MC bias, when unfolding one MC sample with another as learning sample, i.e. EPOS with Pythia 8 as learning sample, or vice versa. Based on the benchmarking shown in the appendix, we decided to use Bayesian unfolding with i=2 iterations as the main unfolding method, and use SVD unfolding as a systematic, with regularisation parameter k=7. The k-parameter selection is a tradeoff between too low a k-value causing any structure at smaller scales than approximately N_{bins}/k to follow the learning sample distribution, and too high a value blowing up small structure from statistical fluctuations. Since the cross section and closure histograms with entries for each SD signal or background class has four to five signal bins out of 12 bins total, we see that at $k = 3$ the ratios between signal classes in an SVD-unfolded histogram comes almost completely from the learning sample, not from the data, while near $k = 12$ any unfortunate statistical fluctuation may cause many points to be move very far with huge error bars in the unfolding. The optimum k-value to minimise both effects was found to be k=6 to 8 for the case of cross-MC unfolding an EPOS sample with learning histograms from a Pythia sample, or vice versa. The $|t|$ and ξ spectra have 22 bins, but they are much more continuous than the single-bin classes in the closure histograms, so the optimal unfolding k-value is still in the single digits, mostly limited by growing short-wavelength fluctuations above k=6 to 9, and bias towards the MC learning distribution below k=4.

The better convergence for the $|t|$-unfolding with properly weighted unfolding also lead to a much smaller contribution from the $|t|$-extrapolation correction, giving a near-zero correction for unfolding with Pythia, and negative corrections for unfolding with EPOS, due to the high-slope second exponential in EPOS being reflected in the unfolded histogram. These negative acceptance corrections are obviously unphysical, so one may either accept the correction only if it is positive, or neglect it due to its small size. We choose the latter in the results presented below on the MC closure ratio, and the SD cross section measurements in Chapter 7.1.

6.4.4 Within-class unfolding

Histograms of variables under study like t and ξ were unfolded for a given RP and SD class, transforming reconstructed variables to generator-level particle variables, with some inevitable unfolding biases. Without correcting for the migration between SD classes, some of these histograms will also be biased by class migration.

6.4.5 Class migration

To unfold variables to SD mass bins – corresponding to the SD classes at MC generator level, before the resolution smearing effects of reconstruction – we apply a simple matrix inversion to a class migration matrix normalised to $\sum_{RECO} M_{RECO,MC} = 1$. This normalised matrix is inverted, and multiplied by a vector of measurements of the variable under study for each RECO-class – the vector may consist of cross sections as bins in a histogram, or individual histograms of the differential cross section as a function of a proton variable, per SD class. The class migration correction gives an approximation for the histogram of events all in the same MC mass bin. In this thesis, only the former, integral cross section class migration correction is used.

Matrix inversion can be used in this correction without drastic loss of significance since the matrix is not singular, nor is the condition number very small. An estimate of the uncertainty of the inverse matrix was obtained by taking the class migration matrix before normalisation, and replacing each number of entries per class $n_{i,j}$ with a Poisson distribution with the same mean,

$$\mathcal{M}^{(k)}_{i,j} = Poiss(n_{i,j}) \tag{6.10}$$

$$\sigma(\mathcal{M}^{-1}) = \text{std.dev.}((\mathcal{M}^{(k)})^{-1}) \tag{6.11}$$

In order not to introduce a bias when summing together measurements from different classes that use different selection requirements – principally the beam halo selection cut only used for SD events without a visible gap, in class 2T2 – we have produced all histograms both with and without the differing requirements. We then make the class-migration corrected cross section for each class by selecting the integral histogram with the same selections as the target SD class.

6.4.6 Proton reconstruction ambiguities

I tested 2D unfolding on the strongly correlated variables (ξ, θ_x) , but was not able to find a region of parameters such that the unfolding converged in a reasonable number of steps, for a given binning in (ξ, θ_x). (This test was done for Bayesian unfolding only, before the improvements noted in Section 6.4.3). Therefore all differential histograms (like ξ spectra, $d\sigma/d\xi$) presented in this thesis are unfolded against only the variable shown.

6.5 Closure test

The closure test is done by analyzing the simulated Pythia 8 and EPOS samples as reconstructed by the TOTEM offline software, running the same analysis code as is used to analyse the real data, as far as possible. To validate the analysis procedure and code, we compare the number of MC truth events in each SD class to the same number, within the uncertainties, as the result of the analysis of the reconstructed tracks produced for these events in the Pythia/EPOS and CMSSW simulation chain. There are unavoidable differences to the real analysis, including luminosity calculation (not used in the MC closure test), and the difference between the backgrounds seen in the real data, with respect to those in the simulation. To simulate pileup we mix in random BX events from the real data at the correct PU fraction (only a few percent). The different points plotted in the closure plots (starting with Fig.6.17) are the $|t|$-extrapolation correction based on an unfolded t-spectrum for that SD class; the background-subtracted net signal; the same net signal, unfolded; and with the class migration inverse matrix applied. As noted above in Section 6.4.3, a $|t|$-correction was not applied to the net signal, since the value was near-zero in most categories for Pythia unfolding, and negative for EPOS, as explained in Section 6.5.2.

Still, the main Pythia sample only contains SD events, including some where the protons may be excited to an N^* baryon state and decay to a proton and pion(s), which may be classified as a two-proton (2P) background event.

To mimic the real data analysis as closely as possible, we use MC samples with real PU mixed in, and subtract the estimated PU and 2P backgrounds.

The closure plots for this test can be found in Figures 6.17, and H.1 – H.3 in the Appendix H. The Figures 6.18 – 6.19 show for Bayesian and SVD unfolding the range of correction factors over the different RPs, for the SD signal classes. The SD signal categories with T2 tracks that we can see in the data, 1T2-0T1 to 2T2, are shown on a zoomed-in scale around a ratio of 1. The closure ratios for the four measured SD classes are given in Table 6.5.

6.5.1 Closure test systematic uncertainty

The systematic uncertainty extracted from the closure tests consists of two parts: the difference between the input generated histograms and the output unfolded histograms, and the difference between that for Pythia 8 and EPOS. The closure ratio for each SD

Table 6.5: Ratio of corrected number of reconstructed events to the simu truth for Pythia 8, the closure ratio. Used for correcting the measurements in real data. Rightmost column for comparison, showing class migration ratio, without t-extrapolation added, as explained in the text. Pythia 8 SD sample of 210 000 events, with real PU mixed in, and background subtraction applied.

Category	Unfolded ratio (Bayes, i=2)	Uncertainty	Unfolded ratio (SVD, k=7)	Uncertainty	Comparison Class Migration ratio	Uncertainty
45_tp						
1T2-0T1	0.918	±0.028	0.908	±0.038	0.815	± 0.035
1T2-1T1	0.939	±0.013	0.939	±0.014	0.848	± 0.013
1T2-2T1	0.953	±0.020	0.981	±0.030	0.916	± 0.032
2T2	0.913	±0.030	0.895	±0.044	0.884	± 0.047
45_bt						
1T2-0T1	0.933	±0.027	0.937	±0.037	0.832	± 0.034
1T2-1T1	0.935	±0.013	0.940	±0.014	0.846	± 0.013
1T2-2T1	0.939	±0.021	0.949	±0.033	0.890	± 0.033
2T2	0.885	±0.031	0.877	±0.046	0.887	± 0.049
56_bt (*)						
1T2-0T1	0.965	±0.034	0.956	±0.046	0.836	± 0.043
1T2-1T1	1.031	±0.014	1.044	±0.015	0.939	± 0.014
1T2-2T1	1.009	±0.021	0.975	±0.032	0.915	± 0.033
2T2	1.069	±0.033	1.113	±0.048	1.082	± 0.051
56_tp (*)						
1T2-0T1	1.062	±0.033	1.104	±0.045	0.967	± 0.041
1T2-1T1	1.043	±0.014	1.048	±0.015	0.942	± 0.014
1T2-2T1	1.040	±0.021	1.050	±0.032	0.983	± 0.033
2T2	1.028	±0.032	1.025	±0.046	1.053	± 0.049
* = not	used					

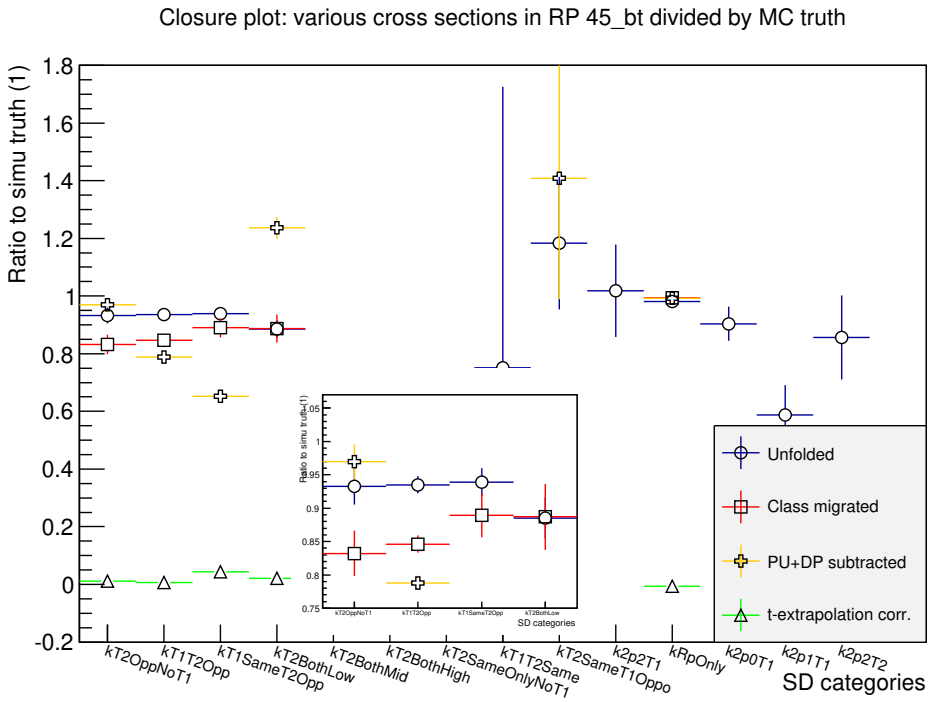

Figure 6.17: Arm 4-5 bottom: Ratio of unfolded and corrected RECO-level event numbers to the generated true distribution with background subtraction applied. Data sample is Pythia 8 SD, 210 000 events, with real BX pileup added. Inset shows the 1T2 and 2T2 classes, zoomed in. No $|t|$-correction applied, Bayes i=2 unfolding.

class is used as a correction factor, and we assign a systematic uncertainty equal to half the difference from 100% for the ratio. Likewise, we take half the difference between the Pythia 8 and EPOS unfolding as another systematic uncertainty, and report the average of the values unfolded with both MCs as the final result. As an unfolding method systematic, we take half the difference between the Bayesian (2 iterations) unfolding and SVD unfolding (regularisation parameter k=7).

6.5.2 EPOS closure plots

With the improved unfolding, running over a large one-million event EPOS sample, we find reasonable closure values in the range 82 – 97% with Bayesian 2-iteration unfolding, and the similar range 84 – 98% with SVD unfolding, with k=7. The latter results are shown in Figure 6.20, and H.8 – H.14 in the Appendix H.2. Note that these plots were produced while subtracting estimated PU and 2P backgrounds, as this EPOS sample did have real pileup events mixed in, at the few percent level.

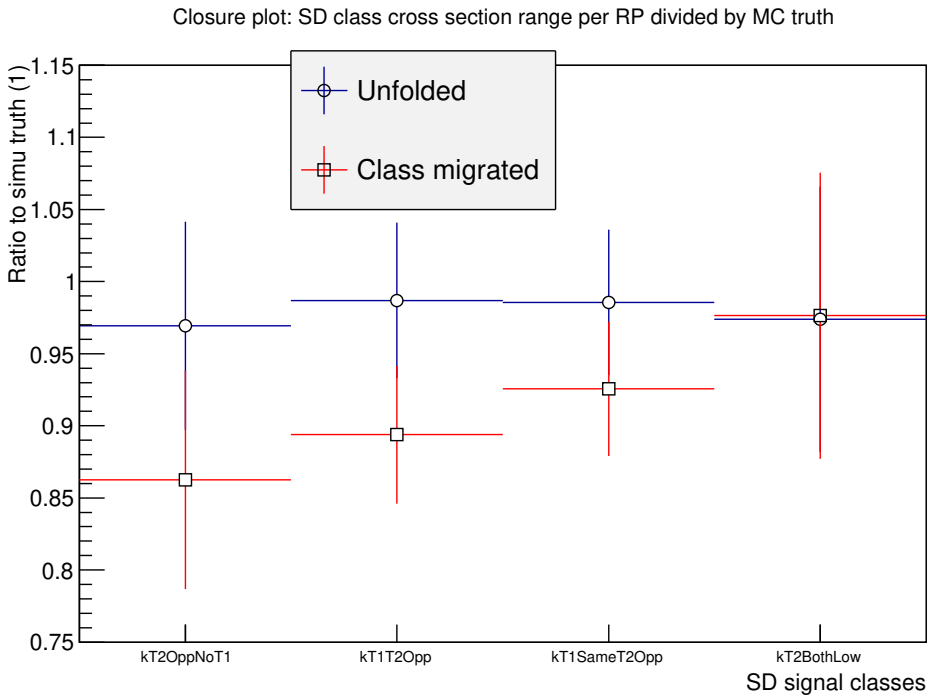

Figure 6.18: Ratio of number SD events after unfolding and application of corrections to the number generated true SD events in MC as function of SD class with background subtraction applied, in blue. Red shows class migration comparison closure ratio range. Data sample is Pythia 8 SD, 210 000 events, with real BX pileup added. Unfolding method is Bayesian, with 2 iterations. Error bar shows the difference between different RPs. No $|t|$-correction applied, see text.

A marked difference compared with the Pythia sample was the SD cross section for events generated in the EPOS sample being peaked closer to $t = 0$ than the pure exponential that we fit on the reconstructed t-spectrum, so the $|t|$-fit at larger $|t|$-values will only fit the component with a small slope; for more details, see Section 6.5.3. Now that the unfolding is working correctly, this gives a negative estimate for how much of the $|t|$-spectrum we are missing due to acceptance limitations, which is obviously nonphysical and must be disregarded. Since the estimated $|t|$-correction is small, we may either accept the correction only when it is positive, or disregard it. We choose the latter since we expect the unfolding correction to learn to include any $|t|$-correction in the MC sample, so it is only in case of the simple matrix-based class migration correction that we may legitimately add the $|t|$-correction as a separate contribution. Even there. the effect is small, at a maximum +0.02 to the closure ratio for class 2T2

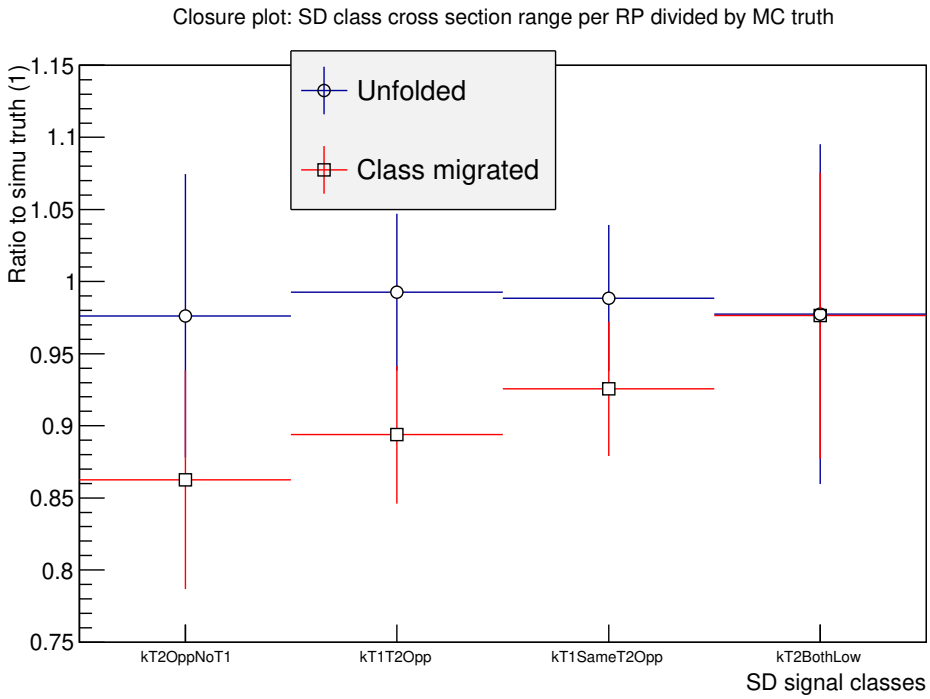

Figure 6.19: Ratio of number SD events after unfolding and application of corrections to the number generated true SD events in MC as function of SD class with background subtraction applied, in blue. Red shows class migration comparison closure ratio range. Data sample is Pythia 8 SD, 210 000 events, with real BX pileup added. Unfolding method is SVD, with k=7 regularisation parameter. Error bar shows the difference between different RPs. No $|t|$-correction applied, see text.

in some RPs. Therefore, we do not include the $|t|$-correction into any of the closure ratios, nor as a separate correction to the real data cross sections.

The closure ratios are given in Table 6.6. The Figures 6.21 – 6.22 show the range of correction factors over the different RPs, for the SD signal classes, using two different unfolding methods, SVD and iterative Bayesian.

6.5.3 EPOS generated t-spectra for SD-like events, compared to Pythia 8

The EPOS generated protons exhibit a second faster-growing exponential at small $|t|$ as can be seen in the Figures 6.23 – 6.24; for other classes, see Figures H.15 – H.17 in Appendix H.3. The second exponential is missing in 2T2 since the minimum $|t|$

Table 6.6: Ratio of corrected number of reconstructed events to the simu truth for EPOS, the closure ratio. Used for correcting the measurements in real data. Rightmost column for comparison, showing class migration ratio, without t-extrapolation added, as explained in the text.

Category	Unfolded ratio (Bayes, i=2)	Uncertainty	Unfolded ratio (SVD, k=7)	Uncertainty	Comparison Class Migration ratio	Uncertainty
45_tp						
1T2-0T1	0.945	±0.038	0.949	±0.052	0.734	± 0.046
1T2-1T1	0.844	±0.026	0.873	±0.033	0.736	± 0.028
1T2-2T1	0.852	±0.030	0.870	±0.046	0.894	± 0.058
2T2	0.875	±0.025	0.982	±0.041	0.950	± 0.033
45_bt						
1T2-0T1	0.971	±0.035	0.978	±0.049	0.760	± 0.043
1T2-1T1	0.876	±0.023	0.864	±0.032	0.770	± 0.025
1T2-2T1	0.824	±0.032	0.845	±0.048	0.855	± 0.062
2T2	0.836	±0.025	0.870	±0.040	0.915	± 0.032
56_bt (*)						
1T2-0T1	0.944	±0.038	0.911	±0.053	0.702	± 0.047
1T2-1T1	0.924	±0.027	0.904	±0.035	0.820	± 0.029
1T2-2T1	0.906	±0.035	0.933	±0.052	0.960	± 0.068
2T2	0.883	±0.028	0.883	±0.044	0.955	± 0.036
56_tp (*)						
1T2-0T1	0.943	±0.039	0.902	±0.054	0.683	± 0.048
1T2-1T1	0.972	±0.027	0.971	±0.036	0.873	± 0.030
1T2-2T1	0.877	±0.031	0.879	±0.049	0.897	± 0.061
2T2	0.932	±0.026	0.964	±0.043	1.022	± 0.034
* = not	used					

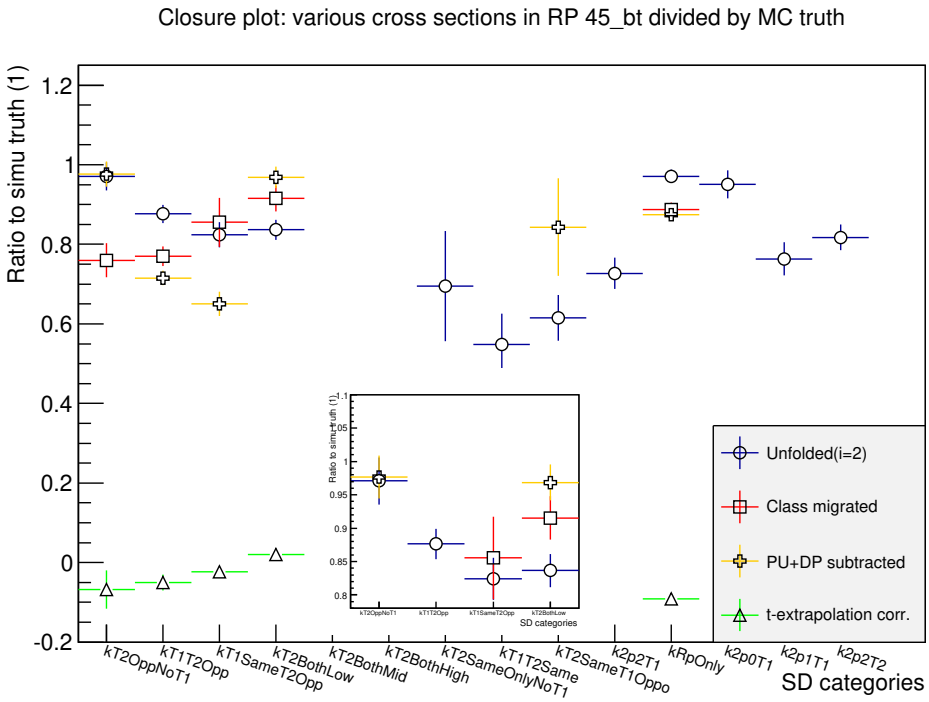

Figure 6.20: Arm 4-5 bottom: Ratio of unfolded and corrected RECO-level event numbers to the generated true distribution with background subtraction applied. Data sample is EPOS inclusive 1 000 000 events, with mixed real BX pileup. Inset shows SD categories 1T2-0T1 to 2T2 zoomed in. Unfolding method is Bayes, 2 iterations. No $|t|$-correction is added, see text for explanation of the negative values.

kinematically allowed is $|t| > 0$ at $\xi < 0$, as explained in Section 6.3.3. These spectra are normalised to have an integral of 1 over the whole $|t|$-range for each category. We fitted them with a sum of two exponentials ($d\sigma/dt = exp(A_1 + B_1 * t) + exp(A_2 + B_2 * t)$), to estimate how much the t-extrapolation correction is biased by the partly unseen second exponential causing the correction evaluated with the smaller slope to be too small. These values can be found in Tables 6.7 and 6.8. To a first approximation, the bias due to the second exponential in EPOS is $\approx 30\%$, explaining a large part of the shortfall observed. Due to the normalisation, in Table 6.8, we expect the integral sum to be 1 for the four RPs, except for the 2T2 category where the exponential slope changes over the $|t|$-range shown in Figure 6.24 due to the kinematic minimum $|t|$ mentioned above; already in 1T2-2T1 the slope change is visible in the first bin, as can be seen for Pythia in Figure H.16.

To see if some other MCs also predict a second exponential, we obtained $|t|$-spectra

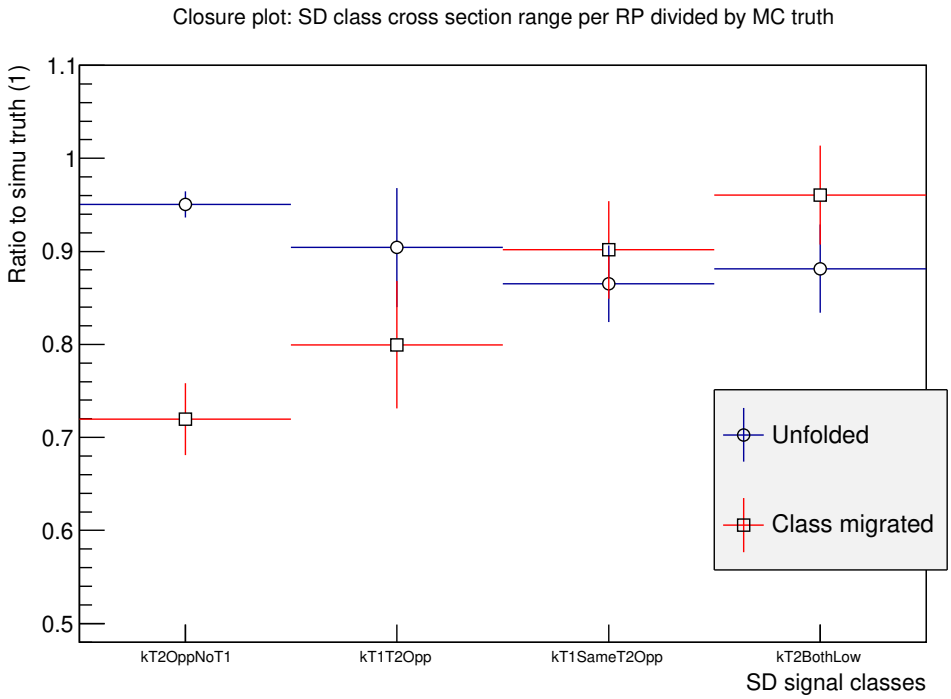

Figure 6.21: Ratio of number of SD events after unfolding and application of corrections to the number generated true SD events in MC as function of SD class with background subtraction applied, in blue. Red shows class migration comparison closure ratio range. Data is an inclusive EPOS sample of 1 000 000 events, with real BX pileup added. Error bar shows the difference between different RPs. Unfolding method is Bayes, 2 iterations.

for the four SD classes that we measure, 1T2-0T1 to 2T2, as predicted by the QGSJet MC, from the author of that MC (priv.comm.). The double exponential fits of the 1T2-class $|t|$-spectra and the single exponential fit for class 2T2 are presented in Table 6.7 and shown in Appendix N.

6.5.4 Difference between EPOS and Pythia unfolding, and the two unfolding methods

The cross-section difference per RP for real data, when using Pythia 8 or EPOS for class migration and unfolding is shown in Figures 6.25 – 6.26, respectively. Half of the observed difference is used to estimate the MC-dependent systematic uncertainty systematic uncertainty for the class migration and the unfolding. The variations of the

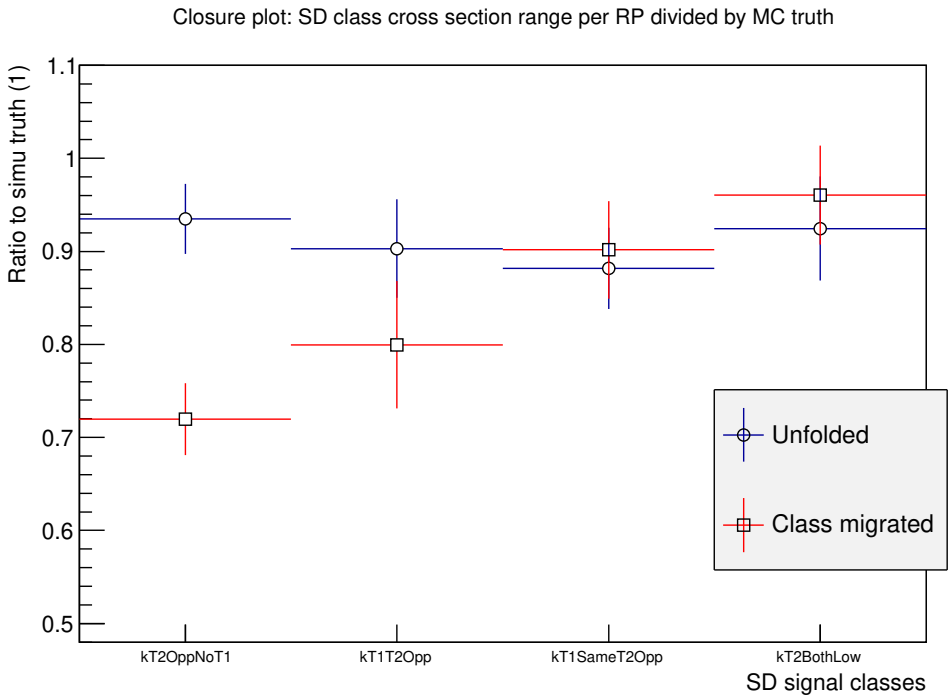

Figure 6.22: Ratio of number of SD events after unfolding and application of corrections to the number generated true SD events in MC as function of SD class with background subtraction applied, in blue. Red shows class migration comparison closure ratio range. Data is an inclusive EPOS sample of 1 000 000 events, with real BX pileup added. Error bar shows the difference between different RPs. Unfolding method is SVD, k=7.

difference between the individual RPs within an SD class are generally small, whereas there are larger differences between the different SD classes. The difference shows the same pattern as a function of SD class for both the class migration and unfolding methods, at least for the first three 1T2 classes.

Figure 6.27 shows the difference between Pythia learning sample Bayesian and SVD unfolding of the real data, after using the appropriate closure correction from Table 6.5. Figure 6.28 shows the same method uncertainty when unfolding real data with EPOS. These unfolding method differences are significantly smaller than the differences when unfolding the real data with different MC samples.

Table 6.7: The exponential slope parameters B from a sum of two exponentials (B_1 and B_2) – except for category 2T2 where only one exponential is visible – for EPOS and from a single exponential (B) for Pythia-generated protons in SD-like events. Fit range is $0 < |t| < 0.3$ GeV^2 for all classes except 2T2 (lower limit 0.05 GeV^2). MC samples used are a Pythia SD sample of 540 000 events and an EPOS sample with about 39 000 SD events. Comparison with fitted slope parameters B for QGSJet all triggered events as extracted in Appendix N.1. Values in parentheses are bad fits.

Category	B_2 EPOS [GeV^{-2}]	B_1 EPOS [GeV^{-2}]	B Pythia 8 [GeV^{-2}]
0T2	-63.8 ± 3.7	-10.14 ± 0.24	-12.25 ± 0.05
1T2-0T1	-63.2 ± 6.6	-10.48 ± 0.44	-11.75 ± 0.07
1T2-1T1	-56.0 ± 3.6	-8.55 ± 0.28	-9.15 ± 0.03
1T2-2T1	-51.3 ± 10.4	-5.62 ± 0.33	-6.56 ± 0.04
2T2	-	-4.46 ± 0.16	-5.93 ± 0.07
Category	B_2 QGSJet [GeV^{-2}]	B_1 QGSJet [GeV^{-2}]	B QGSJet [GeV^{-2}]
1T2-0T1	(-30.78 ± 0.16)	(-3.43 ± 0.06)	(-10.85 ± 0.07)
1T2-1T1	-27.1 ± 0.7	-5.71 ± 0.11	(-8.24 ± 0.07)
1T2-2T1	-22.8 ± 4.0	-4.9 ± 0.3	-5.98 ± 0.17
2T2	-	-	-5.50 ± 0.25

6.6 Systematic uncertainties

The systematic uncertainties come from the closure test ratios, see Section 6.5.1 above, the MC bias from the section above, the 4% CMS luminosity uncertainty from Section 6.1.5, the T2 trigger efficiency correction uncertainty from Section 6.3.2, and the differences between the cross section measurements in the three RPs used. Since the measurements in all four RPs are in principle independent, we assign a systematic uncertainty equal to one third of the largest difference between the cross sections from the three best RPs; we exclude the RP 5-6 top which has a very large BH background, and assign the prefactor $\frac{1}{3}$ due to remaining background in RP 5-6 bottom, as explained in Chapter 7.1. Finally, half the difference between class migration and unfolding is added as a "method" systematic, and similarly half the difference between the main result unfolded with Bayesian (2 iterations), and the corresponding results unfolded with SVD (k=7) is quoted as an "SVD" systematic.

Table 6.8: Integral of the fitted exponentials $\int_0^\infty dt * f_i(t)$ from Table 6.7, as an estimate of the t-extrapolation bias, assumed to only be sensitive to the first exponential. For double exponential, the fraction the second, high-slope component is of the total is shown in brackets. SD class 2T2 is only integrated down to the representative $|t_0| = 0.0061$ GeV^2 chosen in Section 6.3.3

Category	EPOS 2nd	EPOS 1st	Pythia 8 single
0T2	0.264 ± 0.016 $(27.3 \pm 1.4\%)$	0.702 ± 0.022	0.999 ± 0.005
1T2-0T1	0.257 ± 0.027 $(26.5 \pm 2.4\%)$	0.713 ± 0.039	1.001 ± 0.007
1T2-1T1	0.272 ± 0.018 $(28.5 \pm 1.4\%)$	0.68 ± 0.03	0.998 ± 0.003
1T2-2T1	0.088 ± 0.019 $(10 \pm 2\%)$	0.789 ± 0.058	1.003 ± 0.007
2T2	-	0.849 ± 0.035	1.031 ± 0.014

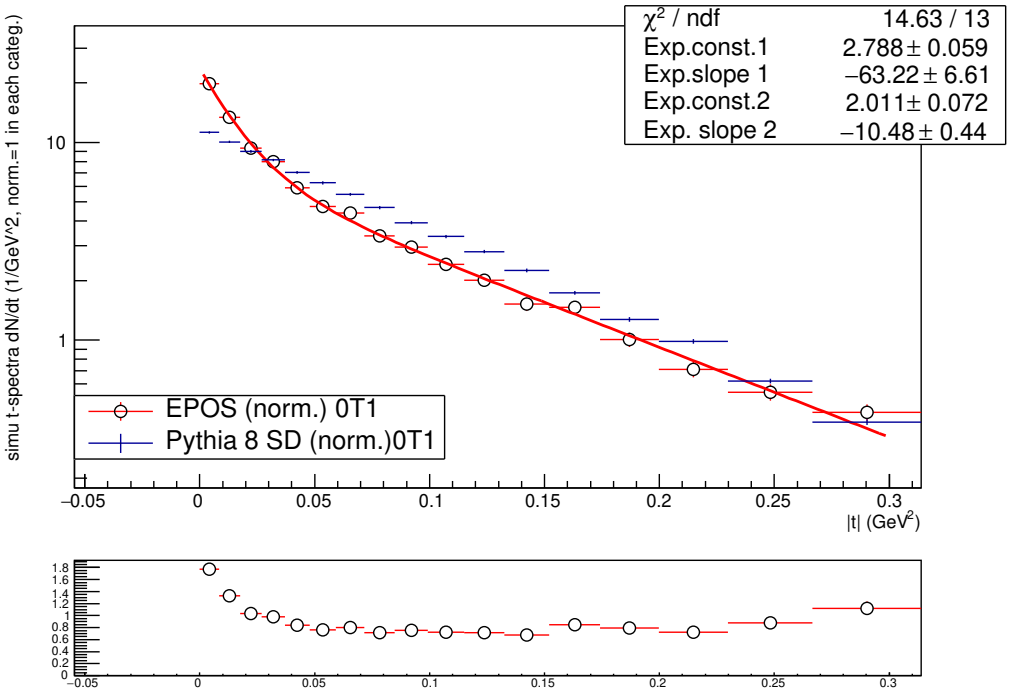

Figure 6.23: Normalised differential proton t-spectrum for EPOS and Pythia 8 events in the 1T2-0T1 SD class using the generator information. The EPOS t-spectrum is fitted with a double exponential shown as a red line and with parameters given in the box. Ratio of EPOS to Pythia 8 $|t|$-spectra shown in lower box.

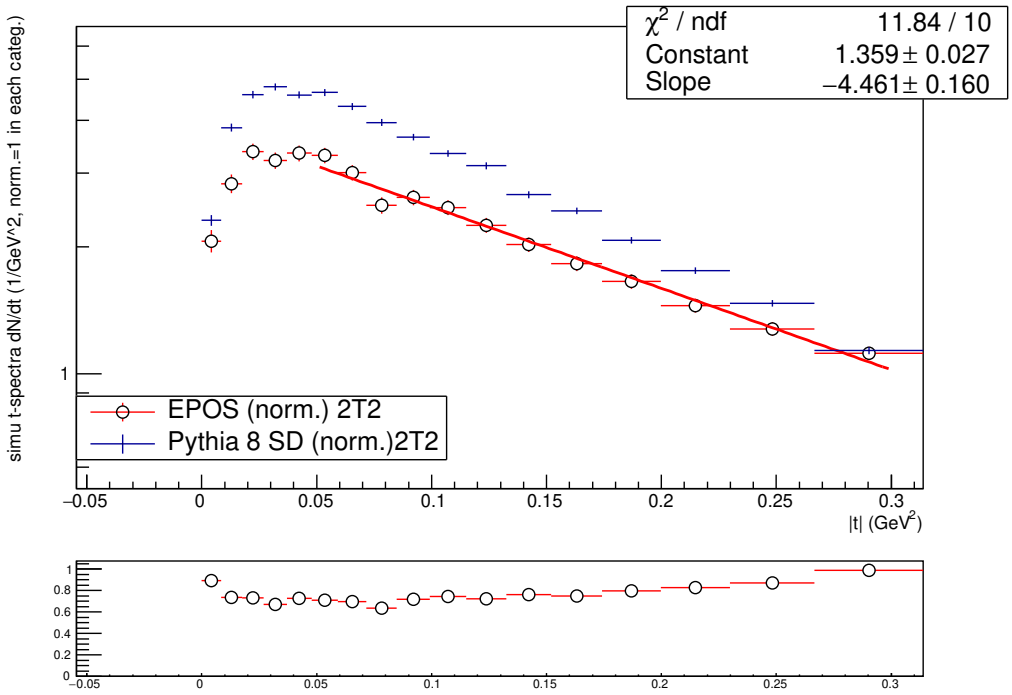

Figure 6.24: Normalised differential proton t-spectrum for EPOS and Pythia 8 events in the 2T2 SD class using the generator information. The EPOS t-spectrum is fitted with an exponential shown as a red line and with parameters given in the box. No acceptance at $t = 0$ because of high-ξ kinematics. Ratio of EPOS to Pythia 8 $|t|$-spectra shown in lower box.

6.6.1 MC $|t|$-slope systematic uncertainty

To get an estimate for the systematic uncertainty on the fitted exponential slope on the differential cross section as a function of $|t|$, we compare the fitted slopes per SD class for generated protons in Table 6.7 with the reconstructed $|t|$-spectra for the same samples, separately for all four vertical RPs, for the same $|t|$-range. This is shown in Tables 6.9 and 6.10. We assign half the difference between the slopes measured for reconstructed t and generated t as a systematic uncertainty on the $|t|$-slope measurement in the next chapter. When this is smaller than the statistical uncertainty of the slope difference, we substitute that as the systematic instead. In analogy with the cross section results, we also quote an "SVD" systematic equal to half the difference between the slopes of Bayesian-unfolded and SVD-unfolded $|t|$-spectra, and an "RP diff." systematic equal to one third of the range of slopes between three of the RPs. Finally, the "MC" systematic is half the difference between Pythia and EPOS-unfolded $|t|$-spectra.

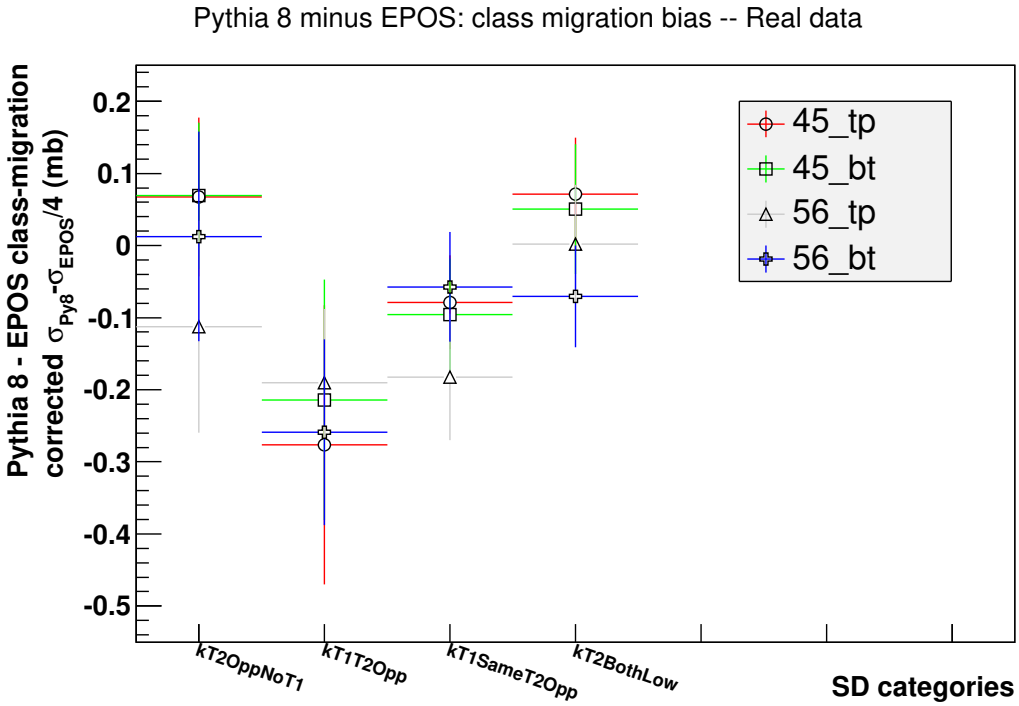

Figure 6.25: The difference between the class-migration-corrected background subtracted cross section for the real data with Pythia 8 and EPOS unfolding per RP for each SD class, after closure correction. The $|t|$-extrapolation correction is not included. Data sample used is 1 439 000 events from Segment 1b.

Examples of reconstructed spectra are shown in Figures 6.29 – 6.30 for Pythia; compare the generated spectra for Pythia and EPOS in Figures 6.23 and H.16. The example fits of EPOS reconstructed $|t|$-spectra can be found in Figures 6.31 – 6.32.

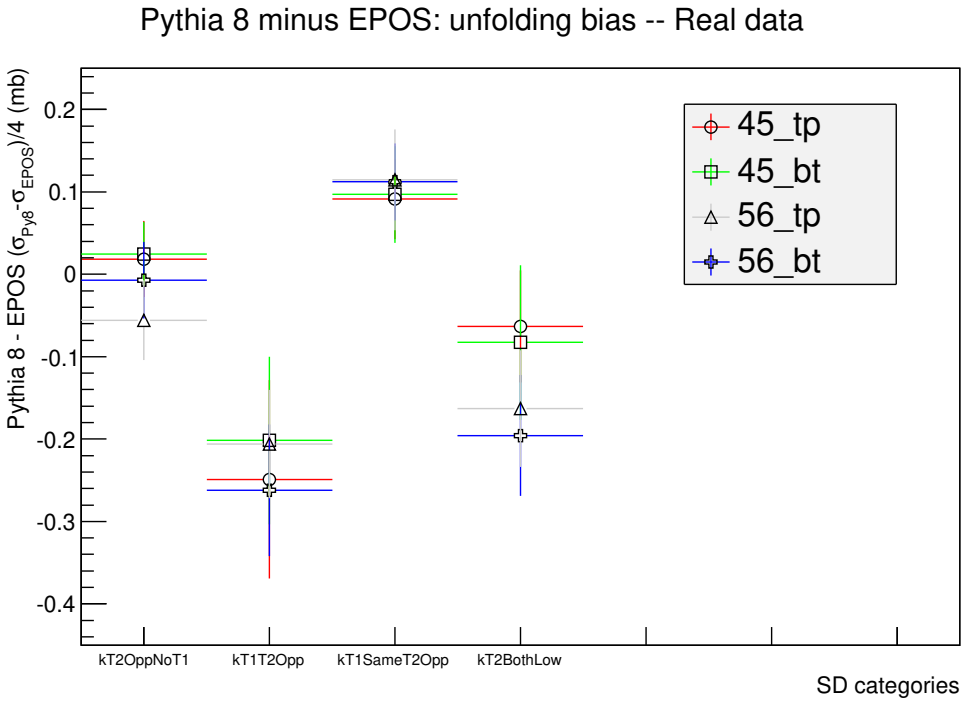

Figure 6.26: The difference between the unfolded cross section from the Pythia 8 and EPOS unfolded real data per RP for each SD class, after closure correction. Bayesian unfolding with 2 iterations.

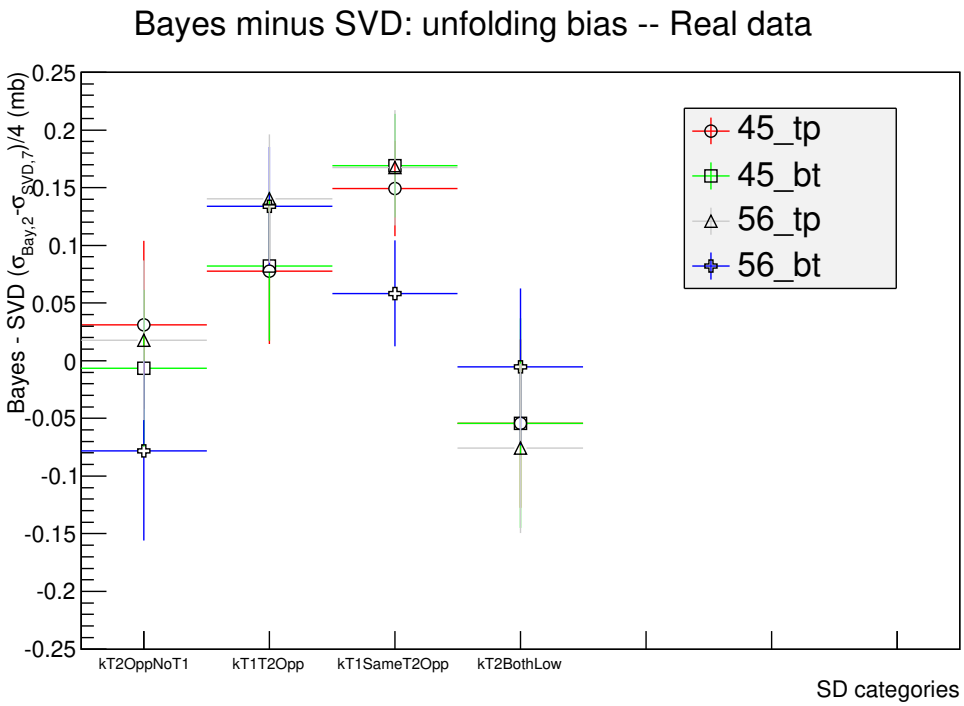

Figure 6.27: The difference between the unfolded cross section from the Pythia 8 unfolded real data when using Bayesian unfolding and using SVD unfolding, per RP for each SD class, after closure correction. MC learning sample is a 210 000 SD event Pythia sample.

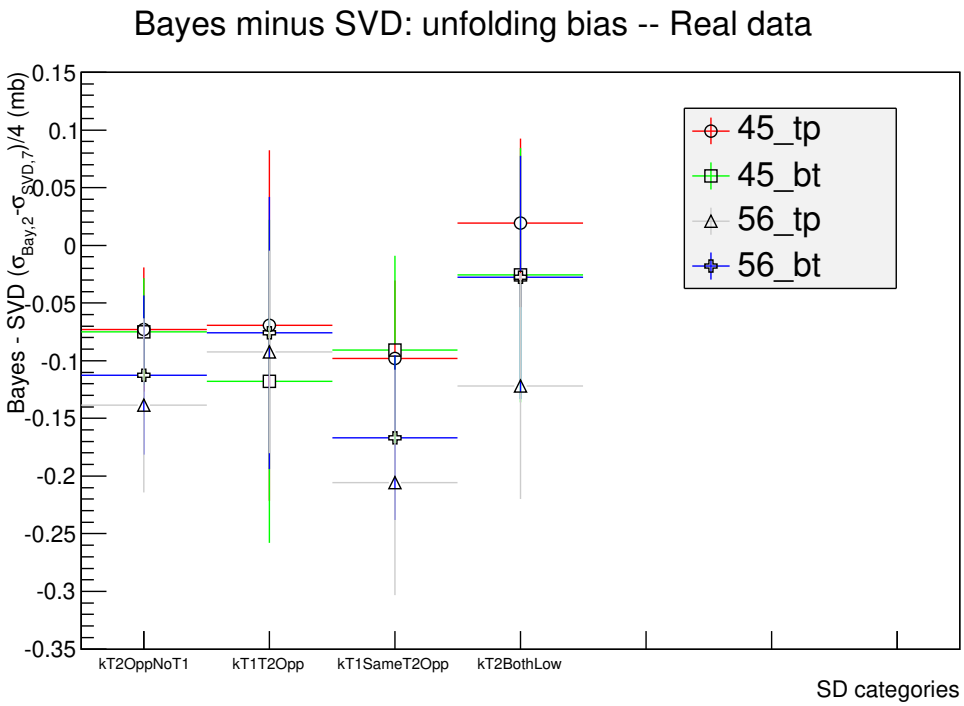

Figure 6.28: The difference between the unfolded cross section from the EPOS-unfolded real data when using Bayesian unfolding and using SVD unfolding, per RP for each SD class, after closure correction. MC learning sample is a 1 000 000 event EPOS sample.

Table 6.9: The single exponential slope parameter B per SD class and RP in SD-like events extracted from EPOS and Pythia MC samples. MC reconstructed $|t|$-values unfolded with the MC sample itself, using Bayesian unfolding, i=2. MC samples used are a Pythia SD sample of 210 000 events and an EPOS sample with 1 000 000 events. The weighted average over all RPs ("B average"), per SD class, is also given.

Category	B(45_tp) [GeV^{-2}]	B(45_bt) [GeV^{-2}]	B(56_tp) [GeV^{-2}]	B(56_bt) [GeV^{-2}]	B average [GeV^{-2}]
Pythia 8:					
1T2-0T1	-11.81±0.23	-12.20±0.20	-11.61±0.23	-11.95±0.20	-11.91±0.11
1T2-1T1	-9.94±0.11	-9.44±0.11	-8.63±0.10	-8.68±0.10	-9.14±0.05
1T2-2T1	-7.53±0.18	-7.08±0.19	-6.40±0.16	-5.67±0.20	-6.68±0.09
2T2	-6.14±0.23	-6.12±0.30	-6.11±0.22	-5.66±0.26	-6.02±0.12
EPOS:					
1T2-0T1	-14.17±0.41	-12.8±0.3	-11.36±0.38	-12.34±0.36	-12.63±0.18
1T2-1T1	-12.02±0.28	-11.75±0.26	-11.07±0.28	-11.54±0.31	-11.60±0.14
1T2-2T1	-7.69±0.36	-6.72±0.41	-6.27±0.36	-6.36±0.37	-6.76±0.19
2T2	-4.73±0.24	-5.05±0.24	-3.63±0.25	-3.85±0.29	-4.37±0.13

Table 6.10: The reconstruction bias for the single exponential slope parameter B per SD class in SD-like events for EPOS and Pythia MC samples.The fit ranges used are 0.07/0.05/0.04 < $|t|$ < 0.3 GeV^2 for classes 2T2 / 1T2-2T1 / all others. The B from reconstructed data is a weighted average over all RPs. MC samples used are a Pythia SD sample of 540 000 events (for the generated protons) and an EPOS sample of 1 000 000 events. Also shown are the systematic uncertainties for B from reconstruction, taken as the maximum of half the reconstruction bias and its statistical uncertainty, to avoid a statistical fluctuation giving a systematic uncertainty estimate that is accidentally too small, and an unfolding systematic equal to half the difference between Bayesian unfolding with i=2, and SVD unfolding with k=7.

Category	Generated proton B [GeV^{-2}]	Reconstructed proton B [GeV^{-2}]	Bias from reconstruction ΔB [GeV^{-2}]	Reconstruction systematic δB [GeV^{-2}]
Pythia 8:				
1T2-0T1	-11.72±0.09	-11.91±0.11	-0.19±0.14	±0.14±0.01(SVD)
1T2-1T1	-9.11±0.04	-9.14±0.05	-0.03±0.06	±0.06±0.02(SVD)
1T2-2T1	-6.69±0.06	-6.68±0.09	+0.00±0.11	±0.11±0.06(SVD)
2T2	-5.90±0.09	-6.02±0.12	-0.12±0.15	±0.15±0.04(SVD)
EPOS:				
1T2-0T1	-11.25±0.32	-12.63±0.18	-1.38	±0.69±0.09(SVD)
1T2-1T1	-9.6±0.2	-11.60±0.14	-2.01	±1.00±0.05(SVD)
1T2-2T1	-5.86±0.25	-6.76±0.19	-0.90	±0.45±0.02(SVD)
2T2	-4.24±0.19	-4.37±0.13	-0.13±0.23	±0.23±0.00(SVD)

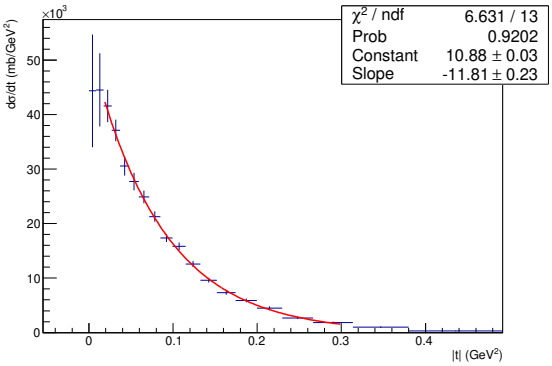

Figure 6.29: Pythia 8 sample with 210 000 SD events and mixed real PU, the fully corrected reconstructed differential cross section as a function of $|t|$ for the SD class 1T2-0T1 in RP 45_tp. Bayesian unfolding with i=2. For the exponential fit, see Sections 7.3 and 6.6.1

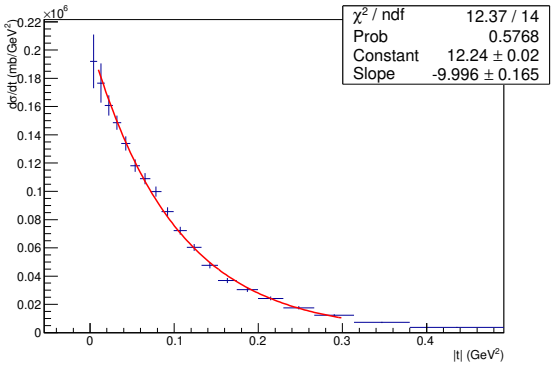

Figure 6.30: Pythia 8 sample with 210 000 SD events and mixed real PU, the fully corrected reconstructed differential cross section as a function of $|t|$ for the SD class 1T2-1T1 in RP 45_tp. SVD unfolding with k=7. For the exponential fit, see Sections 7.3 and 6.6.1

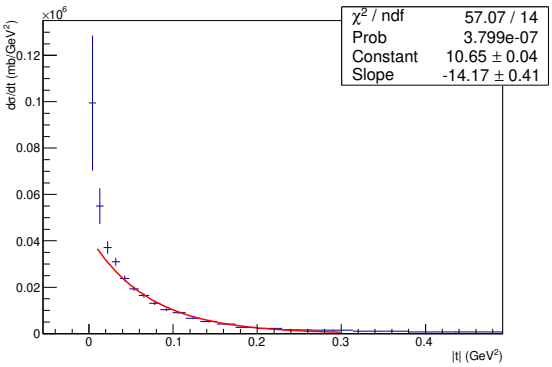

Figure 6.31: EPOS sample with 1 000 000 events and mixed real PU, the fully corrected differential cross section as a function of $|t|$ for the SD class 1T2-0T1 in RP 45_tp. Bayesian unfolding with i=2. For the exponential fit, see Sections 7.3 and 6.6.1

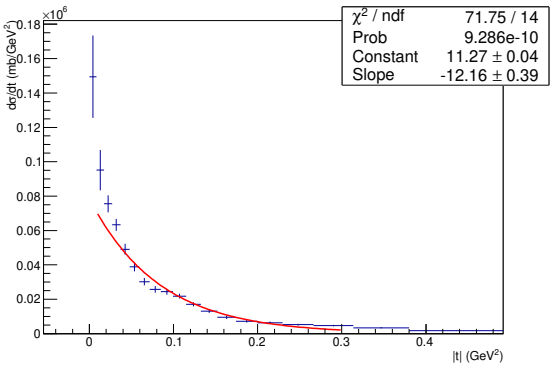

Figure 6.32: EPOS sample with 1 000 000 events and mixed real PU, the fully corrected differential cross section as a function of $|t|$ for the SD class 1T2-1T1 in RP 45_tp. SVD unfolding with k=7. For the exponential fit, see Sections 7.3 and 6.6.1

Chapter 7

Results

7.1 Cross sections

Because the same SD classes are measured independently with each RP, we actually evaluate the total cross section per category as 4 times the weighted average over the two RPs in arm 4-5, excluding both RPs in arm 5-6.

$$\sigma_{SD-class} = 4 * \sum_{4-5} w_i * \sigma_i / \sum_{4-5} w_i \tag{7.1}$$

$$w_i = 1/\delta(\sigma_i)^2 \tag{7.2}$$

$$\delta(\sigma_{SD-class}) = 4/\sqrt{\sum_{4-5} w_i}, \tag{7.3}$$

where σ_i is the measurement in one RP of an SD class, and $\delta(\sigma_i)$ is the statistical uncertainty. The SD classes are then added together without weighting, with all systematics evaluated as described below. The exclusion of arm 5-6 is done because of the large BH background remaining after all selection cuts, especially in RP 5-6 top. Since the 1T2-2T1 class has a large admixture from the 2T2 SD class and BH rejection cannot be used for this class without rejecting the signal, we also exclude the RP 56_bt from the calculated totals, only retaining it for calculating the systematic uncertainty due to variation between RP measurements. This is permissible since 56_bt has approximately double the BH contamination compared to the RPs in arm 4-5, but five times less BH than 56_tp. As explained in Chapter 6.6, we assign a systematic equal to one third of the difference between the three better RPs, excluding RP 56_tp. The largest differences between RPs as a function of how many you select is shown in Table 7.1 for two to four RPs.

Table 7.1: RP differences : Largest differences between RPs in final unfolded cross sections per SD class after all corrections, and class-migration and $|t|$-extrapolation corrected cross sections per SD class after corrections measured from 1 439 000 events in Segment 1b of the real data. The cross sections are unfolded with a Pythia 8 SD sample, having 210 000 events or an EPOS sample with 1 000 000 events. Largest differences are given for all RPs ("4RP"), all except 56_tp ("3RP") and only arm 4-5 ("2RP"). Bayesian unfolding, 2 iterations.

SD class	Class migration largest σ difference			Unfolding largest σ difference		
	4RP (mb)	3RP (mb)	2RP (mb)	4RP (mb)	3RP (mb)	2RP (mb)
Pythia 8						
1T2-0T1	0.14	0.14	0.02	0.09	0.09	0.02
1T2-1T1	0.05	0.01	0.01	0.06	0.03	0.00
1T2-2T1	0.21	0.20	0.03	0.27	0.16	0.05
2T2	0.34	0.11	0.11	0.35	0.11	0.11
sum	0.74	0.46	0.17	0.77	0.39	0.18
EPOS						
1T2-0T1	0.26	0.19	0.02	0.14	0.11	0.01
1T2-1T1	0.07	0.07	0.07	0.09	0.09	0.05
1T2-2T1	0.31	0.18	0.05	0.24	0.14	0.05
2T2	0.41	0.16	0.13	0.45	0.19	0.13
sum	1.05	0.61	0.27	0.92	0.53	0.24

Using the 210 000 event Pythia 8 SD sample for unfolding, the cross sections for the real data segment 1b are presented in Figures 7.1 – 7.3. To go from the raw signal, through background subtraction, unfolding, and closure correction to the final cross section results, we start with Figure 7.1, showing the net background-subtracted signal cross section. After this, we show the final results with the two methods to correct class migration, starting with the simple matrix-based class-migration correction in Figure 7.2, and finally the iteratively unfolded results in Figure 7.3. Both of these figures are corrected with the respective closure correction factor from Table 6.5. The small $|t|$-extrapolation correction that is not added, is shown for reference per SD class in

Figure 7.4.

The same Figures for EPOS unfolding can be found in the Appendix I.

In Table 7.2, you will find cross section values for the individual SD categories extracted from these unfolded cross sections, with an additional correction for the closure ratio not being 1. These are calculated with Pythia unfolding – the difference between EPOS and Pythia results is reported as MC bias, see Appendix I for the corresponding results from EPOS unfolding.

As a cross-check, we also calculated the cross sections using the simple inverse matrix class migration, adding the $|t|$-extrapolation correction. Here we used the closure ratio calculated from class migration plus $|t|$-extrapolation for the Pythia 8 sample, given as the rightmost column in Table 6.5. These cross sections are shown in Table 7.3, and the similar ones for EPOS in Appendix I. The closure-corrected cross sections using the class migration matrix method in Table 7.3 are found to be compatible with the ones obtained using unfolding, shown in Table 7.2 .

Half the difference between this class migration method and unfolding is used as a method systematic on the measured cross sections, the values for which can be found in the Table 7.7. To avoid spuriously small values for the systematic due to a statistical fluctuation, we take the maximum of the method differences for EPOS, Pythia and their average (see below), divided by two, as the systematic for all three – this maximum is given in the last column of the Table 7.7.

Likewise, half the difference between using Bayesian unfolding with 2 iterations, and unfolding with SVD (k=7) is used as an unfolding systematic on the measured cross sections, the values for which can be found in the Table 7.8. To avoid spuriously small values for the systematic due to a statistical fluctuation, we take the maximum of the method differences for EPOS, Pythia and their average (see below), divided by two, as the systematic for all three – this maximum is given in the last column of the Table 7.8.

All the values for the RP with increased background, the RP 56_bt, used only for systematic uncertainty determination, are given in Table 7.4.The values for the RP with high BH background, 56_tp, that is not used, can be found in Appendix J.

The sums over all SD classes are given in Table 7.5, with EPOS values shown also. The systematics from the closure correction, the difference between RPs, and the MC bias of the individual classses are summed up to the systematic uncertainties for the cross section averaged over EPOS and Pythia only, not for each separately. These sums

are to be compared with the default cross sections used by Pythia and EPOS [114], presented in Table 7.10. As can be seen, the EPOS generator describes the ratios of the three 1T2 SD classes much better than Pythia 8, but EPOS overestimates the very low mass 0T2 SD class measured previously indirectly by TOTEM [67]. In addition, as described in Chapter 6.5.3, EPOS exhibits a second faster-rising exponential at low $|t|$ that our data does not have the sensitivity to either verify or contradict; see below, in Section 7.3. Taking all this into account, we cannot select either one of the MCs as unambiguously better at describing all our data. Therefore, we present values unfolded with both MCs and take the average of the two MC unfoldings as the final result. To put an upper limit on the possibility of bias due to using one MC or the other for determining the cross section, we apply an MC systematic of half the difference between the two MCs. The final SD cross sections per class are given in Table 7.6.

To avoid accidentally too small systematic uncertainty estimates, as discussed above in case of the method systematic, we calculated the difference between Pythia and EPOS unfolded or class migration cross sections, both for the main sample of the last 1 439 000 events, and for the initial 900 000 events in Segment 1b. Here the MC systematic presented in Table 7.9 is assigned as half of the bigger difference, for each SD class.

Excluding RP arm 5-6 due to high background remaining after all selections, and averaging the unfolding results with Pythia 8 and EPOS, we find a total SD cross section for the SD mass range $2 * 10^{-7} < \xi < 20\%$, i.e. the range $3.1 < M_X < 3100$ GeV/c^2, of 11.10 $\pm$ 0.13 (stat.) $\pm$ 0.79 (sys.[1]) $\pm$ 0.44 (sys.[2]) $\pm$ 0.87 (sys.[3]) $\pm$ 0.07(sys.[4]) $\pm$ 0.75[5] $\pm$ 0.77[6] mb. Summing the uncertainties in quadrature, this gives a final result for the total cross section of 11.10 $\pm$ 1.66 mb (tot.). Here the central value is chosen to be the unfolded cross section, since data unfolding in the best case should be able to model the detector response better than the simple class migration matrix-based method. Starting from the lowest diffractive masses, the individual SD classes were found to have cross sections of 1.83 $\pm$ 0.35 mb (tot.) for class 1T2-0T1, 4.33 $\pm$ 0.61 mb (tot.) for class 1T2-1T1, 2.10 $\pm$ 0.49 mb (tot.) for class 1T2-2T1, and finally 2.84 $\pm$ 0.40 mb (tot.) for the highest mass 2T2 class.

[1] MC closure ratio + RP cross section differences

[2] Luminosity

[3] MC systematic, half the difference between EPOS and Pythia 8 unfolding

[4] T2 trigger corr. uncertainty

[5] Method systematic, half the difference between unfolding and class migration

[6] Unfolding systematic, half the difference between SVD and Bayesian unfolding

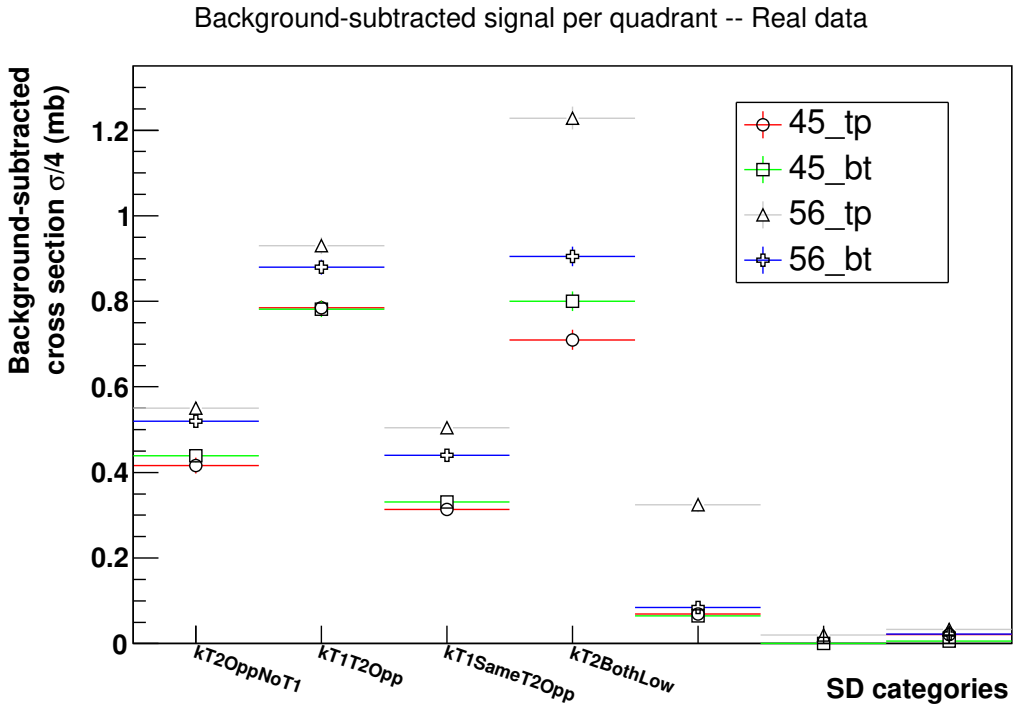

Figure 7.1: The acceptance-corrected and background-subtracted net cross sections for 1 439 000 events of real data in Segment 1b per RP and SD class, before class migration correction and unfolding.

These are between 2% and 50% larger than the preliminary measurement for the different 1T2 SD classes previously shown [79] in a poster at a CERN LHCC open session due to the improved methods for background subtraction and unfolding, and the correction bugs fixed between then and now, as noted in Section 4.1.2, and the selection of EPOS as another MC to use for unfolding. Despite these changes, the new results are still compatible with the previous results with the exception of the result for the 1T2-2T1 class that has the largest discrepancy of 50% due to the large class migration between this class and the 2T2 class, now corrected by unfolding or class migration.

7.2 Differential ξ-distribution

A preliminary measurement of the unfolded differential cross section $d\sigma/d\xi$ visible in each RP can be found in Appendix G, in Figures G.1 – G.8 for the 2T2 SD class; the closure ratio correction is not applied, nor is the $|t|$-extrapolation. A thorough

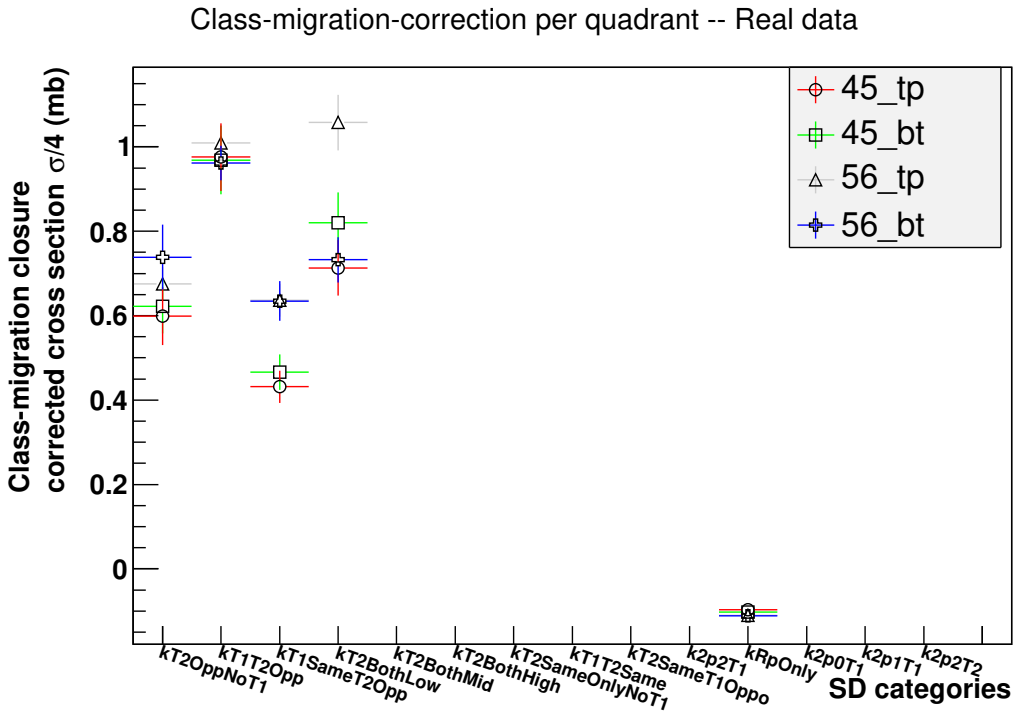

Figure 7.2: The background-subtracted, acceptance-corrected and class-migrated net cross section for real data segment per RP and SD class. The class migration uses SD class migration matrix extracted from a 210 000 event Pythia 8 SD sample with real PU mixed in. Real data sample is 1 439 000 events in Segment 1b. The class migration closure correction is applied. All systematics added in quadrature, including T2 trigger efficiency correction. Method and MC systematic uncertainties not included.

measurement of the ξ spectrum based on these histograms would need to make a bin-by-bin correction for both of these corrections, so instead we choose to present as our result just the SD class-based integral cross sections as a function of $\log_{10}\xi$, presented below in Section 7.2.1.

As can be seen in Figures G.3 and G.7, the top RP in arm 5-6 has a large remaining BH background after all selection requirements, especially at high $\xi < -15\%$. As explained in Appendix G, it would probably not be sufficient to restrict our measurement to $\xi > -15\%$ to exclude the remaining BH background, so we decided not to use 5-6 top at all for the integral cross section SD measurement presented in this thesis.

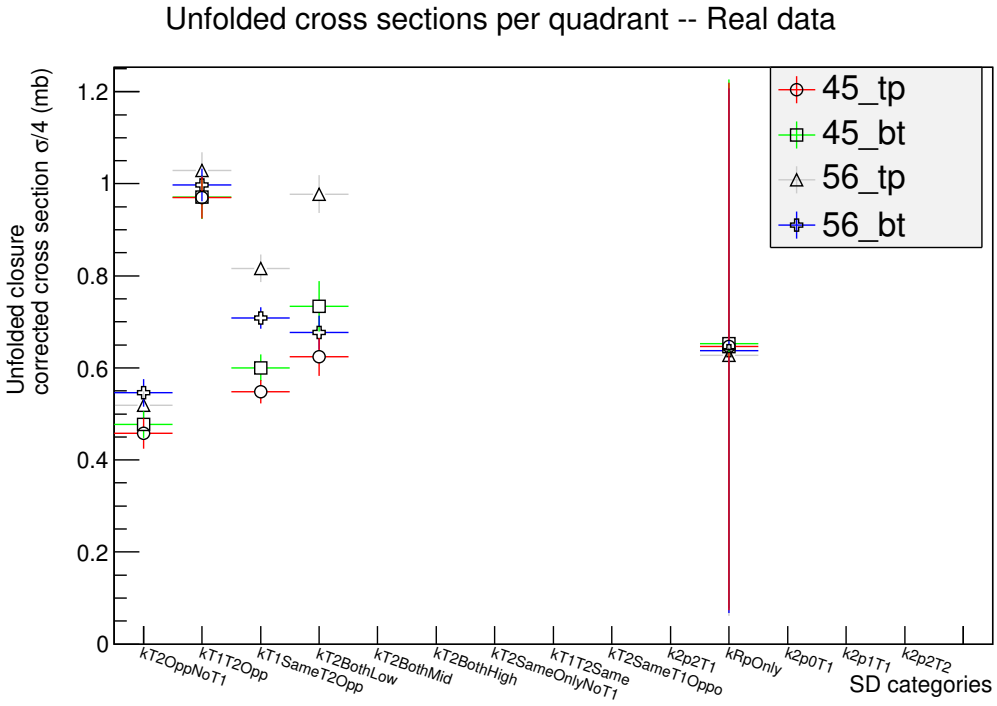

Figure 7.3: The final unfolded cross section for real data segment per RP and SD class. Unfolding was done with a Pythia 8 SD sample of 210 000 events with real PU mixed in, and the real data sample was 1 439 000 events. The closure correction is applied. All systematics added in quadrature, including T2 trigger efficiency correction. Method and MC systematic uncertainties not included.

7.2.1 Inferring ξ from the SD class

We need to use the rapidity gap (or the SD class) to infer the very small ξ-values of the 1T2 SD classes, since the ξ resolution of our reconstruction is about 0.8% at low ξ, and still above 0.25% at very high ξ where the absolute systematic uncertainty gets higher (quoted as a relative 10% uncertainty, so a systematic contribution of 2% at $\xi = -20\%$). Therefore the differential cross section versus $\log_{10}\xi$ shown in Figures 7.5 – 7.6 uses the final unfolded integral measurement for each 1T2 class and is just normalised by the bin width, to obtain a differential cross section. The SD class bin width is extracted from MC samples – separately for EPOS and Pythia 8 – as described in Appendix G.3.1. These plots were also corrected with the closure ratio[7] – for versions without this correction, see Appendix G.3. The first bin shows the undetected

[7] Also added in quadrature as an uncertainty term.

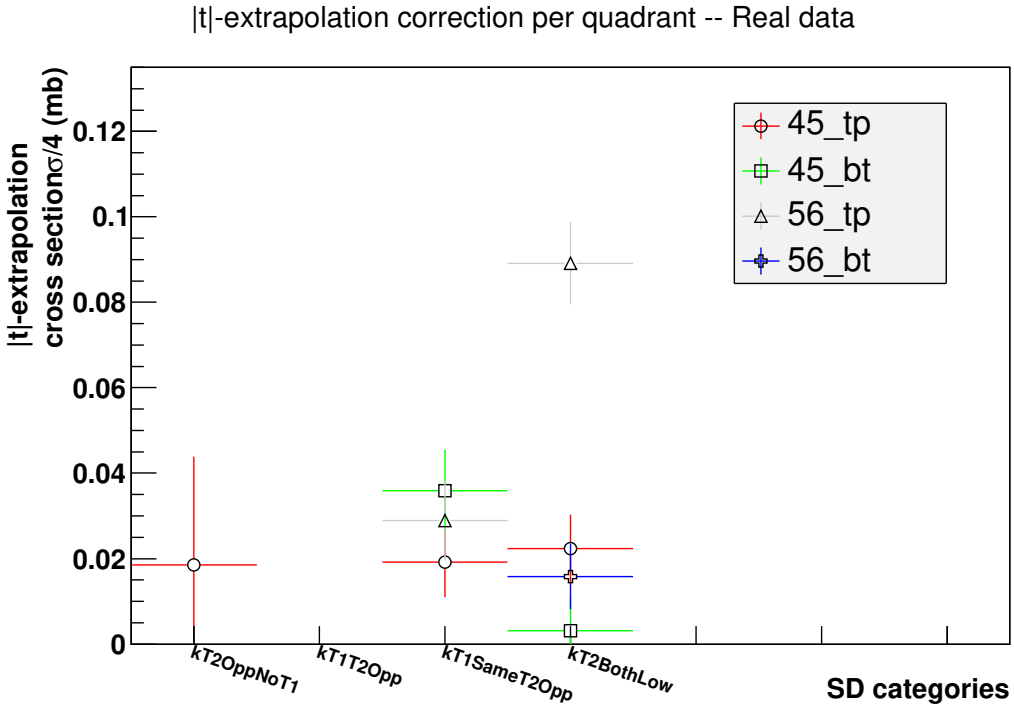

Figure 7.4: The $|t|$-extrapolation correction (not used, see text) for 1 439 000 real data segment 1b events, per RP and SD class, not closure corrected. The $|t|$-spectra are unfolded with a Pythia 8 SD sample of 210 000 events. Exponential fit between $t(peak + 1)$ and $|t|$ = 0.3 GeV^2, taking the difference between extrapolation from $t(peak + 1)$ down to the minimum kinematically allowed t and the data points in the same range, as explained in Section 5.1.2. Missing points have negative calculated correction.

very low mass 0T2 class[8], whose measurement of 2.62 ± 2.17 mb is taken from a TOTEM measurement [67] of the invisible part of the inelastic cross section deduced from the difference between the inferred total inelastic cross section, from a measurement of the total and the elastic cross section, and the measured visible inelastic cross section. As mentioned already in Section 7.1 and seen from Figures 7.5 and 7.6, the EPOS generator describes the cross section ratios of the three central $\log_{10}\xi$ bins much better than Pythia, although EPOS does significantly overestimate the cross section of the first $\log_{10}\xi$ bin.

The final cross section, compared with different MC predictions, is shown in Fig-

[8]Constant value assigned to 0T2 in the background-subtracted histogram. The small differences are introduced by the unfolding.

Table 7.2: Final unfolded cross sections per SD class after all corrections measured from 1 439 000 events in Segment 1b of the real data. The cross sections are unfolded with a Pythia 8 SD sample, having 210 000 events, with real PU mixed in. The table gives the unfolded cross section before closure ratio correction ("Unfold"), and after closure correction ("Closure corr."), and the difference between the closure corrected cross section unfolded with EPOS and with Pythia 8 ("MC Bias"), and between unfolding methods SVD(k=7) and Bayes (i=2) ("SVD bias"). The "Weighted rescaled sum" is the corresponding total cross section per SD class. The "RP diff. sys" is the systematic uncertainty estimated from the difference between the cross sections extracted using different RPs.

SD class	Unfolded (mb)	MC Bias (mb)	Closure corr. (mb)	MC Bias (mb)	SVD bias (mb)	RP diff. sys (mb)
45_tp						
1T2-0T1	0.42 ± 0.02	-0.01	$0.46 \pm 0.03 \pm 0.02$(sys)	-0.02	-0.03	
1T2-1T1	0.91 ± 0.03	+0.12	$0.97 \pm 0.03 \pm 0.03$(sys)	+0.25	-0.08	
1T2-2T1	0.52 ± 0.02	-0.13	$0.55 \pm 0.02 \pm 0.02$(sys)	-0.09	-0.15	
2T2	0.57 ± 0.02	+0.03	$0.62 \pm 0.03 \pm 0.03$(sys)	+0.06	+0.05	
45_bt						
1T2-0T1	0.44 ± 0.02	-0.01	$0.48 \pm 0.02 \pm 0.02$(sys)	-0.02	+0.01	
1T2-1T1	0.91 ± 0.03	+0.12	$0.97 \pm 0.03 \pm 0.03$(sys)	+0.20	-0.08	
1T2-2T1	0.56 ± 0.02	-0.15	$0.60 \pm 0.02 \pm 0.02$(sys)	-0.10	-0.17	
2T2	0.65 ± 0.02	+0.03	$0.73 \pm 0.03 \pm 0.04$(sys)	+0.08	+0.05	
Weighted	rescaled sum					
1T2-0T1	1.74 ± 0.05	-0.02	$1.87 \pm 0.07 \pm 0.07$(sys)	-0.09	-0.05	± 0.03
1T2-1T1	3.64 ± 0.08	+0.48	$3.88 \pm 0.10 \pm 0.12$(sys)	+0.89	-0.32	± 0.01
1T2-2T1	2.18 ± 0.05	-0.57	$2.30 \pm 0.06 \pm 0.08$(sys)	-0.38	-0.63	± 0.05
2T2	2.44 ± 0.06	+0.13	$2.69 \pm 0.09 \pm 0.14$(sys)	+0.29	+0.22	± 0.04

ure 7.7, taking a weighted average over the RPs in arm 4-5 and scaling by 4, with the total systematic uncertainty added in quadrature to the statistical uncertainty. Since the uncertainty on the 0T2 measurement includes systematics, we do not make a weighted average for the 0T2 class, but instead assign the value from [67], divided

Table 7.3: Final class migration-corrected cross sections per SD class after all corrections measured from 1 439 000 events in Segment 1b of the real data. The class migration is done with a Pythia 8 SD sample, having 210 000 events, with real PU mixed in. The table gives the class migration-corrected cross section before closure ratio correction ("Class migrated"), after closure correction ("Class closure corr."), and the difference between the closure-corrected cross section with class migration from EPOS and from Pythia 8 ("MC Bias"). The "Weighted rescaled sum" is the corresponding total cross section per SD class. The "RP diff. sys" is the systematic uncertainty estimated from the difference between the cross sections extracted using different RPs.

SD class	Class migrated (mb)	MC Bias (mb)	Class closure corr. (mb)	MC Bias (mb)	RP diff. sys (mb)
45_tp					
1T2-0T1	0.49 ± 0.02	-0.10	$0.60 \pm 0.04 \pm 0.06$(sys)	-0.07	
1T2-1T1	0.83 ± 0.02	+0.09	$0.98 \pm 0.03 \pm 0.07$(sys)	+0.28	
1T2-2T1	0.39 ± 0.03	+0.06	$0.43 \pm 0.03 \pm 0.02$(sys)	+0.08	
2T2	0.63 ± 0.03	-0.02	$0.71 \pm 0.05 \pm 0.04$(sys)	-0.07	
45_bt					
1T2-0T1	0.52 ± 0.02	-0.10	$0.62 \pm 0.04 \pm 0.05$(sys)	-0.07	
1T2-1T1	0.82 ± 0.02	+0.09	$0.97 \pm 0.03 \pm 0.07$(sys)	+0.21	
1T2-2T1	0.41 ± 0.03	+0.07	$0.47 \pm 0.03 \pm 0.03$(sys)	+0.10	
2T2	0.73 ± 0.03	-0.02	$0.82 \pm 0.06 \pm 0.05$(sys)	-0.05	
Weighted	Rescaled sum				
1T2-0T1	2.02 ± 0.06	-0.39	$2.45 \pm 0.11 \pm 0.21$(sys)	-0.27	± 0.05
1T2-1T1	3.29 ± 0.06	+0.37	$3.89 \pm 0.09 \pm 0.30$(sys)	+0.96	± 0.00
1T2-2T1	1.62 ± 0.07	+0.25	$1.79 \pm 0.09 \pm 0.09$(sys)	+0.34	± 0.07
2T2	2.72 ± 0.08	-0.09	$3.05 \pm 0.15 \pm 0.17$(sys)	-0.24	± 0.04

by the appropriate bin width. In addition to the comparison with the EPOS and Pythia 8 cross-section predictions, Figure 7.7 also shows the comparison with QGSJET-II.04. QGSJet-II shows somewhat similar behaviour to EPOS with an increased differential cross section at small and large $\log_{10} \xi$ compared to medium $\log_{10} \xi$ values. QGSJet-II

Table 7.4: Final unfolded and class migration-corrected cross sections per SD class after all corrections, measured from 1 439 000 events in Segment 1b of the real data for RP 56_bt, which is used for estimating systematic uncertainties only. The unfolding and class migration is done with a Pythia 8 SD sample, having 210 000 events. The table gives the cross sections before closure ratio correction ("Cross section"), after closure correction ("Closure corr."), and the difference between the cross sections extracted using EPOS and Pythia 8 ("MC Bias") and between unfolding methods SVD(k=7) and Bayes (i=2) ("SVD bias").

SD class	Cross section (mb)	MC Bias (mb)	Closure corr. (mb)	MC Bias (mb)	SVD Bias (mb)
Unfolded 56_bt					
1T2-0T1	0.53 ± 0.02	+0.00	$0.55 \pm 0.03 \pm 0.01$(sys)	+0.01	+0.08
1T2-1T1	1.03 ± 0.03	+0.14	$1.00 \pm 0.03 \pm 0.02$(sys)	+0.26	-0.13
1T2-2T1	0.72 ± 0.02	-0.17	$0.71 \pm 0.02 \pm 0.02$(sys)	-0.11	-0.06
2T2	0.72 ± 0.02	+0.05	$0.68 \pm 0.03 \pm 0.04$(sys)	+0.20	+0.01
Class migration 56_bt					
1T2-0T1	0.62 ± 0.02	-0.11	$0.74 \pm 0.04 \pm 0.06$(sys)	-0.01	
1T2-1T1	0.90 ± 0.02	+0.10	$0.96 \pm 0.03 \pm 0.03$(sys)	+0.26	
1T2-2T1	0.58 ± 0.03	+0.08	$0.63 \pm 0.04 \pm 0.03$(sys)	+0.06	
2T2	0.79 ± 0.03	-0.03	$0.73 \pm 0.04 \pm 0.03$(sys)	+0.07	

shows better agreement with the measurement for the lowest $\log_{10}\xi$ bin than EPOS but worse agreement than EPOS for the two highest $\log_{10}\xi$ bins. Pythia 8, on the other hand, provides a good description of the measurement in the $\log_{10}\xi$ range between -6 and -1.6 but significantly underestimates the cross section of the second lowest and highest $\log_{10}\xi$ bin. The final cross section values are also given in Table 7.11 and corresponding MC predictions for the differential cross section are given in Table 7.12.

Table 7.5: Rescaled sum over all RPs of the final unfolded and class migration-corrected cross sections per SD class after all corrections (including closure corrections), measured from 1 439 000 events in Segment 1b of the real data, taken from Tables 7.2 – 7.3 and I.4. The unfolding and class migration is done with a Pythia 8 SD sample of 210 000 events and an EPOS sample with 1 000 000 events. The uncertainties include the statistical uncertainty and the systematic uncertainties due to the closure correction and differences between RPs ("RP diff.+closure", quoted as "s." below), due to differences in the cross sections extracted using EPOS and Pythia 8 ("MC Bias"), and SVD and Bayes unfolding ("SVD Bias"), and due to the luminosity ("lumi") and the T2 trigger efficiency correction ("T2")

SD class	Class migrated (mb)	MC Bias (mb)	Unfolded (mb)	MC Bias (mb)	SVD Bias (mb)	Lumi. (%)	T2 (%)
Pythia 8:							
1T2-0T1	$2.45 \pm 0.11 \pm 0.26$(s.)	-0.27	$1.87 \pm 0.07 \pm 0.10$(s.)	-0.09	-0.05	± 4	± 1.53
1T2-1T1	$3.89 \pm 0.09 \pm 0.30$(s.)	+0.96	$3.88 \pm 0.10 \pm 0.13$(s.)	+0.89	-0.32	± 4	± 0.74
1T2-2T1	$1.79 \pm 0.09 \pm 0.16$(s.)	+0.34	$2.30 \pm 0.06 \pm 0.13$(s.)	-0.38	-0.63	± 4	± 0.51
2T2	$3.05 \pm 0.15 \pm 0.21$(s.)	-0.24	$2.69 \pm 0.09 \pm 0.18$(s.)	+0.29	+0.22	± 4	± 0.10
all, $2 * 10^{-7} < \xi <$ 20%	11.18 ± 0.22 $\pm$0.93(s.)$\pm$0.08(T2)	+0.78	10.74 ± 0.16 $\pm$0.54(s.)$\pm$0.07(T2)	+0.71	-0.79	± 4	
EPOS:							
1T2-0T1	$2.17 \pm 0.13 \pm 0.34$(s.)		$1.79 \pm 0.08 \pm 0.08$(s.)		+0.29	± 4	± 1.53
1T2-1T1	$4.85 \pm 0.16 \pm 0.62$(s.)		$4.77 \pm 0.15 \pm 0.37$(s.)		+0.38	± 4	± 0.74
1T2-2T1	$2.13 \pm 0.14 \pm 0.19$(s.)		$1.91 \pm 0.07 \pm 0.21$(s.)		+0.38	± 4	± 0.51
2T2	$2.80 \pm 0.11 \pm 0.15$(s.)		$2.98 \pm 0.10 \pm 0.38$(s.)		-0.02	± 4	± 0.10
all, $2 * 10^{-7} < \xi < 20\%$	11.96 ± 0.27 $\pm$1.30(s.)$\pm$0.08(T2)		11.46 ± 0.21 $\pm$1.03(s.)$\pm$0.08(T2)		+1.03	± 4	0.08

7.3 Differential t-distributions

In Figures 7.10 to 7.13, the Pythia 8-unfolded $|t|$-spectra for the various signal categories are shown, with all signal requirements and background removal selections

Table 7.6: Rescaled sum over all RPs of the final unfolded and class migration-corrected cross sections per SD class after all corrections, measured from 1 439 000 events in Segment 1b of the real data. The individual cross sections are the average of the values obtained using Pythia 8 and EPOS for unfolding or class migration from Table 7.5. The uncertainties include the statistical uncertainty and the systematic uncertainties due to the closure correction and differences between RPs ("RP.+closure"), due to differences in the cross sections extracted using EPOS and Pythia 8 ("MC", see Table 7.9), due to the method used for unfolding or class migration ("Method", see Table 7.7), the unfolding method ("SVD"), see Table 7.8 the luminosity ("lumi") and the T2 trigger efficiency correction ("T2"). The total uncertainty ("Tot."), estimated as the statistical and systematic uncertainties added in quadrature, is also given.

SD class	Cross section (mb)	RP+ Closure sys. (mb)	MC sys. (mb)	SVD sys. (mb)	Lumi. sys. (mb)	T2 sys. (mb)	Method sys. (mb)	Tot. (mb)
Unfolded:								
1T2-0T1	1.83±0.05	±0.09	±0.05	±0.15	±0.07	±0.03	±0.29	±0.35
1T2-1T1	4.33±0.09	±0.25	±0.48	±0.19	±0.17	±0.03	±0.04	±0.61
1T2-2T1	2.10±0.05	±0.17	±0.19	±0.32	±0.08	±0.01	±0.25	±0.49
2T2	2.84±0.07	±0.28	±0.15	±0.11	±0.11	±0.00	±0.18	±0.40
all, $2 * 10^{-7} < \xi < 20$ %	11.10±0.13	±0.79	±0.87	±0.77	±0.44	±0.07	±0.75	±1.66
Class migrated:								
1T2-0T1	2.31±0.08	±0.30	±0.15		±0.09	±0.04	±0.29	±0.46
1T2-1T1	4.37±0.09	±0.46	±0.51		±0.17	±0.03	±0.04	±0.72
1T2-2T1	1.96±0.08	±0.17	±0.18		±0.08	±0.01	±0.25	±0.37
2T2	2.92±0.09	±0.18	±0.12		±0.12	±0.00	±0.18	±0.32
all, $2 * 10^{-7} < \xi < 20\%$	11.57±0.17	±1.11	±0.96		±0.46	±0.08	±0.75	±1.73

Table 7.7: The method systematic uncertainty estimated from 1 439 000 events in Segment 1b of the real data as half the difference between unfolded and class migrated corrected cross sections for individual SD classes, separately for Pythia 8, EPOS and the final unfolding average. To avoid a statistical fluctuation giving an accidentally too small systematic uncertainty estimate, the systematic uncertainty quoted for all three is the largest of the three for each SD class.

SD class	Pythia (mb)	EPOS (mb)	Unfolding average (mb)	Method sys. (mb)
1T2-0T1	0.29	0.19	0.24	0.29
1T2-1T1	0.00	0.04	0.02	0.04
1T2-2T1	0.25	0.11	0.07	0.25
2T2	0.18	0.09	0.04	0.18
all, $2 * 10^{-7} < \xi < 20\%$	0.72	0.43	0.38	0.75

Table 7.8: The unfolding method systematic uncertainty estimated from 1 439 000 events in Segment 1b of the real data as half the difference between SVD-unfolded (k=7) and Bayes-unfolded (2 iterations) corrected cross sections for individual SD classes, separately for Pythia 8, EPOS and the final unfolding average. To avoid a statistical fluctuation giving an accidentally too small systematic uncertainty estimate, the systematic uncertainty quoted for all three is the largest of the three for each SD class.

SD class	Pythia (mb)	EPOS (mb)	Unfolding average (mb)	SVD sys. (mb)
1T2-0T1	0.03	0.15	0.06	0.15
1T2-1T1	0.16	0.19	0.02	0.19
1T2-2T1	0.32	0.19	0.06	0.32
2T2	0.11	0.01	0.05	0.11
all, $2 * 10^{-7} < \xi < 20\%$	0.39	0.52	0.06	0.77

Table 7.9: The systematic uncertainty due to the MC dependence estimated as half the difference between the cross sections extracted using EPOS and Pythia 8, separately for the first 900 000 ("900k") and the last 1 439 000 events ("1439k") in Segment 1b of the real data. To avoid statistical fluctuations causing one of the estimates to be too small, the systematic uncertainty quoted for both samples is the larger one of the two estimates for each SD class.

SD class	1439k (mb)	900k (mb)	MC sys. (mb)
Unfolded			
1T2-0T1	0.04	0.05	0.05
1T2-1T1	0.45	0.48	0.48
1T2-2T1	0.19	0.19	0.19
2T2	0.15	0.15	0.15
all, $2 * 10^{-7} < \xi < 20\%$	0.36	0.40	0.87
Class migration			
1T2-0T1	0.14	0.15	0.15
1T2-1T1	0.48	0.51	0.51
1T2-2T1	0.17	0.18	0.18
2T2	0.12	0.11	0.12
all, $2 * 10^{-7} < \xi < 20\%$	0.39	0.43	0.96

applied, for the last 1 439 000 events in Segment 1b, as above for ξ-spectra. These plots were automatically fitted with an exponential between the right edge of the highest t-bin up to $|t| = 0.3$ or 0.4 GeV^2, as explained in Chapter 5.1.2. These figures show a representative fit of the $|t|$-distribution for one RP for each SD category from low mass to very high mass, or 1T2-0T1 to 2T2. The other RPs are shown in Figures F.1 – F.12 unfolded with Pythia 8, and Figures F.13 – F.28 for EPOS unfolding, in the Appendix F.

To see if there is any sensitivity in the data for extracting another, steeper exponential at low $|t|$ as predicted by EPOS, we used the $|t|$-spectra unfolded with EPOS and summed over all RPs, and fitted it with the sum of two exponentials. Constrain-

Table 7.10: SD cross sections reported in [114] for EPOS, and for Pythia 8, for comparison with our results in Table 7.5. Individual SD class cross sections estimated according to the fraction of generated events in each SD class. The cross sections for EPOS are scaled with the reported total cross section due to the MC sample being all-inclusive, not SD only. The Pythia 8 sample is SD only, and scaled with the reported SD cross section. Reported SD cross section may not cover SD class 2T2 due to the customary upper ξ limit at 5% or 10%. QGSJet cross sections are estimated from [115] and tables of Appendix N.1 (private communication from QGSJet author) for all events having one ξ > -20% proton ("SD-like") and events with in addition particles in T2 $|\eta|$ acceptance regions according to the SD class definition used in this analysis ("trig.").

SD class	Pythia	EPOS	QGSJet II-04		
			SD-like	All trig.	SD trig.
	(mb)	(mb)	(mb)	(mb)	(mb)
0T2	1.90	5.70	3.66	0.22	0.22
1T2-0T1	1.13	1.58	2.32	1.30	1.30
1T2-1T1	5.22	3.79	3.81	2.80	2.73
1T2-2T1	2.08	1.93	1.26	0.74	0.37
2T2	1.30	4.25	6.29	4.26	0.29
Non-SD topology or $\xi < -20\%$	0.74	80.77	-	-	-
Total	-	98			
Total SD	12.38	12	10.97	9.32	4.91

ing the higher exponential $|t|$-slope to <-40 or <-20, the best fit was found with the higher slope at the selected edge, so no sensitivity to this second parameter was found. For comparison, we also checked the unfolding with Pythia 8; in the case of SD class 1T2-1T1, where the single-exponential fit has a low P-value (see Figure 7.11), adding another exponential improved the fit in Figure 7.8, but the higher exponential slope found is much lower than the EPOS slopes in Table 6.7. This implies the fit is constrained by the bend near $|t|$=0.1 GeV^2, unlike the EPOS high-slope component that was visible only for $|t| < 0.05$ GeV^2. In addition, this particular SD class covers a

Table 7.11: Differential cross section as a function of $\log_{10}\xi$ measured from 1 439 000 events in Segment 1b of the real data. Values for 0T2 from [67], see Section 7.2.1. The cross sections are unfolded with an EPOS or a Pythia 8 SD sample, having respectively 1 000 000 and 210 000 events. TOTEM (final) is the average of Pythia 8 and EPOS unfolding. $\text{Log}_{10}\xi$ ranges extracted from the MC samples, see Table G.4. The uncertainties include the statistical uncertainty and the systematic uncertainties due to the closure correction and differences between RPs ("Sys.1"), due to the differences in the cross sections extracted with Pythia 8 and EPOS ("Sys.2, MC bias"), due to difference in the $\log_{10}\xi$ coverage for individual SD classes in Pythia and EPOS ("Sys.3, $\log_{10}\xi$ width"), due to the T2 trigger efficiency correction and luminosity ("Sys.4, T2 + lumi."), and due to the method used for unfolding or class migration ("Sys.5, Meth."). The total uncertainty ("Tot."), estimated as the quadrature sum of the statistical and systematic uncertainties is also given.

SD class	Midpoint $\text{Log}_{10}\xi$ (1)	Differential Cross section $d\sigma/d\text{Log}_{10}\xi$ (mb)	Sys. 1 σ (mb)	Sys.2 MC bias (mb)	Sys.3 $\log_{10}\xi$ width (%)	Sys.4 T2+ lumi. (%)	Sys.5 Meth. (mb)	Sys. 6 SVD (mb)	Tot. (mb)
0T2	-7.19	2.99	(2.48)		14	-			2.51
1T2-0T1	-6.25	1.83±0.05	0.09	0.05	9.1	4.28	0.29	0.15	0.39
1T2-1T1	-4.16	1.36±0.03	0.08	0.15	2.0	4.07	0.01	0.06	0.19
1T2-2T1	-2.11	2.24±0.05	0.18	0.20	3.7	4.03	0.27	0.34	0.53
2T2	-1.17	3.02±0.07	0.30	0.16	12.1	4.00	0.19	0.12	0.56

large interval in $\log_{10}\xi$ (> 3 units), which could well imply that it is in reality a sum of many $|t|$-distributions with decreasing B-slope that naturally shows a better convergence for a double exponential fit than for a single one. The improvements for other classes covering smaller intervals in $\log_{10}\xi$ were not as large as for the 1T2-1T1 class. Therefore we conclude the sensitivity of the data to a second steeper exponential in $|t|$ like the one in EPOS cannot be demonstrated and hence such a second exponential can neither be verified nor contradicted.

A weighted average of the slope parameter B for single exponential fits in the same $|t|$-range for each SD-class can be found in Table 7.15, together with slopes extracted from MC generators. Just like for the cross section measurement, we select the final exponential B-slope result to be the average of the B-slopes for the Pythia and EPOS

Table 7.12: Predicted MC differential cross sections as a function of $\log_{10}\xi$. Cross sections from Table 7.10. $\mathrm{Log}_{10}\xi$ ranges extracted from the EPOS and Pythia 8 MC samples, see Table G.4, while QGSJet ranges are calculated from diffractive mass ranges given. The bin width systematic uncertainty ("Sys.") is given, expressed as a fraction of the bin width.

SD class	Midpoint $\mathrm{Log}_{10}\xi$ (1)	Differential Cross section $\mathrm{d}\sigma/\mathrm{dLog}_{10}\xi$ (mb)	Sys. $\log_{10}\xi$ width (%)
Pythia 8			
0T2	-7.14	1.95	1.1
1T2-0T1	-6.18	1.19	1.9
1T2-1T1	-4.09	1.62	0.7
1T2-2T1	-2.00	2.19	2.7
2T2	-1.11	1.58	2.2
EPOS			
0T2	-7.24	7.35	18.2
1T2-0T1	-6.33	1.51	14.5
1T2-1T1	-4.24	1.21	2.5
1T2-2T1	-2.21	2.09	6.3
2T2	-1.22	4.04	1.7
QGSJet	(SD-like)		
0T2	-7.17	3.99	
1T2-0T1	-6.31	2.94	
1T2-1T1	-4.22	1.13	
1T2-2T1	-2.05	1.31	
2T2	-1.13	7.23	
QGSJet	(T2 trig.)		
1T2-0T1	-6.52	1.25	
1T2-1T1	-4.22	0.83	
1T2-2T1	-2.05	0.77	
2T2	-1.13	4.90	

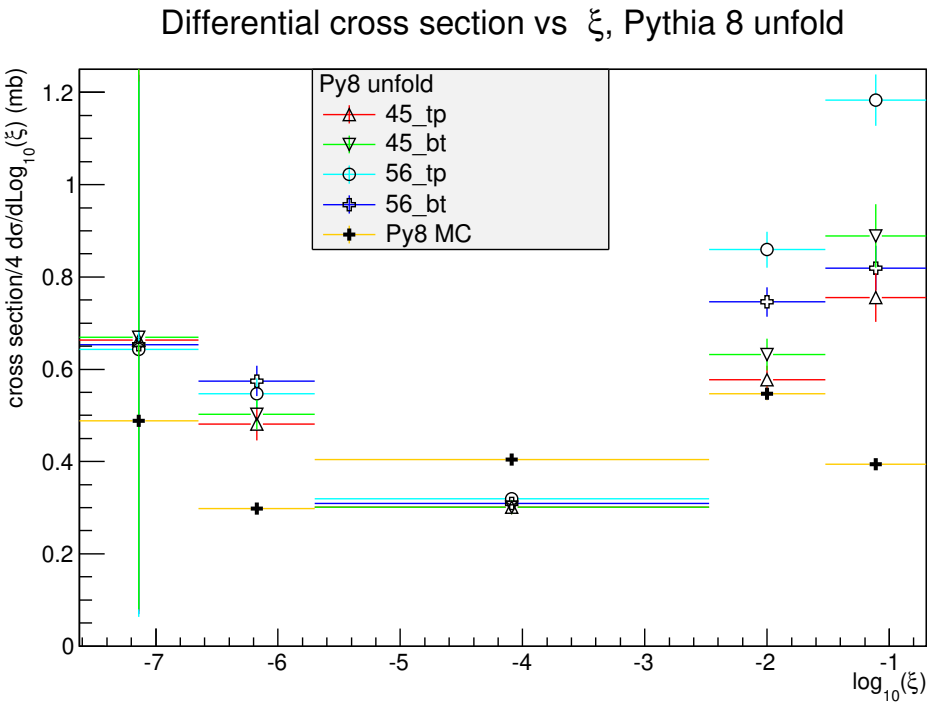

Figure 7.5: Differential spectrum in ξ vs $\log_{10}(\xi)$ for each individual RP, when unfolded with a 210 000 SD event Pythia 8 sample, together with the Pythia 8 prediction, using the MC cross sections given in Table 7.10. The data sample is the last 1 439 000 events of real data in Segment 1b. The differential cross section includes all corrections, and its uncertainty has been estimated by adding all systematics in quadrature. Method and MC systematic uncertainties not included. The first bin is not measured but obtained by initiating with the value given in Ref. [67].

unfolded real data $|t|$-spectra, with an "MC" systematic equal to half the difference between slopes, shown in Table 7.13. These averages can be found in Table 7.16 and are shown as a function of $\log_{10}\xi$ in Figure 7.9, where they are compared with the slope parameters extracted from MC generators, and the slope measurement by ATLAS [29] at 8 TeV, see Section 7.4.1 below. For the data, the weighted average over the RPs in arm 4-5 is reported, with arm 5-6 being excluded due to high background, especially in RP 56_tp. The weights are based on the fit uncertainty, $w_i = 1/\delta^2_{\sigma,i}$. For comparison, in Table 7.15 we also report the B value when averaging over arm 4-5 and 56_bt. The procedure to determine the systematic uncertainty is described in Section 6.6.1. Compatible with expectations, the slope decreases with increasing $\log_{10}\xi$, and the slope for the lowest $\log_{10}\xi$ bin is approximately half the measured

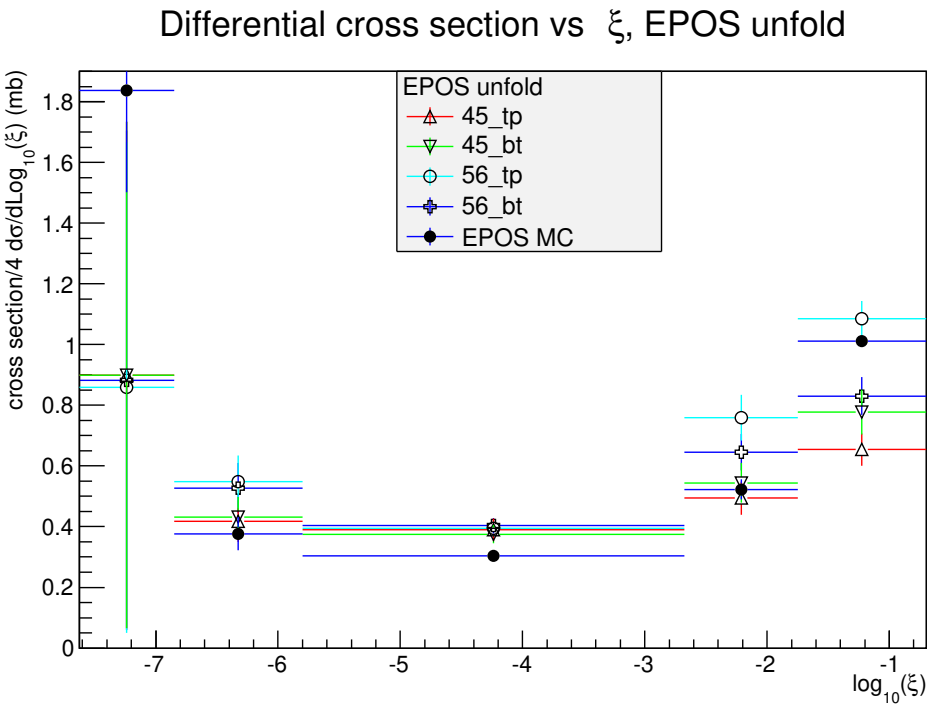

Figure 7.6: Differential spectrum in ξ vs $\log_{10}(\xi)$ for each individual RP, when unfolded with an EPOS sample containing 1 000 000 events, together with the Pythia 8 prediction, using the MC cross sections given in Table 7.10. The data sample is the last 1 439 000 events of real data in Segment 1b. The differential cross section includes all corrections, and its uncertainty has been estimated by adding all systematics in quadrature. Method and MC systematic uncertainties not included. The first bin is not measured but obtained by initiating with the value given in Ref. [67].

elastic t-slope[9], differing by 1.6σ only (adding all uncertainties from our and the elastic measurement in quadrature). Regarding the MCs, QGSJet-II seems to be the closest to the measured B values followed by EPOS, whereas Pythia 8 seems to overestimate the slope parameter over the whole measured range.

7.4 Conclusions and outlook

We presented measurements of the proton-proton SD cross section as a function of the mass of the diffractive system, proton momentum loss ξ and momentum transfer t at $\sqrt{s} = 7$ TeV, based on a direct measurement of both the surviving proton and the

[9]Measured by TOTEM [56], $B_{el} = 19.87 \pm 0.33$(syst.) over the range $0.02 < |t| < 0.2$ GeV^2

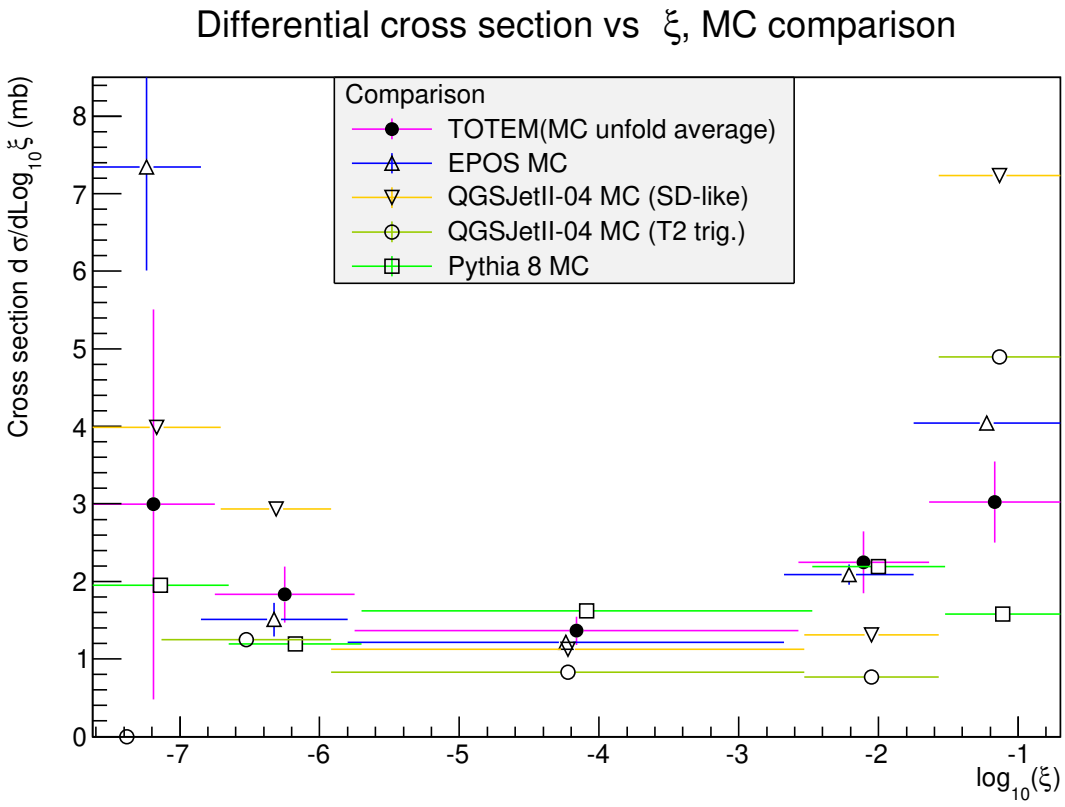

Figure 7.7: Differential spectrum in ξ vs $\log_{10}(\xi)$ together with the EPOS, Pythia 8 and QGSJet predictions, using the MC cross sections given in Table 7.10. The data sample is the last 1 439 000 events of real data in Segment 1b. The differential cross section is the average of the values obtained when unfolding the data with an EPOS sample containing 1 000 000 SD events, and with a Pythia 8 SD sample of 210 000 events. The differential cross section includes all corrections, and its uncertainty has been estimated by adding all systematics in quadrature. The QGSJet predictions are shown both for all SD-like events ("SD-like"), and all SD-like events fulfilling the T2 requirements of the SD classes ("T2 trig.").

dissociated proton system, including a visible rapidity gap. This is a nonperturbative process taking place in $\approx 10\%$ of all proton-proton interactions, and our measurement provides an important constraint for the theorists calculating the evolution of the total, diffractive and elastic cross sections as a function centre-of-mass energy.

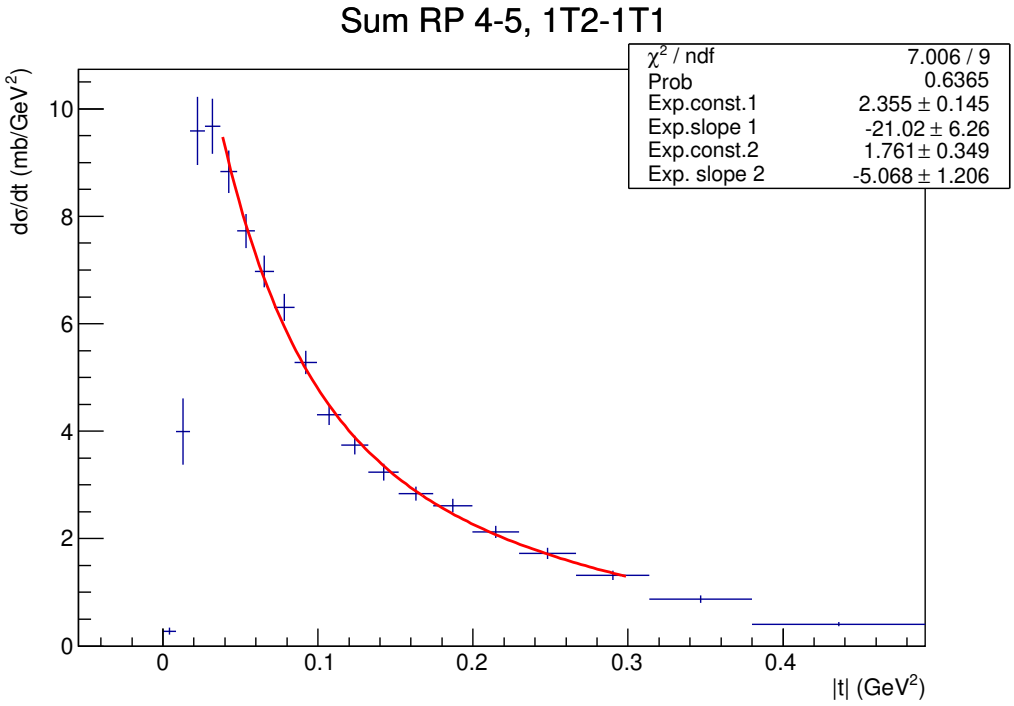

Figure 7.8: Differential cross section in $|t|$ for SD class 1T2-1T1, summed over both RPs in arm 4-5, for the last 1 439 000 events of real data in Segment 1b. After background subtraction and all corrections except for closure ratio, unfolded with a Pythia 8 sample containing 542 000 SD events. Double exponential fit, see Section 7.3.

7.4.1 Comparison with other experiments

Same topology as this thesis, at higher energies

ATLAS has recently published a measurement [29] (erratum [116], on the comparison with the CMS SD measurement [117]) where the ATLAS proton spectrometer ALFA was combined with a diffractive system and a rapidity gap measured in the central detector, on charged particles only, to find the SD cross section between $\xi = 0.01\%$ and 2.5% (i.e. $M_X = 80 \ldots 1270$ GeV/c^2). In their acceptance region, they found an SD cross section smaller by a factor two than the Pythia 8 prediction. The results given are differential cross sections as a function of $\log_{10} \xi$ and $|t|$ (integrated over ξ, in the $|t|$-range 0.016 – 0.43 GeV^2), the slope parameter B and Pomeron intercept, and integral cross sections. Although the ATLAS measurements were at $\sqrt{s}$ =8 TeV instead of 7 TeV, the centre-of-mass energy difference is only expected to give a minor change in the measured quantities – at most on the few-percent level. As can be seen from

Table 7.13: The systematic uncertainty due to the MC dependence estimated as half the difference between the $|t|$-slopes extracted using EPOS and Pythia 8, separately for the first 900 000 ("900k") and the last 1 439 000 events ("1439k") in Segment 1b of the real data. To avoid statistical fluctuations causing one of the estimates to be too small, the systematic uncertainty quoted for both samples is the larger one of the two estimates for each SD class.

SD class	1439k (GeV^{-2})	900k (GeV^{-2})	MC sys. (GeV^{-2})
Unfolded			
1T2-0T1	0.02	0.04	0.04
1T2-1T1	0.36	0.36	0.36
1T2-2T1	0.37	0.39	0.39
2T2	0.28	0.28	0.28

Table 7.14: The unfolding method systematic uncertainty estimated from 1 439 000 events in Segment 1b of the real data as half the difference between fitted exponential slopes on SVD-unfolded (k=7) and Bayes-unfolded (2 iterations) $|t|$-spectra for individual SD classes, separately for Pythia 8, EPOS and the final unfolding average. To avoid a statistical fluctuation giving an accidentally too small systematic uncertainty estimate, the systematic uncertainty quoted for all three is the largest of the three for each SD class.

SD class	Pythia (GeV^{-2})	EPOS (GeV^{-2})	Unfolding average (GeV^{-2})	SVD sys. (GeV^{-2})
1T2-0T1	0.11	0.04	0.07	0.11
1T2-1T1	0.09	0.01	0.05	0.09
1T2-2T1	0.03	0.03	0.00	0.03
2T2	0.09	0.01	0.05	0.09

Equation 2.30, the SD cross section and slope parameter B are expected to mainly depend on ξ, implying a centre-of-mass energy dependence $s^{\alpha(0)-1}$ for the cross section, while ATLAS found $-0.02 < \alpha(0) - 1 < 0.16$ (at 1σ).

Our measurement method has similarities to that of the ATLAS article, but our

Table 7.15: Single exponential slope parameter B measured in the same $|t|$-range from the last 1 439 000 events in Segment 1b, plus Pythia and EPOS generated samples for each SD class. For the data, the weighted average of the two RPs 45_tp and 45_bt is reported, with arm 5-6 being excluded due to higher background. The column "45tp/bt+56bt" averages the RPs 45_tp, 45_bt and 56_bt. The t-spectra are unfolded with an EPOS or a Pythia 8 SD sample, having respectively 1 000 000 and 210 000 events. Pythia and EPOS B-slopes as well as the systematic uncertainty ("Sys.") are taken from Table 6.10. "RP diff." is one third the range of slopes between RPs, see text. "MC" bias, EPOS minus Pythia, see Table 7.13. "SVD" bias, SVD unfolding slope minus Bayesian unfolding slope, see Table 7.14.

SD class	Slope (45tp/bt)+ B (GeV^{-2})	(45tp/bt+ 56bt)	Uncertainty (45tp/bt) δB (GeV^{-2})	(45tp/bt 56bt)	Sys. +RP diff.	MC Bias	SVD Bias
Real Data:	Pythia 8	SD					
1T2-0T1	-9.01	-9.20	0.22	0.16	$\pm$0.15$\pm$0.30	-0.03	+0.21
1T2-1T1	-7.37	-7.48	0.15	0.11	$\pm$0.08$\pm$0.18	-0.72	+0.19
1T2-2T1	-5.26	-5.57	0.26	0.18	$\pm$0.16$\pm$0.22	-0.74	+0.06
2T2	-4.89	-4.78	0.22	0.17	$\pm$0.19$\pm$0.22	-0.55	-0.17
	EPOS						
1T2-0T1	-9.04	-9.19	0.22	0.17	$\pm$0.78$\pm$0.23		+0.07
1T2-1T1	-8.09	-8.21	0.15	0.12	$\pm$1.05$\pm$0.17		+0.03
1T2-2T1	-5.99	-6.25	0.22	0.17	$\pm$0.48$\pm$0.24		-0.06
2T2	-5.44	-5.30	0.20	0.16	$\pm$0.23$\pm$0.17		-0.01
MC data:	Pythia 8	slope	EPOS	slope			
1T2-0T1	-11.72$\pm$0.09		-11.25 $\pm$0.32				
1T2-1T1	-9.11$\pm$0.04		-9.6 $\pm$0.2				
1T2-2T1	-6.69$\pm$0.06		-5.86 $\pm$0.25				
2T2	-5.90$\pm$0.09		-4.24 $\pm$0.19				

measurement extends the region covered both to lower and higher ξ values by an order of magnitude. Our measurement also shows the dependence of the slope parameter B as a function of M_X or ξ.

The slope parameter ATLAS reports, $B = -7.65 \pm 0.26$(stat.) ± 0.22(sys.)$= -7.65 \pm 0.34$, in a ξ-range that covers approximately half of our medium mass and

Table 7.16: Single exponential slope parameter B measured in the same $|t|$-range from the last 1 439 000 events in Segment 1b, averaged over the real data Pythia and EPOS unfoldings for each SD class. For the data, the weighted average of the two RPs 45_tp and 45_bt is reported, with arm 5-6 being excluded due to higher background. The column "45tp/bt+56bt" averages the RPs 45_tp, 45_bt and 56_bt. The t-spectra are unfolded with an EPOS or a Pythia 8 SD sample, having respectively ca. 1 000 000 and 210 000 events. The systematic uncertainty ("Sys.") is taken from Table 7.15. "MC" is half the difference between the averaged slopes for the EPOS and Pythia unfoldings of the real data, from Table 7.13. SVD unfolding systematic from Table 7.14. "Total" adds all systematics in quadrature.

SD class	Slope (45tp/bt) B (GeV^{-2})	(45tp/bt+ 56bt)	MC Sys. δB (GeV^{-2})	SVD Sys.	Sys.	RP diff.	Total Sys.
Real data	Unfolding	average					
1T2-0T1	-9.03±0.15	-9.19±0.12	0.04	0.11	0.47	0.26	0.55
1T2-1T1	-7.73±0.11	-7.84±0.08	0.36	0.09	0.57	0.18	0.70
1T2-2T1	-5.62±0.17	-5.91±0.12	0.39	0.03	0.32	0.23	0.55
2T2	-5.17±0.15	-5.04±0.12	0.28	0.09	0.21	0.20	0.41

not quite all of the high mass SD category (1T2-1T1 and 1T2-2T1), is bracketed by the slope values we found for these categories, see Figure 7.9. Taking a simple average weighted by the fraction of the SD category covered

$$\frac{f * B_{1T1} + B_{2T1}}{1 + f}, \tag{7.4}$$

where $f = \log_{10}(0.3/0.01)/\log_{10}(0.3/0.00012)$ is the ratio of $\log_{10}\xi$ covered by the ATLAS measurement of our SD class 1T2-1T1, we find an average slope parameter over the equivalent ξ-range of B = -5.90 $\pm$ 0.51 with Pythia unfolding, and B = -6.63 $\pm$ 0.83 with EPOS unfolding, when combining the statistical and systematic uncertainties. By further averaging the results with the two different unfoldings, we obtain a slope parameter B = -6.26 $\pm$ 0.61, assuming uncorrelated unfolding systematic uncertainties. This is within two standard deviations (2.0σ) of the ATLAS value, taking the uncertainties of the two measurements into account. The weighted slope parameters and their detailed uncertainties for the rapidity coverage-based weights are given in Table 7.17.

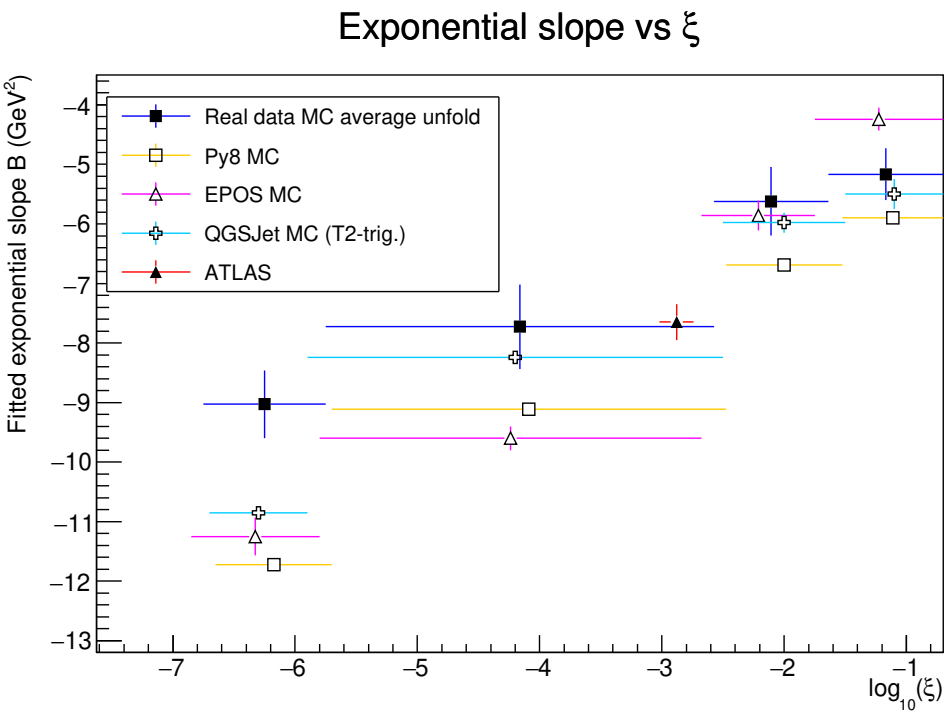

Figure 7.9: Measured single exponential slope parameter B as a function of $\log_{10}\xi$ from the last 1 439 000 events in Segment 1b, compared to the slope parameters of MC generators and the one measured by ATLAS at 8 TeV [29]. For the data, the weighted average of RPs 45_tp and 45_bt, and unweighted average over the two MC unfoldings, Pythia and EPOS, is shown. The systematic uncertainties are added in quadrature to the fit uncertainty, see Table 7.16. The t-spectra are unfolded with an EPOS or a Pythia 8 SD sample, having respectively 1 000 000 and 210 000 SD events. Pythia and EPOS values are taken from Table 6.10, while the ATLAS measurement [29] is put at its representative ξ value. QGSJet B-values shown only for all SD-like events satisfying the T2 trigger requirements ("trig.,all" or "trig.") of each SD class, see Table N.4.

SD class weights can also be determined from the fraction of MC events per class that are in the range of $\log_{10}\xi$ of the ATLAS measurement, see Appendix M. To do this using all the MC weights, we would also need a slope measurement for the 0T2 class, which has an MC weight of 4 – 11%. In the absence of such a measurement, we average over all the other 1T2 and 2T2 classes. This gives averaged slope parameters over the ATLAS $\log_{10}\xi$ range of B = -6.07 $\pm$ 0.49 with Pythia 8 unfolding, and B = -6.64 $\pm$ 0.80 with EPOS unfolding, combining the uncertainties in quadrature. The average of the result for the two unfoldings gives a slope parameter of B = -6.35 $\pm$

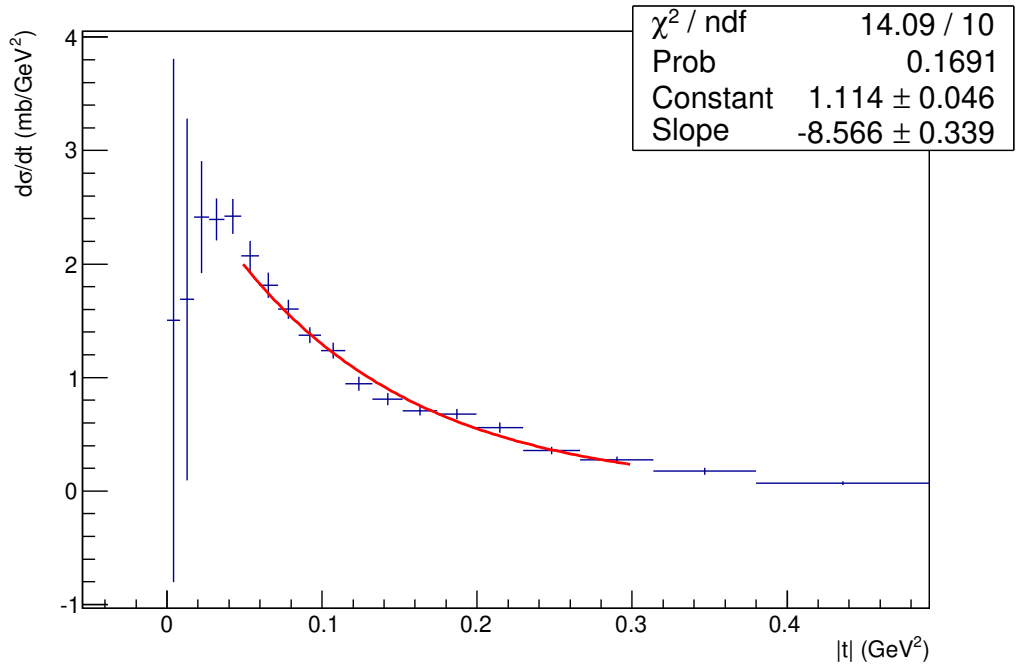

Figure 7.10: The fully corrected differential cross section as a function of $|t|$ for the SD class 1T2-0T1 in RP 45_tp using 1 439 000 events from real data segment 1b. Unfolded using a Pythia 8 SD sample of 210 000 events. For the exponential fit, see Section 7.3

0.47, assuming uncorrelated unfolding systematic uncertainties. This a little above 2σ (2.24σ) off the ATLAS value. The weighted slope parameters and their detailed uncertainties for the MC coverage-based weights are given in Table 7.17.

Comparing the results based on the different weighting schemes and unfoldings, we find slope parameters that differ from the ATLAS measurement by not more than 2.85σ, and in several cases nearer 1σ, after taking into account the uncertainties of both measurements. This difference of 2.85σ or less may be considered compatible, but the choice of MC for unfolding could not be resolved for our cross section measurement and also gives values differing by about 2σ for the weighted slope parameters.

To similarly compare our SD cross section measurement with the one of ATLAS, we sum the cross sections for SD classes 1T2-1T1 and 1T2-2T1 from Tables 7.5 (EPOS and Pythia 8 unfolded) and 7.6 (final), with rapidity coverage-based weights $f_1 = f \approx 0.435$ defined above, and $f_2 = \log_{10}(2.5/0.3)/\log_{10}(2.7/0.3) \approx 0.965$, assuming constant $\mathrm{d}\sigma/d\log_{10}\xi$ over both SD classes. Likewise, the individual cross sections

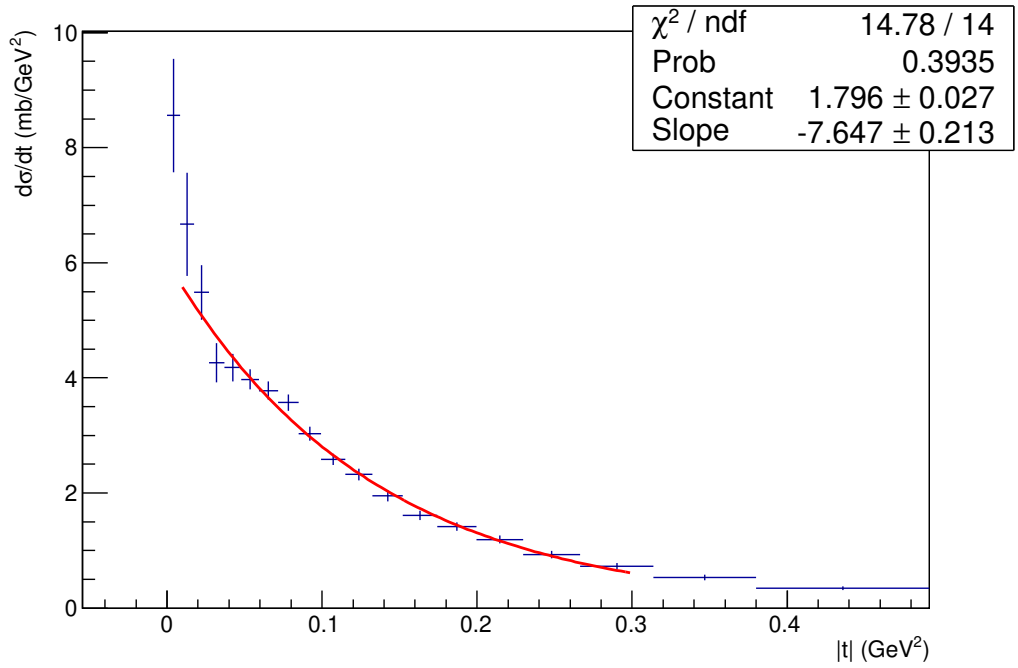

Figure 7.11: The fully corrected differential cross section as a function of $|t|$ for the SD class 1T2-1T1 in RP 45_tp using 1 439 000 events from real data segment 1b. Unfolded using a Pythia 8 SD sample of 210 000 events. For the exponential fit, see Section 7.3

from Table 7.5 unfolded with EPOS and Pythia 8 have been combined using MC-based weights from Appendix M. For these averages, the indirect TOTEM measurement of the 0T2 cross section [67] is used since it has not been measured in the present analysis. All resulting cross sections can be found in Table 7.19. Our cross sections are larger by a factor two or more, with the difference being 3.2 – 3.3σ for the Pythia 8 unfolded cross sections, and 2.4 – 2.9σ for EPOS, with the final cross section near 3.0σ; in all cases when taking the uncertainties of both measurements into account. This factor two can also be seen for the differential cross section versus $\log_{10}\xi$ from Figure 7.14

Also at $\sqrt{s} = 8$ TeV, a measurement of the integral SD and DD cross sections using multivariate analysis-based event classification [63] has been performed using combined CMS-TOTEM data. These measurements have never been published, but were accepted to be presented in a PhD thesis. The SD measurement by the CMS-TOTEM event classification method is compared with our measurements in Table 7.18 and found to be well within 1σ of our measurements.

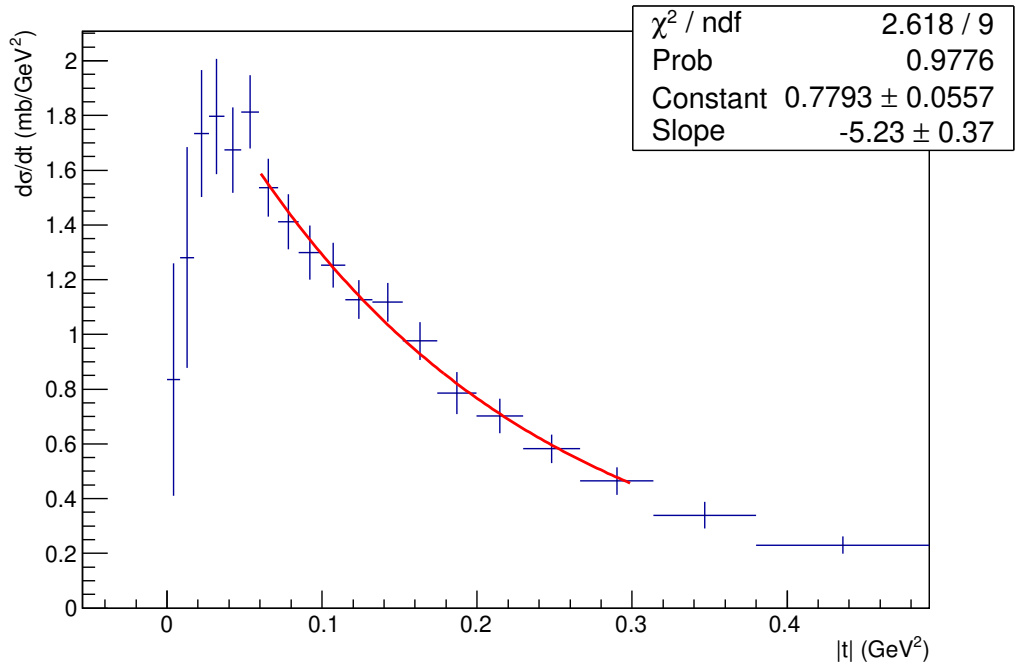

Figure 7.12: The fully corrected differential cross section as a function of $|t|$ for the SD class 1T2-2T1 in RP 45_tp using 1 439 000 events from real data segment 1b. Unfolded using a Pythia 8 SD sample of 210 000 events. For the exponential fit, see Section 7.3

At $\sqrt{s} = 7$ TeV

CMS [117] and ALICE [18] have measured SD at 7 TeV

The measurements are compared with our results in Tables 7.20 – 7.21, as in the previous Section 7.4.1, using both the rapidity coverage-based and the MC coverage-based weighting. We find our weighted cross sections are well within 1σ of the measurements by CMS, and about 1σ below the ALICE measurement. Our measurements of the differential cross section as a function of $\log_{10}\xi$ are compared with those of CMS and ATLAS in Figure 7.14.

At lower energies

The ALICE publication also presented SD values at 2.76 TeV and 900 GeV. SD measurements at Tevatron have been done at 1.8 TeV and 546 GeV [49, 118].

All measurements, from the Tevatron energies and above, of SD-related cross sections are presented in Table 7.22. For earlier results, see the appendix C Tables C.2

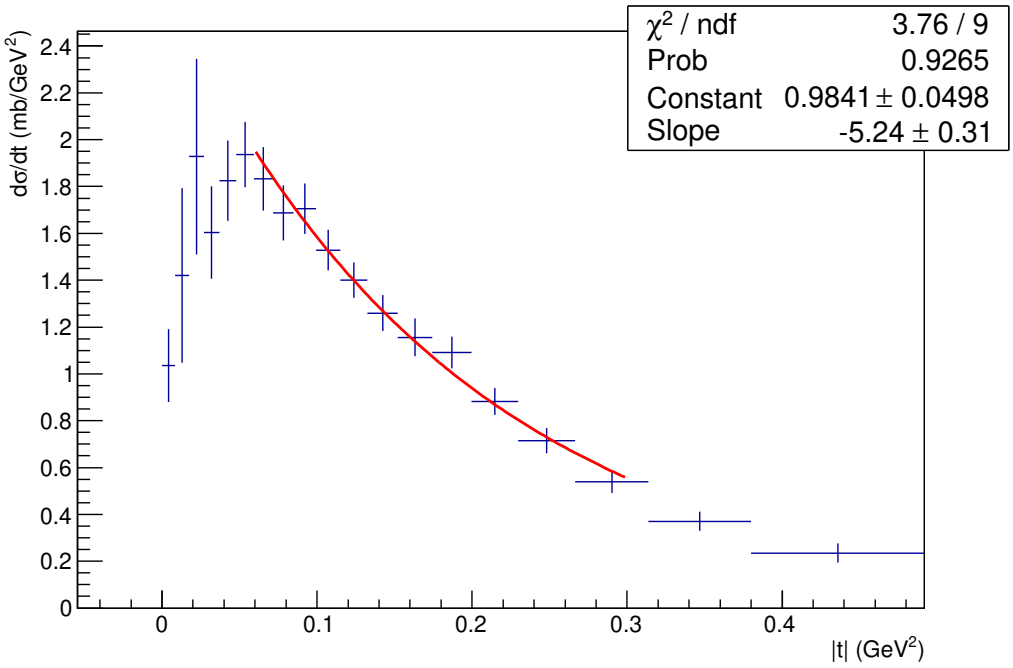

Figure 7.13: The fully corrected differential cross section as a function of $|t|$ for the SD class 2T2 in RP 45_tp including BH veto applied for this class only. Data sample used is 1 439 000 events from real data segment 1b. Unfolded using a Pythia 8 SD sample of 210 000 events. For the exponential fit, see Section 7.3

to C.4, with values recalculated to a common definition of diffraction from Goulianos(1998) in Table C.5.

Table 7.17: Comparison of the single exponential slope parameter with the one measured by ATLAS at 8 TeV [29]. To facilitate a direct comparison, the measured slope parameters given in Tables 7.15 – 7.16 for individual SD classes have been combined using a rapidity coverage-based ("rap-weight") or MC-coverage based ("MC-weight") weighting for Pythia 8 and EPOS-unfolded data. For the average of both unfoldings, only rapidity coverage weighting is shown. For MC-weight averages, the missing 0T2 slope parameter not measured in this work was neglected, so we average only over SD classes 1T2 and 2T2. Unfolding systematic uncertainties from Table 7.16, all combined in quadrature.

Name	Slope Rap.	Slope MC
ATLAS	-7.65±0.26±0.22(sys)	
(this work) Weighted sum, 1T2 only	Pythia 8 unfolding -5.91±0.22±0.45(sys)	-6.07±0.21±0.44(sys)
Weighted sum, 1T2 only	EPOS unfolding -6.64±0.20±0.79(sys)	-6.64±0.20±0.78(sys)
Weighted sum, 1T2 only	Averaged unfoldings -6.28±0.15±0.38(MC) ±0.05(SVD)±0.40(sys) ±0.21(RP diff.)	

Table 7.18: Comparison of the cross section measurements with the one measured by the CMS-TOTEM event-classification method at 8 TeV [63]. The indirect TOTEM measurement of the 0T2 cross section [67] is added to the sum of 1T2 and 2T2 SD class cross sections from Tables 7.5 – 7.6, since it is not measured in the present analysis. All uncertainties added in quadrature.

Data sample	Cross section (this work) (mb)	Cross section +0T2 [67] (mb)
CMS-TOTEM [63]	16±3.5	
Pythia 8 unfolding 1T2 + 2T2	10.74±1.56	13.36±2.67
EPOS unfolding 1T2 + 2T2	11.46±1.80	14.08±2.82
Averaged unfoldings 1T2 + 2T2	11.10±1.66	13.72±2.73

Table 7.19: Comparison of the cross section measurements with the one measured by ATLAS at 8 TeV [29]. To facilitate a direct comparison, the final cross sections given in Table 7.6 have been combined using a rapidity coverage-based weighting ("rap-weight"). In addition, the measured cross sections given in Table 7.5 for the individual SD classes have been combined using both a rapidity coverage-based and MC coverage-based ("MC-weight") weighting for both Pythia 8 and EPOS-unfolded data. For MC-weight averages, the indirect TOTEM measurement of the 0T2 cross section [67] is used, since it is not measured in the present analysis. All systematics added in quadrature.

SD class	This work		ATLAS
	Rap.	MC	
	(mb)	(mb)	(mb)
Final, averaged: Weighted Sum	3.91 ± 0.06 $\pm$0.65(sys)		1.88$\pm$ 0.15
+ $0.016 < \|t\| < 0.43$ GeV^2			1.59$\pm$0.03 $\pm$0.13 (sys.)
Pythia 8 unfolding Weighted Sum	3.90 ± 0.07 $\pm$0.62(sys)	3.94$\pm$0.11 $\pm$0.60(sys)	
EPOS unfolding Weighted Sum	3.92 ± 0.10 $\pm$0.69(sys)	3.39$\pm$0.25 $\pm$0.55(sys)	

Table 7.20: Comparison of the cross section measurements with the one measured by CMS [117] at 7 TeV. To facilitate a direct comparison, the final cross sections given in Table 7.6 have been combined using a rapidity coverage-based weighting ("rap-weight"). In addition, the measured cross sections given in Table 7.5 for the individual SD classes have been combined using both a rapidity coverage-based and MC coverage-based ("MC-weight") weighting for both Pythia 8 and EPOS-unfolded data. For MC-weight averages, the indirect TOTEM measurement of the 0T2 cross section [67] is used, since it is not measured in the present analysis. All systematics added in quadrature.

SD class	Phase space	Cross section Rap. (mb)	MC weight (mb)
CMS [117]	-5.5 < $\log_{10}\xi$ < -2.5	4.06 ± 0.04 $^{+0.69}_{-0.63}$ (sys.)	
(this work) Weighted sum	Pythia 8 unfolding	$\approx$ 3.43$\pm$0.09$\pm$0.49(sys)	3.59$\pm$0.13 $\pm$0.50(sys)
Weighted sum	EPOS unfolding	$\approx$ 4.21$\pm$0.14$\pm$0.59(sys)	4.22$\pm$0.33 $\pm$0.55(sys)
Weighted sum	averaged unfoldings	$\approx$ 3.82$\pm$0.08$\pm$0.22(sys)$\pm$0.42(MC) $\pm$0.15(lumi)$\pm$0.03(T2)$\pm$0.03(Met.) $\pm$ 0.17(SVD) $\approx$ 3.82 $\pm$ 0.54(tot)	

Table 7.21: Comparison of the cross section measurements with the one measured by ALICE [18] at 7 TeV. To facilitate a direct comparison, the final cross sections given in Table 7.6 have been combined using a rapidity coverage-based weighting ("rap-weight"). In addition, the measured cross sections given in Table 7.5 for the individual SD classes have been combined using both a rapidity coverage-based and MC coverage-based ("MC-weight") weighting for both Pythia 8 and EPOS-unfolded data. For MC-weight averages, the indirect TOTEM measurement of the 0T2 cross section [67] is used, since it is not measured in the present analysis. All systematics added in quadrature.

SD class	Phase space	Cross section Rap. (mb)	MC weight (mb)
ALICE	M_X <200 GeV ξ <0.08%	$14.9^{+3.4}_{-5.9}$(sys)	
(this work) Weighted sum	Pythia 8 unfolding (1T2)	5.11±0.11±0.70(sys)	4.84±0.10 ±0.66(sys)
+ [67]	M_X <200 GeV	7.73±2.28	7.37±2.20
(this work) Weighted sum	EPOS unfolding (1T2)	5.77±0.15±0.78(sys)	5.60±0.15 ±0.75(sys)
+ [67]	M_X <200 GeV	8.39±2.31	7.69±1.89
(this work) Weighted sum	averaged unfoldings (1T2)	5.44±0.13±0.30(sys)±0.45(MC) ±0.22(lumi)±0.05(T2)±0.32(Met.) ±0.31(SVD) ≈ 5.44 ± 0.74(tot)	
+ [67]	M_X <200 GeV	8.06±2.29(tot)	

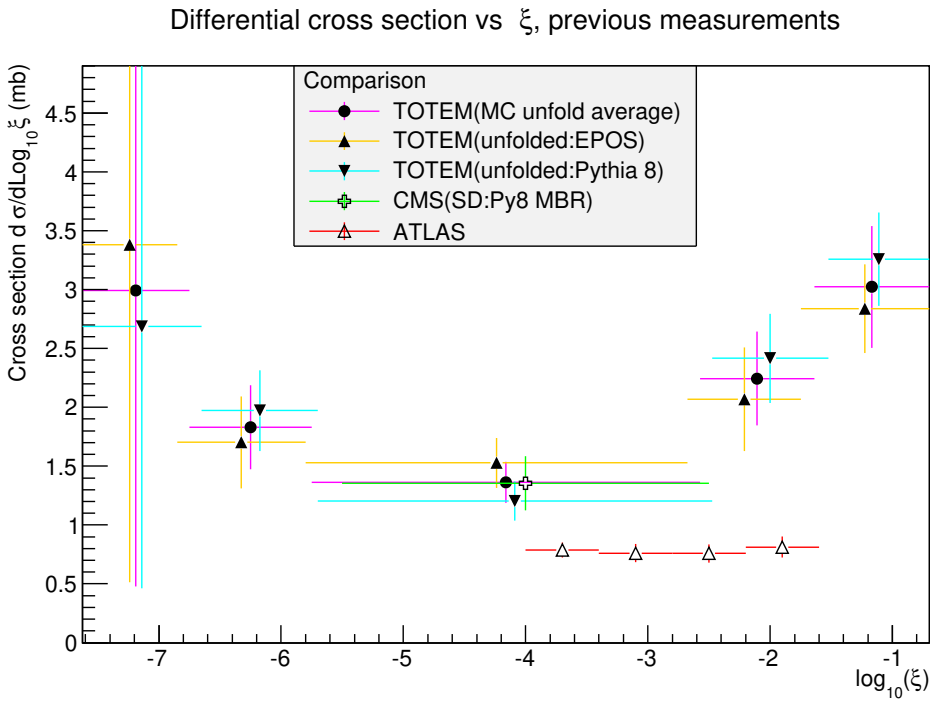

Figure 7.14: Differential cross section as a function of $\log_{10}\xi$ using the last 1 439 000 events of real data in Segment 1b unfolded with EPOS and Pythia SD samples as well as their average ("TOTEM(MC unfold average)"), compared with the ATLAS [29] and CMS [117] SD measurements.

Table 7.22: SD-related measurements at Tevatron energies or above. "RP" stands for proton detected, "RP:$\overline{p}$" for antiproton detected, and CG for central gap detected. "$\overline{\xi}$" refers to the representative point in ξ. Different systematic uncertainties added in quadrature.

Experiment (ref.)	Year	$\sqrt{s}$ (GeV)	Type	Range	Cross section (unless stated otherwise)
ATLAS [29]	2012	8000	RP+CG	$10^{-4} < \xi < 2.5\%$	1.88 ± 0.15 mb (tot)
			fit exp(Bt)	$\log_{10}\overline{\xi} = -2.88$	$B = 7.65 \pm 0.26$(stat)
				± 0.14 (sys)	± 0.22 (sys) GeV^{-2}
			fit $\alpha(0)$		$\alpha(0) = 1.07 \pm 0.09$ (tot)
TOTEM [63]	2012	8000	classification	all	16 ± 3.5 mb (tot)
TOTEM	(2020)	7000	RP+CG	$2 * 10^{-7} < \xi$	11.10 $\pm$ 0.13 mb (stat)
(this work)				$< 20\%$	$\pm$ 1.66 mb (sys)
			fit exp(Bt)	$2 * 10^{-7} < \xi$	$B = 9.03 \pm 0.15$ (stat)
				$< 20\%$	± 0.55 (sys) GeV^{-2} to 5.17
					± 0.15 (stat) ± 0.41 (sys)
					GeV^{-2} (depending on ξ range)
CMS [117]	2010	7000	CG	$3 * 10^{-6} < \xi_1$	4.06 ± 0.04 mb (stat)
					$^{+0.69}_{-0.63}$ mb (sys)
			MC extrapol.	$\xi < 5\%$	8.84 ± 0.08 mb (stat)
					$^{+1.49}_{-1.38}$ mb (sys)
					$^{+1.17}_{-0.37}$ mb (extrap.)
ALICE [18]	2010	7000	SD	$M_X < 200 \frac{\text{GeV}}{\text{c}^2}$	$14.9^{+3.4}_{-5.9}$ mb (sys)
	2011	2760	SD	$M_X < 200$	$12.2^{+3.9}_{-5.3}$ mb (sys)
	2010	900	SD (inel.	$\xi < 5\%$	$11.2^{+1.6}_{-2.1}$ mb (tot)
			not meas.)		
		7000	MC extrap.	$\xi < 5\%$	$17.9^{+7.8}_{-4.6}$ mb (extrap.)
		2760	MC extrap.	$\xi < 5\%$	$14.0^{+4.9}_{-6.7}$ mb (extrap.)
CDF [118]	(1993)	1800	RP:$\overline{p}$	$\xi < 15\%$	9.46 ± 0.44 mb (tot)
		576		$\xi < 15\%$	7.89 ± 0.33 mb (tot)
E710 [119, 120]	(1992)	1800	RP:$\overline{p}$	$\xi < 5\%$	9.4 ± 1.4 mb (tot)

Chapter 8

Summary

Single diffractive (SD) proton-proton interactions are characterized by a proton with nearly the beam momentum at very small scattering angles opposite to a hadronic system with a rapidity gap in between. In this thesis, the SD process has been studied using forward proton detectors at CERN's Large Hadron Collider (LHC). The detection of the forward protons using Roman Pots (RPs) allows the reconstruction of the proton kinematics, notably the absolute momentum transfer squared, $|t|$. The studies were performed using a dedicated low pile-up sample taken during a run with special β^* = 90 m optics at $\sqrt{s}$ = 7 TeV by the TOTEM experiment. The T1 and T2 telescopes were used to the measure the hadronic system and define the size of the rapidity gap.

Single diffractive candidate events were required to have a single proton with a momentum loss ξ of less than 20 % and a hadronic system with activity in the T2 in the opposite hemisphere to the proton. The candidates were selected from an event sample triggered using the T2. The candidates were categorized into four SD classes in diffractive mass, ranging from 3.1 GeV to 3.1 TeV. The inelastic proton reconstruction was improved to allow an efficient measurement of protons with ξ's larger than 5 %. The pileup, beam halo and two proton backgrounds were subtracted from the SD class net signal, which was also corrected for DAQ, T2 trigger and proton reconstruction inefficiencies as well as limited azimuthal and $|t|$-acceptance of the RPs. The resulting SD class signals were converted to cross sections using the luminosity measurement from the CMS experiment that shares the same LHC interaction point with TOTEM, for the corresponding data taking periods. Next, the resulting SD class cross sections were unfolded using both Pythia 8 and EPOS MC samples. As a cross check of the unfolding, class migration matrix-based corrections were also applied, yielding

consistent cross sections.

The average of the obtained cross sections, when unfolding with Pythia 8 and EPOS, are reported as the final SD class cross sections, since based on the data neither of the MCs could be consistently favoured. The relation between the gap size and ξ was used to produce the differential SD cross section $d\sigma_{SD}/d\log_{10}\xi$, which was compared to MC predictions and previous LHC measurements. The measurements in this thesis, which cover a significantly larger range in $\log_{10}\xi$ than the previous ones, was found to be compatible with the CMS measurement [117] but about a factor two larger than the ATLAS one [29] within their respective measurement ranges. The present measurement also indicates a larger SD cross section at low and high $\log_{10}\xi$ compared to medium $\log_{10}\xi$ values. None of the MCs analyzed is able to predict the cross section over the whole $\log_{10}\xi$-range. The resulting total SD cross section is 11.10 ± 1.66 mb for the range $2.7 * 10^{-7} < \xi < 20$ %.

The single exponential slope parameters B were extracted for each SD class separately from the differential cross sections $d\sigma/d|t|$ spectra, unfolded with both Pythia 8 and EPOS. As with the cross sections, the average of the B's obtained from the Pythia 8 and EPOS unfolding is reported for each SD class. The relation between the gap size and ξ was used to show the B dependence on $\log_{10}\xi$, which was compared to MC predictions and the ATLAS measurement [29]. The B dependence measured in this thesis, which covers a significantly larger range in $\log_{10}\xi$ than previous measurements, was found to be compatible with the ATLAS B measurement within its measurement range. The B dependence observed is similar to the predicted one from the MCs and various models, i.e. that the $d\sigma/d|t|$ spectra become less steep with increasing ξ. This is, to our knowledge, the first experimental evidence of this predicted B-dependence on $\log_{10}\xi$ for the single diffractive process at LHC energies, although Regge fits of the exponential $|t|$-slope parameter have been done previously [118].

Bibliography

[1] G. Antchev, *et al.* (TOTEM collaboration), "Performance of the TOTEM Detectors at the LHC," *Int. J. Mod. Phys.*, vol. A28, p. 1330046, 2013.

[2] G. Antchev, *et al.* (TOTEM collaboration), "Proton-proton elastic scattering at the LHC energy of $\sqrt{s}$ = 7-TeV," *EPL*, vol. 95, no. 4, p. 41001, 2011.

[3] G. Antchev, *et al.* (TOTEM collaboration), "Double diffractive cross-section measurement in the forward region at the LHC," *Phys. Rev. Lett.*, vol. 111, no. 26, p. 262001, 2013.

[4] S. Chatrchyan, *et al.* (CMS and TOTEM collaborations), "Measurement of pseudorapidity distributions of charged particles in proton-proton collisions at $\sqrt{s}$ = 8 TeV by the CMS and TOTEM experiments," *Eur. Phys. J.*, vol. C74, no. 10, p. 3053, 2014.

[5] G. Antchev, *et al.* (TOTEM collaboration), "First measurement of elastic, inelastic and total cross-section at $\sqrt{s} = 13$ TeV by TOTEM and overview of cross-section data at LHC energies," *Eur. Phys. J.*, vol. C79, no. 2, p. 103, 2019.

[6] S. Mandelstam, "Determination of the pion - nucleon scattering amplitude from dispersion relations and unitarity. General theory," *Phys. Rev.*, vol. 112, p. 1344, 1958.

[7] G. Aad, *et al.* (ATLAS collaboration), "Observation of a new particle in the search for the Standard Model Higgs boson with the ATLAS detector at the LHC," *Phys. Lett.*, vol. B716, p. 1, 2012.

[8] S. Chatrchyan, *et al.* (CMS collaboration), "Observation of a New Boson at a Mass of 125 GeV with the CMS Experiment at the LHC," *Phys. Lett.*, vol. B716, p. 30, 2012.

[9] J. C. Maxwell, "A dynamical theory of the electromagnetic field," *Phil. Trans. Roy. Soc. Lond.*, vol. 155, p. 459, 1865.

[10] S. Weinberg, "A Model of Leptons," *Phys. Rev. Lett.*, vol. 19, p. 1264, 1967.

[11] A. Einstein, "The Foundation of the General Theory of Relativity," *Annalen Phys.*, vol. 49, no. 7, p. 769, 1916. [Annalen Phys.354,no.7,769(1916)].

[12] M. Tanabashi, *et al.* (Particle Data Group), "Review of Particle Physics," *Phys. Rev.*, vol. D98, no. 3, p. 030001, 2018.

[13] A. Martin, W. Stirling, R. Thorne, and G. Watt, "Parton distributions for the LHC," *Eur. Phys. J. C*, vol. 63, p. 189, 2009.

[14] G. Antchev, *et al.* (TOTEM collaboration), "Luminosity-independent measurements of total, elastic and inelastic cross-sections at $\sqrt{s} = 7$ TeV," *EPL*, vol. 101, no. 2, p. 21004, 2013.

[15] M. L. Good and W. D. Walker, "Diffraction disssociation of beam particles," *Phys. Rev.*, vol. 120, p. 1857, 1960.

[16] R. Hagedorn, "Statistical thermodynamics of strong interactions at high-energies," *Nuovo Cim. Suppl.*, vol. 3, p. 147, 1965.

[17] V. A. Khoze, A. D. Martin, and M. G. Ryskin, "Multiple interactions and rapidity gap survival," *J. Phys.*, vol. G45, no. 5, p. 053002, 2018.

[18] B. Abelev, *et al.* (ALICE collaboration), "Measurement of inelastic, single- and double-diffraction cross sections in proton–proton collisions at the LHC with ALICE," *Eur. Phys. J.*, vol. C73, no. 6, p. 2456, 2013.

[19] R. F. Dashen and S. C. Frautschi, "General S-Matrix Methods for Calculation of Perturbations on the Strong Interactions," *Phys. Rev.*, vol. 137, p. B1318, 1965.

[20] D. Zwanziger, "Unstable Particles in S-Matrix Theory," *Phys. Rev.*, vol. 131, p. 888, 1963.

[21] G. F. Chew, "The search for s-matrix axioms," *Physics Physique Fizika*, vol. 1, no. 2, p. 77, 1964.

[22] H. Burkhardt, *Dispersion Relation Dynamics*. London: North-Holland Pub. Co., 1969.

[23] T. Regge, "Introduction to complex orbital momenta," *Nuovo Cim.*, vol. 14, p. 951, 1959.

[24] P. D. B. Collins, *An Introduction to Regge Theory and High-Energy Physics*. Cambridge Monographs on Mathematical Physics, Cambridge, UK: Cambridge Univ. Press, 1977. (Reprinted 2009).

[25] M. Froissart, "Asymptotic behavior and subtractions in the Mandelstam representation," *Phys. Rev.*, vol. 123, p. 1053, 1961.

[26] G. Pancheri and Y. N. Srivastava, "Introduction to the physics of the total cross-section at LHC," *Eur. Phys. J.*, vol. C77, no. 3, p. 150, 2017.

[27] A. B. Kaidalov, "Diffractive Production Mechanisms," *Phys. Rept.*, vol. 50, p. 157, 1979.

[28] V. A. Khoze, A. D. Martin, and M. G. Ryskin, "The Extraction of the bare triple-Pomeron vertex: A Crucial ingredient for diffraction," *Phys. Lett.*, vol. B643, p. 93, 2006.

[29] G. Aad, *et al.* (ATLAS collaboration), "Measurement of differential cross sections for single diffractive dissociation in $\sqrt{s} = 8$ TeV pp collisions using the ATLAS ALFA spectrometer," *JHEP*, vol. 02, p. 042, 2020.

[30] A. Donnachie and P. V. Landshoff, "Does the hard pomeron obey Regge factorization?," *Phys. Lett.*, vol. B595, p. 393, 2004.

[31] A. Donnachie and P. V. Landshoff, "Total cross-sections," *Phys. Lett.*, vol. B296, p. 227, 1992.

[32] A. Donnachie and P. V. Landshoff, "pp and $\bar{p}p$ total cross sections and elastic scattering," *Phys. Lett.*, vol. B727, p. 500, 2013. [Erratum: Phys. Lett.B750,669(2015)].

[33] M. G. Ryskin, A. D. Martin, and V. A. Khoze, "Proton Opacity in the Light of LHC Diffractive Data," *Eur. Phys. J.*, vol. C72, p. 1937, 2012.

[34] M. Gell-Mann, "A Schematic Model of Baryons and Mesons," *Phys. Lett.*, vol. 8, p. 214, 1964.

[35] J. D. Bjorken and E. A. Paschos, "Inelastic Electron Proton and gamma Proton Scattering, and the Structure of the Nucleon," *Phys. Rev.*, vol. 185, p. 1975, 1969.

[36] J. E. Augustin, *et al.* (SLAC-SP-017 collaboration), "Discovery of a Narrow Resonance in e^+e^- Annihilation," *Phys. Rev. Lett.*, vol. 33, p. 1406, 1974. [Adv. Exp. Phys.5,141(1976)].

[37] J. J. Aubert, *et al.* (E598 collaboration), "Experimental Observation of a Heavy Particle J," *Phys. Rev. Lett.*, vol. 33, p. 1404, 1974.

[38] S. W. Herb *et al.*, "Observation of a Dimuon Resonance at 9.5-GeV in 400-GeV Proton-Nucleus Collisions," *Phys. Rev. Lett.*, vol. 39, p. 252, 1977.

[39] C. W. Darden *et al.*, "Observation of a Narrow Resonance at 9.46-GeV in electron-Positron Annihilations," *Phys. Lett.*, vol. 76B, p. 246, 1978.

[40] S. Aoki *et al.*, "Review of lattice results concerning low-energy particle physics," *Eur. Phys. J.*, vol. C77, no. 2, p. 112, 2017.

[41] V. Crede and W. Roberts, "Progress towards understanding baryon resonances," *Rept. Prog. Phys.*, vol. 76, p. 076301, 2013.

[42] R. D. Schamberger *et al.*, "Cross-Sections for Diffractive $pp \to p$ x from 100-GeV to 400-GeV," *Phys. Rev. Lett.*, vol. 34, p. 1121, 1975.

[43] H. Bialkowska *et al.*, "Study of Reactions with an Identified Proton in p p Interactions at 69-GeV/c," *Nucl. Phys.*, vol. B110, p. 300, 1976. DOI.

[44] G. Giacomelli and M. Jacob, "Physics at the CERN ISR," *Phys. Rept.*, vol. 55, p. 1, 1979.

[45] G. Bellettini, "Results from the Pisa-Stony Brook ISR Experiment," *AIP Conf. Proc.*, vol. 15, p. 9, 1973. DOI.

[46] R. Battiston, *et al.* (UA4 collaboration), "The 'Roman Pot' Spectrometer and the Vertex Detector of Experiment Ua4 at the CERN SPS Collider," *Nucl. Instrum. Meth.*, vol. A238, p. 35, 1985.

[47] G. Alberi and G. Goggi, "Diffraction of Subnuclear Waves," *Phys. Rept.*, vol. 74, p. 1, 1981.

[48] K. A. Goulianos, "Diffractive Interactions of Hadrons at High-Energies," *Phys. Rept.*, vol. 101, p. 169, 1983.

[49] K. A. Goulianos and J. Montanha, "Factorization and scaling in hadronic diffraction," *Phys. Rev.*, vol. D59, p. 114017, 1999.

[50] V. A. Khoze, A. D. Martin, and M. G. Ryskin, "Black disk radius constrained by unitarity," *Phys. Lett.*, vol. B787, p. 167, 2018.

[51] J. Pumplin, "Eikonal models for diffraction dissociation on nuclei," *Phys. Rev.*, vol. D8, p. 2899, 1973.

[52] O. S. Bruning *et al.*, *LHC Design Report Vol.1: The LHC Main Ring*. CERN, 2004. CERN-2004-003-V-1.

[53] V. Baglin, "Three years of LHC operation: What went wrong? What was successful, and lessons for the future." OLAV IV Workshop: NSRRC, Hsinchu, Taiwan, April 1-4, 2014 PDF.

[54] G. Antchev, *et al.* (TOTEM collaboration), "LHC Optics Measurement with Proton Tracks Detected by the Roman Pots of the TOTEM Experiment," *New J. Phys.*, vol. 16, p. 103041, 2014.

[55] G. Anelli, *et al.* (TOTEM collaboration), "The TOTEM experiment at the CERN Large Hadron Collider," *JINST*, vol. 3, p. S08007, 2008.

[56] G. Antchev, *et al.* (TOTEM collaboration), "Measurement of proton-proton elastic scattering and total cross-section at $\sqrt{S}$ = 7-TeV," *EPL*, vol. 101, no. 2, p. 21002, 2013.

[57] G. Antchev, *et al.* (TOTEM collaboration), "Luminosity-Independent Measurement of the Proton-Proton Total Cross Section at $\sqrt{s} = 8$ TeV," *Phys. Rev. Lett.*, vol. 111, no. 1, p. 012001, 2013.

[58] G. Antchev, *et al.* (TOTEM collaboration), "Evidence for non-exponential elastic proton–proton differential cross-section at low $|t|$ and $\sqrt{s}$=8 TeV by TOTEM," *Nucl. Phys.*, vol. B899, p. 527, 2015.

[59] G. Antchev, *et al.* (TOTEM collaboration), "Measurement of elastic pp scattering at $\sqrt{\mathrm{s}} = 8$ TeV in the Coulomb–nuclear interference region: determination of the ρ -parameter and the total cross-section," *Eur. Phys. J.*, vol. C76, no. 12, p. 661, 2016.

[60] G. Antchev, *et al.* (TOTEM collaboration), "First determination of the ρ parameter at $\sqrt{s} = 13$ TeV – probing the existence of a colourless C-odd three-gluon compound state," *Eur. Phys. J.*, vol. C79, no. 9, p. 785, 2019.

[61] G. Antchev, *et al.* (TOTEM collaboration), "Elastic differential cross-section measurement at $\sqrt{s} = 13$ TeV by TOTEM," *Eur. Phys. J.*, vol. C79, no. 10, p. 861, 2019.

[62] G. Antchev, *et al.* (TOTEM collaboration), "Elastic differential cross-section $\mathrm{d}\sigma/\mathrm{d}t$ at $\sqrt{s} = 2.76$ TeV and implications on the existence of a colourless C-odd three-gluon compound state," *Eur. Phys. J. C*, vol. 80, no. 2, p. 91, 2020.

[63] J. Welti, *Inelastic, non-diffractive and diffractive proton-proton cross-section measurements at the LHC*. PhD thesis, Helsinki U., 2017. e-Thesis.

[64] P. Aspell *et al.*, "The VFAT production test platform for the TOTEM experiment," in *Electronics for particle physics. Proceedings, Topical Workshop, TWEPP-08, Naxos, Greece, 15-19 September 2008*, p. 544, 2008. CDS.

[65] F. Sauli, "GEM: A new concept for electron amplification in gas detectors," *Nucl. Instrum. Meth.*, vol. A386, p. 531, 1997.

[66] The CMS collaboration, "Measurement of CMS Luminosity," tech. rep., CERN, 2010. CMS-PAS-EWK-10-004.

[67] G. Antchev, *et al.* (TOTEM collaboration), "Measurement of proton-proton inelastic scattering cross-section at $\sqrt{s}$ = 7 TeV," *EPL*, vol. 101, no. 2, p. 21003, 2013.

[68] R. Avila, P. Gauron, and B. Nicolescu, "How can the Odderon be detected at RHIC and LHC," *Eur. Phys. J.*, vol. C49, p. 581, 2007.

[69] G. Antchev, *et al.* (TOTEM collaboration), "Measurement of the forward charged particle pseudorapidity density in pp collisions at $\sqrt{s} = 7$ TeV with the TOTEM experiment," *EPL*, vol. 98, no. 3, p. 31002, 2012.

[70] M. Berretti, *Measurement of the forward charged particle pseudorapidity density in pp collisions at $\sqrt{s} = 7$ TeV with the TOTEM experiment.* PhD thesis, Siena U., 2012-09-27. CERN-THESIS-2012-231.

[71] G. Antchev, *et al.* (TOTEM collaboration), "First measurement of the total proton-proton cross section at the LHC energy of $\sqrt{s}$ =7 TeV," *EPL*, vol. 96, no. 2, p. 21002, 2011.

[72] G. Antchev, *et al.* (TOTEM collaboration), "Measurement of the forward charged particle pseudorapidity density in pp collisions at $\sqrt{s} = 8$ TeV using a displaced interaction point," *Eur. Phys. J.*, vol. C75, no. 3, p. 126, 2015.

[73] T. Sjostrand, S. Mrenna, and P. Z. Skands, "A Brief Introduction to PYTHIA 8.1," *Comput. Phys. Commun.*, vol. 178, p. 852, 2008.

[74] A. Donnachie and P. V. Landshoff, "Elastic Scattering and Diffraction Dissociation," *Nucl. Phys.*, vol. B244, p. 322, 1984. [,813(1984)] DOI.

[75] T. Sjostrand, S. Mrenna, and P. Z. Skands, "PYTHIA 6.4 Physics and Manual," *JHEP*, vol. 05, p. 026, 2006.

[76] S. Ostapchenko, "Monte Carlo treatment of hadronic interactions in enhanced Pomeron scheme: I. QGSJET-II model," *Phys. Rev.*, vol. D83, p. 014018, 2011.

[77] S. Ostapchenko, "Total and diffractive cross sections in enhanced Pomeron scheme," *Phys. Rev.*, vol. D81, p. 114028, 2010.

[78] S. Ostapchenko, "LHC data on inelastic diffraction and uncertainties in the predictions for longitudinal extensive air shower development," *Phys. Rev.*, vol. D89, no. 7, p. 074009, 2014.

[79] F. Oljemark, "Studies of soft diffraction with TOTEM at the LHC." LHC student poster session Mar 13, 2013 Indico.

[80] T. Pierog *et al.*, "EPOS LHC: Test of collective hadronization with data measured at the CERN Large Hadron Collider," *Phys. Rev.*, vol. C92, no. 3, p. 034906, 2015.

[81] K. Werner, "The hadronic interaction model EPOS," *Nucl. Phys. Proc. Suppl.*, vol. 175-176, p. 81, 2008. DOI.

[82] K. Werner, F.-M. Liu, and T. Pierog, "Parton ladder splitting and the rapidity dependence of transverse momentum spectra in deuteron-gold collisions at RHIC," *Phys. Rev.*, vol. C74, p. 044902, 2006.

[83] T. Pierog and K. Werner, "EPOS Model and Ultra High Energy Cosmic Rays," *Nucl. Phys. Proc. Suppl.*, vol. 196, p. 102, 2009. DOI.

[84] H. J. Drescher *et al.*, "Parton based Gribov-Regge theory," *Phys. Rept.*, vol. 350, p. 93, 2001.

[85] K. Werner *et al.*, "Jets, Bulk Matter, and their Interaction in Heavy Ion Collisions at Several TeV," *Phys. Rev.*, vol. C85, p. 064907, 2012.

[86] K. Werner *et al.*, "Event-by-Event Simulation of the Three-Dimensional Hydrodynamic Evolution from Flux Tube Initial Conditions in Ultrarelativistic Heavy Ion Collisions," *Phys. Rev.*, vol. C82, p. 044904, 2010.

[87] S. Agostinelli, *et al.* (GEANT4 Group), "GEANT4: A Simulation toolkit," *Nucl. Instrum. Meth.*, vol. A506, p. 250, 2003. DOI.

[88] P. Arce *et al.*, "Use of GEANT4 in CMS. The OSCAR project," in *Proceedings, 11th International Conference on Computing in High-Energy and Nuclear Physics (CHEP 2000): Padua, Italy, February 7-11, 2000*, p. 201, 2000. Abstract.

[89] F. Ferro, *The simulation of the TOTEM inelastic telescopes in OSCAR*, May 2005. CERN-TOTEM-NOTE-2005-003.

[90] J. Kaspar, *Elastic scattering at the LHC*. PhD thesis, Prague, Inst. Phys., 2011. CERN-THESIS-2011-214.

[91] H. Niewiadomski, *Reconstruction of protons in the TOTEM roman pot detectors at the LHC*. PhD thesis, Manchester U., 2008. CERN-THESIS-2008-080.

[92] R. Brun and F. Rademakers, "ROOT: An object oriented data analysis framework," *Nucl. Instrum. Meth.*, vol. A389, p. 81, 1997. DOI.

[93] L. Mascetti *et al.*, "Disk storage at CERN," *J. Phys. Conf. Ser.*, vol. 664, no. 4, p. 042035, 2015. DOI.

[94] X. Espinal *et al.*, "Disk storage at CERN: Handling LHC data and beyond," *J. Phys. Conf. Ser.*, vol. 513, p. 042017, 2014. DOI.

[95] T. Adye, "Unfolding algorithms and tests using RooUnfold," in *Proceedings, PHYSTAT 2011 Workshop on Statistical Issues Related to Discovery Claims in Search Experiments and Unfolding, CERN,Geneva, Switzerland 17-20 January 2011*, (Geneva), p. 313, CERN, 2011. CDS.

[96] K. A. Goulianos, "Renormalization of hadronic diffraction and the structure of the pomeron," *Phys. Lett.*, vol. B358, p. 379, 1995. [Erratum: Phys. Lett.B363,268(1995)].

[97] V. A. Khoze, A. D. Martin, and M. G. Ryskin, "Soft diffraction and the elastic slope at Tevatron and LHC energies: A MultiPomeron approach," *Eur. Phys. J.*, vol. C18, p. 167, 2000.

[98] M. G. Ryskin, A. D. Martin, and V. A. Khoze, "Soft processes at the LHC. I. Multi-component model," *Eur. Phys. J.*, vol. C60, p. 249, 2009.

[99] M. G. Ryskin, A. D. Martin, and V. A. Khoze, "High-energy strong interactions: from 'hard' to 'soft'," *Eur. Phys. J.*, vol. C71, p. 1617, 2011.

[100] E. Gotsman, E. Levin, U. Maor, and J. S. Miller, "A QCD motivated model for soft interactions at high energies," *Eur. Phys. J.*, vol. C57, p. 689, 2008.

[101] E. Gotsman, E. Levin, and U. Maor, "N=4 SYM and QCD motivated approach to soft interactions at high energies," *Eur. Phys. J.*, vol. C71, p. 1553, 2011.

[102] E. Gotsman, E. Levin, and U. Maor, "Description of LHC data in a soft interaction model," *Phys. Lett.*, vol. B716, p. 425, 2012.

[103] A. B. Kaidalov and M. G. Poghosyan, "Description of soft diffraction in the framework of reggeon calculus: Predictions for LHC," in *Elastic and Diffractive Scattering. Proceedings, 13th International Conference, Blois Workshop, CERN, Geneva, Switzerland, June 29-July 3, 2009*, p. 91, 2009. CDS.

[104] J. Bleibel, L. V. Bravina, A. B. Kaidalov, and E. E. Zabrodin, "How many of the scaling trends in pp collisions will be violated at $\sqrt{s_{NN}}$ = 14 TeV ? - Predictions from Monte Carlo quark-gluon string model," *Phys. Rev.*, vol. D93, no. 11, p. 114012, 2016.

[105] M. Deile, D. d'Enterria, and A. De Roeck, eds., *Elastic and Diffractive Scattering. Proceedings, 13th International Conference, Blois Workshop, CERN, Geneva, Switzerland, June 29-July 3, 2009*, 2010. CERN-PROCEEDINGS-2010-002.

[106] K. Goulianos, "Diffractive and Total pp Cross Sections at LHC," in *Elastic and Diffractive Scattering. Proceedings, 13th International Conference, Blois Workshop, CERN, Geneva, Switzerland, June 29-July 3, 2009*, 2010. CDS.

[107] R. Ciesielski and K. Goulianos, "MBR Monte Carlo Simulation in PYTHIA8," *PoS*, vol. ICHEP2012, p. 301, 2013. DOI.

[108] G. A. Schuler and T. Sjostrand, "Hadronic diffractive cross-sections and the rise of the total cross-section," *Phys. Rev.*, vol. D49, p. 2257, 1994.

[109] J. R. Cudell, *et al.* (COMPETE collaboration), "Benchmarks for the forward observables at RHIC, the Tevatron Run II and the LHC," *Phys. Rev. Lett.*, vol. 89, p. 201801, 2002.

[110] H. Grote and F. Schmidt, "MAD-X: An upgrade from MAD8," *Conf. Proc.*, vol. C030512, p. 3497, 2003. CERN-AB-2003-024-ABP.

[111] L. Deniau, "MAD-X Progress and Future Plans," in *Proceedings, 11th International Computational Accelerator Physics Conference (ICAP 2012): Rostock-Warnemünde, Germany, August 19-24, 2012*, p. THAAI3, 2012. PDF.

[112] G. D'Agostini, "A Multidimensional unfolding method based on Bayes' theorem," *Nucl. Instrum. Meth.*, vol. A362, p. 487, 1995.

[113] A. Hocker and V. Kartvelishvili, "SVD approach to data unfolding," *Nucl. Instrum. Meth. A*, vol. 372, pp. 469–481, 1996.

[114] K. Akiba, *et al.* (LHC Forward Physics Working Group), "LHC Forward Physics," *J. Phys.*, vol. G43, p. 110201, 2016.

[115] S. Ostapchenko, "On the model dependence of the relation between minimum-bias and inelastic proton-proton cross sections," *Phys. Lett.*, vol. B703, p. 588, 2011.

[116] G. Aad, *et al.* (ATLAS collaboration), "Erratum: Measurement of differential cross sections for single diffractive dissociation in $\sqrt{s} = 8$ TeV pp collisions using the ATLAS ALFA spectrometer," *JHEP*, vol. 10, p. 182, 2020.

[117] V. Khachatryan, *et al.* (CMS collaboration), "Measurement of diffraction dissociation cross sections in pp collisions at $\sqrt{s}$ = 7 TeV," *Phys. Rev.*, vol. D92, no. 1, p. 012003, 2015.

[118] F. Abe, *et al.* (CDF collaboration), "Measurement of $\bar{p}p$ single diffraction dissociation at $\sqrt{s} = 546$ GeV and 1800 GeV," *Phys. Rev.*, vol. D50, p. 5535, 1994.

[119] N. A. Amos, *et al.* (E-710 collaboration), "Diffraction dissociation in $\bar{p}p$ collisions at $\sqrt{s}$ = 1.8-TeV," *Phys. Lett.*, vol. B301, p. 313, 1993.

[120] N. A. Amos, *et al.* (E-710 collaboration), "A Luminosity Independent Measurement of the $\bar{p}p$ Total Cross-section at $\sqrt{s}$ = 1.8-TeV," *Phys. Lett.*, vol. B243, p. 158, 1990.

[121] G. Matthiae and M. Haguenauer, "Total cross-section and diffractive processes at the Large Hadron Collider (LHC)," in *Lausanne/Geneva 1984, Proceedings, Large Hadron Collider In The Lep Tunnel, Vol.1*, p. 303, 1985. CDS.

[122] A. M. Asner *et al.*, *The Large Hadron Collider in the LEP tunnel*. CERN, 1987. CERN-87-05.

[123] M. Tigner, "Where is the SSC Today?," *IEEE Trans. Nucl. Sci.*, vol. 32, p. 1556, 1985. DOI.

[124] T. Elioff, "A Chronicle of Costs," 1994. SSCL-SR-1242.

[125] J. D. McCarthy, "Operational Experience with Tevatron I Antiproton Source," *Conf. Proc.*, vol. C870316, p. 1388, 1987. PDF.

[126] M. Bajko *et al.*, "Report of the task force on the incident of 19th September 2008 at the LHC," tech. rep., 2009. CERN-LHC-PROJECT-REPORT-1168.

[127] E. Todesco *et al.*, "Training Behavior of the Main Dipoles in the Large Hadron Collider," *IEEE Trans. Appl. Supercond.*, vol. 27, no. 4, p. 4702807, 2017. DOI.

[128] K. Johnsen, "Cern intersecting storage rings," *Kerntech.*, vol. 12, p. 541, 1970. CDS.

[129] The ISR Staff, "First observation of colliding beam events in the CERN intersecting storage rings (ISR)," *Phys. Lett.*, vol. 34B, p. 425, 1971.

[130] U. Amaldi *et al.*, "The Energy dependence of the proton proton total cross-section for center-of-mass energies between 23 and 53 GeV," *Phys.Lett.*, vol. B44, p. 112, 1973.

[131] U. Amaldi, "Small-angle physics at the intersecting storage rings forty years later," in *Proceedings, 40th Anniversary of the First Proton-Proton Collisions in the CERN Intersecting Storage Rings (ISR): Geneva, Switzerland, January 18, 2011*, 2012. CDS.

[132] M. Albrow, "Double Pomeron Exchange at the CERN Intersecting Storage Rings and $Sp\bar{p}S$ Collider," *Int. J. Mod. Phys.*, vol. A29, no. 28, p. 1446014, 2014.

[133] V. E. Barnes (CDF collaboration), "Status and Prospects of the Fermilab Collider Detector, TeVatron Collider, and Antiproton Source," *Conf. Proc.*, vol. C871008, p. 141, 1987. Inspire.

[134] M. Bozzo, *et al.* (UA4 collaboration), "Single Diffraction Dissociation at the CERN SPS Collider," *Phys. Lett.*, vol. 136B, p. 217, 1984.

[135] D. Bernard, *et al.* (UA4 collaboration), "The Cross-section of Diffraction Dissociation at the CERN SPS Collider," *Phys. Lett.*, vol. B186, p. 227, 1987.

[136] M. G. Albrow, *et al.* (CHLM collaboration), "Inelastic Diffractive Scattering at the CERN ISR," *Nucl. Phys.*, vol. B108, p. 1, 1976.

[137] J. C. M. Armitage *et al.*, "Diffraction Dissociation in Proton Proton Collisions at ISR Energies," *Nucl. Phys.*, vol. B194, p. 365, 1982.

[138] D. S. Ayres *et al.*, "Inelastic Diffractive Scattering at FNAL Energies," *Phys. Rev. Lett.*, vol. 37, p. 1724, 1976.

[139] R. L. Cool *et al.*, "Diffraction Dissociation of $\pi^{\pm}$, $K^{\pm}$, and $\rho^{\pm}$ at 100-GeV/c and 200-GeV/c," *Phys. Rev. Lett.*, vol. 47, p. 701, 1981. [Erratum: Phys. Rev. Lett.48,61(1982)].

[140] G. J. Alner, *et al.* (UA5 collaboration), "UA5: A general study of proton-antiproton physics at $\sqrt{s}$ = 546-GeV," *Phys. Rept.*, vol. 154, p. 247, 1987.

[141] G. J. Alner, *et al.* (UA5 collaboration), "Antiproton-proton cross sections at 200 and 900 GeV c.m. energy," *Z.Phys.*, vol. C32, p. 153, 1986.

[142] A. Brandt, *et al.* (UA8 collaboration), "Measurements of single diffraction at $\sqrt{s}$ = 630-GeV: Evidence for a nonlinear α_t of the Pomeron," *Nucl. Phys.*, vol. B514, p. 3, 1998.

[143] M. G. Albrow *et al.*, "Missing mass spectra in p p inelastic scattering at total energies of 23 GeV and 31 GeV," *Nucl. Phys.*, vol. B72, p. 376, 1974.

[144] M. G. Albrow *et al.*, "The spectrum of protons produced in p p collisions at 31 GeV total energy," *Nucl. Phys.*, vol. B54, p. 6, 1973.

[145] J. Whitmore, "Experimental Results on Strong Interactions in the NAL Hydrogen Bubble Chamber," *Phys. Rept.*, vol. 10, p. 273, 1974.

[146] J. W. Chapman *et al.*, "The diffractive component in p p collisions at 102-GeV and 405-GeV," *Phys. Rev. Lett.*, vol. 32, p. 257, 1974.

[147] M. Derrick, "Some Aspects of Diffraction as Seen in Bubble Chamber Experiments," in *High energy physics. Proceedings, 17th International Conference, ICHEP 1974, London, England, July 01-July 10, 1974*, p. I.3, 1974. Inspire.

[148] J. Benecke, *et al.* (Bonn-Hamburg-Munich collaboration), "Rapidity Gap Separation and Study of Single Diffraction Dissociation in p p Collisions at 12-GeV/c and 24-GeV/c," *Nucl. Phys.*, vol. B76, p. 29, 1974.

[149] M. Wunsch, "Vergleich inelastischer Proton-Proton, Alpha-Proton und Alpha-Alpha Wechselwirkungen," Master's thesis, Heidelberg U., 1983. RX-1005.

[150] J. C. Sens, "Intersecting storage rings: review of recent results from the European Center for Nuclear Research," in *American Physical Society Meeting New York, New York, January 29-February 1, 1973*, p. 155, 1973. Inspire.

[151] K. Abe *et al.*, "Measurement of P P $\rightarrow$ P X between 50-GeV/c and 400-GeV/c.," *Phys. Rev. Lett.*, vol. 31, p. 1527, 1973.

[152] V. D. Shiltsev, "Status of Tevatron Collider Run II and Novel Technologies for the Tevatron Luminosity Upgrades," in *9th European Particle Accelerator Conference (EPAC 2004) Lucerne, Switzerland, July 5-9, 2004*, 2004. PDF.

[153] J. L. Crawford and D. A. Finley, "The 1987 Tevatron Collider Run in Retrospect," 1987. FERMILAB-PUB-87-244-PPD.

[154] B. De Raad, "The CERN SPS Proton-Antiproton Collider," *IEEE Trans. Nucl. Sci.*, vol. 32, p. 1650, 1985. DOI.

[155] J. B. Adams, "The CERN 400 GeV Proton Synchrotron (CERN SPS)," in *Proceedings: 10th International Conference on High-Energy Accelerators, Protvino, Jul 1977. 1.*, vol. 1, p. 17, 1977. CDS.

[156] E. Malamud and J. K. Walker, "Progress and prospects at the National Accelerator Laboratory," 1970. FERMILAB-NAL-050. Presented at ICHEP 70, Kiev, Aug. 26 – Sep. 4, 1970?

[157] Institute of High Energy Physics of the SCUAE *et al.*, "Serpukhov 70 GeV Proton Synchrotron," in *Proceedings, 6th International Conference on High-Energy Accelerators, HEACC 1967: Cambridge, Massachusetts, September 11-15, 1967*, p. 248, 1967. Inspire.

[158] R. E. Ansorge, *et al.* (UA5 collaboration), "Diffraction Dissociation at the CERN Pulsed Collider at CM Energies of 900-GeV and 200-GeV," *Z. Phys.*, vol. C33, p. 175, 1986.

[159] R. D. Schamberger, J. Lee-Franzini, R. McCarthy, S. Childress, and P. Franzini, "Mass Spectrum of Proton Proton Inelastic Interactions From 55-GeV/c to 400-GeV/c at Small Momentum Transfer," *Phys. Rev.*, vol. D17, p. 1268, 1978.

[160] S. Barish *et al.*, "Updated Charged-Particle Multiplicity Distribution from 205-GeV/c Proton Proton Interactions," *Phys. Rev.*, vol. D9, p. 2689, 1974.

[161] F. T. Dao *et al.*, "pp Interactions at 303-GeV/c: Analysis of Diffraction Excitation in the Reaction $pp \to pX$.," *Phys. Lett.*, vol. 45B, p. 399, 1973.

Appendix A

TOTEM paper on measuring the trigger & tracking efficiency for Roman Pots from calibration data - Aug 2011

A.1 Introduction

The TOTEM Roman Pot detectors at 220m & 147m from the interaction point IP5 (CMS + TOTEM) are strip-based (1-dimensional readout) silicon detectors deployed within a movable "Pot" structure, which can approach the beam as near as about half a mm, plus a multiple of the beam width for safety (7-20*σ_{beam}, depending on the collision rate). Each detector station has 6 pots (2 horizontal, 2 vertical above the beam and 2 below). Each pot has 10 detector planes, which have their strips oriented orthogonally (90 degrees) to their nearest neighbours, and all of them are positioned diagonally with respect the local horizontal (i.e. $\pm 45^{\circ}$). These two coordinates are called U & V.

Finally, each RP detector consists of 512 strips ($66\mu m$ wide), that are aggregated into 16 Trigger Sectors (0-15. The elastic protons are seen in sector (U,V)=(12,12) in all other pots than arm56*top, where (U,V)=(11,12) in the near pot (nearer to the IP5, that is) and (U,V)=(11,12) and =(12,13) in the far pot.

The data is read out of these detectors by digital chips called VFATs, which are also used to read out the trigger data from the Trigger Mezzanine Card.

I measured the trigger & tracking efficiency for the data.

A.1.1 Trigger Efficiency

The trigger efficiency was measured using a series of test runs from Oct 14 & Oct 24, 2010, see Table A.7. In each of these runs we read out all the VFAT data (including the TMC - Trigger Mezzanine Card - data showing the trigger bits sent to the trigger), but we triggered only on one pot per arm, different for each run : first we asked for symmetric configuration (arm 45_tp + arm 56_tp etc)., then for the diagonal case (arm 45_tp + arm 56_bt, etc. We always asked for far pot+far pot & same for near+near.

The method used was to look at the trigger output of the nontriggering pot which was in the same arm and vertical position as the triggering pot, and count the fraction of events where the non-triggering pot's trigger input data would have lead to a trigger. To exclude events where you don't expect a track, and the trigger should thus be off , I also demanded that the triggering pot should have a track that points to the nontriggering pot under study. (Because of confusion limitations, at present we reconstruct at most one track per pot, although this year we have also added to our reconstruction and simulation software as a secondary, and at present rarely used, a multitrack producer). The pointing requirement was first done by extrapolating the track (line segment) fitted using just the data from the triggering pot (a lever arm of ca. 5m, giving an extrapolation uncertainty of a few mm). Later we found one could get a much better precision for elastic proton tracks by exploiting the correlation between the track position in the near & far pots. This was done by making correlation plots, for each pair of near-far pots, of the measured x- & y-coordinates of tracks in those two pots (x vs. x & y vs. y). This was done both for all good tracks (many millions of events), and for all events fulfilling "elastic-only" criteria. These criteria were called "TMC-cut" (demand only sector 12 triggered in both U & V in the pot) and "spectrometer cut". Using these correlations we the extrapolated the position of the fitted track at the middle plane of the triggering pot, to the same plane in the nontriggering pot, by scaling the x & y values by previously fitted constants (i.e. $x_{Extrapol} = fitConst * x_{track}$ - see Table A.1 for fitted values)

To check the accuracy of this "optical" scaling extrapolation I measured the difference between the extrapolated coordinates & the coordinates of tracks found in the pot under study, and found a dispersion of a few hundred microns in y and 1-2mm in x (as a shorthand I will define $\sigma_x \equiv 1mm$ & $\sigma_y \equiv 0.1mm$). I show representative plots for

Table A.1: Scaling constants when going from track in near-IP pot to further-from-IP pot extrapolation - divide by this if triggering on far pot

coord.	elastic	general
both arms x-	0.87	0.87
arm 45 bottom y-	1.01	1.09
arm 45 tp y-	1.02	1.09
arm 56 y-	1.02	1.09

all RP pairs for the y- coordinate in Figures A.1 to A.4.

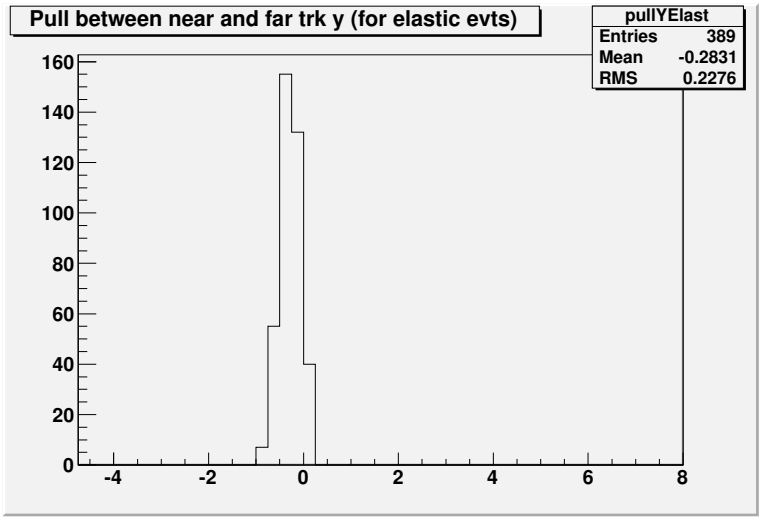

Figure A.1: Pull in y (extrapolated y minus measured y, divided by σ_y), for quarter 45_tp

Taking this dispersion into account, and so as to minimize the non-trigger-inefficiency systematic, I demanded that the events under study should have extrapolated coordinates well within the sensitive volume of the nontriggering pot: i.e. that the x-coordinate shouldn't be nearer to the edge than 2mm ($2 * \sigma_x$), and that the extrapolated y-coord. should be farther than 0.3mm ($3 * \sigma_y$) from the edge. Since real elastic protons are observed in a very small interval in the x-coordinate (different from pot to pot, but $|x| < 1mm$ for all pots), a selection cut on x was also added.

The 4 pots nearest to IP5 were found to be displaced up to 1mm, towards the beam, from their position in the corrected geometry used. Therefore a selection cut was added, such that if the triggering pot track was nearer to the edge than the cut value, the event was counted as a non-neighbour-pointing track, since no track or trigger signal

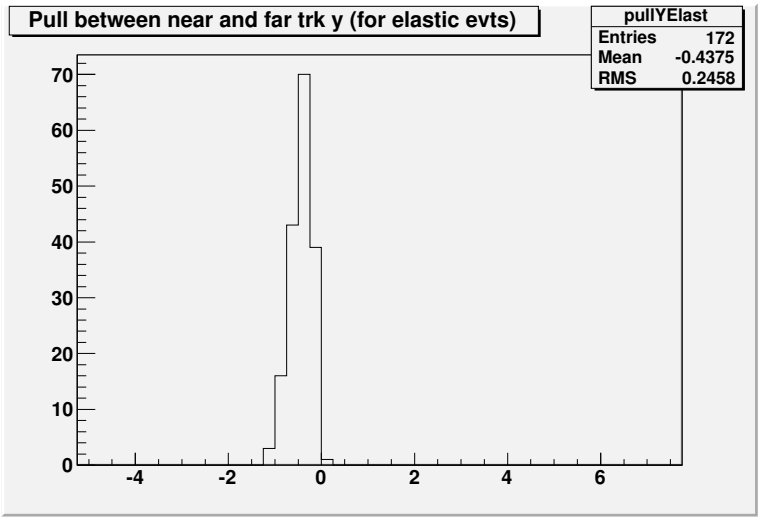

Figure A.2: Pull in y (extrapolated y minus measured y, divided by σ_y), for quarter 45_bt

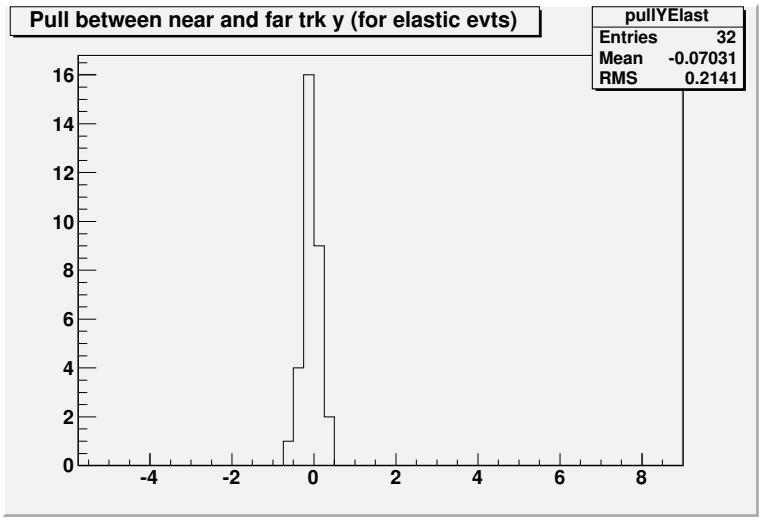

Figure A.3: Pull in y (extrapolated y minus measured y, divided by σ_y), for quarter 56_tp

was expected in the pot under study. The requirement was applied to the beam-track distance at the position of the triggering pot, so there was a pot-dependent constant offset found from the data. The selection cut values used on the triggering pot can be found in Table A.2, and the efficiencies in Table A.3. Table A.4 shows the efficiency for the case where one of the trigger fibers wasn't working, so we were triggering only on U- or else only on V-planes.Since we don't know which of these weren't triggering, the table is the average of the two cases.

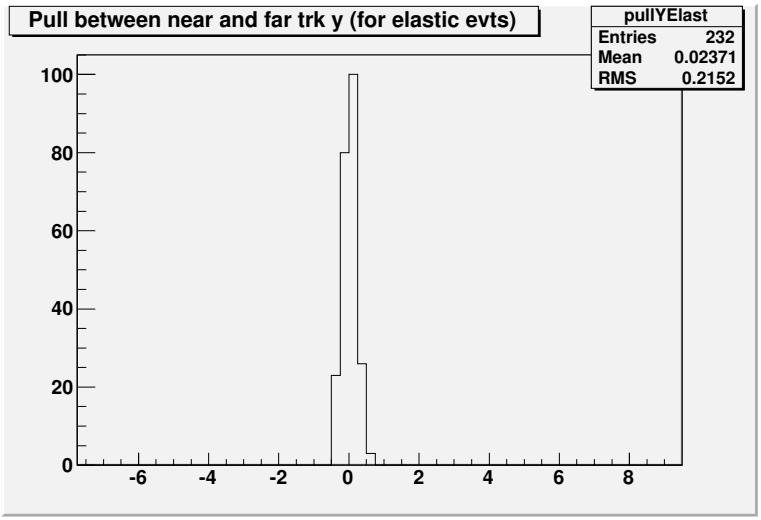

Figure A.4: Pull in y (extrapolated y minus measured y, divided by σ_y), for quarter 56_bt

The final elastic-proton trigger efficiency selections used were:

- triggering pot has track
- track points to neighbour pot
- hits sensitive detector area, further than $2 * \sigma_x \& 3 * \sigma_y$ from the edge
- neighbour pot has only trigger sector 12 on in both U & V
- except for arm 56 top pots, where the adjacent sectors are used, and $U = V + 1$ is demanded
- a pot-dependent x-cut, $\approx 1mm$ wide
- if the triggering pot track was nearer to the edge than the cut value, the event was counted as a non-neighbour-pointing track

A.1.2 Tracking Efficiency

Similar to the method used for measuring the trigger efficiency, I looked at the all events with a track in the triggering pot that pointed to the nontriggering pot, and counted them as efficient if that target pot had a track within $2 * \sigma_x$ & $3 * \sigma_y$ of the triggering pot track's extrapolation. See Table A.6 for the efficiencies. The generally

Table A.2: Near pot selection cut values

pot	edge distance (mm)	Selection cut value (mm)
020	0.2	8.0
021	0.3	8.1
120	1.1	8.5
121	1.1	8.5

Table A.3: Trigger efficiency & elastic purity for (TMC U=V=12 only) "elastic" events. Consider as triggered if U or V planes trigger. Statistical uncertainties only.

pot	efficiency w/o x-cut (%)	purity w/o x-cut (%)	efficiency+x-cut	purity w/ x-cut
020	79.5 ± 1.1	58	89.8 ± 1.1	79
021	84.1 ± 1.4	42	88.9 ± 1.7	65
024	97.7 ± 0.6	70	99.1 ± 0.5	90
025	97.0 ± 0.6	46	98.9 ± 0.5	67
120	97.2 ± 0.5	14	97.7 ± 0.6	26
121	92.2 ± 0.5	16	95.8 ± 0.6	43
124	97.7 ± 0.3	8	98.4 ± 0.5	30
125	83.5 ± 1.3	33	86.5 ± 1.5	49

large inefficiency is caused by the reconstruction algorithm only looking for events with a single track, meaning if two tracks can be found then none will actually be reconstructed. Also, when I calculated this efficiency with the RPSingleTrackFinder (finds straight tracks only) instead of RPNonParallelTrackFinder, I found efficiencies to be on average 3% lower than the numbers in Table A.6.

The final elastic-proton tracking efficiency requirements used were:

- neighbour pot has track

Table A.4: Trigger efficiency for (TMC U=V=12 only) "elastic" events. In some runs these two pots only triggered on one orientation, U or V. Here is shown the average of U-only and V-only efficiency. Statistical uncertainties only.

pot	efficiency w/o x-cut (%)	efficiency+x-cut
020	77.7 ± 0.8	89.0 ± 0.8
120	96.6 ± 0.4	97.6 ± 0.5

Table A.5: Trigger efficiency for all events fulfilling the edge cutoff in y, from Table A.2 & also the $2 * \sigma_y, 3 * \sigma_x$ selection cuts. Consider as triggered if (U or V) or (U and V) planes trigger. Statistical uncertainties only. Large drop for pot 025 because one trigger sector unconnected, always off.

pot	efficiency u+v (%)	efficiency u*v (%)
020	87.6 ± 0.2	86.7 ± 0.2
021	91.4 ± 0.2	87.7 ± 0.2
024	92.5 ± 0.2	92.0 ± 0.2
025	94.7 ± 0.1	73.4 ± 0.1
120	96.1 ± 0.1	95.7 ± 0.1
121	88.8 ± 0.1	88.0 ± 0.1
124	97.69 ± 0.05	97.48 ± 0.05
125	90.3 ± 0.2	89.8 ± 0.2

- track points to pot under study
- hits sensitive detector area, further than $2 * \sigma_x$&$3 * \sigma_y$ from the edge
- look for a track in target pot within $2 * \sigma_x$ & $3 * \sigma_y$ of the extrapolated neighbour track
- for comparison, I also looked at "halfway out the window": a situation where Y is within 3 sigma, but X is $2 < x/\sigma < 3$
- or vice versa : X is within 2 sigma and Y is $3 < y/\sigma < 5$

A.2 Miscellaneous track & trigger systematics

The ideal measurement of elastic scattering would be to see both scattered protons in the same RP diagonal, such that a track is found in all four pots, and each pot has one single trigger sector on, in the corresponding position. Our selection procedure was that (after applying some track quality requirements), we accepted events with three or four pots in the same diagonal having a track, such that they could kinematically belong to the same elastic interaction.

To check the quality of our sample, I calculated from the $7 - \sigma$ data (called "tracking" in Table A.7) the combinations in Table A.8

Table A.6: Tracking efficiency for (TMC U=V=elastic (11/12/13) only + x-cut) "elastic" events. Consider as correct track if found within $2*3\sigma$ of extrapolation. Statistical uncertainties only.

pot	efficiency (%)
020	76 ± 5 ($\approx 12\%$ spread)
021	74.3 ± 2.3
024	85.9 ± 1.6
025	69.1 ± 1.9
120	48.0 ± 1.8
121	74.3 ± 1.3
124	67.7 ± 1.9
125	77.2 ± 1.8

Table A.7: Runs used for data analysis. (Elastic events are diagonal.)

run	date (2010)	type	comments
3464	Oct 14	trigger	020*120 (nondiagonal)
3465	Oct 14	trigger	021*121 (nondiagonal)
3466	Oct 14	trigger	024*124 (nondiagonal)
3467	Oct 14	trigger	025*125 (nondiagonal)
3468	Oct 14	trigger	020*121
3469	Oct 14	trigger	021*120
3470	Oct 14	trigger	024*125
3578	Oct 24	trigger	021*120
3580	Oct 24	trigger	025*124
3581	Oct 24	trigger	024*125
3717	Oct 30	tracking	410k events, 2 arm U or V
3719	Oct 30	tracking	2.13M events, 2 arm U or V
3720	Oct 30	tracking	2.32M events, 2 arm U or V
3721	Oct 30	tracking	194k events, 2 arm U or V
3722	Oct 30	tracking	422k events, 2 arm U or V

Table A.8: Calculated trigger & tracking quantities for systematics elimination.Diag0= diagonal 45_tp+56_bt=020+121 etc.. Diag1=45_bt+56_tp

name	average value (%) diag0	diag1 (%)
4*(1 TS on in U and V)	0	0
4*(0 TS on)	0	0
3*(0 TS on)+1*(0,0)	0	0
3*(0 TS on)+1*(0,1)	0	0

Appendix B

LHC history

The Large Hadron Collider (LHC) was proposed as a hadron collider that would reuse the LEP tunnel. It was first mooted in the 1980s [121, 122]. To compete with the U.S. Superconducting Supercollider (SSC) [123] [1] it was decided to maximize the luminosity of the LHC to compensate for the lower energy of the LHC compared to the SSC, which was due to the LHC having a shorter tunnel. By using proton-proton collisions, the constraints and inefficiencies from antiproton production, deceleration, storage, and reacceleration that had plagued among others the TeVatron [125], would also be relieved. Of course, this advantage was bought at the cost of making the dipole magnets more complicated, because the counterrotating beams could not go through the same vacuum pipe. This is in contrast to the case of proton and antiproton beams which could share a common vacuum pipe, having opposite charges going opposite ways.

B.1 Magnet failure incident and lower proton collision energy as safety margin

The LHC was built from 2000 to 2008, at which point proton beams were first circulated around the ring. During the initial commissioning period in September 2008, an undetected defect [126,127] in the normal-conduction "bus bar" bypass circuit (for use in case of quench of superconduction) for one of the superconducting magnets, lead a part of the circuit to lose superconductivity and reach thermal runaway within less than a second at a magnet current of $I_{s.c.} = 8.7$ kA. This pierced the liquid Helium

[1] Afterwards, the SSC was cancelled in 1994 [124].

cooling lines and produced a high-pressure pulse (> 8 atm) in the secondary vacuum as more than 2 tonnes of He blew through the beamline vacuum structures, ripping parts along to do downstream damage up to 700 m away from the initial incident. Following this incident, all magnets and interconnects were checked for similar defects and extensively retrained (quenched many times at progressively higher currents), and after repairs data taking finally began in 2010, at beam energies limited to 7-13 TeV (LHC energy had originally been planned for 14 TeV).

Appendix C

SD cross section measurements up to CERN UA5 (1982-86)

C.1 LHC Predecessors : proton-proton collisions

Before LEP, the CERN accelerator most relevant to this thesis was the Intersecting Storage Ring (ISR [128]), that ran from 1971 to 1984. This was the first proton-hadron collider that collided two proton beams in flight [129], unlike previous fixed-target colliders. This increased the available centre-of-mass collision energy quite a lot, since the final collision energy reached (62 GeV), corresponds to a fixed-target collider with an energy of 2 TeV, but also demanded many advances in beam handling to have particle beams that interact strongly at designated collision points but still have a circulating lifetime of multiple hours.

Moveable proton detectors for near-beam detection of quasi-elastically scattered protons were also pioneered at the ISR [130], allowing measurements of SD and elastic scattering [131]. ISR also pioneered measurements of double Pomeron exchange [132] (with a small acceptance, since DPE conventionally has two rapidity gaps of at least 3 units each, whereas the rapidity range produced at s^{ISR}_{max} was only $2\ln(\sqrt{s}/m_p) \approx 8.4$).

C.2 LHC Predecessors : proton-antiproton collisions

At high energies all the $p+p$ and $p+\bar{p}$ cross sections are expected (and observed) to reach equal values, differing by $\mathcal{O}(1\%)$ at $\sqrt{s} = 10^2$ GeV. Therefore, previous measurements of SD quoted in Tables 7.22 to C.5 are given for both proton and proton-

antiproton colliders.

In 1976, CERN built a new proton accelerator, the SPS, that was used as a proton-antiproton collider ($Sp\bar{p}S$) at $\sqrt{s} = 540$ GeV from 1981, reaching 630 GeV later. Afterwards, it was used to accelerate and inject electrons and positrons into LEP, and (as noted above), it is still used for injecting protons into the LHC at $\sqrt{s} = 900$ GeV.

At Fermilab near Chicago, another large antiproton collider, the TeVatron [133], was built in the main ring of an older circular fixed-target accelerator whose magnets were converted to superconductive ones for higher field-operation, operating from 1987 to 2011 at energies $\sqrt{s} = 1.8 - 1.96$ TeV.

A table of all the preceding colliders and accelerators from which measurements are quoted in this thesis are given in Table C.1.

C.2.1 Historical comparison with older experiments

UA4 had previously used RPs [46] to measure [134, 135] single diffraction, citing previous measurements at the ISR [136, 137] and Fermilab [138, 139]. Later, UA5 [140] presented SD mass spectra [141], and the UA8 collaboration measured [142] nonlinearity in the Pomeron trajectory. In the 1970s and 60s, SD measurements were made at tens of GeV [143, 144], and in bubble chambers [43, 145–148], Fermilab [42] and ISR [137, 149]. SD measurements at $\xi < 10\%$ had been done at the CERN ISR [150] and NAL [151].

All older measurements, up to the CERN UA5, of the total SD (or sometimes total diffraction, including DD) cross section are presented in Tables C.2 to C.4.

Table C.5 presents recalculated best-fit values from [49], where the triple-Pomeron form factor had been changed for low-t measurements, and normalisations were allowed to float by $\mathcal{O}(10\%)$.

Table C.1: Previous colliders and fixed-target accelerators whose SD cross sections measurements are quoted in this thesis.

Name	Place	Type	$\sqrt{s}$ (GeV)	p_{Lab} (GeV/c)	Radius (km)	Operated (year)
TeVatron	Fermilab	$p+\bar{p}$ coll.	1960		1	2001 – 2011
(Run II) [152]	(IL,USA)					
(Run I) [153]			1800			1987 – 1996
$Sp\bar{p}S$ [154]	CERN	$p+\bar{p}$ coll.	540 – 900		1.1	1981 – 1991
SPS [155]		p, fix.		400		1976 –
ISR	CERN	p+p coll.	23 – 62		0.15	1971 – 1984
NAL [156]	Fermilab	p+$(C_n)H_{2n}$ fix.		130 – 400	1	1972 – 1982
IHEP [157]	Protvino	p+H fix.		70	0.24	1967 –
	(Russia)					

Table C.2: High energy older SD measurements

Experiment (ref.)	Year	$\sqrt{s}$ (GeV)	Type	Range	Value (mb)
UA5 [140]	1982	546	central (1/2-arm) $\lvert\eta\rvert < 5.6$		5.4 ± 1.1
UA5 [158]	1985	900	p not seen	$\xi < 5\%$	7.8 ± 0.5 ± 1.1 (sys)
		200		$\xi < 5\%$	4.8 ± 0.5 ± 0.8 (sys)
UA4 [135]	(1986)	546	RP:$\overline{p}$	$\xi < 5\%$	9.4 ± 0.7
				$\xi < 10\%$	10.0 ± 0.7

Table C.3: Older SD measurements (fixed=fixed-target experiment, $M_X^{-\alpha}$ = powerlaw component in fit)

Experiment (ref.)	Year	$\sqrt{s}$ (GeV)	Type	Range	Value (mb)
CHLM [137]	(1980)	23.5	p meas.	$\xi < 5\%$	6.5 ± 0.2
		23.5		$\xi < 10\%$	7.8 ± 0.4
		27.4		$\xi < 5\%$	6.3 ± 0.2
		27.4		$\xi < 10\%$	7.6 ± 0.4
		32.4		$\xi < 5\%$	6.5 ± 0.2
		32.4		$\xi < 10\%$	7.8 ± 0.5
		35.5		$\xi < 5\%$	7.5 ± 0.5
		35.5		$\xi < 10\%$	8.9 ± 0.6
		38.5		$\xi < 5\%$	7.3 ± 0.4
		38.5		$\xi < 10\%$	8.8 ± 0.5
		44.7		$\xi < 5\%$	7.3 ± 0.3
		44.7		$\xi < 10\%$	8.9 ± 0.4
		53.7		$\xi < 5\%$	7.0 ± 0.3
		53.7		$\xi < 10\%$	8.6 ± 0.4
		62.3		$\xi < 10\%$	9.1 ± 0.4
		62.3		$\xi < 5\%$	7.5 ± 0.3
CHLM [136]	(1975)	38.3		$\xi < 5\%$	6.80 ± 0.29
		35.2		$\xi < 5\%$	7.01 ± 0.28
		32.4		$\xi < 5\%$	6.32 ± 0.22
		30.6		$\xi < 5\%$	6.37 ± 0.15
		26.9		$\xi < 5\%$	6.05 ± 0.22
		23.4		$\xi < 5\%$	6.07 ± 0.17
[159]	(1978)	27.2	fixed	$M_X^{-\alpha}$	3.6 ± 0.4

Table C.4: Older SD measurements (cont.; bubble=bubble chamber, diff=total diffractive)

Experiment (ref.)	Year	$\sqrt{s}$ (GeV)	Type	Range	Value (mb)
[42]	(1974)	16.2	fixed	$\xi < 6\%$	2.41 ± 0.06
		16.2		$\xi < 10\%$	3.20 ± 0.07
		17.9		$\xi < 6\%$	2.46 ± 0.06
		17.9		$\xi < 10\%$	3.14 ± 0.07
		19.4		$\xi < 6\%$	2.44 ± 0.06
		19.4		$\xi < 10\%$	3.10 ± 0.07
[42]	(1974)	23.8	fixed	$\xi < 6\%$	2.44 ± 0.06
		23.8		$\xi < 10\%$	3.11 ± 0.07
		25.6		$\xi < 6\%$	2.55 ± 0.09
		25.6		$\xi < 10\%$	3.03 ± 0.10
		26.7		$\xi < 6\%$	2.63 ± 0.07
		26.7		$\xi < 10\%$	3.04 ± 0.08
		27.4		$\xi < 6\%$	2.53 ± 0.09
		27.4		$\xi < 10\%$	3.09 ± 0.10
Protvino [43]	(1974)	11.5	bubble	$\xi < 7.6\%$	5.1 ± 0.2
NAL [146]	(1973)	13.9	bubble	$\xi < 10\%$	6.6 ± 0.5
		27.6		$\xi < 10\%$	6.8 ± 0.7
		13.9		$M^2 < 10$	4.5 ± 0.4
		27.6		$M^2 < 10$	3.5 ± 0.5
NAL [160]	(1974)	19.7	bubble	rap.gap	5.64 ± 0.30
NAL [145]	1973	13.9	bubble	diff.	5.89 ± 0.80
		19.7			5.69 ± 0.40
		23.9			5.00 ± 0.60
		6.1		SD	4.3 ± 0.6
		7.4		SD	3.4 ± 0.6
		13.9		SD	5.0 ± 0.7
		19.7		SD	5.2 ± 0.6
		23.9		SD	4.3 ± 0.5
		27.6		SD	4.1 ± 0.5
NAL [161]	1973	23.9	diff.	$\xi < 10\%$	5.6 ± 0.8

Table C.5: SD measurements up to 1998 recalculated by [49] (ISR and CHLM values not changed; wide t coverage)

Experiment (ref.)	Year	$\sqrt{s}$ (GeV)	Type	Range	Value (mb)
CDF [118]	(1993)	1800	RP:$\overline{p}$	$\xi < 5\%$	9.12 ± 0.46
		546		$\xi < 5\%$	8.34 ± 0.36
E710 [119]	(1992)	1800	RP:$\overline{p}$	$\xi < 5\%$	8.46 ± 1.77
UA4 [135]	(1986)	546	RP:$\overline{p}$	$\xi < 5\%$	9.4 ± 0.7
CHLM [137]	(1980)	62.3	p meas.	$\xi < 5\%$	7.5 ± 0.3
		53.7		$\xi < 5\%$	7.0 ± 0.3
		44.7		$\xi < 5\%$	7.3 ± 0.3
		38.5		$\xi < 5\%$	7.3 ± 0.4
		35.5		$\xi < 5\%$	7.5 ± 0.5
		32.4		$\xi < 5\%$	6.5 ± 0.2
		27.4		$\xi < 5\%$	6.3 ± 0.2
		23.5		$\xi < 5\%$	6.5 ± 0.2
CHLM [136]	(1975)	38.3		$\xi < 5\%$	6.80 ± 0.29
		35.2		$\xi < 5\%$	7.01 ± 0.28
		32.4		$\xi < 5\%$	6.32 ± 0.22
		30.6		$\xi < 5\%$	6.37 ± 0.15
		26.9		$\xi < 5\%$	6.05 ± 0.22
		23.4		$\xi < 5\%$	6.07 ± 0.17
[159]	(1978)	27.2	fixed	$\xi < 5\%$	5.42 ± 0.09
		23.8		$\xi < 5\%$	5.19 ± 0.08
		19.1		$\xi < 5\%$	4.94 ± 0.08
		17.6		$\xi < 5\%$	4.96 ± 0.08
		16.2		$\xi < 5\%$	4.87 ± 0.08
M6W [139]	(1981)	20	fixed	$\xi < 5\%$	4.46 ± 0.25
		14		$\xi < 5\%$	3.94 ± 0.20

Appendix D

Determining two-proton backgrounds to SD

D.1 Elastic selection

The data sample used had the full "elastic" alignment correction applied to the Roman Pots. This corrected for misalignments in an individual pot position in space and rotation angle with respect to its neighbouring near or far pot, and with respect to the diagonally opposite vertical pot in the other LHC arm. As a result, plotting two-proton events in Segment 3 we find an elastic peak symmetrically distributed around $\sum \theta_y = 0$, with beam divergence smearing the elastic event distribution into a gaussian of width $\sigma_{BD} \approx 3.44 \mu rad$. This is bigger by a factor $\sqrt{2}$ than the measured BD angle $\theta_y^{BD} = (2.47 \pm 0.07)\,\mu$rad quoted in the elastic analysis [56], since this sum combines the BD distribution for two protons, giving a Gaussian width $2 * \sigma_{BD}^2$.

Looking separately at each diagonal, 45_bt*56_tp and 45_tp*56_bt, in Fig.s D.1 – D.2 we see a small difference, with best fits displaced by $\pm 0.4 \mu rad$, and the σ_{BD} being a few percent smaller at 3.2 μrad. This is not caused by bias from setting $x_{IP} = 0$ in the proton reconstruction. Using the old unconstrained inelastic reconstruction module, and on the other hand using the optical function values at $\xi = 0$ to extract the proton parameters directly from the RP tracks (as is done in the elastic analysis, and applying all 7 elastic selection cuts from Table 2 in that paper[1]), I see a similar offset of $\pm 0.4\,\mu$rad. These validation plots for Segment 3 data are shown in Figures D.3 – D.4, using RP tracks and all elastic selection cuts.

[1] Priv.comm. from J. Kaspar : selection cut 7 was actually a 2-dimensional cut on $x_{45}^{IP} - x_{56}^{IP}$ vs θ_x^{IP}

Actually, from the alignment uncertainty we can calculate that we expect to find an offset of this size; looking at the 8 TeV analysis [58] with the same β^* = 90 m optics, a vertical alignment uncertainty of $100\,\mu m$ was quoted, which gives an expected uncertainty in θ_y^{IP}, $\delta\theta_y^{IP} \approx 100\,\mu\text{m}/L_y \approx 10^{-4}\,\text{m}/240\,\text{m} \approx 0.4\,\mu\text{rad}$.

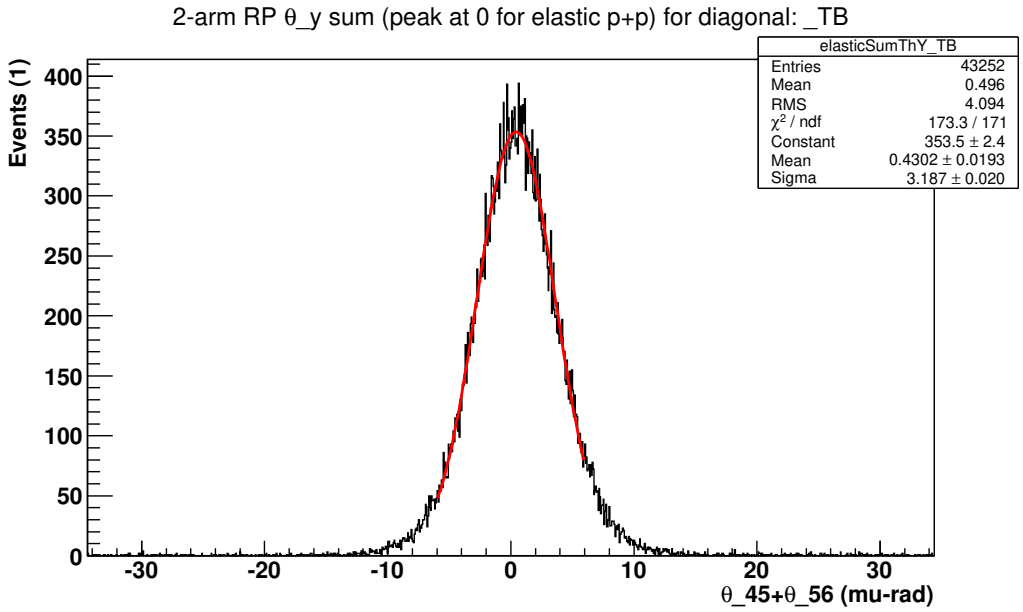

Figure D.1: Diagonal 45_tp*56_bt: Sum of $\theta_y^{IP,4-5}$ and $\theta_y^{IP,5-6}$. Proton variables from the proton reconstruction, with demands for RP 2-arm triggered events with 2p reconstructed and 4 RP-V tracks on the same diagonal only, measured from the big Segment 1b

D.2 Beam Divergence elastic 1p veto

For elastic protons with $\xi = 0$, $y_{RP} \propto \theta_y^{IP}$, so the sum $y_{45}^{RP} + y_{56}^{RP}$ should average zero, unless we are cutting away a part of the acceptance over the BD distribution by being near the edge. Figures D.5 – D.8 show the average bias vs y_{RP}, and the size of $4 * \sigma_{BD} * L_y$, for segment 1b. The event selection is based on RP two-arm triggers with exactly 4 RPs in a diagonal configuration, and two reconstructed protons. We do not use the 5σ selection for elastics based on θ_y^{IP}, since we want to diagnose BD bias on the distribution. The red line is the constant fit, the blue is the visible active edge in y_{RP} for having acceptance for both protons in an elastic pair, and the cyan is offset by $4 * \sigma_{BD}$ from the active edge. For each data segment we look at the inflection point,

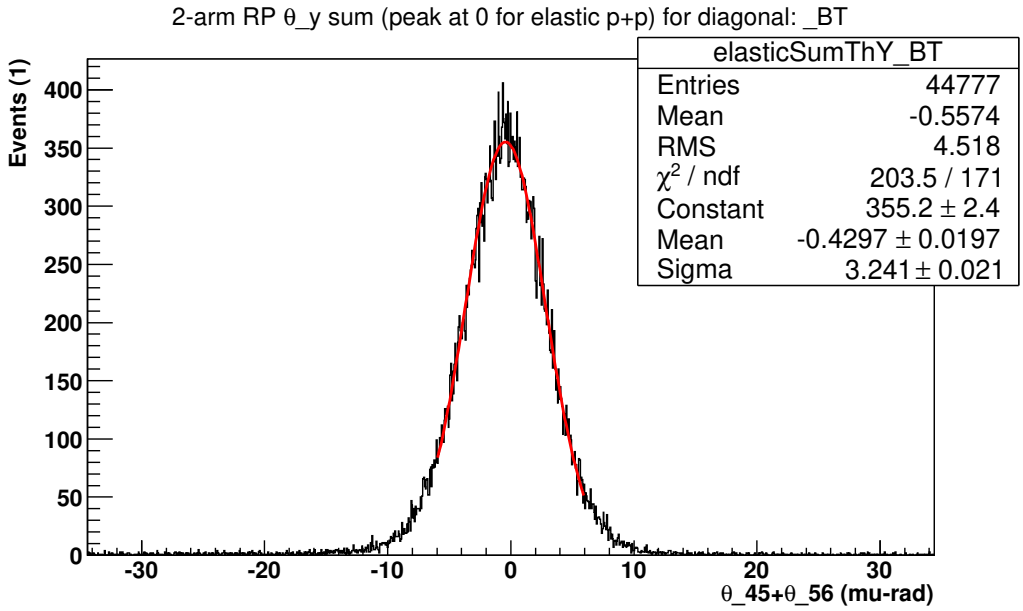

Figure D.2: Diagonal 45_bt*56_tp: Sum of $\theta_y^{IP,4-5}$ and $\theta_y^{IP,5-6}$. Proton variables from the proton reconstruction, with demands for RP 2-arm triggered events with 2p reconstructed and 4 RP-V tracks on the same diagonal only, measured from the big Segment 1b

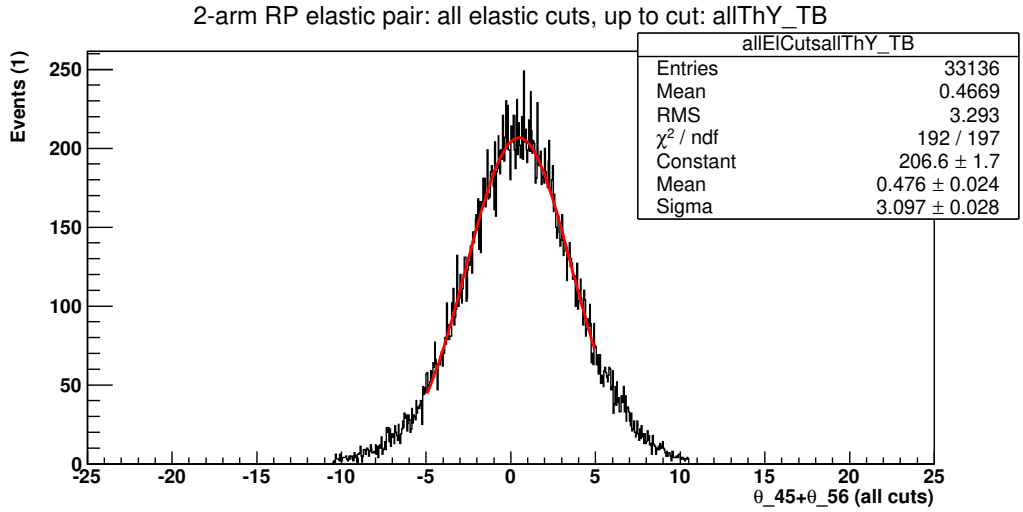

Figure D.3: Diagonal 45_tp*56_bt: Sum of $\theta_y^{IP,4-5}$ and $\theta_y^{IP,5-6}$. RP 2-arm triggered events with 4 RP-V tracks on the same diagonal only, all proton parameters reconstructed from RP tracks, all 7 cuts applied, measured from Segment 1b, 1 500 000 events

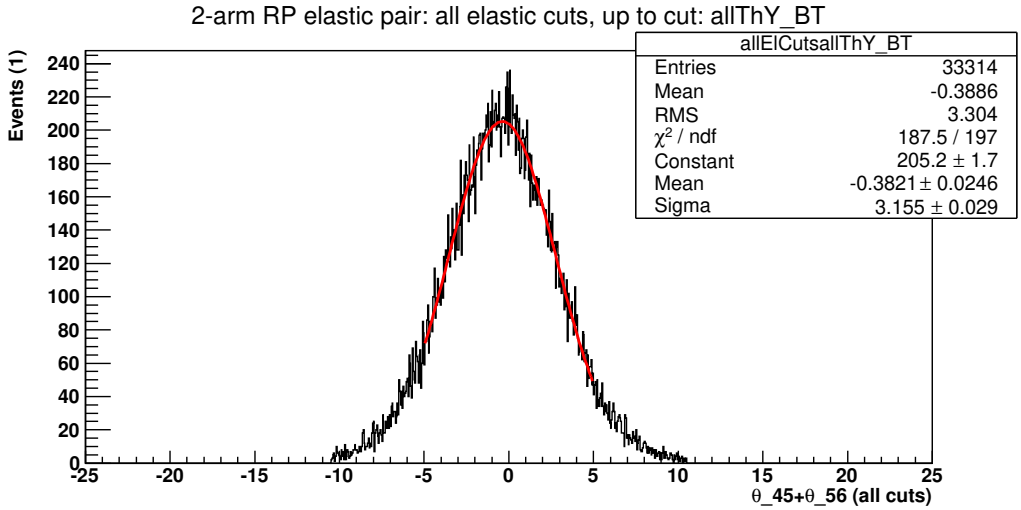

Figure D.4: Diagonal 45_bt*56_tp: Sum of $\theta_y^{IP,4-5}$ and $\theta_y^{IP,5-6}$. RP 2-arm triggered events with 4 RP-V tracks on the same diagonal only, all proton parameters reconstructed from RP tracks, all 7 cuts applied, measured from Segment 1b, 1 500 000 events

where we visibly start losing some elastics, for each RP, and then select a conservative $|y_{RP}| >$ inflection $+ 0.5$ mm requirement. This gives a selection cut of 8 mm, 7.4 mm, and 6.6 mm for data segments 1b, 2 and 3, respectively. Figures D.9 – D.16 show the BD loss bias vs y_{RP}, for segments 2 and 3.

D.3 Nonelastic 2p $t_1 \to 0$ estimation

The nonelastic two-proton background can be extrapolated to below the acceptance threshold in θ_y and therefore in t for one of the protons, by making an exponential fit of the t-spectrum for each pot and finding the t-bin where the real data starts falling off, then estimating the missing cross section of this small t-range. Looking at the Figures D.17 – D.20 it looks like there is acceptance still at $|t| = 0.01$ GeV^2, so the expected Central Diffraction background in SD is quite low, of the order $\sigma_{1p,CD} \approx t_{min} * d\sigma/dt|_{max}$.

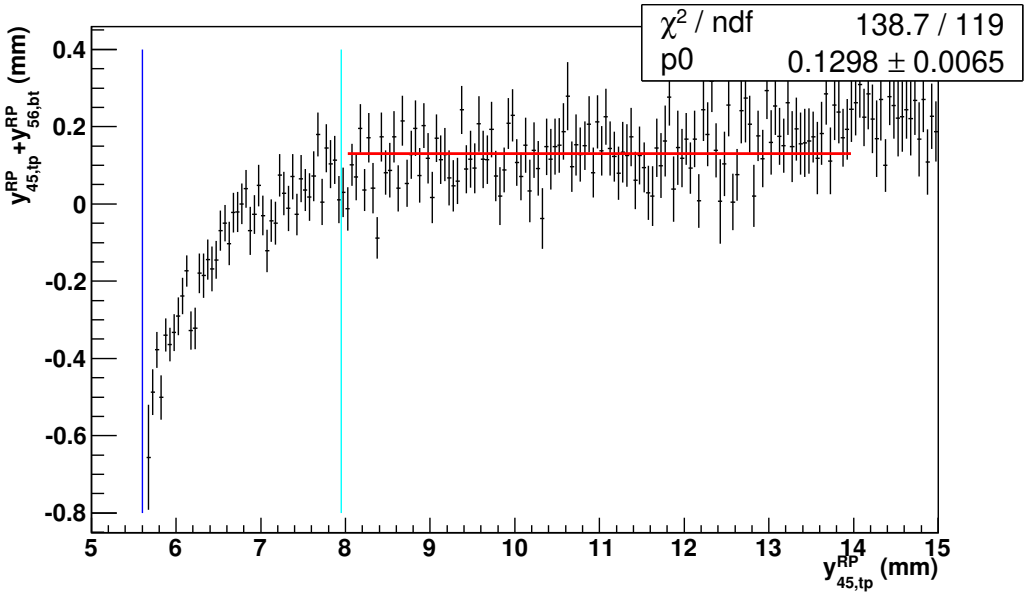

Figure D.5: Diagonal 45_tp*56_bt: For RP 2-arm triggered events with 4 RPs in a diagonal configuration, show elastic loss due to BD biasing the sum of $y^{RP}_{45} + y^{RP}_{56}$ in pot 45_tp. Data sample used is 800 000 real data events in Segment 1b. Blue line active edge, cyan line 4σ from edge.

D.4 Two-proton background in 1 arm: top and bottom tracks

Our demand for exactly two tracks in RP-V gives an inefficiency from missing events with a PU proton in the same arm giving multiple tracks in both top and bottom RPs. This was checked by looking for SD candidate events at the trigger bit level, with the T2 trigger on and the RP-V 2-arm trigger veto bit off, and tabulating the fraction with more than two RP tracks. Here we demanded tracks in both the near and far RP for the RP pairs quoted in Tables D.1 – D.2. The total inefficiency found, 1.5% – 7.4%, is highest for pot 56_bt, since there was so much BH in 56_tp.

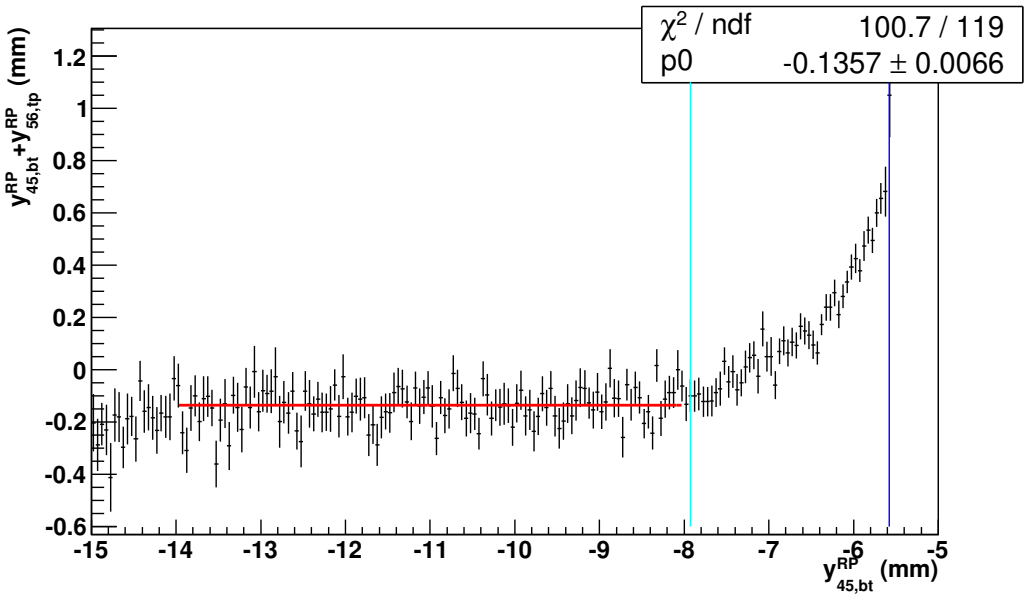

Figure D.6: Diagonal 45_bt*56_tp: RP 2-arm triggered events with 4 RPs in a diagonal configuration, show elastic loss due to BD biasing the sum of $y_{45}^{RP} + y_{56}^{RP}$ in pot 45_bt. Data sample used is 800 000 real data events in Segment 1b. Blue line active edge, cyan line 4σ from edge.

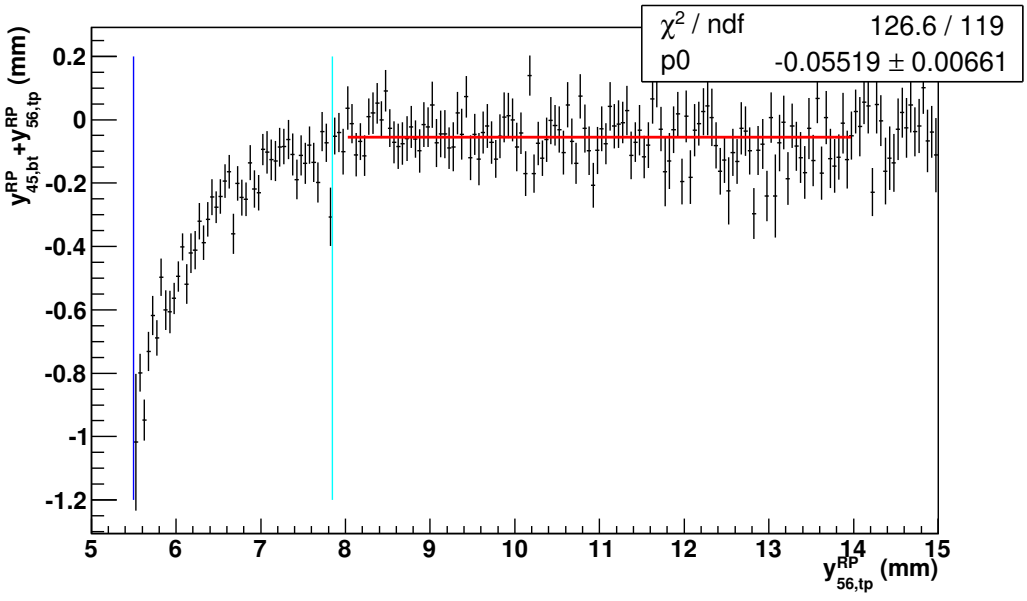

Figure D.7: Diagonal 45_bt*56_tp: RP 2-arm triggered events with 4 RPs in a diagonal configuration, show elastic loss due to BD biasing the sum of $y_{45}^{RP} + y_{56}^{RP}$ in pot 56_tp. Data sample used is 800 000 real data events in Segment 1b. Blue line active edge, cyan line 4σ from edge.

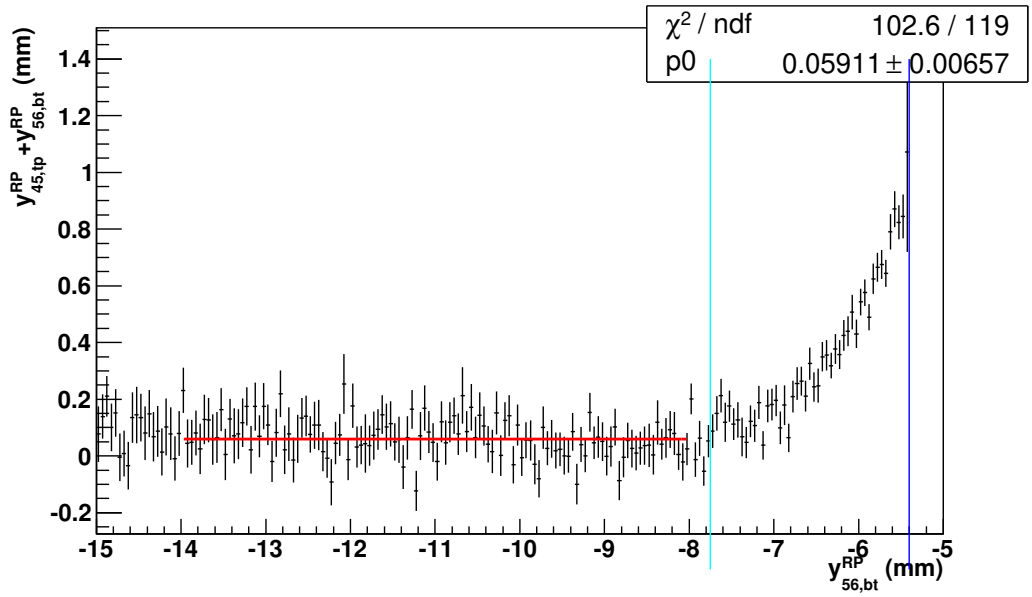

Figure D.8: Diagonal 45_tp*56_bt: RP 2-arm triggered events with 4 RPs in a diagonal configuration, show elastic loss due to BD biasing the sum of $y_{45}^{RP} + y_{56}^{RP}$ in pot 56_tp. Data sample used is 800 000 real data events in Segment 1b. Blue line active edge, cyan line 4σ from edge.

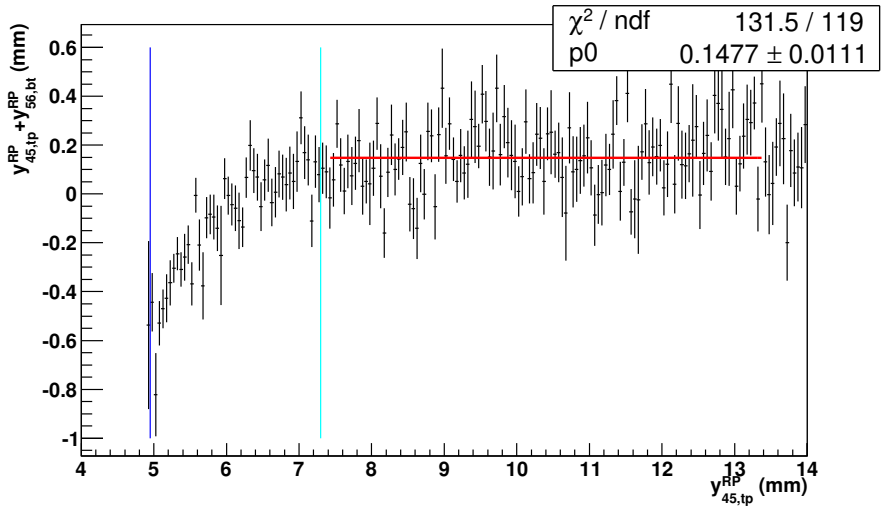

Figure D.9: Diagonal 45_tp*56_bt: RP 2-arm triggered events with 4 RPs in a diagonal configuration, show elastic loss due to BD biasing the sum of $y_{45}^{RP} + y_{56}^{RP}$ in pot 45_tp – real data, Segment 2, 281 000 events. Blue line active edge, cyan line 4σ from edge.

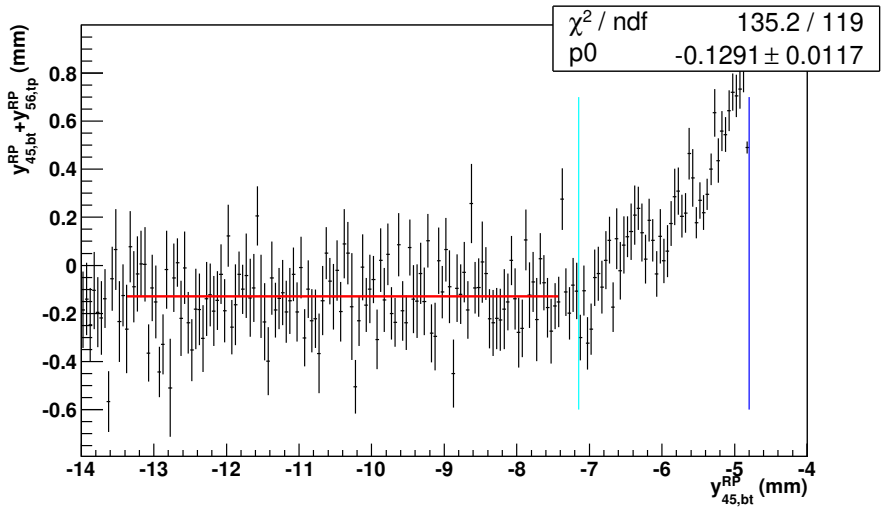

Figure D.10: Diagonal 45_bt*56_tp: RP 2-arm triggered events with 4 RPs in a diagonal configuration, show elastic loss due to BD biasing the sum of $y_{45}^{RP} + y_{56}^{RP}$ in pot 45_bt – real data, Segment 2, 281 000 events. Blue line active edge, cyan line 4σ from edge.

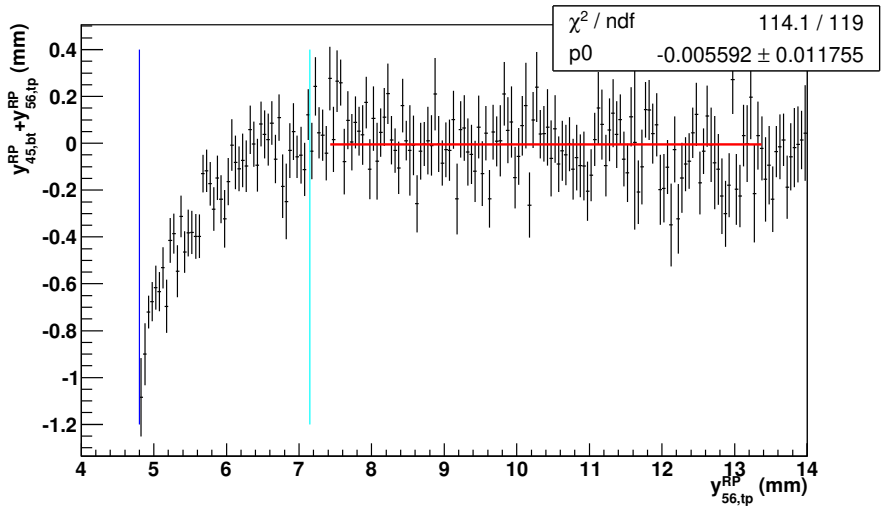

Figure D.11: Diagonal 45_bt*56_tp: RP 2-arm triggered events with 4 RPs in a diagonal configuration, show elastic loss due to BD biasing the sum of $y_{45}^{RP} + y_{56}^{RP}$ in pot 56_tp – real data, Segment 2, 281 000 events. Blue line active edge, cyan line 4σ from edge.

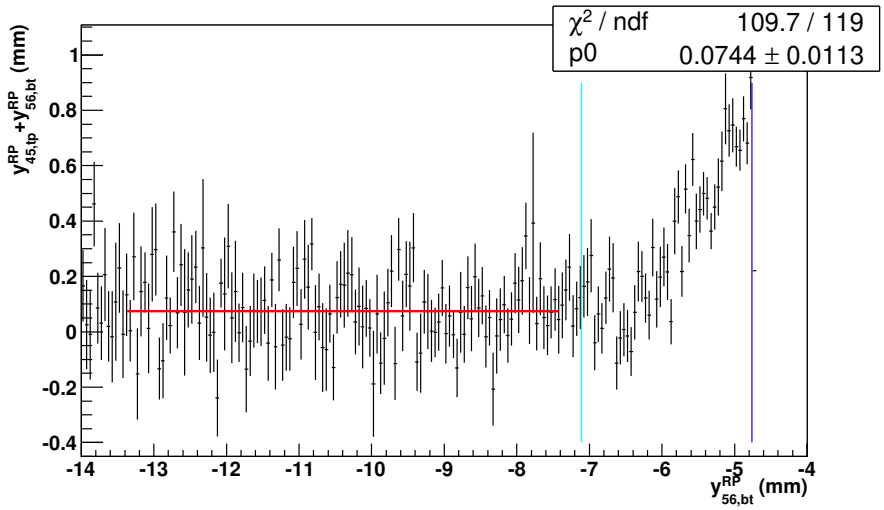

Figure D.12: Diagonal 45_tp*56_bt: RP 2-arm triggered events with 4 RPs in a diagonal configuration, show elastic loss due to BD biasing the sum of $y_{45}^{RP} + y_{56}^{RP}$ in pot 56_bt – real data, Segment 2, 281 000 events. Blue line active edge, cyan line 4σ from edge.

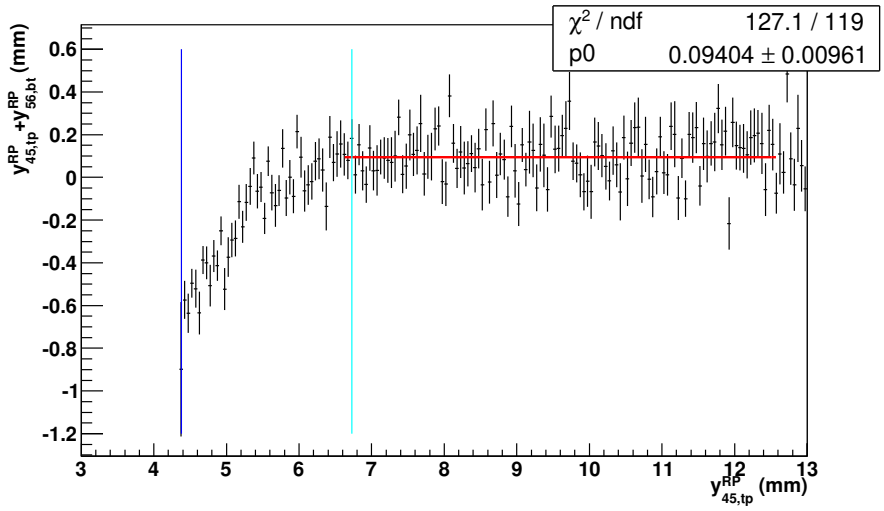

Figure D.13: Diagonal 45_tp*56_bt: RP 2-arm triggered events with 4 RPs in a diagonal configuration, show elastic loss due to BD biasing the sum of $y_{45}^{RP} + y_{56}^{RP}$ in pot 45_tp – real data, Segment 3, 422 000 events. Blue line active edge, cyan line 4σ from edge.

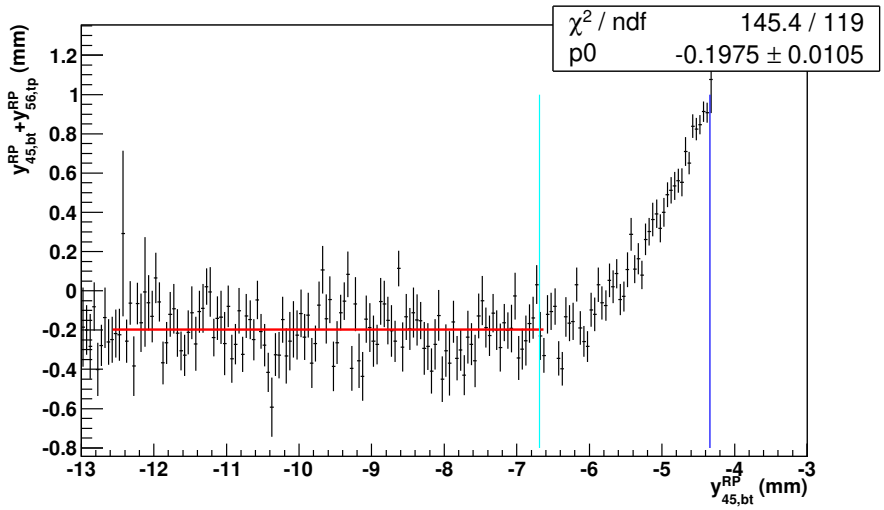

Figure D.14: Diagonal 45_bt*56_tp: RP 2-arm triggered events with 4 RPs in a diagonal configuration, show elastic loss due to BD biasing the sum of $y_{45}^{RP} + y_{56}^{RP}$ in pot 45_bt – real data, Segment 3, 422 000 events. Blue line active edge, cyan line 4σ from edge.

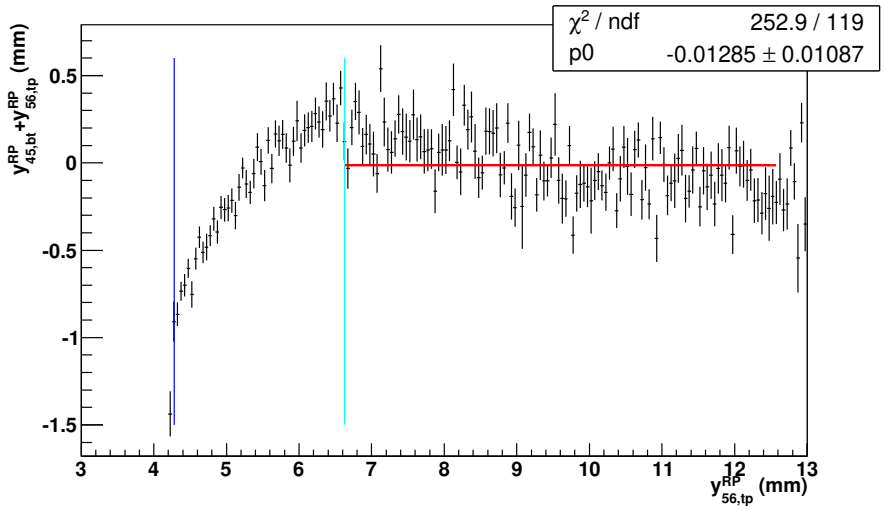

Figure D.15: Diagonal 45_bt*56_tp: RP 2-arm triggered events with 4 RPs in a diagonal configuration, show elastic loss due to BD biasing the sum of $y_{45}^{RP} + y_{56}^{RP}$ in pot 56_tp – real data, Segment 3, 422 000 events. Blue line active edge, cyan line 4σ from edge.

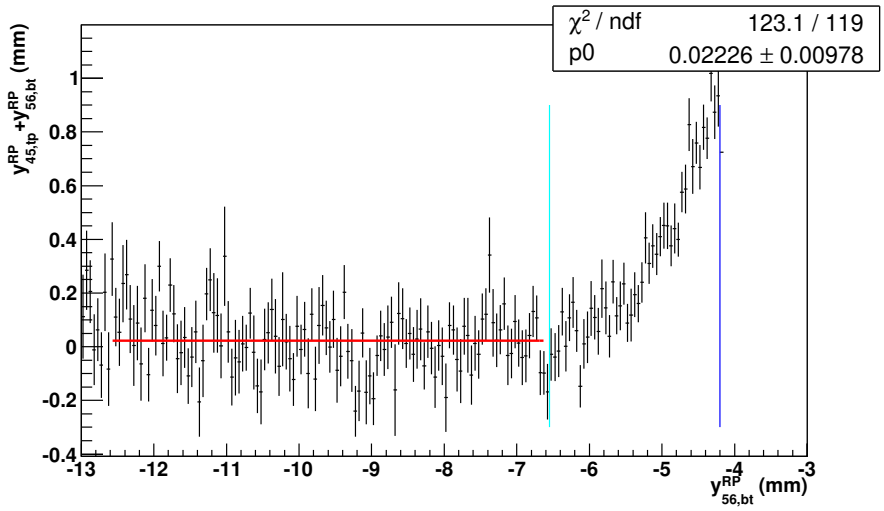

Figure D.16: Diagonal 45_tp*56_bt: RP 2-arm triggered events with 4 RPs in a diagonal configuration, show elastic loss due to BD biasing the sum of $y_{45}^{RP} + y_{56}^{RP}$ in pot 56_bt – real data, Segment 3, 422 000 events. Blue line active edge, cyan line 4σ from edge.

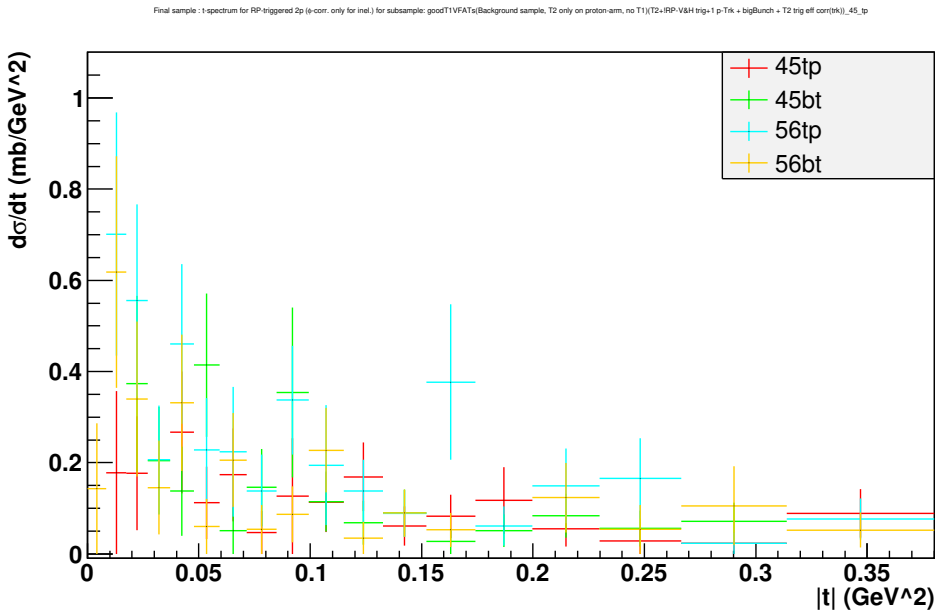

Figure D.17: RP 2-arm triggered events with 2p reconstructed and elastics vetoed, named RP t-spectrum with 1T2,0T1 topology compatible with the other proton

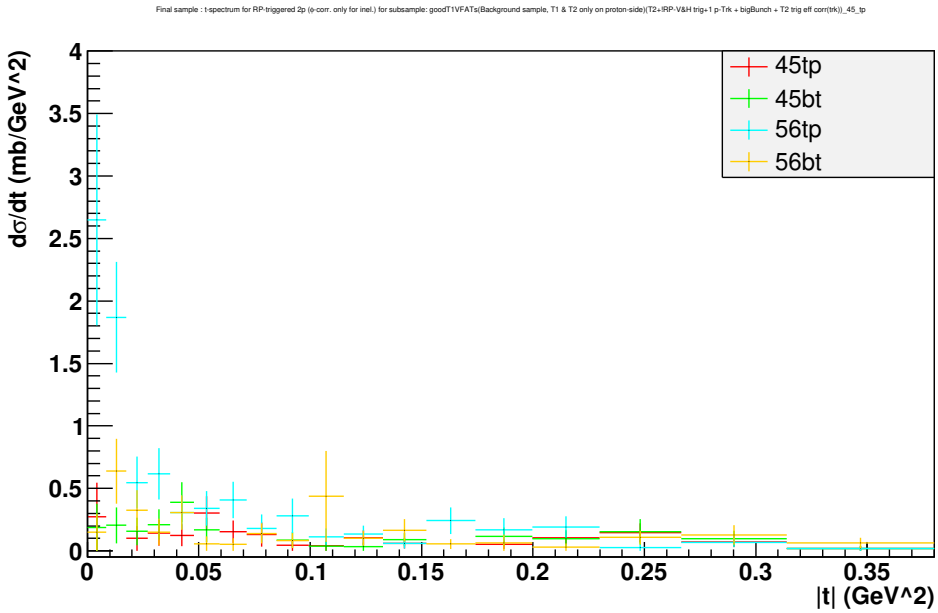

Figure D.18: RP 2-arm triggered events with 2p reconstructed and elastics vetoed, named RP t-spectrum with 1T2,1T1 topology compatible with the other proton

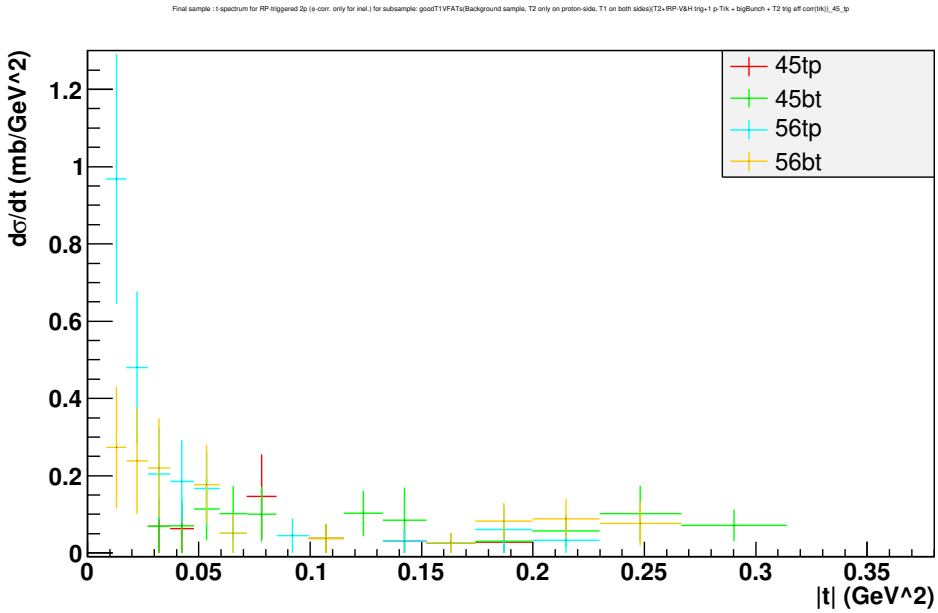

Figure D.19: RP 2-arm triggered events with 2p reconstructed and elastics vetoed, named RP t-spectrum with 1T2,2T1 topology compatible with the other proton

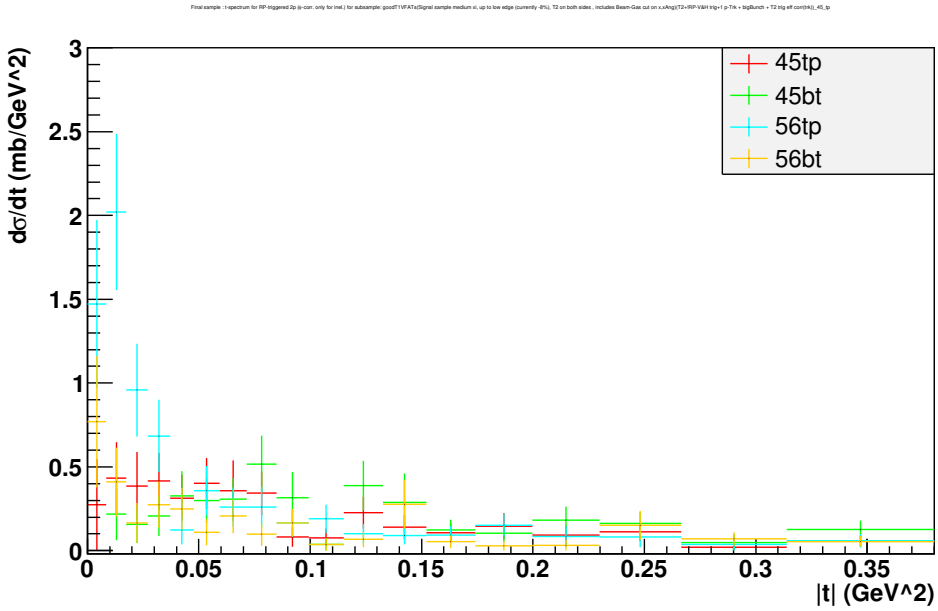

Figure D.20: RP 2-arm triggered events with 2p reconstructed and elastics vetoed, named RP t-spectrum with 2T2 topology compatible with the other proton

Table D.1: Number of events with extra RP-V tracks in SD-like trigger conditions: T2=on and RP220V 2-arm=off. Real data Segment 3, constrained ($x_{IP} = 0$) proton reconstruction. In case of RP-V 1-arm, we do not count events with 2 reconstructed protons, from horizontal RP on the other side. In RP-V 2-arm, el. means two protons on the same diagonal, looking like an elastic pair due to the inefficiency of the 2-arm trigger

RP-V 1-arm:					
Num. tracks	Num. RECO-p	Events in 45tp	45bt	56tp	56bt
2	0	1	1	0	2
2	1	4559	5198	12514	5919
2	2				
3	0	18	15	51	59
3	1	none			
3	2	not counted			
4	0	62	62	415	415
4	1	1	1	1	1
4	2	not counted			
RP-V 2-arm tracks:					
4	2 el.	0	1	1	0
5	0	1	1	0	0
5	1-2	none			
6-8	0-2	none			

Table D.2: Same as Table D.1, but expressed in percent. Real data segment 3. Poisson-distributed uncertainty assumed.

Number tracks RP-V 1-arm	Num. RECO-p	45tp (%)	45bt (%)	56tp (%)	56bt (%)
2	0	0.02±0.02	0.02±0.02	0	0.03±0.02
2	1	98.21±1.45	98.47±1.37	96.40±0.86	92.54±1.20
3	0	0.39±0.09	0.28±0.07	0.39±0.06	0.92±0.12
3	1	none			
4	0	1.34±0.17	1.17±0.15	3.20±0.16	6.49±0.32
4	1	0.02±0.02	0.02±0.02	0.01±0.01	0.02±0.02
RP-V 2-arm					
4 elast.	2	0	0.02±0.02	0.01±0.01	0
5	0	0.02±0.02	0.02±0.02	0	0
5	1	none			
> 5	$0 \ldots 2$	none			

Table D.3: Number of events with extra RP-V tracks in SD-like trigger conditions: T2=on and RP220V 2-arm=off. Real data Segment 2, constrained ($x_{IP} = 0$) proton reconstruction.

RP-V 1-arm:					
Num. tracks	Num. RECO-p	Events in 45tp	45bt	56tp	56bt
2	0	0	0	1	1
2	1	3225	3375	8342	4067
3	0	2	12	44	31
3	1	none			
4	0	17	17	226	226
4	1	none			

Table D.4: Same as Table D.3, but expressed in percent. Real data segment 2. Poisson-distributed uncertainty assumed.

Number tracks RP-V 1-arm	Num. RECO-p	45tp (%)	45bt (%)	56tp (%)	56bt (%)
2	0	0	0	0.01±0.01	0.02±0.02
2	1	99.41±1.75	99.15±1.71	96.85±1.06	94.03±1.47
3	0	0.06±0.04	0.35±0.10	0.51±0.08	0.72±0.13
3	1	none			
4	0	0.52±0.13	0.50±0.12	2.62±0.17	5.23±0.35
4	1	none			

Table D.5: Number of events with extra RP-V tracks in SD-like trigger conditions: T2=on and RP220V 2-arm=off. Real data 1 600 000 events from Segment 1b, constrained ($x_{IP} = 0$) proton reconstruction.

RP-V 1-arm:					
Num. tracks	Num. RECO-p	Events in 45tp	45bt	56tp	56bt
2	0	3	6	6	5
2	1	18385	19018	38795	22101
3	0	63	66	126	135
3	1	0	0	1	0
4	0	98	98	781	781
4	1	0	0	1	1
RP-V 2-arm:					
4 elast.	2	0	1	1	0

Table D.6: Same as Table D.5, but expressed in percent. Real data 1 600 000 events from segment 1b. Poisson-distributed uncertainty assumed.

Number tracks RP-V 1-arm	Num. RECO-p	45tp (%)	45bt (%)	56tp (%)	56bt (%)
2	0	0.02±0.01	0.03±0.01	0.02±0.01	0.02±0.01
2	1	99.12±0.73	99.11±0.72	97.69±0.50	96.00±0.65
3	0	0.34±0.04	0.34±0.04	0.32±0.03	0.59±0.05
3	1	0	0	0.00±0.00	0
4	0	0.53±0.05	0.51±0.05	1.97±0.07	3.39±0.12
4	1	0	0	0.00±0.00	0.00±0.00
RP-V 2-arm					
4 elast.	2	0	0.01±0.01	0.00±0.00	0

Appendix E

Single-proton backgrounds to SD

E.1 Beam Halo

The RP with the largest beam halo background is 56_tp, a figure of which was shown in Chapter 6.2.2. Here, the other three RPs are shown in Figures E.1 – E.3. This data was taken with a 1-arm RP trigger, and the figures show events in the very low mass 0T2 SD-like class, with only one proton and no T2 tracks. It is dominated by BH; the distribution away from the BH line may be true low-mass SD not visible in the main data sample, where we trigger on T2 only for single proton events. The two variables shown in these plots are x_{nr}^{RP} and θ_x^{RP}.

$$A_1 * \theta_x^{RP} + (x_{nr}^{RP} - C_1) = 0 \tag{E.1}$$

Here A_1 is the slope and C_1 an offset. The BH line was fitted from a profile histogram of the same two variables with all data points further than 10 σ from the line excluded.

The fit results are shown in Table E.1.

Table E.1: Fitted BH line constants for each RP.

RP	Slope (m/rad)	Offset (mm)
45_tp	39.02	0.135
45_bt	38.92	0.024
56_tp	37.90	0.0005
56_bt	39.73	0.064

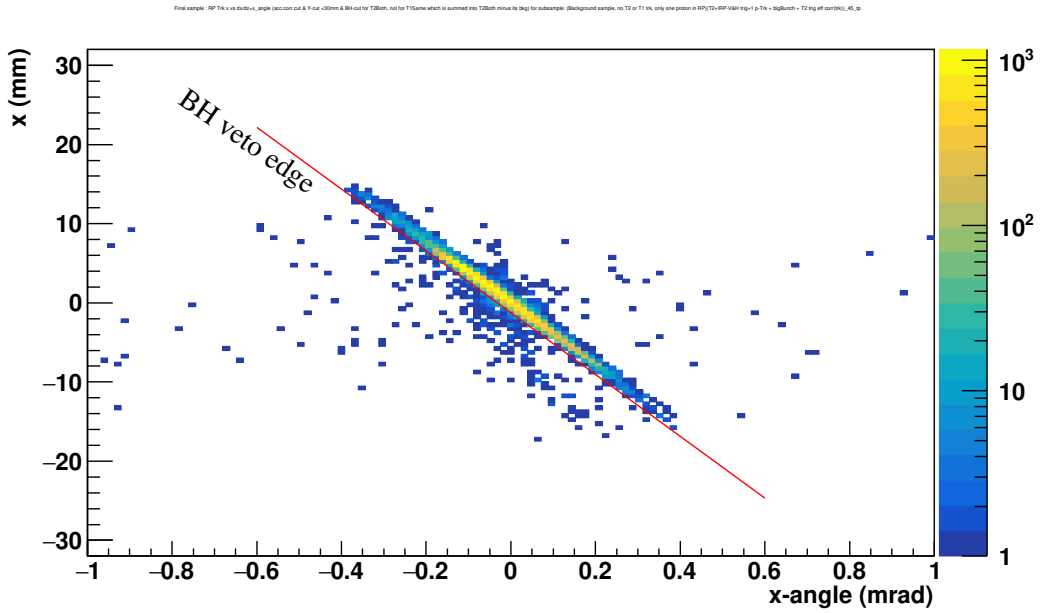

Figure E.1: Beam Halo line in RP-OR run, for pot **45_tp**, with BH veto line shown in red.

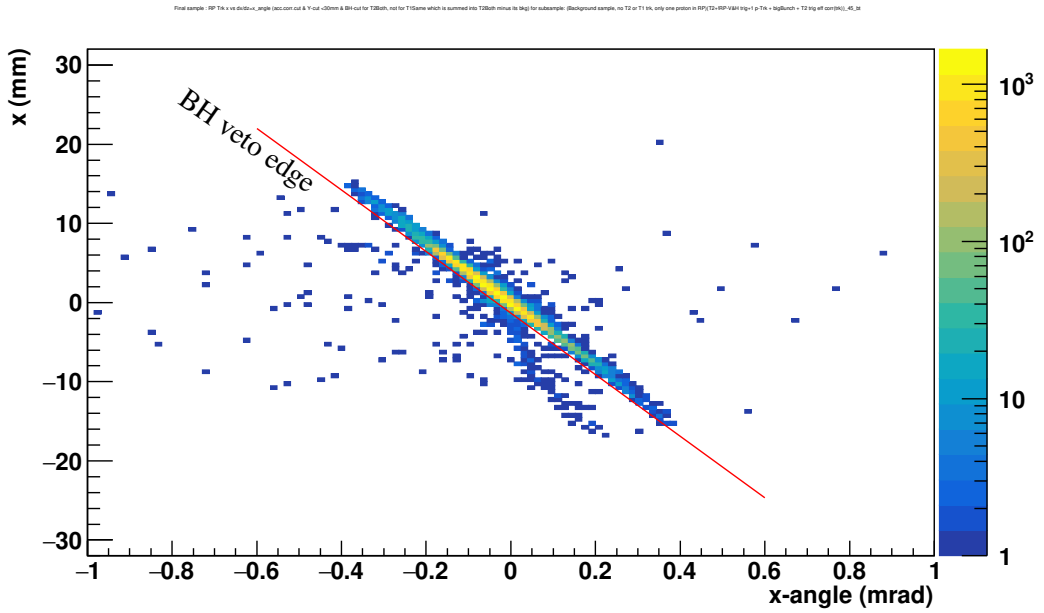

Figure E.2: Beam Halo line in RP-OR run, for pot **45_bt**, with BH veto line shown in red.

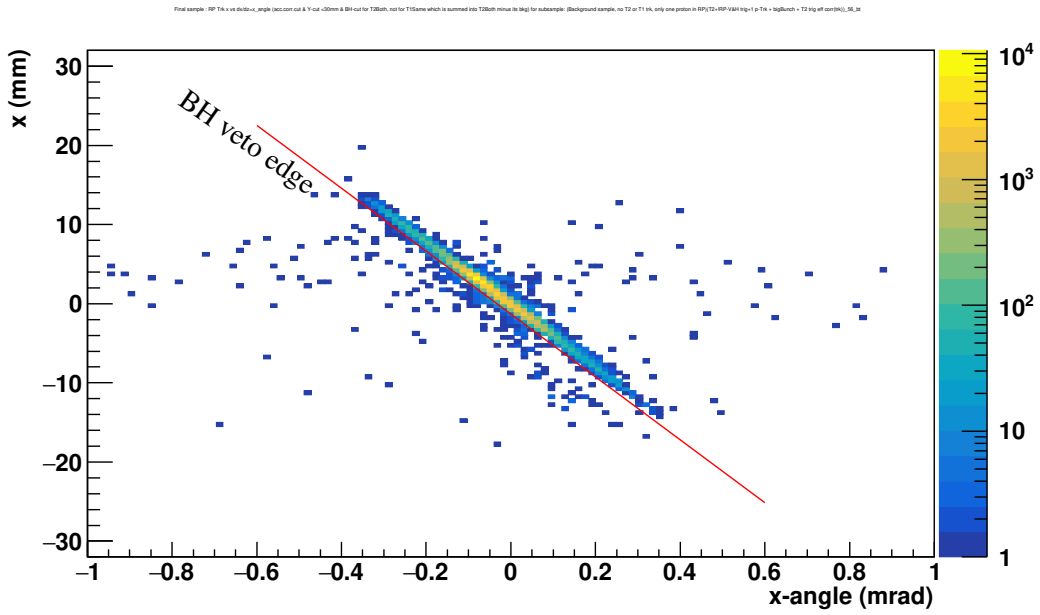

Figure E.3: Beam Halo line in RP-OR run, for pot **56_bt**, with BH veto line shown in red.

Appendix F

Real data differential SD cross sections vs. $|t|$, all RPs

All figures for the measured differential cross section vs $|t|$. The $|t|$-spectra were unfolded with either Pythia 8 or EPOS. The figures were not corrected for class migration with the simple matrix-multiplication method described in Chapter 6.4.5.

F.1 Pythia 8 Unfolding

The following Figures F.1 – F.12 were unfolded with a Pythia 8 SD sample of 210 000 events, with mixed-in real PU from BX events, and estimated backgrounds subtracted. Closure corrections not applied, since these $|t|$-spectra were used to make $|t|$-extrapolation corrections for both unfolded and class migration-corrected integral cross section histograms.

F.2 EPOS unfolding

The following figures F.13 – F.28 were unfolded with an inclusive EPOS sample with 1 000 000 events total, mixed with real PU from BX events, and estimated backgrounds subtracted.

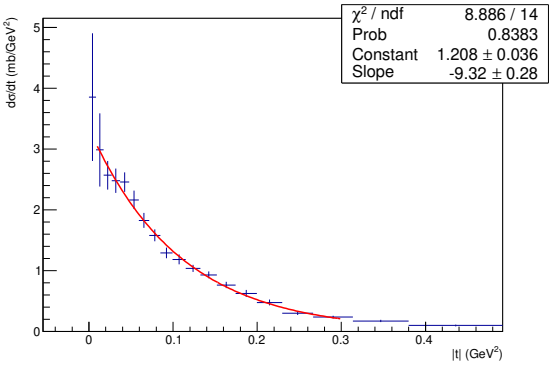

Figure F.1: The fully corrected differential cross section as a function of $|t|$ for the SD class 1T2-0T1 in RP 45_bt using 1 439 000 events from real data segment 1b. Unfolded using a Pythia 8 SD sample of 210 000 events. For the exponential fit, see Section 7.3

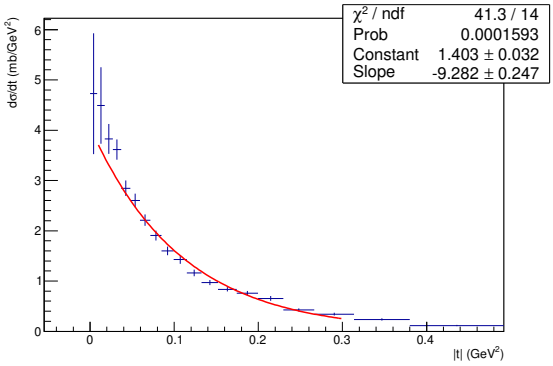

Figure F.2: The fully corrected differential cross section as a function of $|t|$ for the SD class 1T2-0T1 in RP 56_tp using 1 439 000 events from real data segment 1b. Unfolded using a Pythia 8 SD sample of 210 000 events. For the exponential fit, see Section 7.3

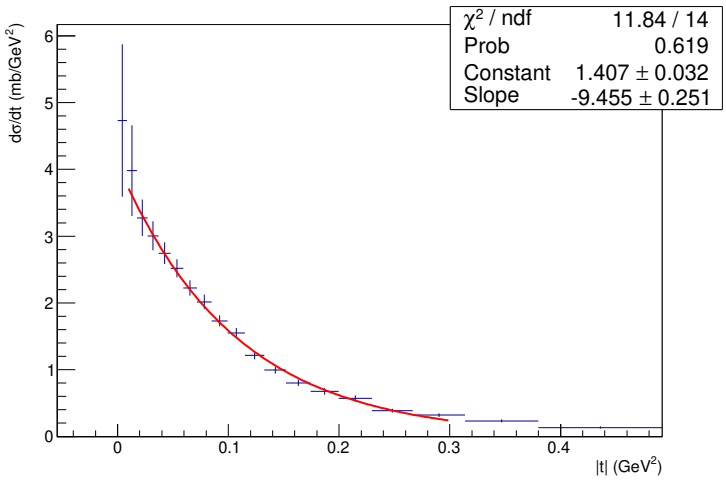

Figure F.3: The fully corrected differential cross section as a function of $|t|$ for the SD class 1T2-0T1 in RP 56_bt using 1 439 000 events from real data segment 1b. Unfolded using a Pythia 8 SD sample of 210 000 events. For the exponential fit, see Section 7.3

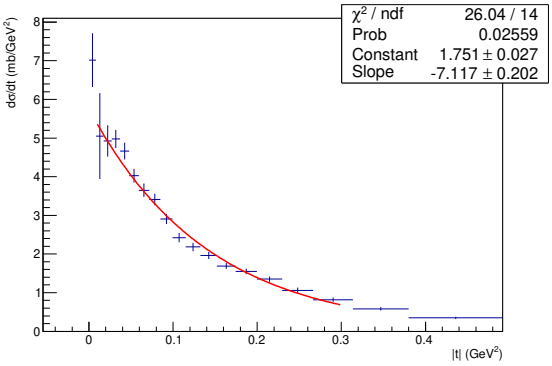

Figure F.4: The fully corrected differential cross section as a function of $|t|$ for the SD class 1T2-1T1 in RP 45_bt using 1 439 000 events from real data segment 1b. Unfolded using a Pythia 8 SD sample of 210 000 events. For the exponential fit, see Section 7.3

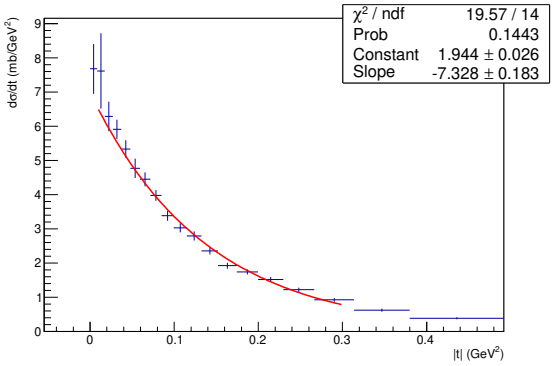

Figure F.5: The fully corrected differential cross section as a function of $|t|$ for the SD class 1T2-1T1 in RP 56_tp using 1 439 000 events from real data segment 1b. Unfolded using a Pythia 8 SD sample of 210 000 events. For the exponential fit, see Section 7.3

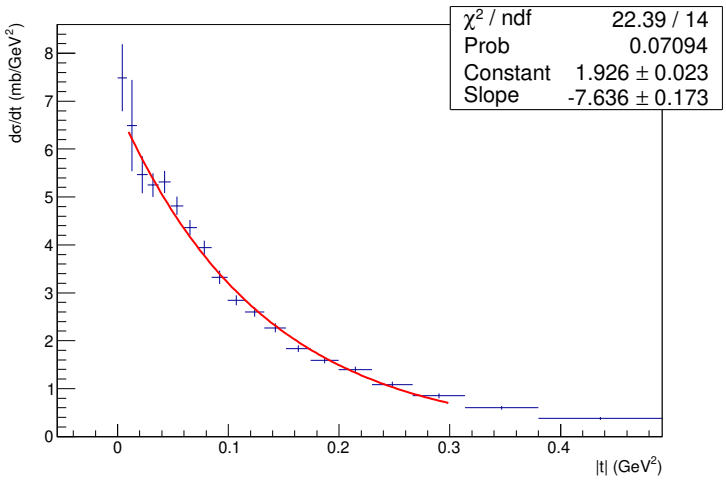

Figure F.6: The fully corrected differential cross section as a function of $|t|$ for the SD class 1T2-1T1 in RP 56_bt using 1 439 000 events from real data segment 1b. Unfolded using a Pythia 8 SD sample of 210 000 events. For the exponential fit, see Section 7.3

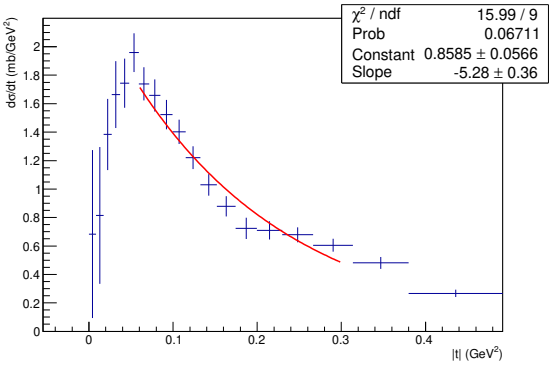

Figure F.7: The fully corrected differential cross section as a function of $|t|$ for the SD class 1T2-2T1 in RP 45_bt using 1 439 000 events from real data segment 1b. Unfolded using a Pythia 8 SD sample of 210 000 events. For the exponential fit, see Section 7.3

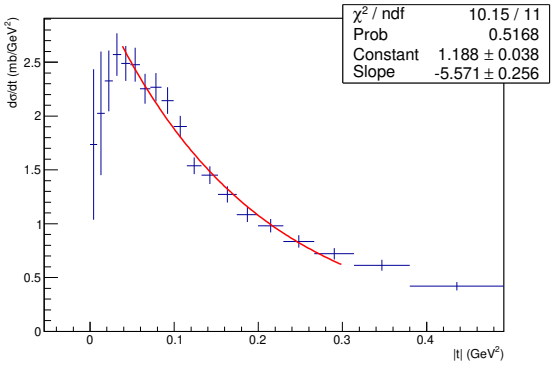

Figure F.8: The fully corrected differential cross section as a function of $|t|$ for the SD class 1T2-2T1 in RP 56_tp using 1 439 000 events from real data segment 1b. Unfolded using a Pythia 8 SD sample of 210 000 events. For the exponential fit, see Section 7.3

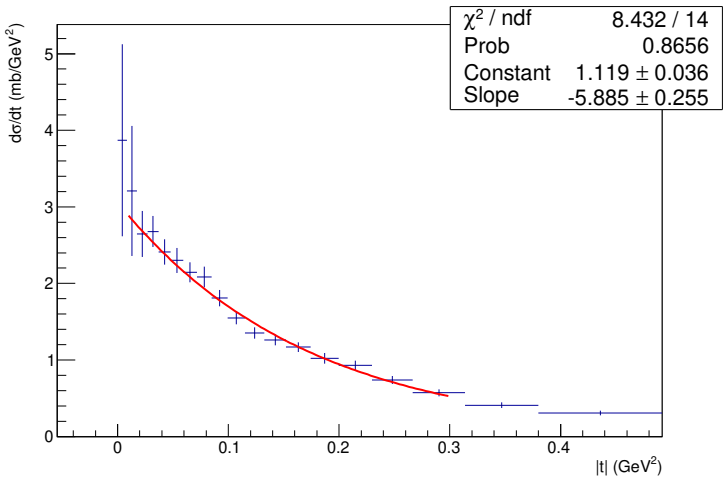

Figure F.9: The fully corrected differential cross section as a function of $|t|$ for the SD class 1T2-2T1 in RP 56_bt using 1 439 000 events from real data segment 1b. Unfolded using a Pythia 8 SD sample of 210 000 events. For the exponential fit, see Section 7.3

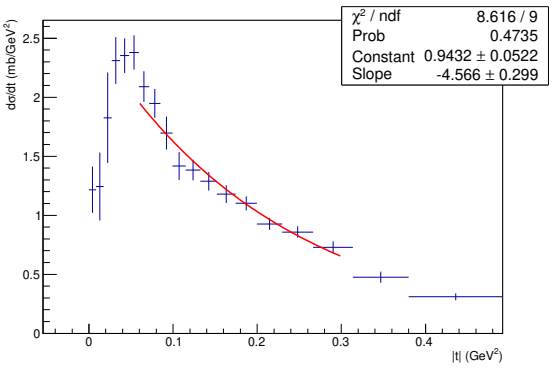

Figure F.10: The acceptance-corrected differential cross section as a function of $|t|$ for the SD class 2T2 in RP 45_bt including BH veto applied for this class only. Acceptance-corrected, background-subtracted real data. Data sample used is 1 439 000 events from real data segment 1b. Unfolded using a Pythia 8 SD sample of 210 000 events. For the exponential fit, see Section 7.3

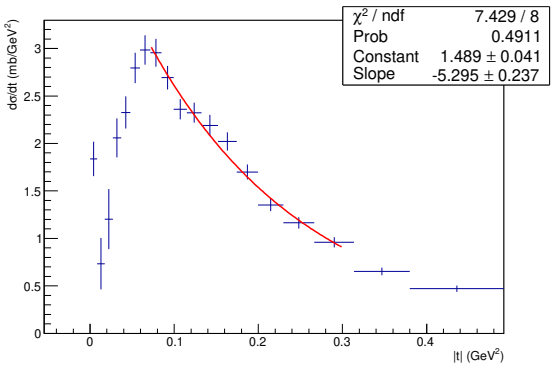

Figure F.11: The acceptance-corrected differential cross section as a function of $|t|$ for the SD class 2T2 in RP 56_tp including BH veto applied for this class only. Acceptance-corrected, background-subtracted real data. Data sample used is 1 439 000 events from real data segment 1b. Unfolded using a Pythia 8 SD sample of 210 000 events. For the exponential fit, see Section 7.3

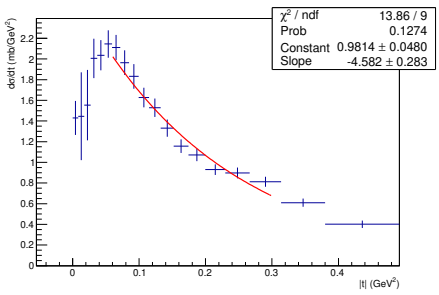

Figure F.12: The fully corrected differential cross section as a function of $|t|$ for the SD class 2T2 in RP 56_bt including BH veto applied for this class only. Acceptance-corrected, background-subtracted real data. Data sample used is 1 439 000 events from real data segment 1b. Unfolded using a Pythia 8 SD sample of 210 000 events.

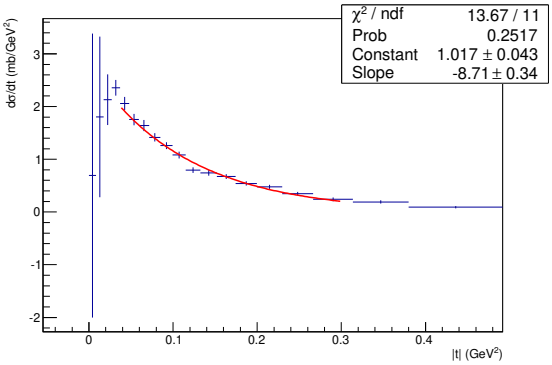

Figure F.13: The fully corrected differential cross section as a function of $|t|$ for the SD class 1T2-0T1 in RP 45_tp, using 1 439 000 events from data segment 1b, after EPOS unfolding correction. For the exponential fit, see Section 7.3

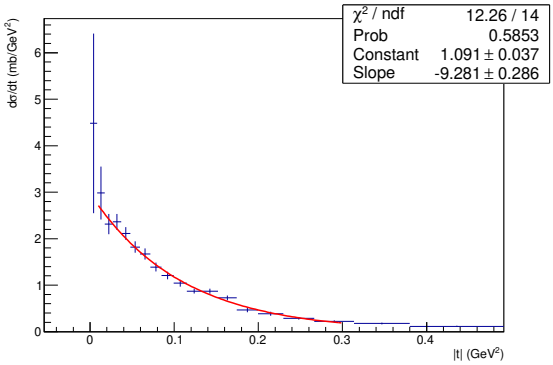

Figure F.14: The fully corrected differential cross section as a function of $|t|$ for the SD class 1T2-0T1 in RP 45_bt, using 1 439 000 events from data segment 1b, after EPOS unfolding correction. For the exponential fit, see Section 7.3

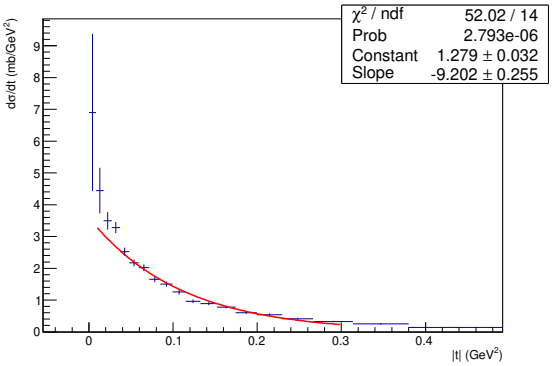

Figure F.15: The fully corrected differential cross section as a function of $|t|$ for the SD class 1T2-0T1 in RP 56_tp, using 1 439 000 events from data segment 1b, after EPOS unfolding correction. For the exponential fit, see Section 7.3

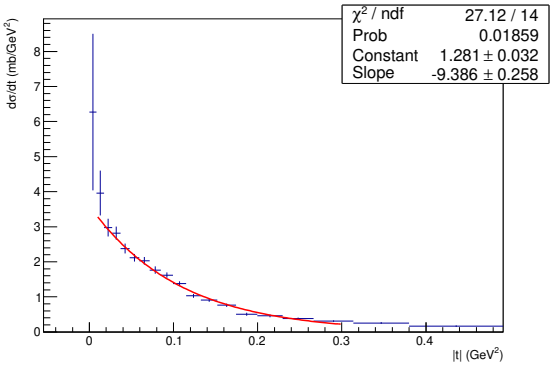

Figure F.16: The fully corrected differential cross section as a function of $|t|$ for the SD class 1T2-0T1 in RP 56_bt, using 1 439 000 events from data segment 1b, after EPOS unfolding correction. For the exponential fit, see Section 7.3

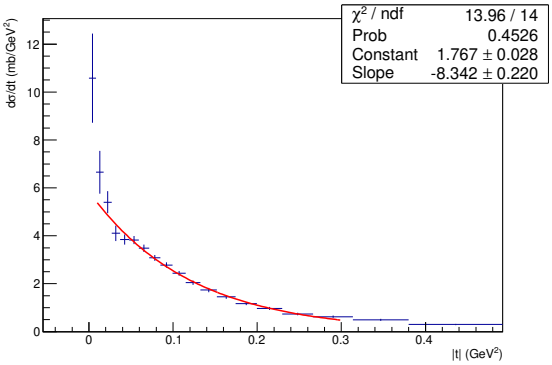

Figure F.17: The fully corrected differential cross section as a function of $|t|$ for the SD class 1T2-1T1 in RP 45_tp, using 1 439 000 events from data segment 1b, after EPOS unfolding correction. For the exponential fit, see Section 7.3

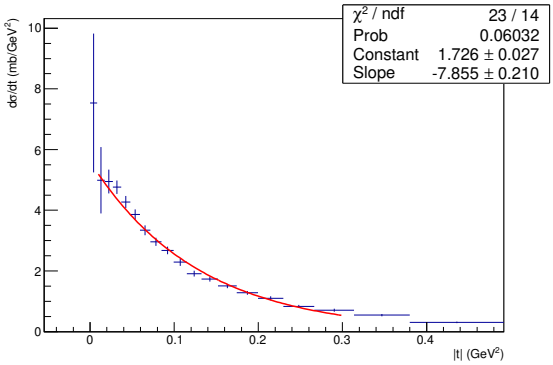

Figure F.18: The fully corrected differential cross section as a function of $|t|$ for the SD class 1T2-1T1 in RP 45_bt, using 1 439 000 events from data segment 1b, after EPOS unfolding correction. For the exponential fit, see Section 7.3

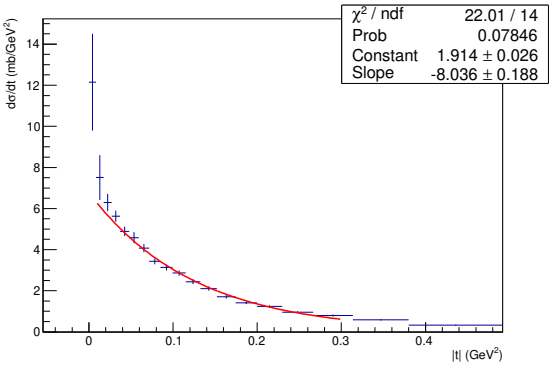

Figure F.19: The fully corrected differential cross section as a function of $|t|$ for the SD class 1T2-1T1 in RP 56_tp, using 1 439 000 events from data segment 1b, after EPOS unfolding correction. For the exponential fit, see Section 7.3

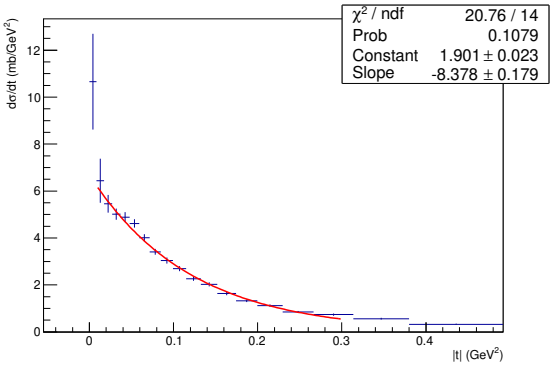

Figure F.20: The fully corrected differential cross section as a function of $|t|$ for the SD class 1T2-1T1 in RP 56_bt, using 1 439 000 events from data segment 1b, after EPOS unfolding correction. For the exponential fit, see Section 7.3

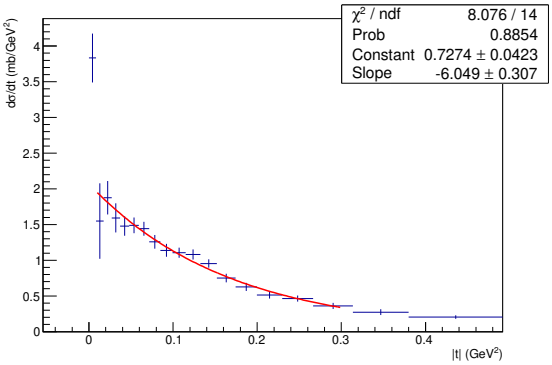

Figure F.21: The fully corrected differential cross section as a function of $|t|$ for the SD class 1T2-2T1 in RP 45_tp, using 1 439 000 events from data segment 1b, after EPOS unfolding correction. For the exponential fit, see Section 7.3

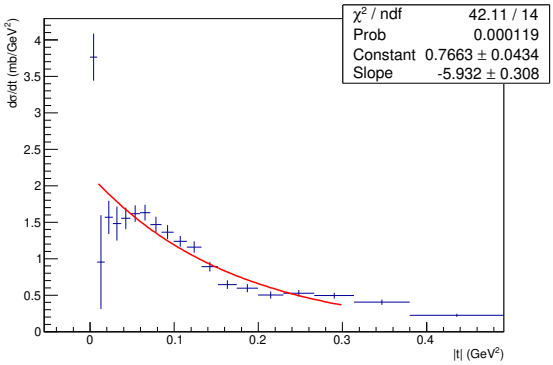

Figure F.22: The fully corrected differential cross section as a function of $|t|$ for the SD class 1T2-2T1 in RP 45_bt, using 1 439 000 events from data segment 1b, after EPOS unfolding correction. For the exponential fit, see Section 7.3

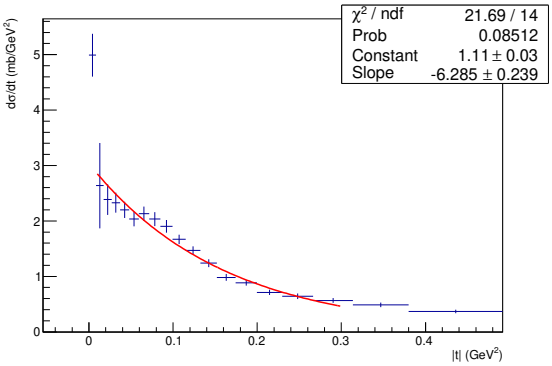

Figure F.23: The fully corrected differential cross section as a function of $|t|$ for the SD class 1T2-2T1 in RP 56_tp, using 1 439 000 events from data segment 1b, after EPOS unfolding correction. For the exponential fit, see Section 7.3

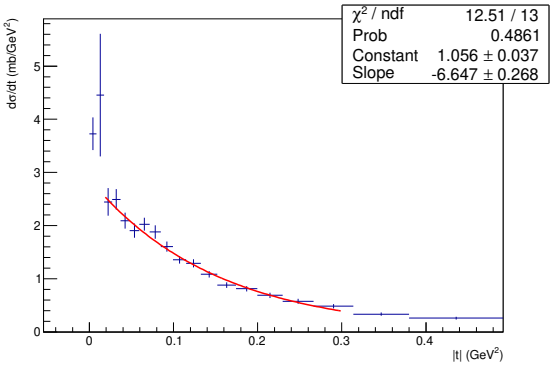

Figure F.24: The fully corrected differential cross section as a function of $|t|$ for the SD class 1T2-2T1 in RP 56_bt, using 1 439 000 events from data segment 1b, after EPOS unfolding correction. For the exponential fit, see Section 7.3

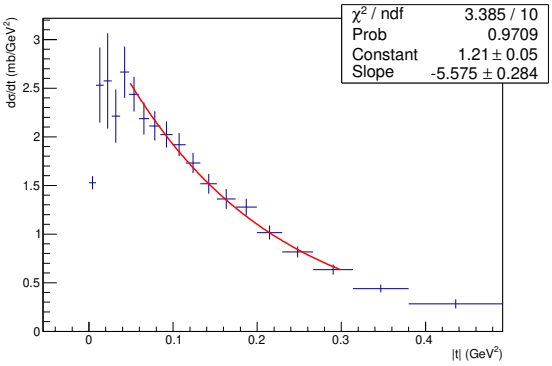

Figure F.25: The fully corrected differential cross section as a function of $|t|$ for the SD class 2T2 in RP 45_tp, using 1 439 000 events from data segment 1b, including BH veto applied for this class only and an EPOS unfolding correction. For the exponential fit, see Section 7.3

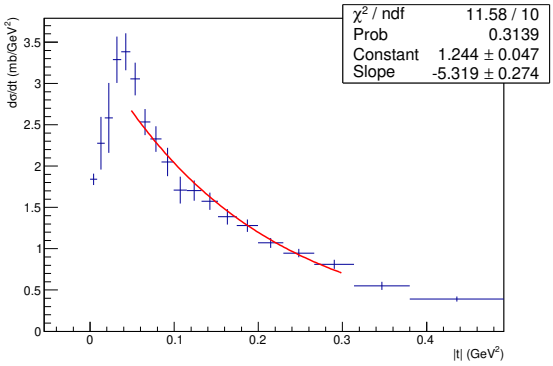

Figure F.26: The fully corrected differential cross section as a function of $|t|$ for the SD class 2T2 in RP 45_bt, using 1 439 000 events from data segment 1b, including BH veto applied for this class only and an EPOS unfolding correction. For the exponential fit, see Section 7.3

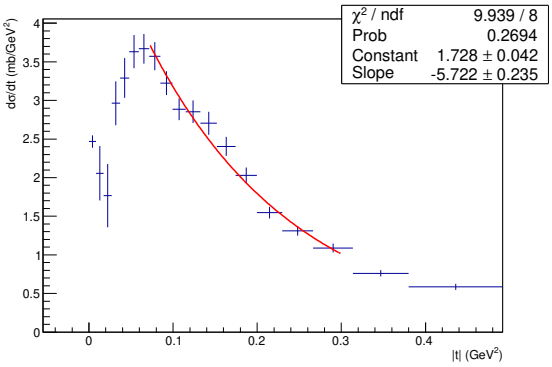

Figure F.27: The fully corrected differential cross section as a function of $|t|$ for the SD class 2T2 in RP 56_tp, using 1 439 000 events from data segment 1b, including BH veto applied for this class only and an EPOS unfolding correction. For the exponential fit, see Section 7.3

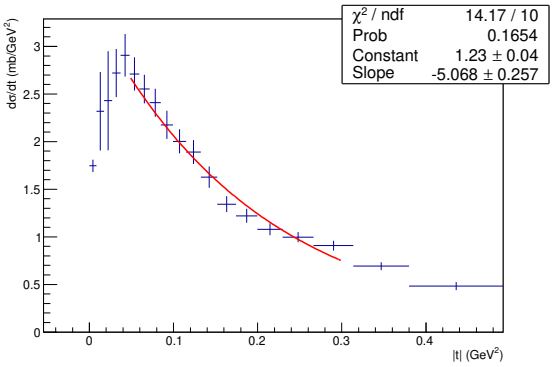

Figure F.28: The fully corrected differential cross section as a function of $|t|$ for the SD class 2T2 in RP 56_bt, using 1 439 000 events from data segment 1b, including BH veto applied for this class only and an EPOS unfolding correction. For the exponential fit, see Section 7.3

Appendix G

Real data SD class 2T2 differential cross sections as a function of ξ, for all RPs

The RP proton reconstruction has a resolution of $\sigma(\xi) \leq 0.8\%$, but with a relative systematic uncertainty of approximately 10%. Because of the ξ resolution being worst at $\xi = 0$ and getting better at high ξ, we can only precisely measure ξ-values larger than $\xi \approx 3 * \sigma(\xi) \approx 2.4\%$, which means only in the very high mass SD class 2T2. Unfortunately, in this SD class the diagnostic rapidity gap does not cover an entire arm of the T2 detector, while the presence of secondary tracks makes it fraught to try to diagnose a gap partially covering T2 based on the reconstructed track pseudorapidity η. This means background Beam Halo protons, with misreconstructed ξ due to lateral displacement from the beam, distort the measured ξ spectra, even after applying BH cuts, as explained in Chapter 6.2.2.

All the RPs except the top RP in arm 5-6 follow a similar pattern, where the cross section is approximately constant at 40 μb/% from the RP acceptance edge at ξ =-20% up to ξ ≈5%, after which the cross section grows small near the upper edge of the 2T2 SD class at ξ =2.7%, with the fall-off smeared by the ξ reconstruction resolution, and class migration from the neighbouring SD class 1T2-2T1. As can be seen in Figure G.3, the top RP in arm 5-6 has a large remaining BH background after all selection requirements, especially at high ξ between -20% and -15%, and was not used for the integral cross section SD measurement presented in this thesis. One could ask whether limiting the measurement to the ξ-range between -15% and -2.7% would be enough to

avoid the BH background; this is most likely not true, since the level of the remaining constant part between $\xi \approx$-15% and $\xi \approx$-5% in 56_tp is similar to 56_bt, which also has an increased BH background, and about 20 – 30% higher than in 45_tp and 45_bt, where we expect the vast majority of the BH background to have been removed. Due to this irreducible BH background 56_tp was not used for any of the SD measurements presented here and 56_bt only for cross-checks.

The total differential cross section is the sum over both arms and both top and bottom RPs, so approximately four times larger.

In this Appendix, we present the measured differential cross section vs ξ for the very high mass 2T2 SD class in all RPs. The ξ-spectra were unfolded with either Pythia 8 or EPOS, but the closure ratio correction was not applied; since closure ratio was calculated per SD class in this analysis, it would be a constant multiplier and contributing term to the uncertainty if applied. The figures were not corrected for class migration with the simple matrix-multiplication method described in Chapter 6.4.5. Since in general we do not expect the differential cross section to simply factorize into two independent functions of one variable each, $d^2\sigma/d\xi dt \neq f_1(\xi) * f_2(t)$, but for there to be some correlation between the momentum transfer and the diffractive mass, we did not make a simple scaling correction using the $|t|$-extrapolation to the kinematic minimum of $|t|$ either.

G.1 Pythia 8 Unfolding

The following Figures G.1 – G.4 were unfolded with a Pythia 8 SD sample of 210 000 events, with mixed-in real PU from BX events.

G.2 EPOS unfolding

The following figures G.5 – G.8 were unfolded with an inclusive EPOS sample with 1 000 000 events total, mixed with real PU from BX events.

G.3 Differential cross section versus $\log_{10}\xi$

The Figures G.9 – G.11 show the logarithmic differential cross section per RP for the SD signal classes, using the final unfolded cross section per category, without the

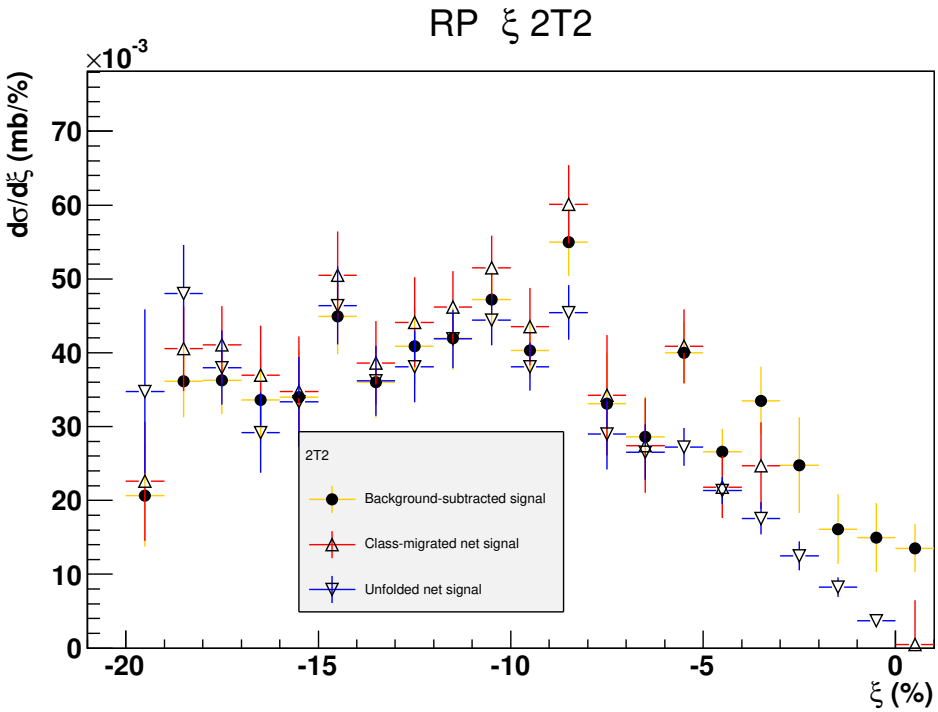

Figure G.1: The unfolded cross section in the 2T2 class as a function of ξ in blue for the RP 45_tp, together with the corresponding class-migrated and background-subtracted cross sections in red and yellow, respectively. Data samples used are the last 1 439 000 real events from Segment 1b, and a Pythia SD sample of 210 000 events for unfolding and class migration correction. Closure and $|t|$-extrapolation corrections not applied, see Section 7.2.

closure test ratio correction. The closure ratio correction is included as a correction and as a systematic uncertainty contribution in Figures G.12 – G.14. These figures do not include the MC and method uncertainties; we did not add these uncertainties to the per-RP figures, only to the total cross section-based ones, summed over RPs.

G.3.1 SD category $\log_{10}\xi$ ranges in MC

Since we use Pythia 8 and EPOS to unfold the cross sections, we validated the ξ-ranges calculated from the pseudorapidity gap size expected between the rapidity of a beam proton[1] and the edges for the T2 and T1 detectors in pseudorapidity η, from Sections 3.2.2 – 3.2.2. We did this by checking the generated ξ distribution for events in each SD signal class, for both Pythia 8 and EPOS MCs. This check was done using both

[1] see Table 3.1

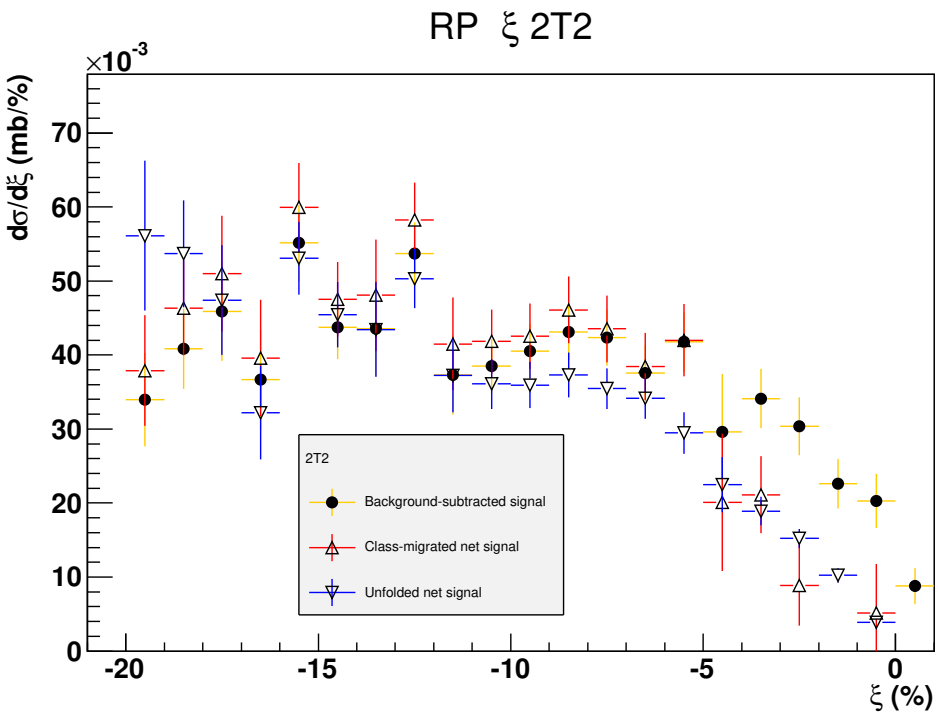

Figure G.2: A preliminary unfolded cross section in the 2T2 class as a function of ξ in blue for the RP 45_bt, together with the corresponding class-migrated and background-subtracted cross sections in red and yellow, respectively. Data samples used are the last 1 439 000 real events from Segment 1b, and a Pythia SD sample of 210 000 events for unfolding and class migration correction. Closure and $|t|$-extrapolation corrections not applied, see Section 7.2.

the SD classification based on reconstructed detector tracks, and the simple generator-level SD classification where we check if the event has particles in the η-range of the T2 or T1, and has one proton with $\xi > -20\%$. In Figures G.15 – G.16 you will find both these plots for Pythia 8, and likewise for EPOS in Figures G.17 – G.18. Due to categories overlapping significantly for the SD classification based on reconstructed tracks, we defined the edges of each category as being where they reach 50% of the plateau for that category. For the generated particle SD classification, we used the point where lines for two classes crossed, generally near an event fraction 0.5. These edges are shown in Figure G.19 as a function of diffractive mass, and also given in Tables G.1 – G.2, with the $\log_{10}\xi$ bin width values presented in Table G.3; the uncertainty on the detector rapidity coverage is based on the precision of the T1 and T2 pseudorapidity coverage. The two MCs, EPOS and Pythia 8, are averaged in Table G.4.

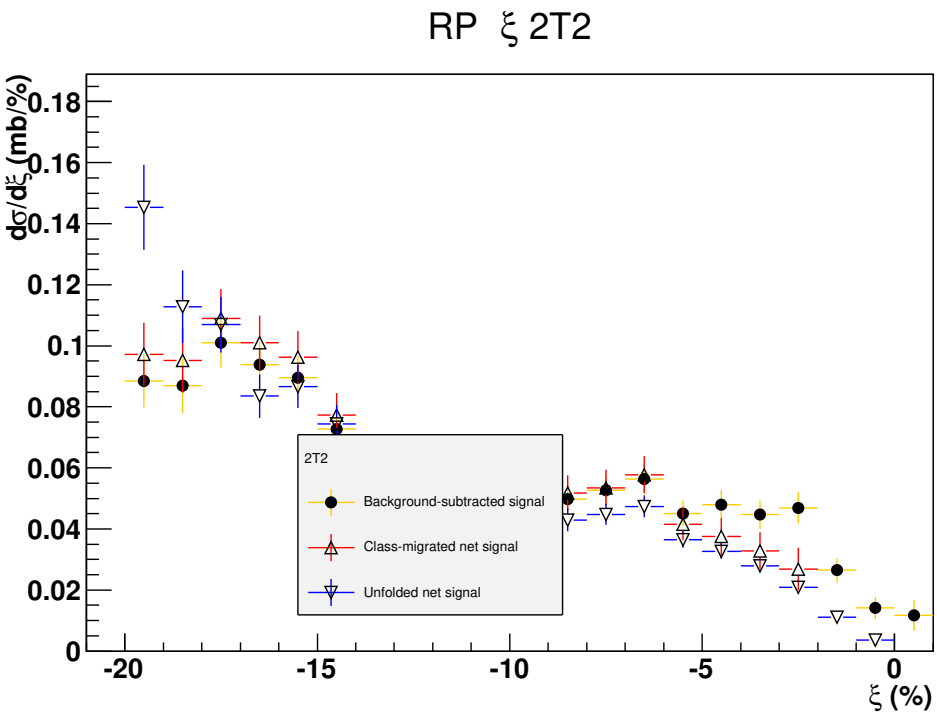

Figure G.3: A preliminary unfolded cross section in the 2T2 class as a function of ξ in blue for the RP 56_tp, together with the corresponding class-migrated and background-subtracted cross sections in red and yellow, respectively. This RP had a large BH background and was therefore not used for the cross sections. Data samples used are the last 1 439 000 real events from Segment 1b, and a Pythia SD sample of 210 000 events for unfolding and class migration correction. Closure and $|t|$-extrapolation corrections not applied, see Section 7.2.

The differential $\log_{10}\xi$ cross sections using these MC based SD class ranges for binning are shown in Figures G.9 – G.14 for EPOS and Pythia 8; see also Chapter 7.2.1.

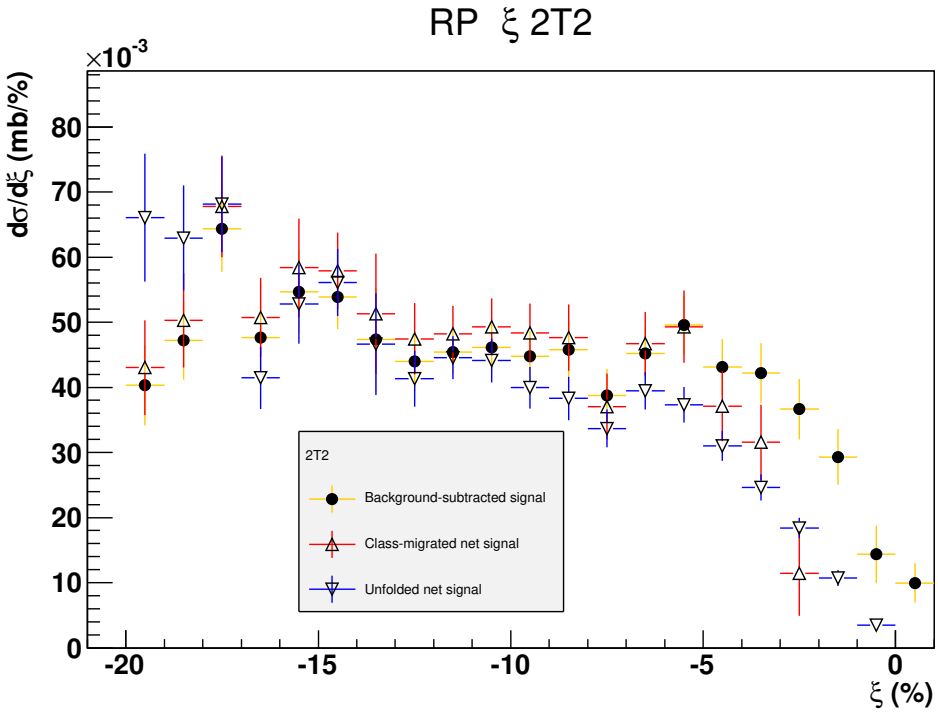

Figure G.4: A preliminary unfolded cross section in the 2T2 class as a function of ξ in blue for the RP 56_bt, together with the corresponding class-migrated and background-subtracted cross sections in red and yellow, respectively. Data samples used are the last 1 439 000 real events from Segment 1b, and a Pythia SD sample of 210 000 events for unfolding and class migration correction. Closure and $|t|$-extrapolation corrections not applied, see Section 7.2.

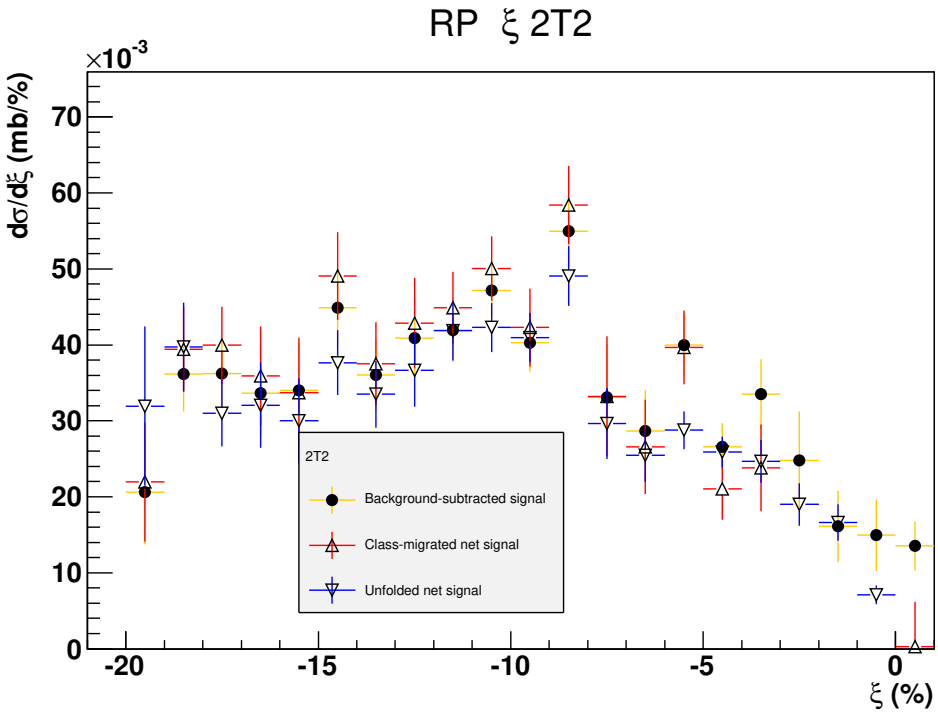

Figure G.5: A preliminary unfolded cross section in the 2T2 class as a function of ξ in blue for the RP 45_tp, together with the corresponding class-migrated and background-subtracted cross sections in red and yellow, respectively. Data samples used are the last 1 439 000 real events from Segment 1b, and an inclusive EPOS sample of 1 000 000 events for unfolding and class migration correction.

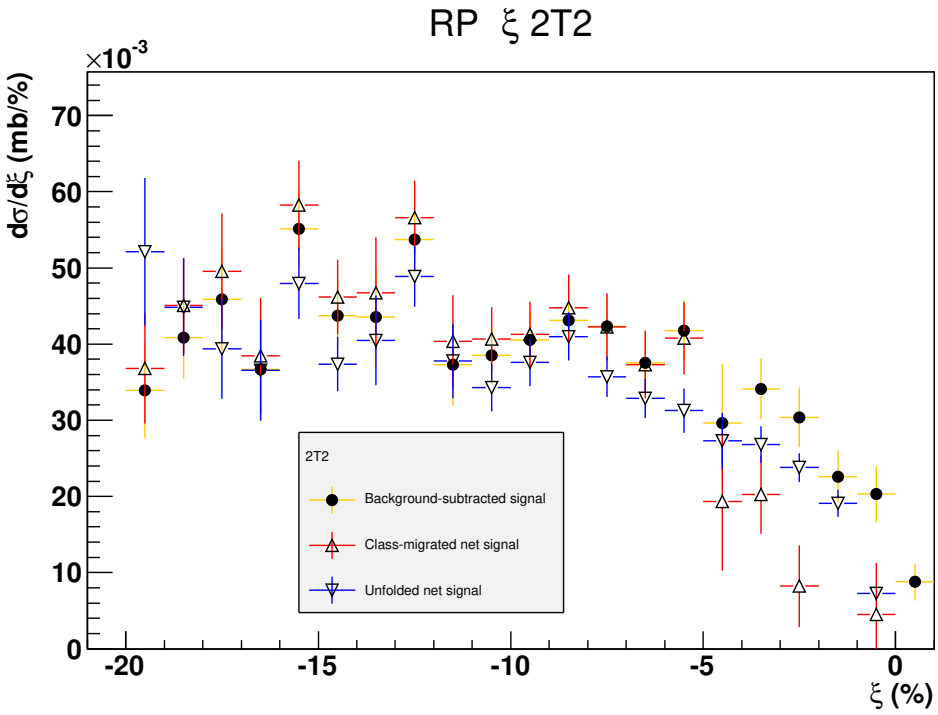

Figure G.6: A preliminary unfolded cross section in the 2T2 class as a function of ξ in blue for the RP 45_bt, together with the corresponding class-migrated and background-subtracted cross sections in red and yellow, respectively. Data samples used are the last 1 439 000 real events from Segment 1b, and an inclusive EPOS sample of 1 000 000 events for unfolding and class migration correction.

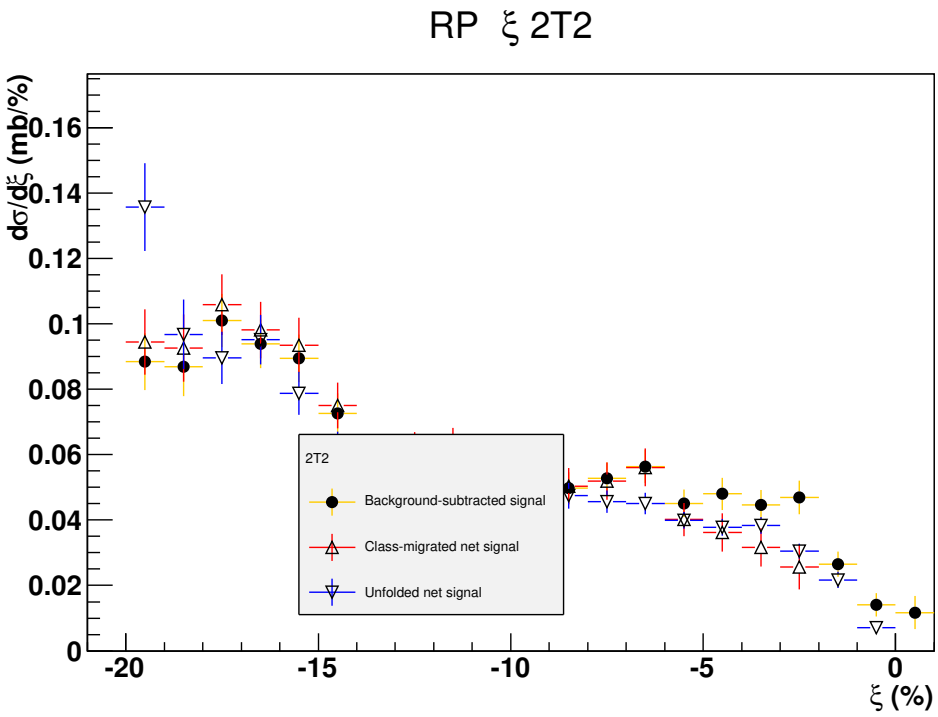

Figure G.7: A preliminary unfolded cross section in the 2T2 class as a function of ξ in blue for the RP 56_tp, together with the corresponding class-migrated and background-subtracted cross sections in red and yellow, respectively. This RP had a large background and was not counted in the integral cross sections. Data samples used are the last 1 439 000 real events from Segment 1b, and an inclusive EPOS sample of 1 000 000 events for unfolding and class migration correction.

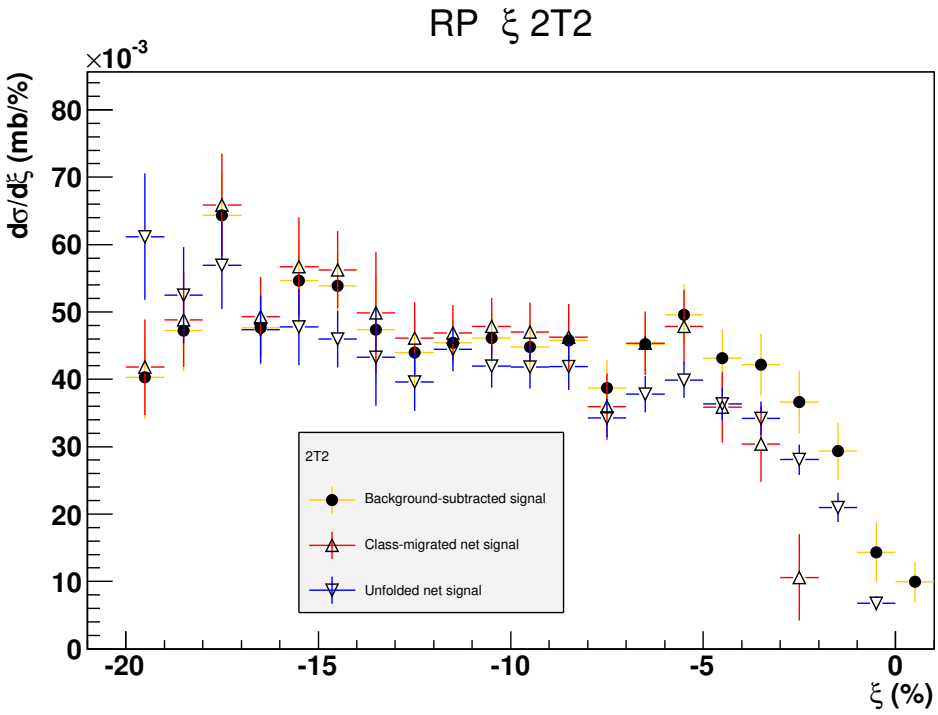

Figure G.8: A preliminary unfolded cross section in the 2T2 class as a function of ξ in blue for the RP 56_bt, together with the corresponding class-migrated and background-subtracted cross sections in red and yellow, respectively. Data samples used are the last 1 439 000 real events from Segment 1b, and an inclusive EPOS sample of 1 000 000 events for unfolding and class migration correction.

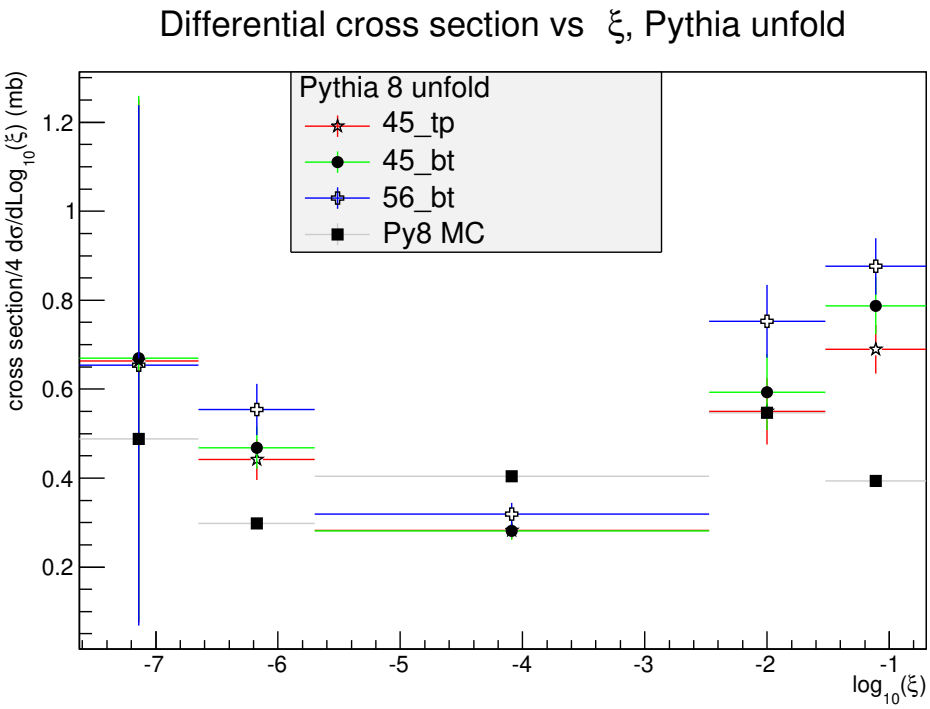

Figure G.9: Differential spectrum in ξ vs $\log_{10}(\xi)$, for the last 1 439 000 events of real data in Segment 1b. Cross section per quadrant, total is four times larger. Edges in ξ for SD classes from the MC sample, see Section G.3.1. After all corrections and background subtraction, unfolded with a 210 000 SD event Pythia 8 sample, without closure ratio correction. All systematics added in quadrature to error bars.

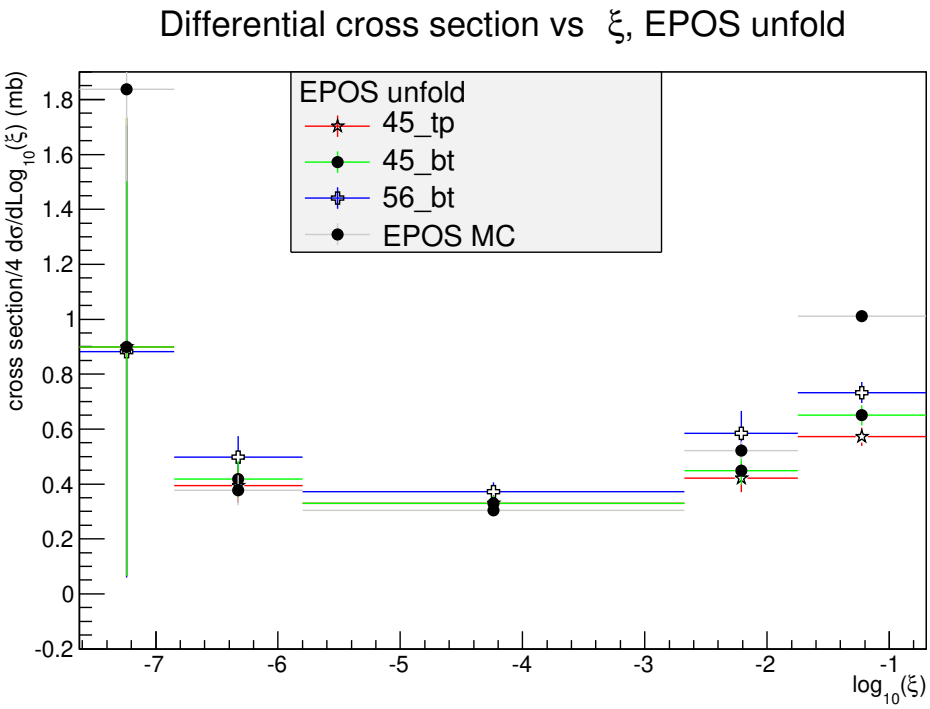

Figure G.10: Differential spectrum in ξ vs $\log_{10}(\xi)$, for the last 1 439 000 events of real data in Segment 1b. Cross section per quadrant, total is four times larger. Edges in ξ for SD classes from the MC sample, see Section G.3.1. After all corrections and background subtraction, unfolded with a 1 000 000 event inclusive EPOS sample, without closure ratio correction. All systematics added in quadrature to error bars.

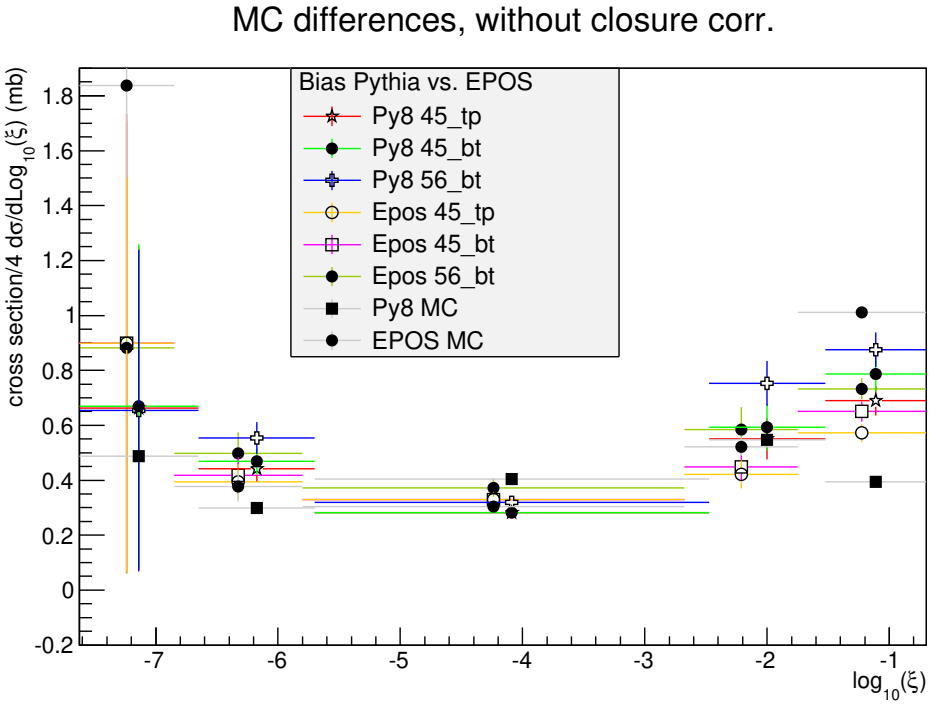

Figure G.11: MC unfolding bias for the differential cross section vs $\log_{10}(\xi)$, for the last 1 439 000 events of real data in Segment 1b. Edges in ξ for SD classes from the MC sample, see Section G.3.1. After all corrections, but not including closure ratio, showing difference between unfolding with a 210 000 SD event Pythia 8 sample and an EPOS sample with 1 000 000 events. All systematics added in quadrature to error bars.

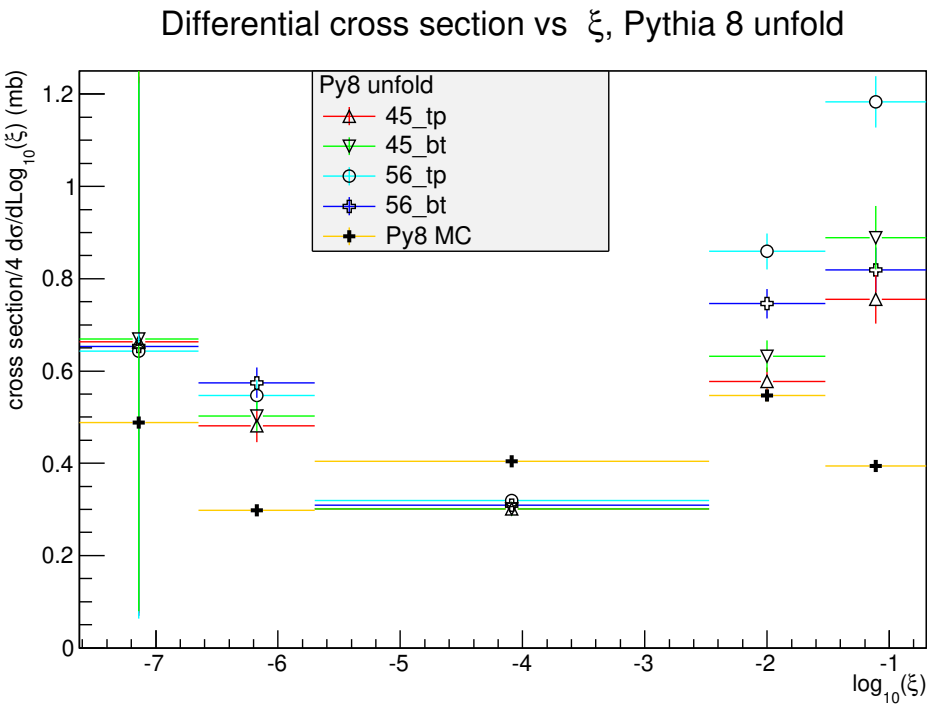

Figure G.12: Differential spectrum in ξ vs $\log_{10}(\xi)$, for the last 1 439 000 events of real data in Segment 1b. Cross section per quadrant, total is four times larger. Edges in ξ for SD classes from the MC samples, see Section G.3.1. After all corrections, including for closure ratio, and background subtraction, unfolded with a 210 000 SD event Pythia 8 sample. All systematics added in quadrature to error bars. Method and MC systematic uncertainties not included.

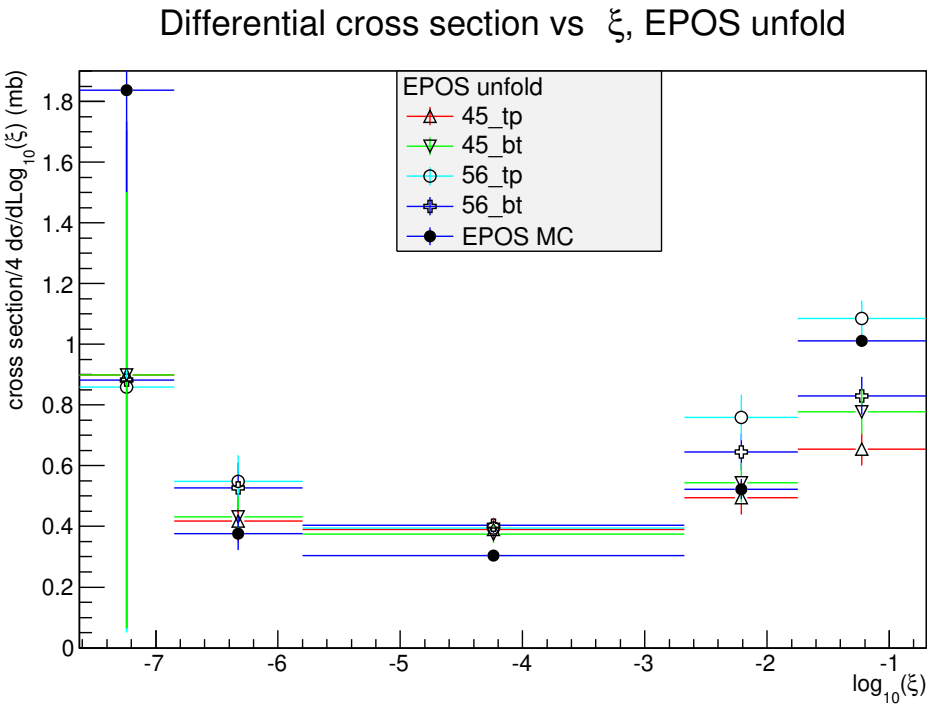

Figure G.13: Differential spectrum in ξ vs $\log_{10}(\xi)$, for the last 1 439 000 events of real data in Segment 1b. Cross section per quadrant, total is four times larger. Edges in ξ for SD classes from the MC sample, see Section G.3.1. After all corrections, including for closure ratio, and background subtraction, unfolded with a 1 000 000 event inclusive EPOS sample. All systematics added in quadrature to error bars. Method and MC systematic uncertainties not included.

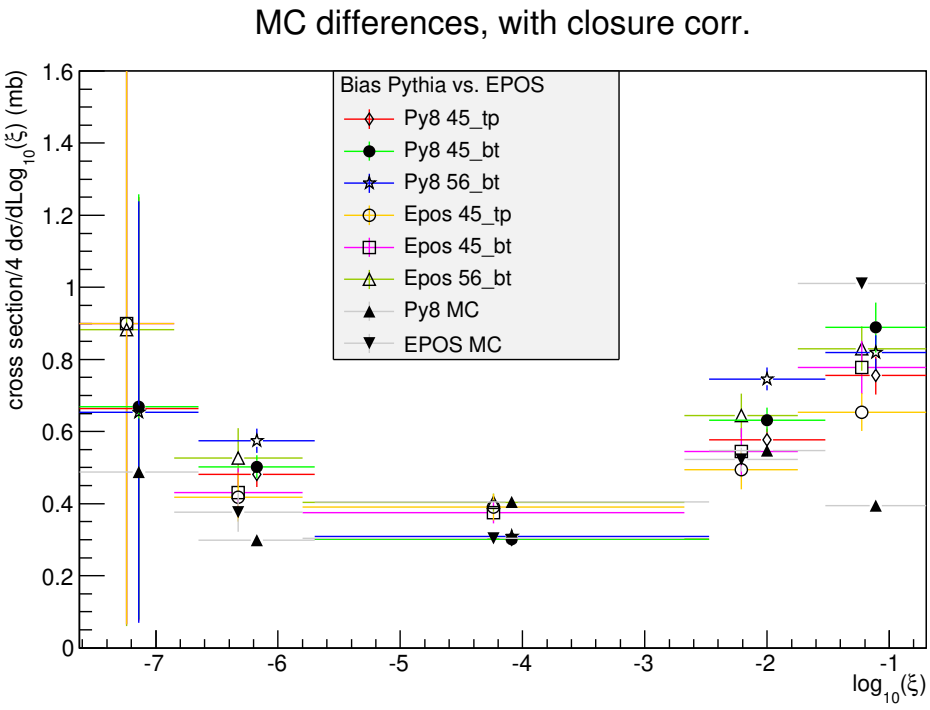

Figure G.14: MC unfolding bias for the differential cross section vs $\log_{10}(\xi)$, with closure ratio correction, for the last 1 439 000 events of real data in Segment 1b. Edges in ξ for SD classes from the MC sample, see Section G.3.1. After all corrections and background subtraction, showing real data unfolded with both a 210 000 SD event Pythia 8 sample and an EPOS sample with 1 000 000 events. All systematics added in quadrature to error bars. Method and MC systematic not included.

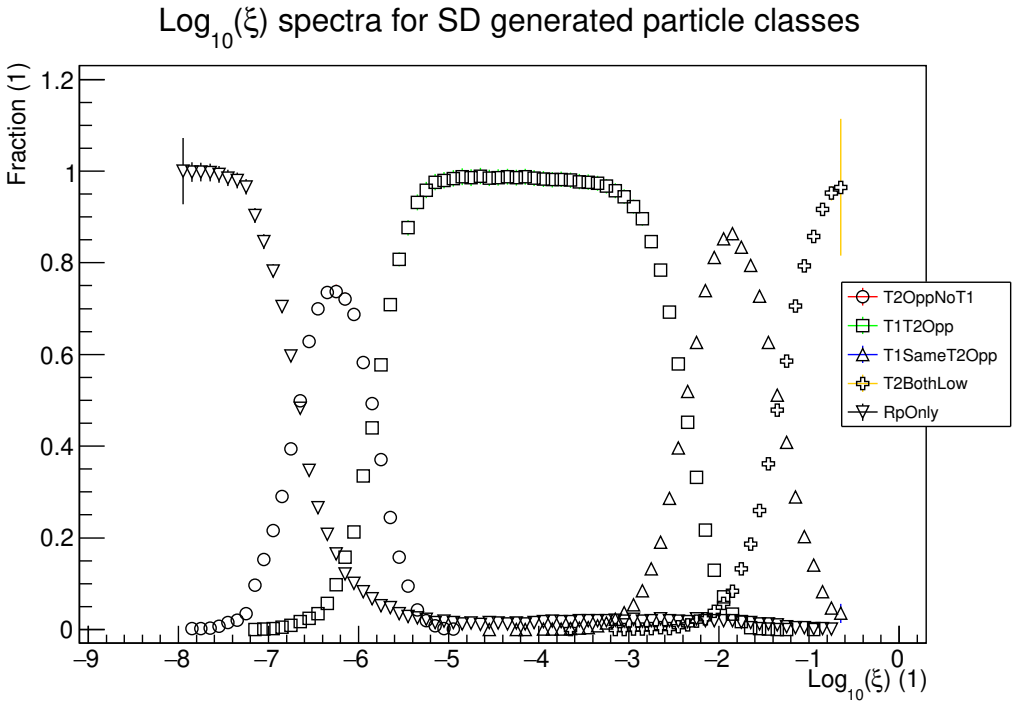

Figure G.15: SD signal classes, classified using generated particles, plotted as a function of $\log_{10}(\xi)$, for 540 000 Pythia 8 SD events.

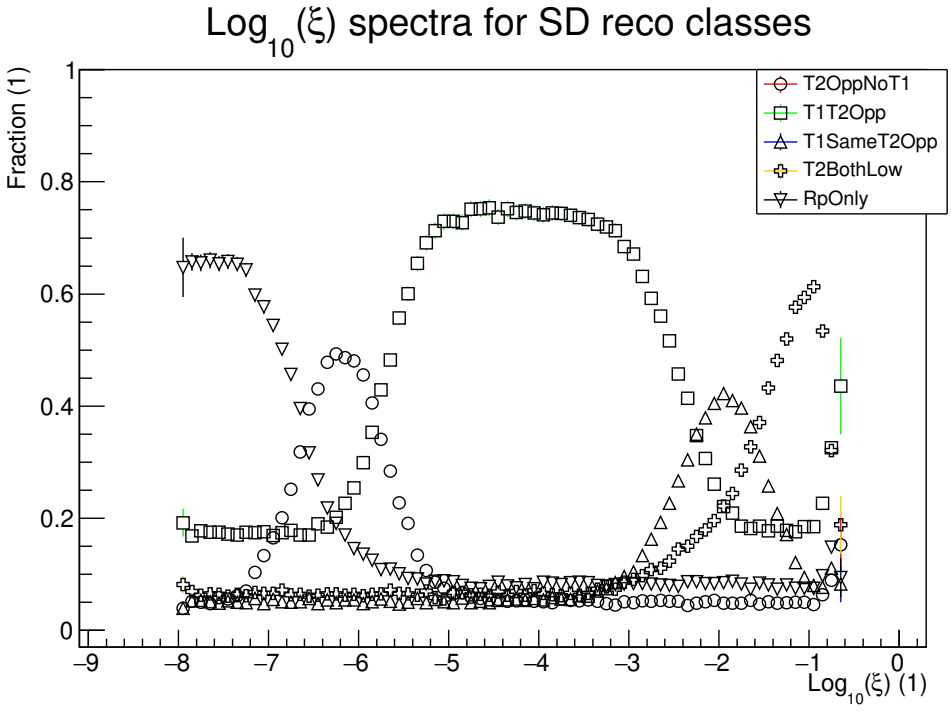

Figure G.16: SD signal classes, classified using reconstructed tracks, plotted as a function of $\log_{10}(\xi)$, for 540 000 Pythia 8 SD events.

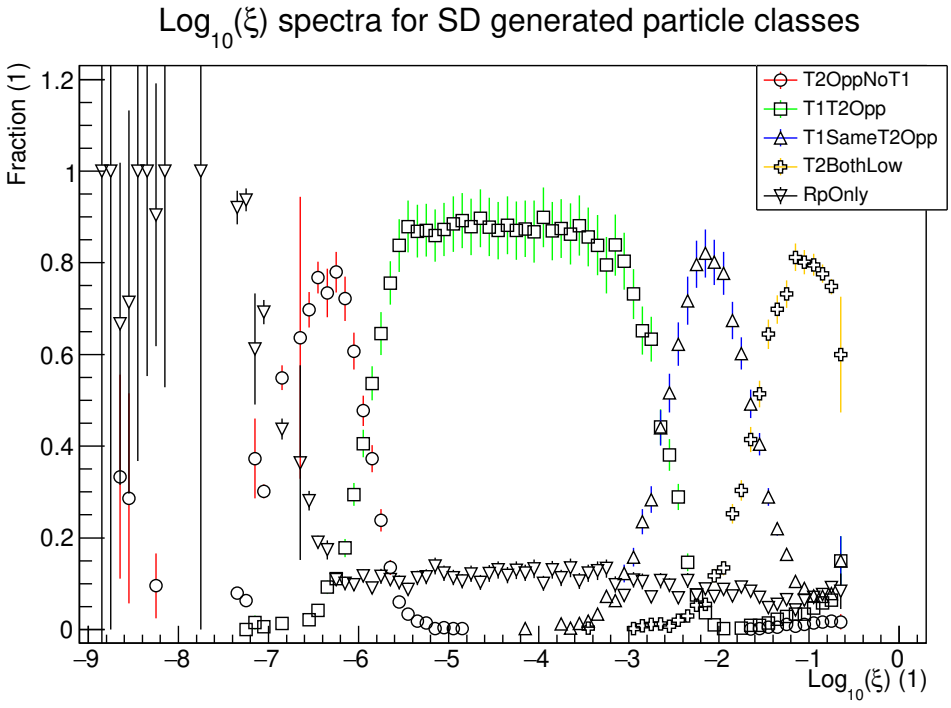

Figure G.17: SD signal classes, classified using generated particles, plotted as a function of $\log_{10}(\xi)$, for 352 000 EPOS events, of which 39 000 are classified as SD.

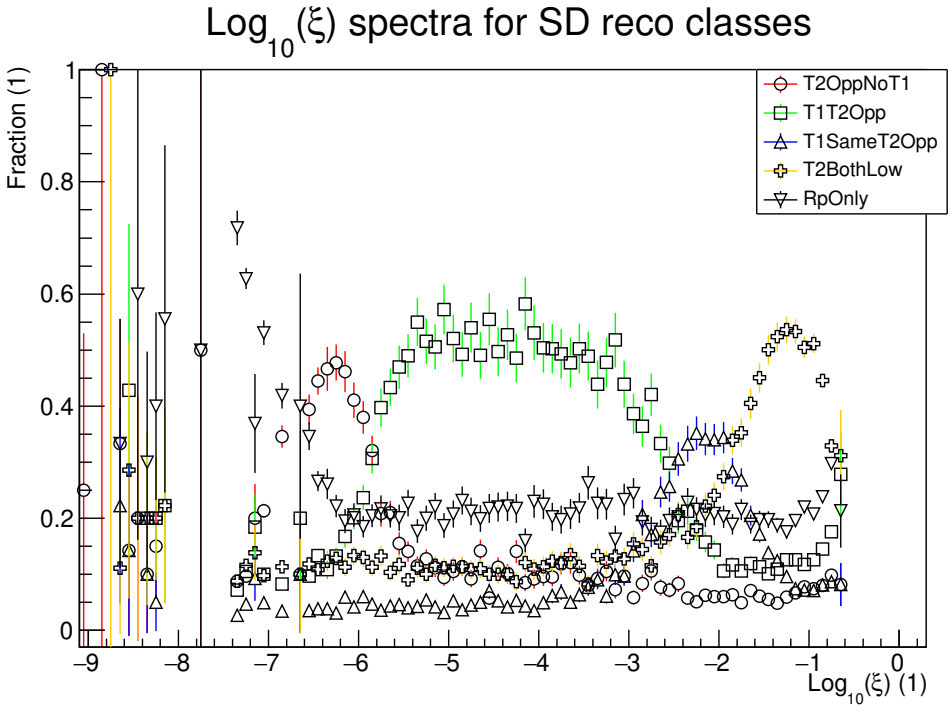

Figure G.18: SD signal classes, classified using reconstructed tracks, plotted as a function of $\log_{10}(\xi)$, for 352 000 EPOS events, of which 39 000 are classified as SD.

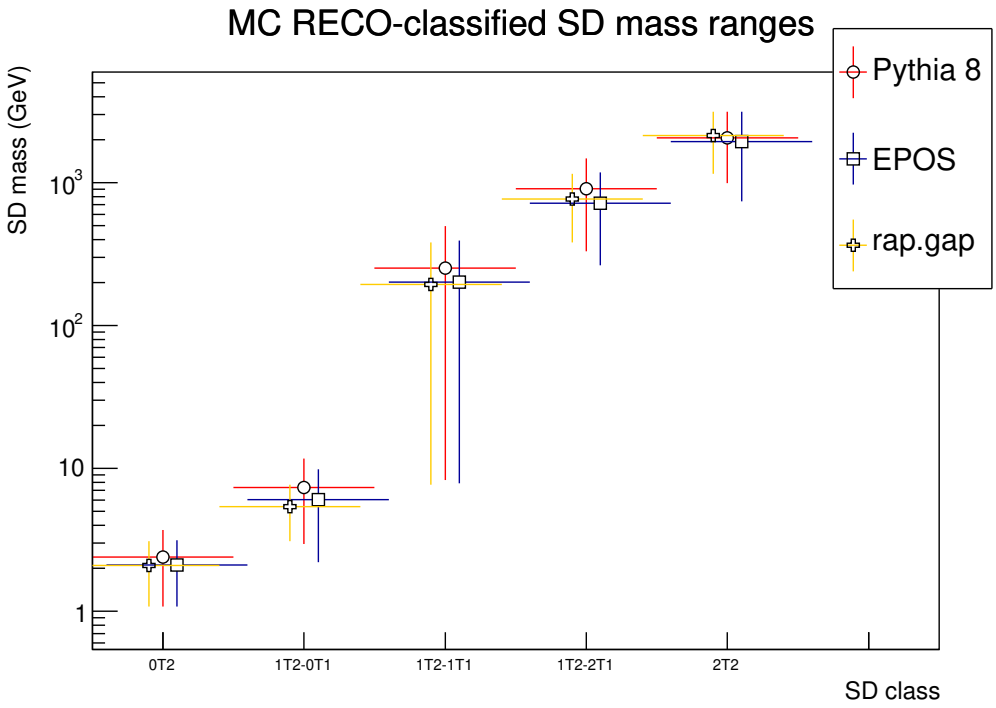

Figure G.19: Lower and upper edges for SD signal classes, classified using reconstructed tracks, plotted as the diffractive mass $M_X = \sqrt{s} * \xi$. Values shown extracted from samples of 250 000 Pythia SD events and 39 000 EPOS SD-like events, and for comparison, the rapidity gap-based class intervals from Table 5.1. Data points horizontally displaced within each bin for easier readability.

Table G.1: Diffractive mass ranges for SD signal classes in EPOS and Pythia 8. Edges extracted from Figures G.15 – G.18, for procedure see text, G.3.1. Lowest edge for diffraction is near $m_p + m_\pi$, and upper edge is set at $\xi = 20\%$. MC samples used are a Pythia 8 SD sample with 250 000 events, and an inclusive EPOS sample with 352 000 events, of which 39 000 are SD-like.

SD class	lower edge (reco.)	upper edge (reco.)	edge (gen.)
Pythia 8 SD			
0T2	($\approx$1.078)	3.72$\pm$0.04	3.31$\pm$0.04
1T2-0T1	2.95$\pm$0.07	11.8$\pm$0.3	8.3$\pm$0.2
1T2-1T1	8.3$\pm$0.2	496$\pm$12	468$\pm$11
1T2-2T1	331$\pm$12	1480$\pm$40	1480$\pm$30
2T2	990$\pm$30	$\approx$3130	$\approx$3130
EPOS			
0T2	($\approx$1.078)	3.1$\pm$0.8	2.34$\pm$0.14
1T2-0T1	2.2$\pm$0.6	9.9$\pm$1.2	7.7$\pm$0.5
1T2-1T1	7.9$\pm$0.5	390$\pm$20	331$\pm$8
1T2-2T1	260$\pm$30	1180$\pm$40	1110$\pm$40
2T2	740$\pm$20	$\approx$3130	$\approx$3130

Table G.2: Geometrically averaged edge masses for neighbouring SD signal classes in EPOS and Pythia 8, compared with diffractive mass ranges in Table 5.1. MC samples used are a Pythia 8 SD sample with 250 000 events, and an inclusive EPOS sample with 352 000 events, of which 39 000 are SD-like.

SD class	geometric average mass limit (Pythia)	geometric average mass limit (EPOS)	rapidity gap mass limit
0T2 to 1T2-0T1	3.31	2.63	3.1
1T2-0T1 to 1T1	9.89	8.81	7.7
1T2-1T1 to 2T1	405	322	380
1T2-2T1 to 2T2	1209	933	1150

Table G.3: Bin widths of diffractive mass ranges in $\log_{10}\xi$ for SD signal classes in EPOS and Pythia 8, compared with the rapidity gap-based estimate from Table 5.1. MC samples used are a Pythia 8 SD sample with 250 000 events, and an inclusive EPOS sample with 352 000 events, of which 39 000 are SD-like.

SD class	$\log_{10}\xi$ range (Pythia 8)	$\log_{10}\xi$ range (EPOS)	$\log_{10}\xi$ range (rapidity gap)
0T2	0.98±0.01	0.78±0.14	0.93±0.02
1T2-0T1	0.95±0.02	1.05±0.15	0.78±0.02
1T2-1T1	3.23±0.02	3.13±0.08	3.39±0.02
1T2-2T1	0.95±0.03	0.93±0.06	0.96±0.02
2T2	0.83±0.02	1.05±0.02	0.87±0.02

Table G.4: Midpoints and bin widths of diffractive mass ranges in $\log_{10}\xi$ for SD signal classes, final results averaged over EPOS and Pythia 8. MC samples used are a Pythia 8 SD sample with 250 000 events, and an inclusive EPOS sample with 352 000 events, of which 39 000 are SD-like. "Sys" is the MC systematic uncertainty, equal to half the difference between MCs.

SD class	$\log_{10}(\xi)$ midpoint	$\log_{10}(\xi)$ width
0T2	-7.19±0.07±0.05(sys)	0.88±0.10±0.07(sys)
1T2-0T1	-6.25±0.08±0.07(sys)	1.00±0.05±0.08(sys)
1T2-1T1	-4.16±0.04±0.07(sys)	3.18±0.05±0.04(sys)
1T2-2T1	-2.11±0.03±0.11(sys)	0.94±0.01±0.03(sys)
2T2	-1.17±0.01±0.06(sys)	0.94±0.11±0.01(sys)

Appendix H

Closure test plots

H.1 Pythia 8 SD closure test, real PU mixing

Figures H.1 – H.3 show the Pythia 8 closure test, with an SD sample of 210 000 events, and using Bayesian unfolding with two iterations. The corresponding closure test with SVD (k=7) can be found in Figures H.4 – H.7

H.2 EPOS closure test, real PU mixing

Figures H.8 – H.10 show the EPOS closure test, with an inclusive MC sample of 1 000 000 events, with 2-iteration Bayesian unfolding. This MC sample was mixed with real BX pileup, and backgrounds were subtracted. The comparable closure test with SVD unfolding (k=7) are shown in Figures H.11 – H.14.

H.3 EPOS second exponential fit

Figures H.15 – H.17 show the generated $|t|$-spectra for EPOS and Pythia, for event samples of 352 000 inclusive EPOS events and 540 000 Pythia SD events, for SD classes 1T2-1T1 and 1T2-2T1, and 0T2.

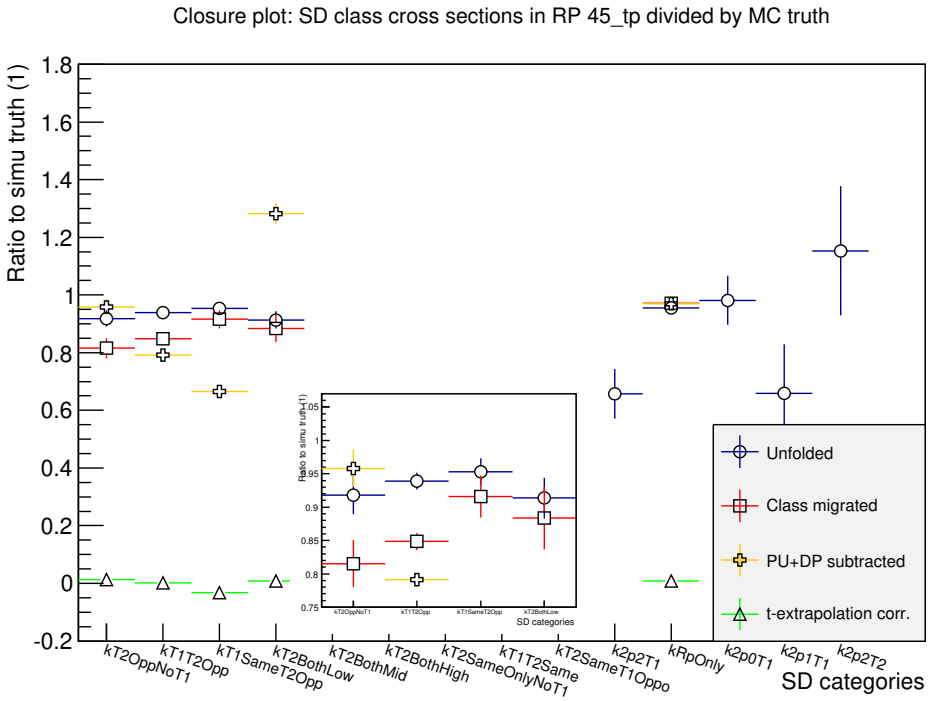

Figure H.1: Arm 4-5 top: Ratio of number SD events after unfolding and application of corrections to the number generated true SD events in MC as function of SD class with background subtraction applied, and real PU mixed in. Data sample is Pythia 8 SD, 210 000 events. Inset shows the 1T2 and 2T2 classes, zoomed in.

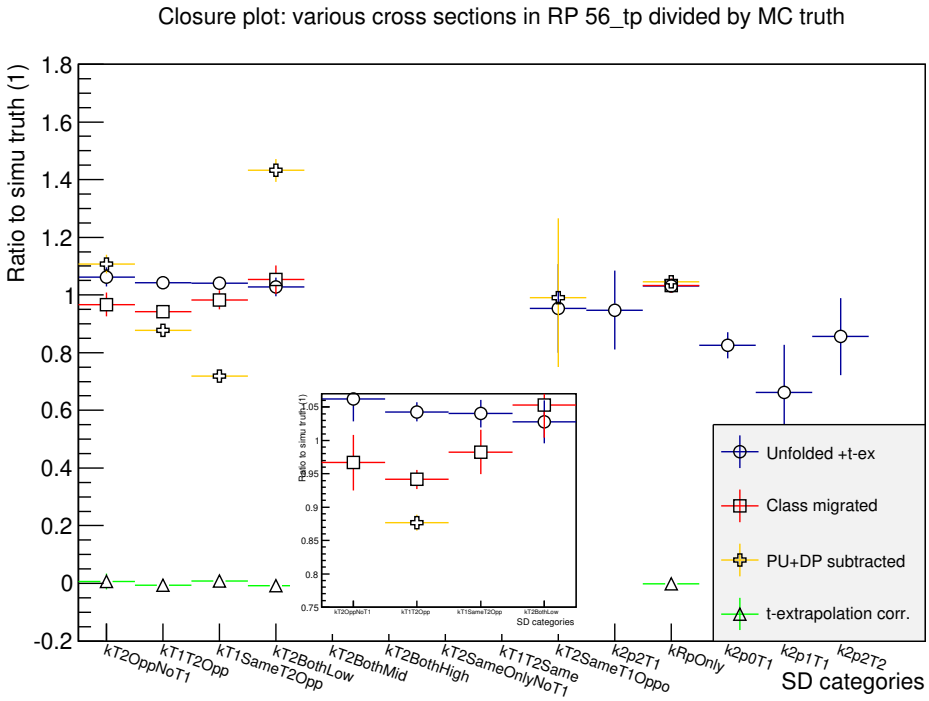

Figure H.2: Arm 5-6 top: Ratio of unfolded and corrected RECO-level event numbers to the generated true distribution with background subtraction applied. Data sample is Pythia 8 SD, 210 000 events, with real BX pileup added. Inset shows the 1T2 and 2T2 classes, zoomed in.

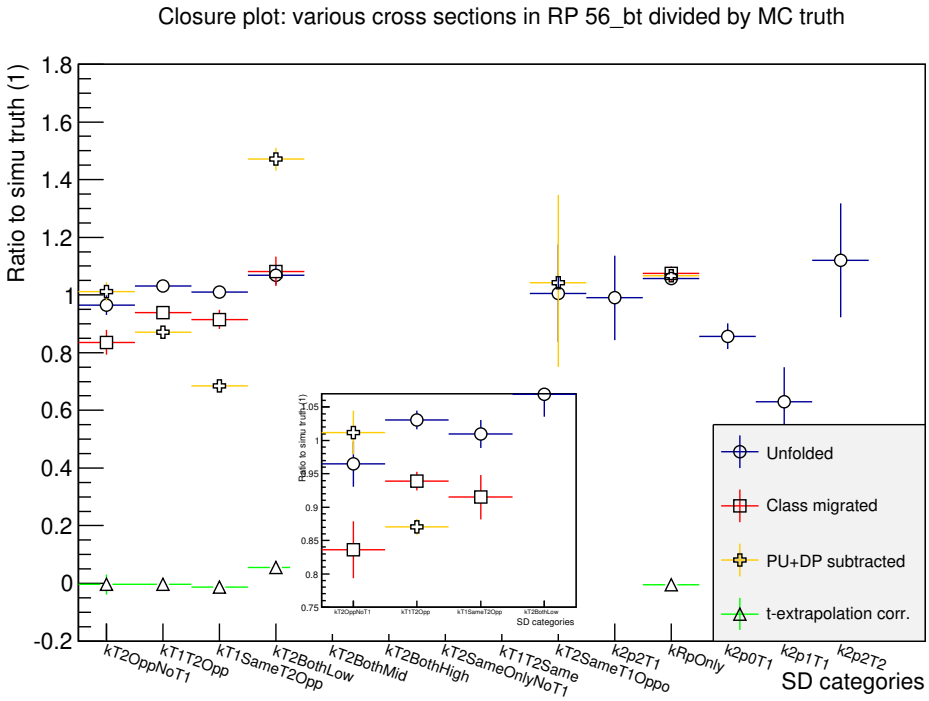

Figure H.3: Arm 5-6 bottom: Ratio of unfolded and corrected RECO-level event numbers to the generated true distribution with background subtraction applied. Data sample is Pythia 8 SD, 210 000 events, with real BX pileup added. Inset shows the 1T2 and 2T2 classes, zoomed in.

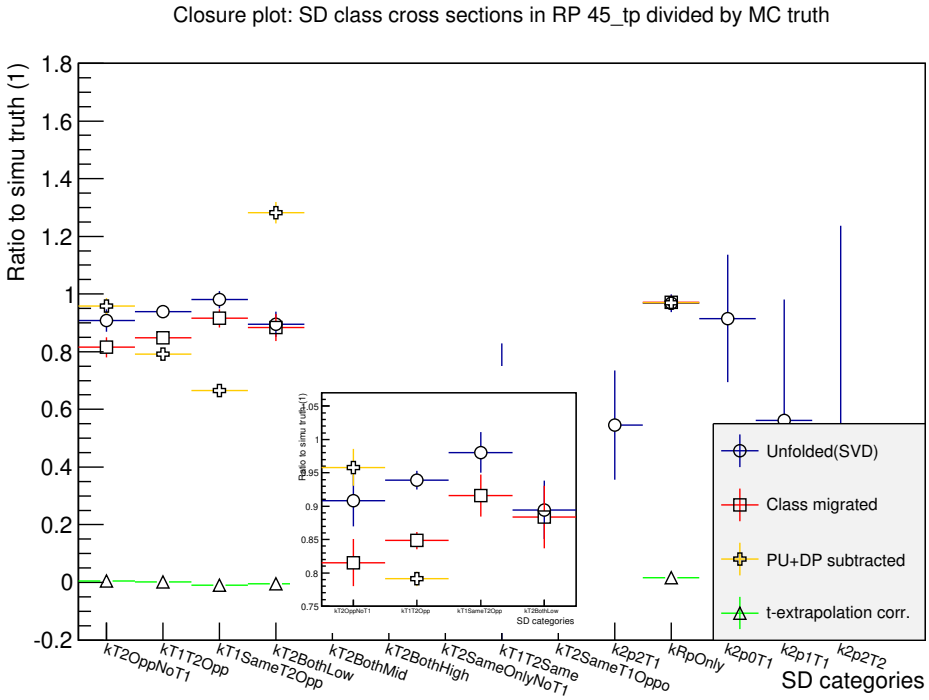

Figure H.4: Arm 4-5 top: Ratio of number SD events after SVD unfolding and application of corrections to the number generated true SD events in MC as function of SD class with background subtraction applied, and real PU mixed in. Data sample is Pythia 8 SD, 210 000 events. Inset shows the 1T2 and 2T2 classes, zoomed in.

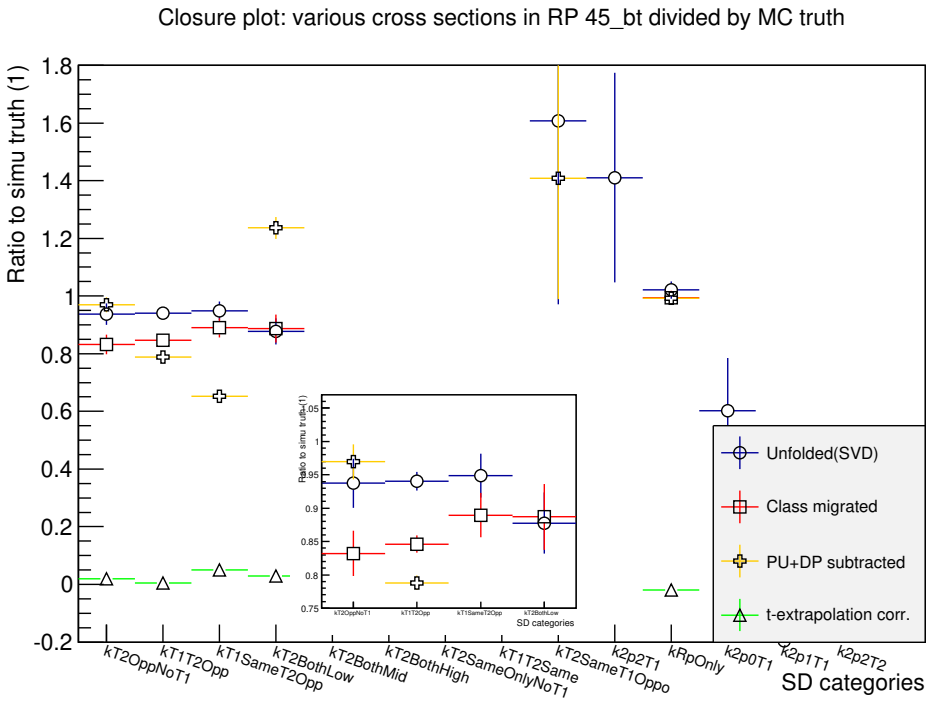

Figure H.5: Arm 4-5 bottom: Ratio of number SD events after SVD unfolding and application of corrections to the number generated true SD events in MC as function of SD class with background subtraction applied, and real PU mixed in. Data sample is Pythia 8 SD, 210 000 events. Inset shows the 1T2 and 2T2 classes, zoomed in.

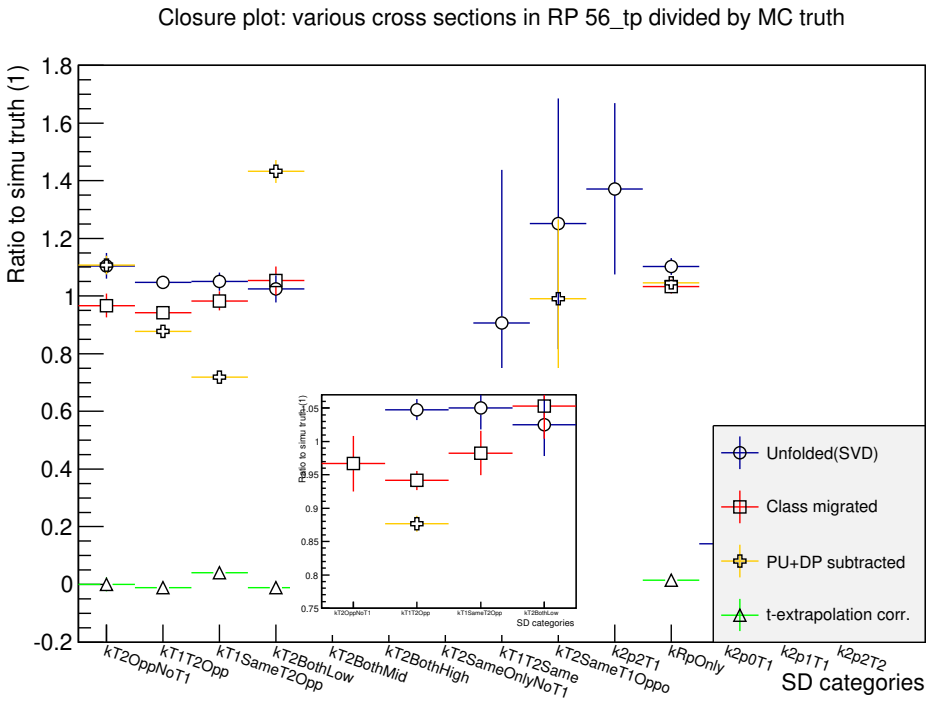

Figure H.6: Arm 5-6 top: Ratio of number SD events after SVD unfolding and application of corrections to the number generated true SD events in MC as function of SD class with background subtraction applied, and real PU mixed in. Data sample is Pythia 8 SD, 210 000 events. Inset shows the 1T2 and 2T2 classes, zoomed in.

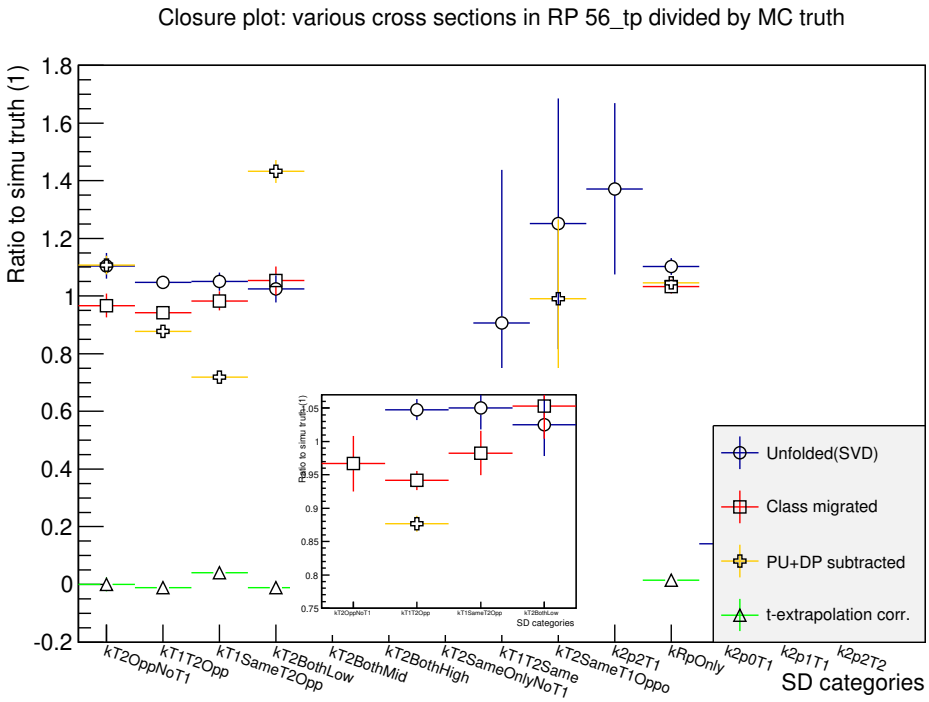

Figure H.7: Arm 5-6 bottom: Ratio of number SD events after SVD unfolding and application of corrections to the number generated true SD events in MC as function of SD class with background subtraction applied, and real PU mixed in. Data sample is Pythia 8 SD, 210 000 events. Inset shows the 1T2 and 2T2 classes, zoomed in.

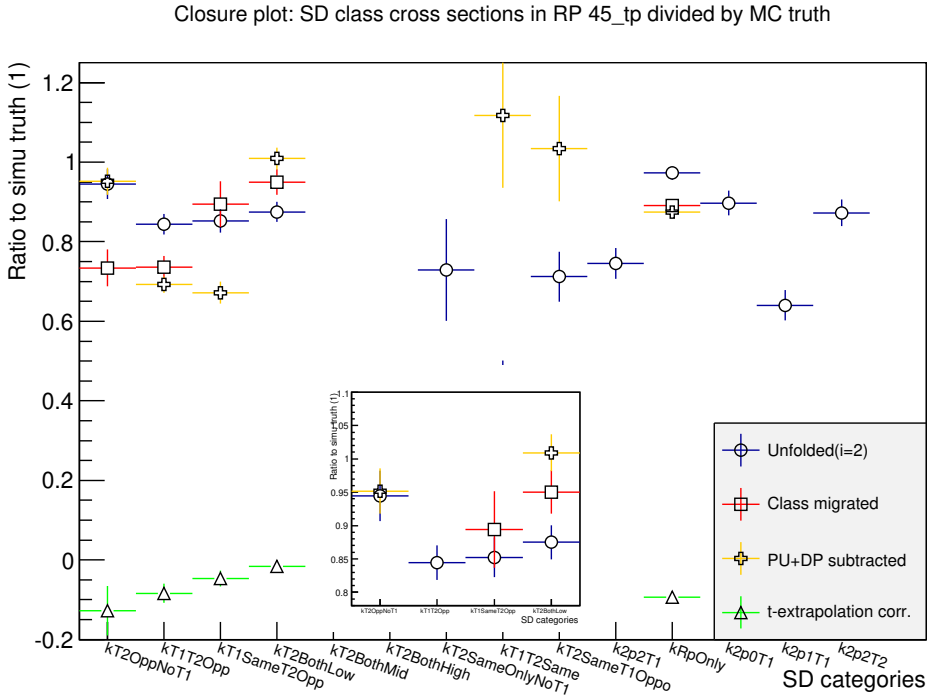

Figure H.8: Arm 4-5 top: Ratio of number SD events after unfolding and application of corrections to the number generated true SD events in MC as function of SD class with background subtraction applied. Data sample is EPOS inclusive 1 000 000 events, with mixed real BX pileup. Inset shows the 1T2 and 2T2 classes, zoomed in. Unfolding method is Bayes, 2 iterations. No $|t|$-correction is applied, see text.

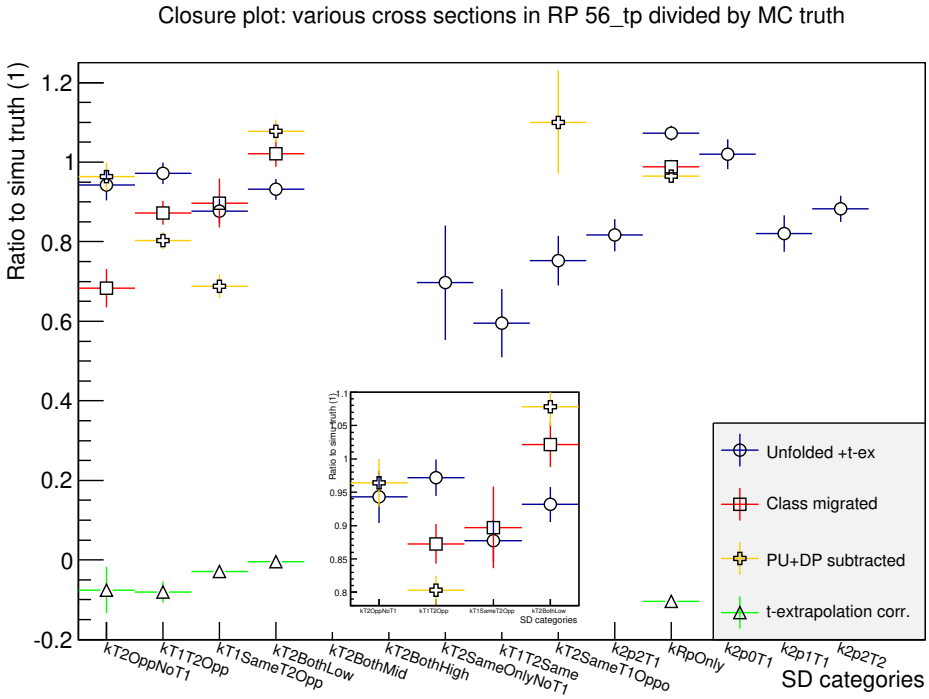

Figure H.9: Arm 5-6 top: Ratio of unfolded and corrected RECO-level event numbers to the generated true distribution with background subtraction applied. Data sample is EPOS inclusive 1 000 000 events, with mixed real BX pileup. Inset shows SD categories 1T2-0T1 to 2T2 zoomed in. Unfolding method is Bayes, 2 iterations. No $|t|$-correction is applied, see text.

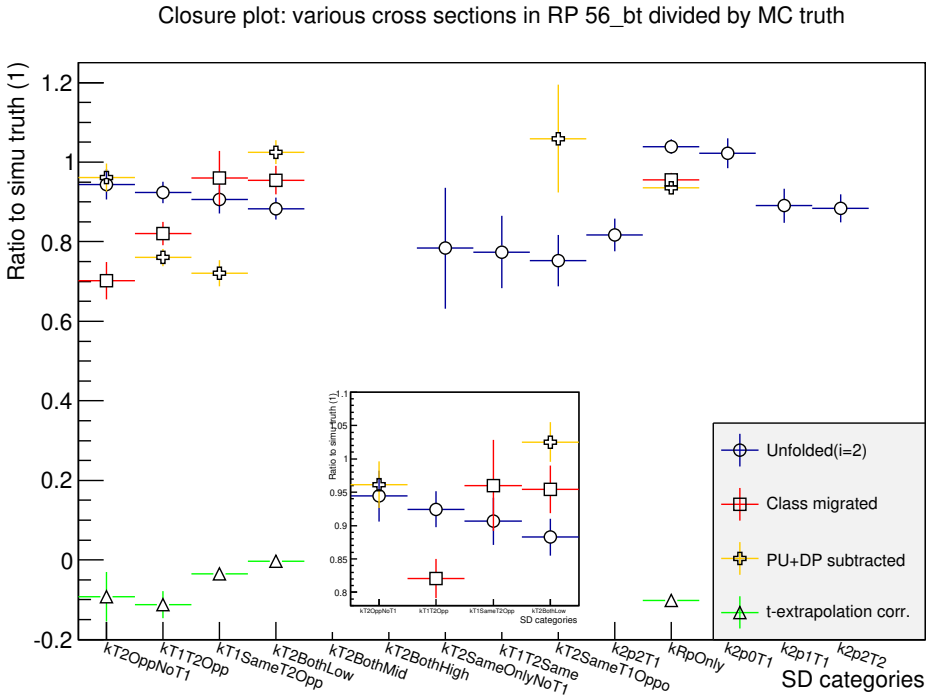

Figure H.10: Arm 5-6 bottom: Ratio of unfolded and corrected RECO-level event numbers to the generated true distribution with background subtraction applied. Data sample is EPOS inclusive 1 000 000 events, with mixed real BX pileup. Inset shows SD categories 1T2-0T1 to 2T2 zoomed in. Unfolding method is Bayes, 2 iterations. No $|t|$-correction is applied, see text.

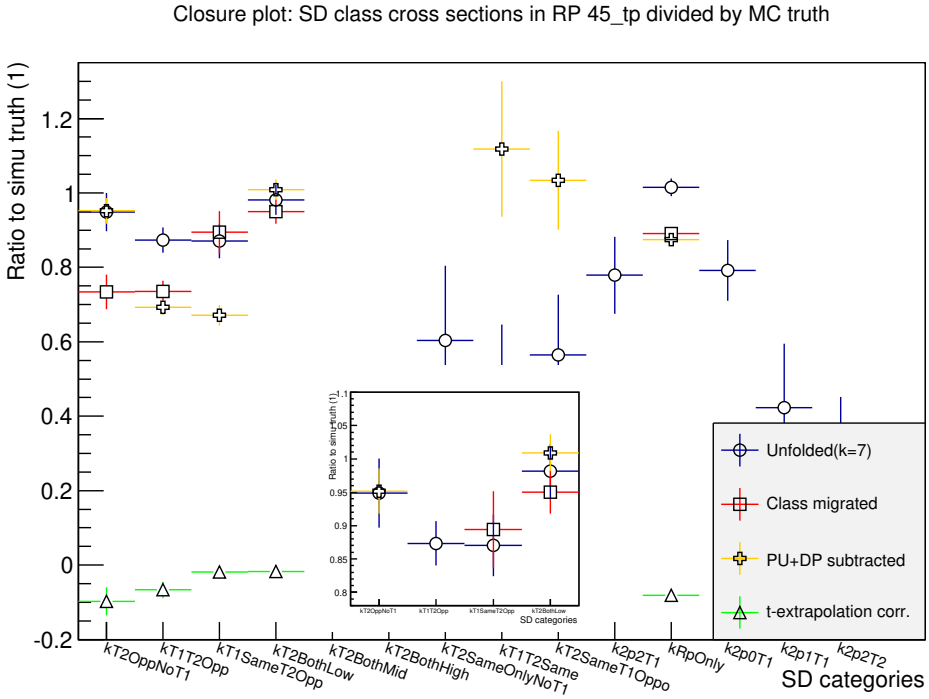

Figure H.11: Arm 4-5 top: Ratio of number SD events after SVD-unfolding and application of corrections to the number generated true SD events in MC as function of SD class with background subtraction applied. Data sample is EPOS inclusive 1 000 000 events, with mixed real BX pileup. Inset shows the 1T2 and 2T2 classes, zoomed in. Unfolding method is SVD, k=7. No $|t|$-correction is applied, see text.

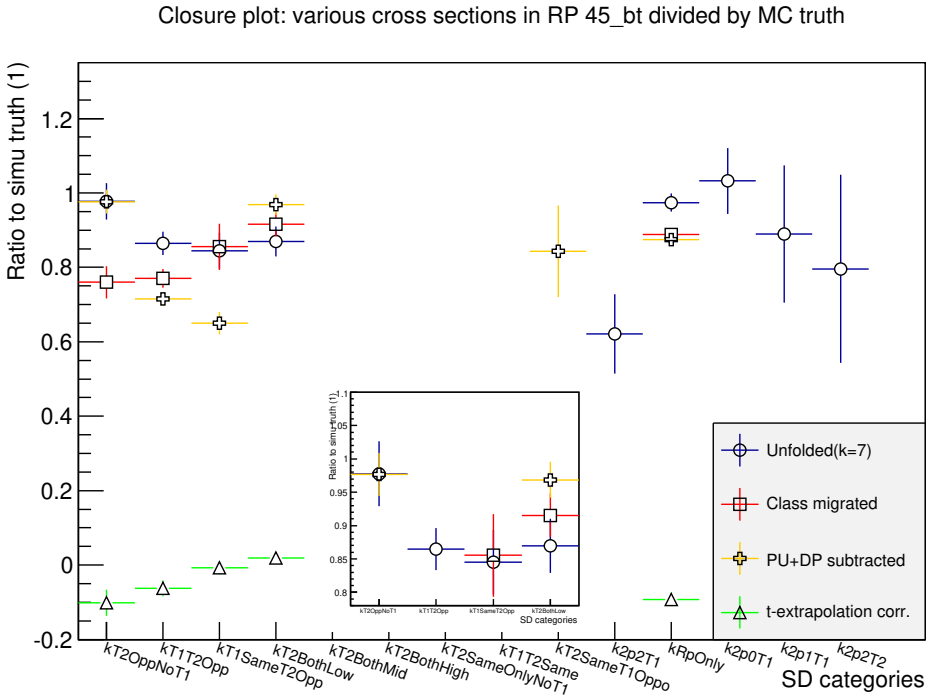

Figure H.12: Arm 4-5 bottom: Ratio of number SD events after SVD-unfolding and application of corrections to the number generated true SD events in MC as function of SD class with background subtraction applied. Data sample is EPOS inclusive 1 000 000 events, with mixed real BX pileup. Inset shows the 1T2 and 2T2 classes, zoomed in. Unfolding method is SVD, k=7. No $|t|$-correction is applied, see text.

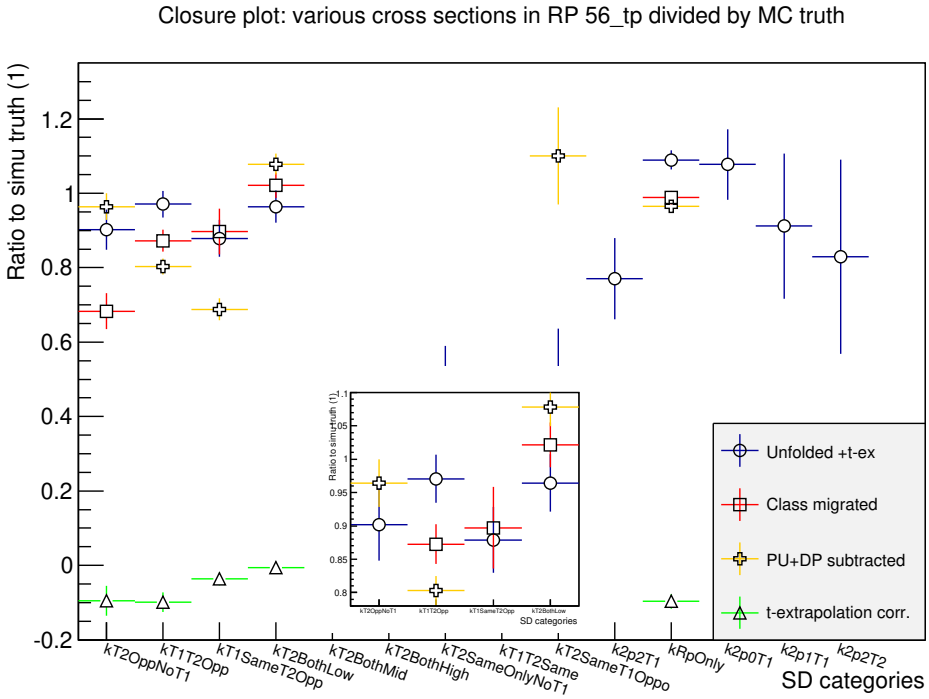

Figure H.13: Arm 5-6 top: Ratio of SVD-unfolded and corrected RECO-level event numbers to the generated true distribution with background subtraction applied. Data sample is EPOS inclusive 1 000 000 events, with mixed real BX pileup. Inset shows SD categories 1T2-0T1 to 2T2 zoomed in. Unfolding method is SVD, k=7. No $|t|$-correction is applied, see text.

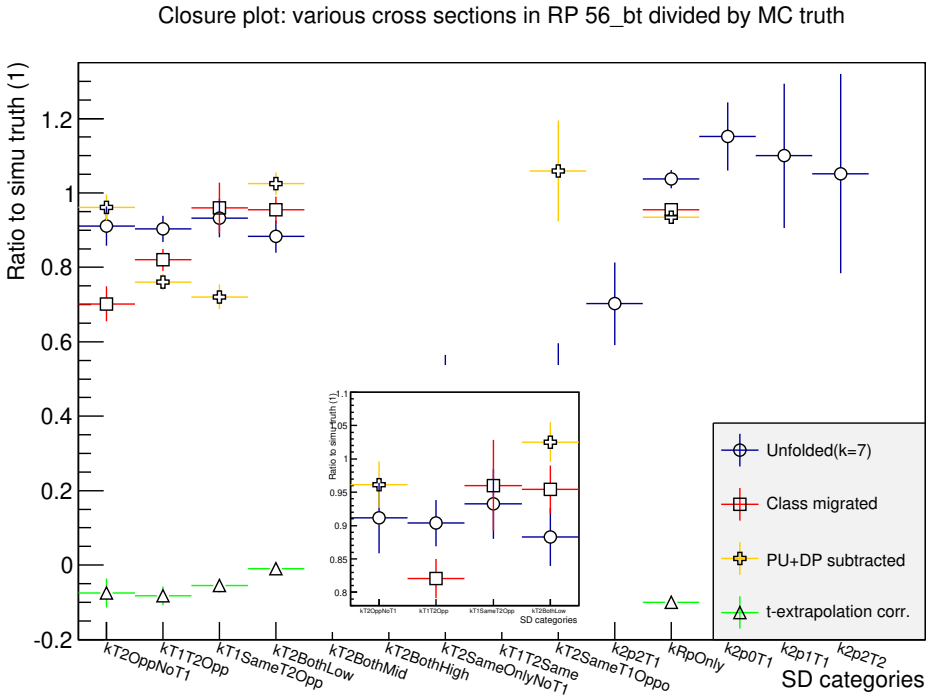

Figure H.14: Arm 5-6 bottom: Ratio of SVD-unfolded and corrected RECO-level event numbers to the generated true distribution with background subtraction applied. Data sample is EPOS inclusive 1 000 000 events, with mixed real BX pileup. Inset shows SD categories 1T2-0T1 to 2T2 zoomed in. Unfolding method is SVD, k=7. No $|t|$-correction is applied, see text.

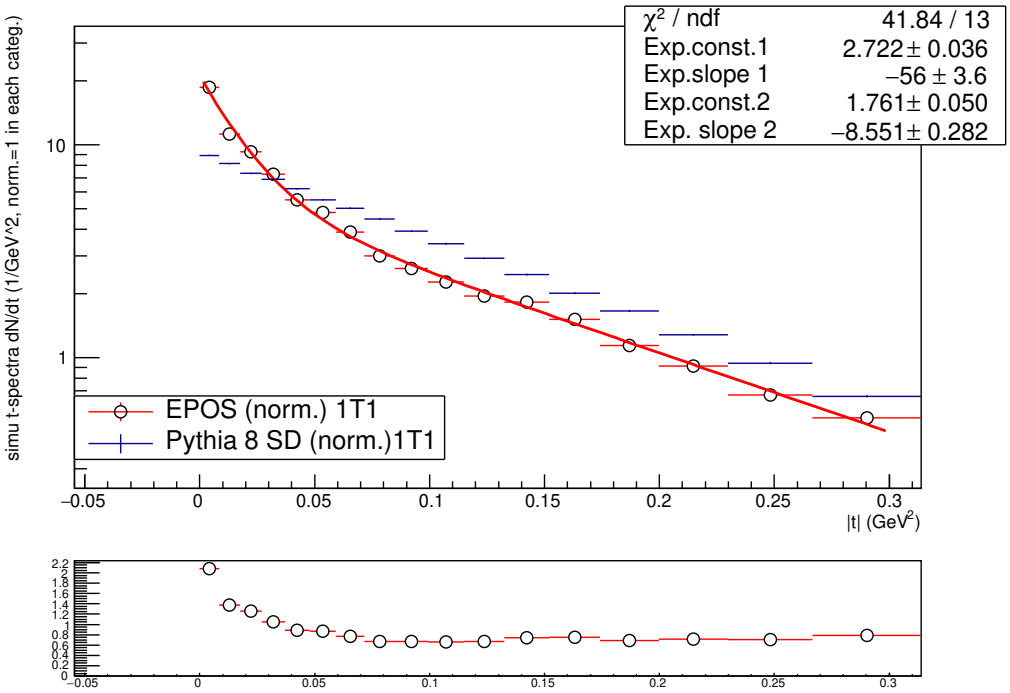

Figure H.15: Normalised differential proton t-spectrum for EPOS and Pythia 8 events in the 1T2-1T1 SD class using the generator information. The EPOS t-spectrum is fitted with a double exponential shown as a red line and with parameters given in the box. Ratio of EPOS to Pythia 8 $|t|$-spectra shown in lower box.

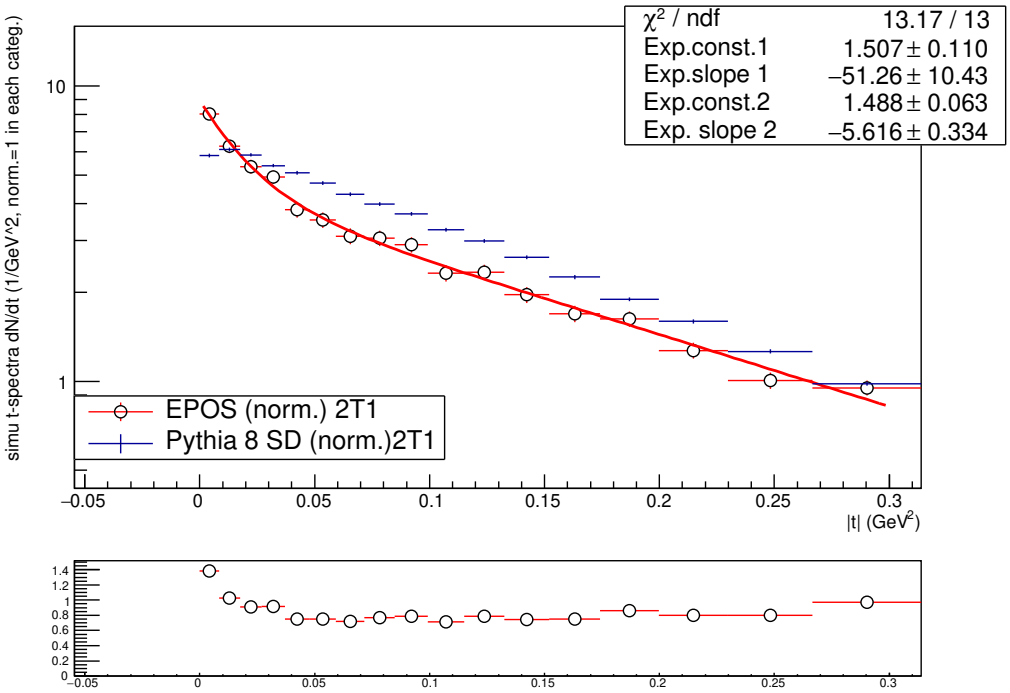

Figure H.16: Normalised differential proton t-spectrum for EPOS and Pythia 8 events in the 1T2-2T1 SD class using the generator information. The EPOS t-spectrum is fitted with a double exponential shown as a red line and with parameters given in the box. Ratio of EPOS to Pythia 8 $|t|$-spectra shown in lower box.

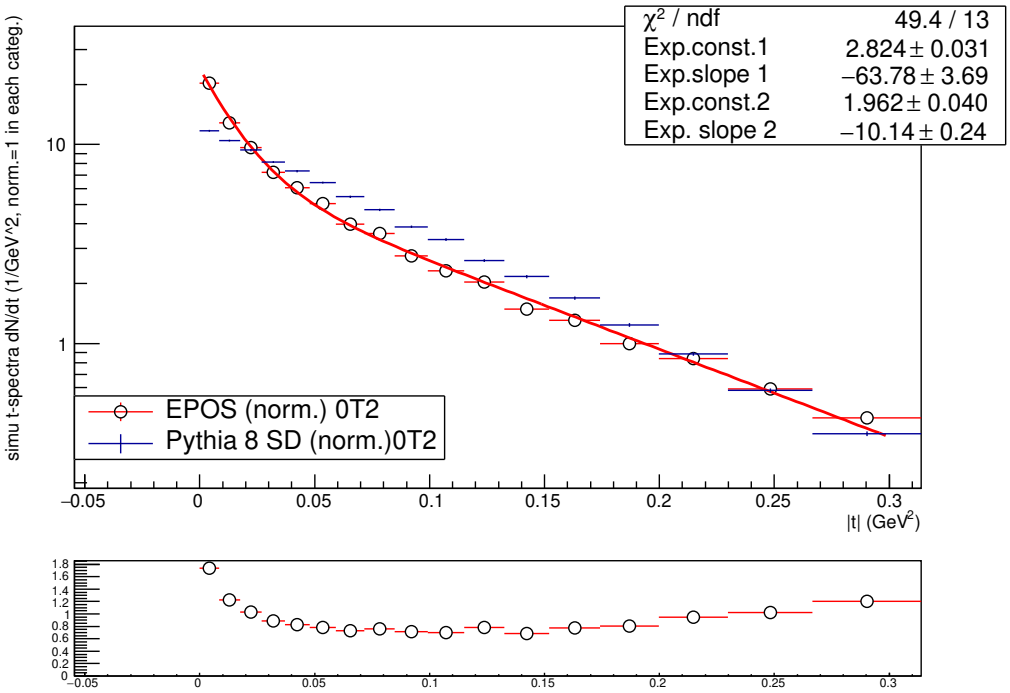

Figure H.17: Normalised differential proton t-spectrum for EPOS and Pythia 8 events in the 0T2 SD class using the generator information. The EPOS t-spectrum is fitted with a double exponential shown as a red line and with parameters given in the box. Ratio of EPOS to Pythia 8 $|t|$-spectra shown in lower box.

Appendix I

Cross section results with EPOS

The total cross section we reported in Chapter 7.1 is an average of Pythia 8 and EPOS unfolded real data, since both MCs have strong points and neither could be excluded. Here we present the cross sections measured using EPOS unfolding. The difference between the two MC-unfolded cross sections we call MC bias, with half the difference assigned as a systematic uncertainty.

Preliminarily, using EPOS for unfolding we find – using only the RPs in 4-5, with 56_bt used for systematic uncertainty estimation, as explained in Chapter 7.1, – a total SD cross section for the SD mass range $2 * 10^{-7} < \xi < 20\%$, i.e. the range $3.1 < M_X < 3100$ GeV/c^2, of 11.46 $\pm$ 0.21 (stat.) $\pm$ 1.03 (sys.[1]) $\pm$ 0.87 (sys.[2]) $\pm$ 0.77 (sys.[3]) $\pm$ 0.46 (sys.[4]). This leads to an MC bias of 0.71 mb for the total cross section.

Doing for comparison the matrix-based class migration with EPOS, without adding the $|t|$-extrapolation correction, we find a total cross section of 11.96 mb $\pm$ 0.27 (stat.) $\pm$ 1.30 (sys.[5]) $\pm$ 0.96 (sys.[6]) $\pm$ 0.48 (sys.[7]). For the class-migration total cross section, the MC bias is therefore 0.78 mb.

Summing the uncertainties in quadrature and adding also a method systematic [8] , this gives a final result for the total cross section unfolded with EPOS of 11.46 $\pm$ 1.80

[1] EPOS closure ratio + RP cross section differences
[2] MC sys., half the difference EPOS - Pythia
[3] Half of SVD minus Bayesian Unfolding
[4] Luminosity
[5] EPOS class-mig. closure ratio + RP cross section differences
[6] MC sys., half the difference EPOS - Pythia
[7] Luminosity
[8] equal to half the difference between unfolded and class-migration corrected

mb (tot.). Here the central value is chosen to be the unfolded cross section, since data unfolding in the best case should be able to model the detector response better than the simple class migration matrix-based method. Starting from the lowest diffractive masses, the individual SD classes were found to have cross sections of 1.79 ± 0.35 mb (tot.) for class 1T2-0T1, 4.77 ± 0.68 mb (tot.) for class 1T2-1T1, 1.91 ± 0.50 mb (tot.) for class 1T2-2T1, and finally 2.98 ± 0.48 mb (tot.) for the highest mass 2T2 class.

Using the 1 000 000 event EPOS inclusive sample for unfolding, the cross sections for the real data segment 1b are presented in Figures I.1 to I.4, with the closure ratio correction used when noted in the figure label.

In Table I.1, you will find cross section values for the individual SD categories extracted from these EPOS unfolded cross sections, with an additional correction for the closure ratio not being 1. The corresponding check for class-migration only is shown in Table I.2. All these values are also shown for the high-background RP 56_tp that is not used, in Appendix J, Table J.2, and the RP 56_bt used only for systematic estimation in Table I.3.

The cross sections summed over all RPs and categories are given in Table I.4.

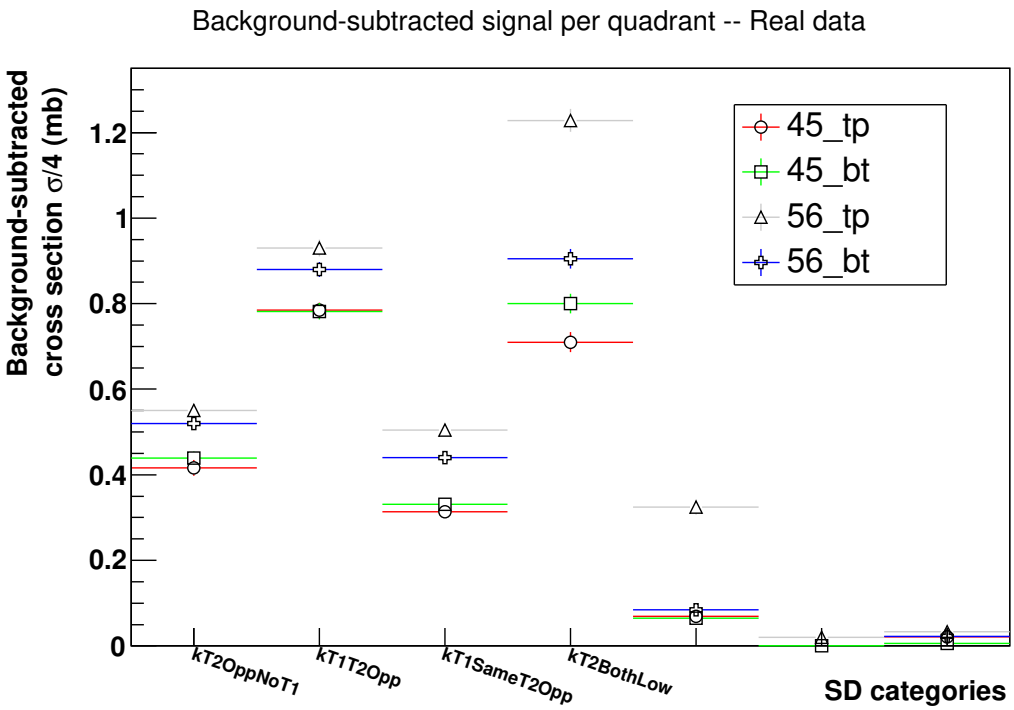

Figure I.1: The acceptance-corrected and background-subtracted net cross section for real data Segment 1b per RP and SD class, before class migration correction and unfolding.

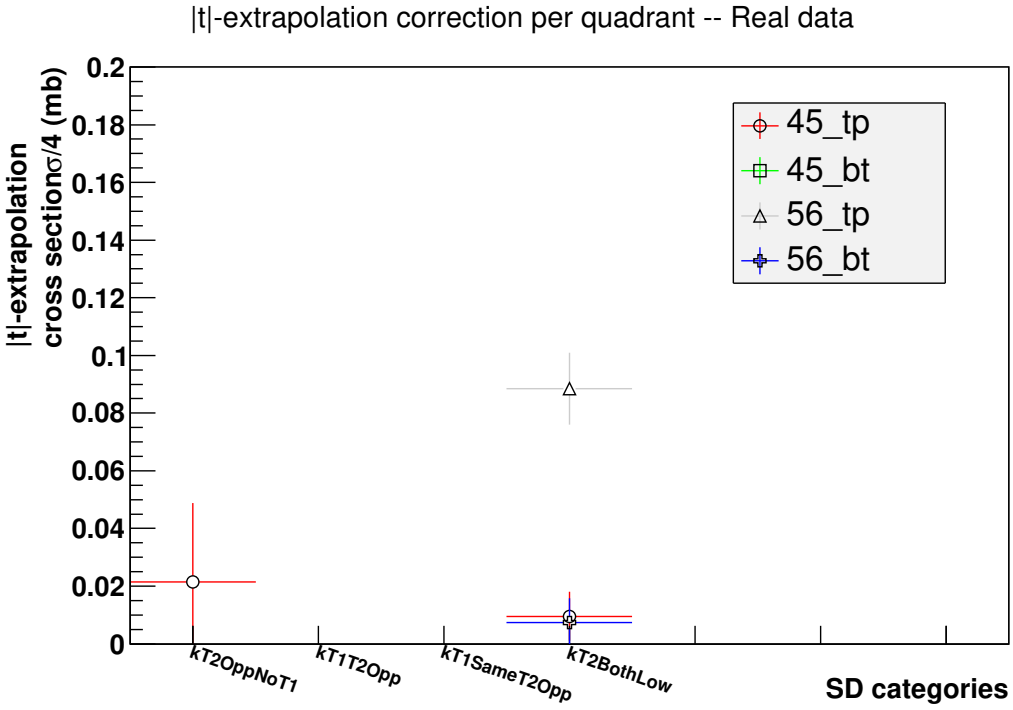

Figure I.2: The $|t|$-extrapolation correction for 1 439 000 real data segment 1b events, per RP and SD class, not closure corrected. The $|t|$-spectra are unfolded with an EPOS sample with 1 000 000 events. Exponential fit between $t(peak+1)$ and $|t|$ = 0.3 GeV^2, taking the difference between extrapolation from $t(peak+1)$ down to the minimum kinematically allowed t and the data points in the same range, as explained in Section 5.1.2. Missing points have negative correction value.

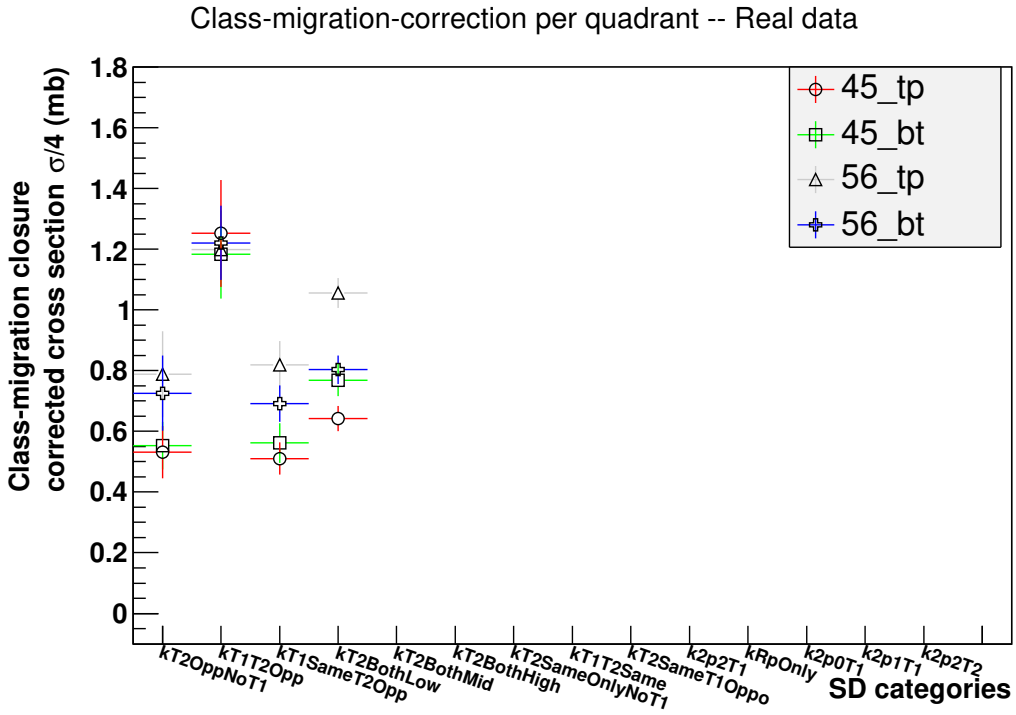

Figure I.3: The background-subtracted, acceptance-corrected and class-migrated net cross section for real data segment per RP and SD class. The class migration uses SD class migration matrix extracted from a 1 000 000 event EPOS inclusive sample with real PU mixed in. Real data sample is 1 439 000 events in Segment 1b. The class migration closure correction is applied. All systematics added in quadrature, including T2 trigger efficiency correction.

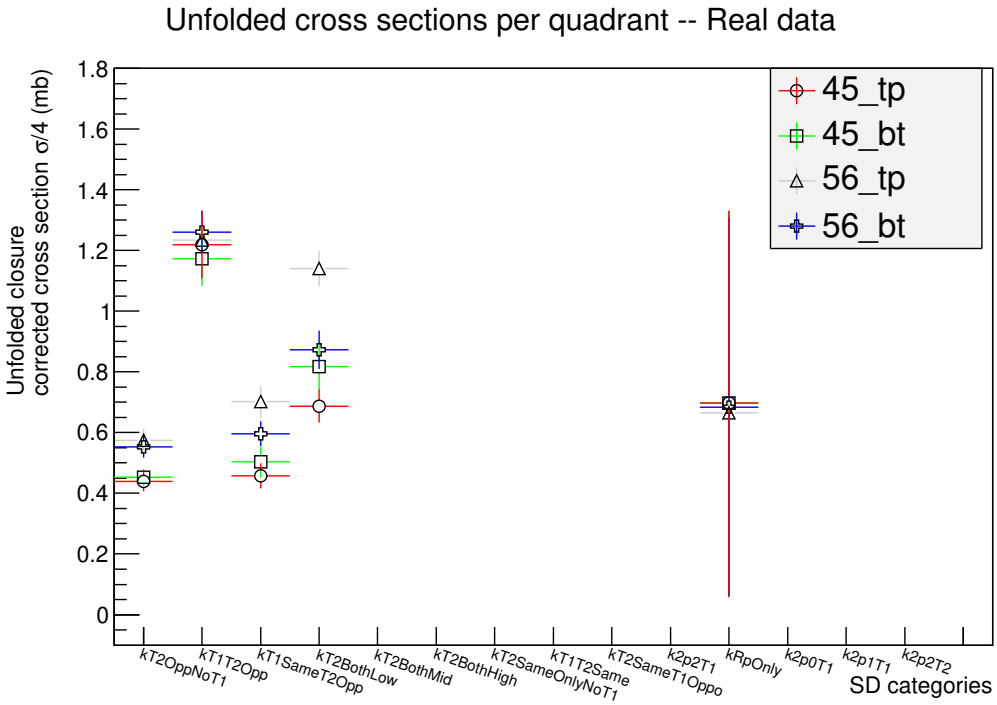

Figure I.4: The final unfolded cross section for real data segment per RP and SD class. Unfolding was done with an EPOS inclusive sample of 1 000 000 events, with real PU mixed in; the real data sample was 1 439 000 events. The closure correction is applied. All systematics added in quadrature, including T2 trigger efficiency correction.

Table I.1: Final unfolded cross sections per SD class after all corrections measured from 1 439 000 events in Segment 1b of the real data. The cross sections are unfolded with an EPOS sample having 1 000 000 events, with real PU mixed in. The table gives the unfolded cross section before closure ratio correction ("Unfold"), and after closure correction ("Closure corr."). The "Weighted rescaled sum" is the corresponding total cross section per SD class. The "RP diff. sys" is the systematic uncertainty estimated from the difference between the cross sections extracted using different RPs. "SVD Bias" is the difference to the quoted Bayesian-unfolded cross sections.

SD class	Unfolded (mb)	SVD Bias (mb)	Closure corr. (mb)	SVD Bias (mb)	RP diff. sys (mb)
45_tp					
1T2-0T1	0.41 ± 0.02	+0.07	$0.44 \pm 0.03 \pm 0.01$(sys)	+0.07	
1T2-1T1	1.03 ± 0.04	+0.10	$1.22 \pm 0.06 \pm 0.10$(sys)	+0.07	
1T2-2T1	0.39 ± 0.02	+0.09	$0.46 \pm 0.02 \pm 0.03$(sys)	+0.10	
2T2	0.60 ± 0.02	+0.05	$0.69 \pm 0.03 \pm 0.08$(sys)	-0.02	
45_bt					
1T2-0T1	0.44 ± 0.02	+0.08	$0.45 \pm 0.03 \pm 0.01$(sys)	+0.07	
1T2-1T1	1.03 ± 0.04	+0.09	$1.17 \pm 0.05 \pm 0.07$(sys)	+0.12	
1T2-2T1	0.41 ± 0.01	+0.09	$0.50 \pm 0.03 \pm 0.05$(sys)	+0.09	
2T2	0.68 ± 0.02	+0.05	$0.82 \pm 0.04 \pm 0.07$(sys)	+0.03	
Weighted	rescaled	sum *4			
1T2-0T1	1.72 ± 0.06		$1.79 \pm 0.08 \pm 0.04$(sys)	+0.29	± 0.04
1T2-1T1	4.11 ± 0.11		$4.77 \pm 0.15 \pm 0.34$(sys)	+0.38	± 0.03
1T2-2T1	1.61 ± 0.04		$1.91 \pm 0.07 \pm 0.16$(sys)	+0.38	± 0.05
2T2	2.57 ± 0.07		$2.98 \pm 0.10 \pm 0.32$(sys)	-0.02	± 0.06

Table I.2: Final class migration-corrected cross sections per SD class after all corrections measured from 1 439 000 events in Segment 1b of the real data. The class migration is done with an EPOS sample having 1 000 000 events, with real PU mixed in. The table gives the class migration-corrected cross section before closure ratio correction ("Class migrated"), and after closure correction ("Class closure corr."). The "Weighted rescaled sum" is the corresponding total cross section per SD class. The "RP diff. sys" is the systematic uncertainty estimated from the difference between the cross sections extracted using different RPs.

SD class	Class migrated (mb)	Class closure corr. (mb)	RP diff. sys (mb)
45_tp			
1T2-0T1	0.39 ± 0.03	$0.53 \pm 0.05 \pm 0.07$(sys)	
1T2-1T1	0.92 ± 0.03	$1.25 \pm 0.06 \pm 0.17$(sys)	
1T2-2T1	0.46 ± 0.03	$0.51 \pm 0.05 \pm 0.03$(sys)	
2T2	0.61 ± 0.03	$0.64 \pm 0.04 \pm 0.02$(sys)	
45_bt			
1T2-0T1	0.42 ± 0.02	$0.55 \pm 0.04 \pm 0.07$(sys)	
1T2-1T1	0.91 ± 0.03	$1.18 \pm 0.05 \pm 0.14$(sys)	
1T2-2T1	0.48 ± 0.03	$0.56 \pm 0.05 \pm 0.04$(sys)	
2T2	0.70 ± 0.03	$0.77 \pm 0.04 \pm 0.03$(sys)	
Weighted	rescaled	sum	*4
1T2-0T1	1.63 ± 0.07	$2.17 \pm 0.13 \pm 0.27$(sys)	± 0.06
1T2-1T1	3.66 ± 0.07	$4.85 \pm 0.16 \pm 0.59$(sys)	± 0.02
1T2-2T1	1.88 ± 0.08	$2.13 \pm 0.14 \pm 0.13$(sys)	± 0.06
2T2	2.64 ± 0.08	$2.80 \pm 0.11 \pm 0.09$(sys)	± 0.05

Table I.3: Final unfolded and class migration-corrected cross sections per SD class after all corrections, measured from 1 439 000 events in Segment 1b of the real data for RP 56_bt, which is used for estimating systematic uncertainties only. The unfolding and class migration is done with an EPOS sample having 1 000 000 events. The table gives the cross sections before closure ratio correction ("Cross section"), and after closure correction ("Closure corr."). "SVD Bias" is the difference to the quoted Bayesian-unfolded cross sections.

SD class	Cross section (mb)	SVD Bias (mb)	Closure corr. (mb)	SVD Bias (mb)
Unfolded 56_bt				
1T2-0T1	0.52 ± 0.02	+0.08	$0.55 \pm 0.03 \pm 0.02$(sys)	+0.11
1T2-1T1	1.16 ± 0.03	+0.04	$1.26 \pm 0.05 \pm 0.05$(sys)	+0.08
1T2-2T1	0.54 ± 0.02	+0.17	$0.60 \pm 0.03 \pm 0.03$(sys)	+0.17
2T2	0.77 ± 0.02	+0.02	$0.87 \pm 0.04 \pm 0.05$(sys)	+0.03
Class migration 56_bt				
1T2-0T1	0.51 ± 0.02		$0.73 \pm 0.06 \pm 0.11$(sys)	
1T2-1T1	1.00 ± 0.03		$1.22 \pm 0.05 \pm 0.11$(sys)	
1T2-2T1	0.66 ± 0.03		$0.69 \pm 0.06 \pm 0.01$(sys)	
2T2	0.77 ± 0.03		$0.80 \pm 0.04 \pm 0.02$(sys)	

Table I.4: Rescaled sum over all RPs of the final unfolded and class migration-corrected cross sections per SD class after all corrections (including closure corrections), measured from 1 439 000 events in Segment 1b of the real data, taken from Tables I.1 – I.2. The unfolding and class migration is done with an EPOS sample with 1 000 000 events. The uncertainties include the statistical uncertainty and the systematic uncertainties due to the closure correction and differences between RPs ("RP diff.+closure", quoted as "sys" below), due to the luminosity ("lumi") and the T2 trigger efficiency correction ("T2")

SD class	Class migrated (mb)	T2 (mb)	Unfolded (mb)	Lumi. (%)	T2 (mb)
1T2-0T1	$2.17 \pm 0.13 \pm 0.34$(sys)	0.03	$1.79 \pm 0.08 \pm 0.08$(sys)	± 4	0.03
1T2-1T1	$4.85 \pm 0.16 \pm 0.62$(sys)	0.04	$4.77 \pm 0.15 \pm 0.37$(sys)	± 4	0.04
1T2-2T1	$2.13 \pm 0.14 \pm 0.19$(sys)	0.01	$1.91 \pm 0.07 \pm 0.21$(sys)	± 4	0.01
2T2	$2.80 \pm 0.11 \pm 0.15$(sys)	0.00	$2.98 \pm 0.10 \pm 0.38$(sys)	± 4	0.00
all, $2 * 10^{-7} < \xi < 20\%$	$11.96 \pm 0.27 \pm 1.30$(sys)	0.08	$11.46 \pm 0.21 \pm 1.03$(sys)	± 4	0.08

Appendix J

SD cross sections for high-background RP 5-6 top

The Tables J.1 – J.2 show – for Pythia 8 and EPOS, respectively – the calculated SD cross sections for the unused RP 5-6 top, that was excluded due to high background. The data set used is the 1 439 000 events from data segment 1b used in Chapter 7.1.

Table J.1: Final unfolded and class-migration corrected cross sections per SD class after all corrections, measured from 1 439 000 events in Segment 1b of the real data for the high-background RP 56_tp. The cross sections are unfolded with a Pythia 8 SD sample, having 210 000 events. The table gives the cross sections before closure ratio correction ("Cross section"), after closure correction ("Closure corr."), and the difference between the cross sections extracted using EPOS and Pythia 8 ("MC Bias"). "SVD Bias" is the difference to the quoted Bayesian-unfolded cross sections. RP not used in final results.

SD class	Cross section (mb)	MC Bias (mb)	Closure corr. (mb)	MC Bias (mb)	SVD Bias (mb)
Unfolded 56_tp					
1T2-0T1	0.55 ± 0.02	-0.01	$0.52 \pm 0.02 \pm 0.03$(sys)	+0.06	-0.02
1T2-1T1	1.07 ± 0.03	+0.13	$1.03 \pm 0.03 \pm 0.02$(sys)	+0.21	-0.14
1T2-2T1	0.85 ± 0.02	-0.23	$0.82 \pm 0.02 \pm 0.02$(sys)	-0.11	-0.17
2T2	1.00 ± 0.02	+0.06	$0.98 \pm 0.04 \pm 0.11$(sys)	+0.16	+0.08
Class migration 56_tp					
1T2-0T1	0.65 ± 0.02	-0.11	$0.67 \pm 0.04 \pm 0.01$(sys)	+0.11	
1T2-1T1	0.95 ± 0.02	+0.10	$1.01 \pm 0.03 \pm 0.03$(sys)	+0.19	
1T2-2T1	0.63 ± 0.03	+0.11	$0.64 \pm 0.04 \pm 0.01$(sys)	+0.18	
2T2	1.11 ± 0.03	-0.04	$1.06 \pm 0.06 \pm 0.03$(sys)	+0.00	

Table J.2: Final unfolded and class-migration corrected cross sections per SD class after all corrections, measured from 1 439 000 events in Segment 1b of the real data for the high-background RP 56_tp. The cross sections are unfolded with an EPOS sample having 1 000 000 events. The table gives the cross sections before closure ratio correction ("Cross section"), and after closure correction ("Closure corr."). "SVD Bias" is the difference to the quoted Bayesian-unfolded cross sections. RP not used in final results.

SD class	Cross section (mb)	Closure corr. (mb)	SVD Bias (mb)
Unfolded 56_tp			
1T2-0T1	0.54 ± 0.02	$0.57 \pm 0.03 \pm 0.03$(sys)	+0.14
1T2-1T1	1.20 ± 0.03	$1.23 \pm 0.05 \pm 0.02$(sys)	+0.09
1T2-2T1	0.62 ± 0.02	$0.70 \pm 0.03 \pm 0.04$(sys)	+0.21
2T2	1.06 ± 0.03	$1.14 \pm 0.04 \pm 0.05$(sys)	+0.12
Class migration 56_tp			
1T2-0T1	0.54 ± 0.02	$0.79 \pm 0.06 \pm 0.12$(sys)	
1T2-1T1	1.05 ± 0.03	$1.20 \pm 0.05 \pm 0.08$(sys)	
1T2-2T1	0.73 ± 0.03	$0.82 \pm 0.07 \pm 0.04$(sys)	
2T2	1.08 ± 0.03	$1.06 \pm 0.05 \pm 0.01$(sys)	

Appendix K

SD cross section background and signal tables

Tables K.1 – K.4 show the raw signal before background subtraction, and the background SD cross sections. The data set used is the 1 439 000 events from data segment 1b used in Chapter 7.1.

Table K.1: Pileup background SD cross sections

SD class	Cross section (μb)	Cross section (μb)
45_tp		56_tp
1T2-0T1	0.7±0.4	0.5±0.3
1T2-1T1	0.1±0.1	1.8±0.7
1T2-2T1	0.7±0.5	1.6±0.6
2T2	5.8±1.7	5.2±1.9
45_bt		56_bt
1T2-0T1	0.2±0.2	0.3±0.3
1T2-1T1	0.7±0.5	0.7±0.4
1T2-2T1	0.2±0.2	0.9±0.5
2T2	1.5±0.5	3.3±1.2

Table K.2: Two-proton background SD cross sections

SD class	Cross section (mb)	Cross section (mb)
45_tp		56_tp
1T2-0T1	0.08±0.01	0.023±0.004
1T2-1T1	0.09±0.01	0.045±0.007
1T2-2T1	0.04±0.01	0.008±0.002
2T2	0.10±0.01	0.044±0.008
45_bt		56_bt
1T2-0T1	0.068±0.009	0.034±0.005
1T2-1T1	0.09±0.01	0.033±0.005
1T2-2T1	0.032±0.006	0.008±0.002
2T2	0.07±0.01	0.037±0.008

Table K.3: SD signal cross sections before background subtraction

SD class	Cross section (mb)	Cross section (mb)
45_tp		56_tp
1T2-0T1	0.49±0.01	0.57±0.01
1T2-1T1	0.88±0.02	0.98±0.02
1T2-2T1	0.35±0.01	0.51±0.01
2T2	0.81±0.02	1.28±0.03
45_bt		56_bt
1T2-0T1	0.51±0.01	0.55±0.01
1T2-1T1	0.87±0.02	0.91±0.02
1T2-2T1	0.36±0.01	0.45±0.01
2T2	0.87±0.02	0.94±0.02

Table K.4: SD signal cross sections after background subtraction

SD class	Cross section (mb)	Cross section (mb)
45_tp		56_tp
1T2-0T1	0.42±0.02	0.55±0.01
1T2-1T1	0.78±0.02	0.93±0.02
1T2-2T1	0.31±0.01	0.50±0.01
2T2	0.71±0.02	1.23±0.03
45_bt		56_bt
1T2-0T1	0.44±0.02	0.52±0.01
1T2-1T1	0.78±0.02	0.88±0.02
1T2-2T1	0.33±0.01	0.44±0.01
2T2	0.80±0.02	0.90±0.02

Appendix L

SD class T1 and T2 multiplicities

In Figures L.1 – L.8 we show the multiplicities per T1 or T2 arm, for the SD classes with T2 tracks. For the SD class 2T2 we do not show T1 multiplicity since it is not used in classification; for the class 1T2-2T1 the intermediate T1 arm on the same side as the T2 trigger is also not used for classification, and may thus have zero entries. For the fractions with zero entries, see the following section.

L.1 T1 and T2 inefficiency systematic uncertainties

The probability to have an interior rapidity gap covering a full arm of T1 can be ascertained from the data, by looking for events that are classified as high mass or very high mass, since we only demand a proton, tracks in T2 opposite the proton, and tracks in the nearest arm of T1 and T2 to the proton. The intermediate T1 arms may be empty, but we still classify the event as 1T2-2T1 or 2T2. Looking at Figure L.9, you see that 4% to 8% of events have empty T1 arms for all three cases in the real data, and in EPOS MC, while the Pythia 8 SD-only sample has a much lower zero probability on the opposite side from the proton.

The probability to have a rapidity gap cover all of T2 in the arm opposite to the proton can be crudely estimated by assuming all events with a topology p+T2+gap – that is, with a proton in the same arm as the T2 tracks – are actually SD class 2T2, with an extra rapidity gap covering T2 in the opposite arm. To remove a large source of pileup background to both classes, we apply a beam halo cut and all other fiducial cuts on the proton for both 2T2 and 1T2-background.

As you can see in Figure L.10, the fraction of events in 1T2-background after

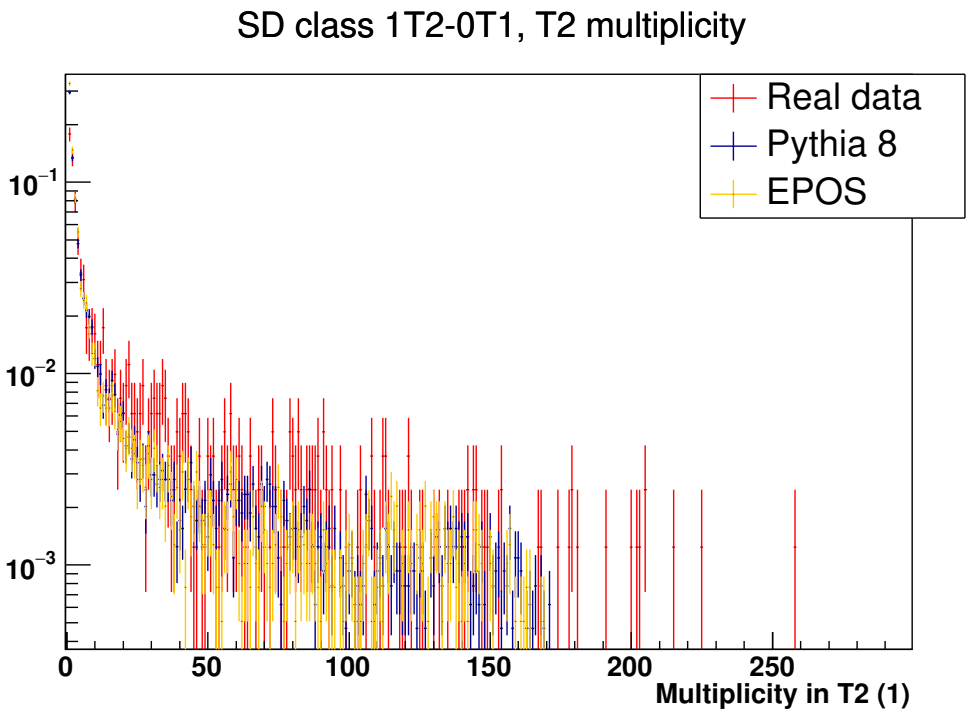

Figure L.1: Multiplicity in T2 for SD class 1T2-0T1. Histogram normalised to 1. Real Data is 1 439 000 events from Segment 1b. The Pythia 8 SD sample has 540 000 events, while the EPOS inclusive sample was 250 000 events, with 27 000 SD events.

these cuts is 12% to 19% for the real data and EPOS, but only 3% for Pythia 8. This is presumably since the latter is SD only, whereas the inclusive EPOS sample also contains other diffractive processes. This was seen in the generator-level classification, where the Pythia SD sample did not have any events in the anti-SD 1T2 classes, while EPOS had approximately one tenth as many such events as SD class 2T2 events.

Since any SD events found in anti-SD class 1T2-background due to the proposed extra rapidity gap covering 1T2 must belong to the very high mass 2T2 SD class, we checked the ξ spectrum of the putative SD events in the background 1T2 class, but found it covered the same high-ξ range as the 2T2 SD signal class, because of the low-ξ suppression by the BH selection cut applied.

In contrast to the case for intermediate T1 arms with no tracks, if there are zero tracks in the T2 arm opposite the proton, we do not classify this event as a 2T2 SD event. This means any T1 inefficiency due to extra rapidity gaps only moves SD events between SD classes, for example an event in class 1T2-2T1 being seen in class 1T2-1T1. T2 inefficiency, on the other hand, will in principle give a correction of 12% or

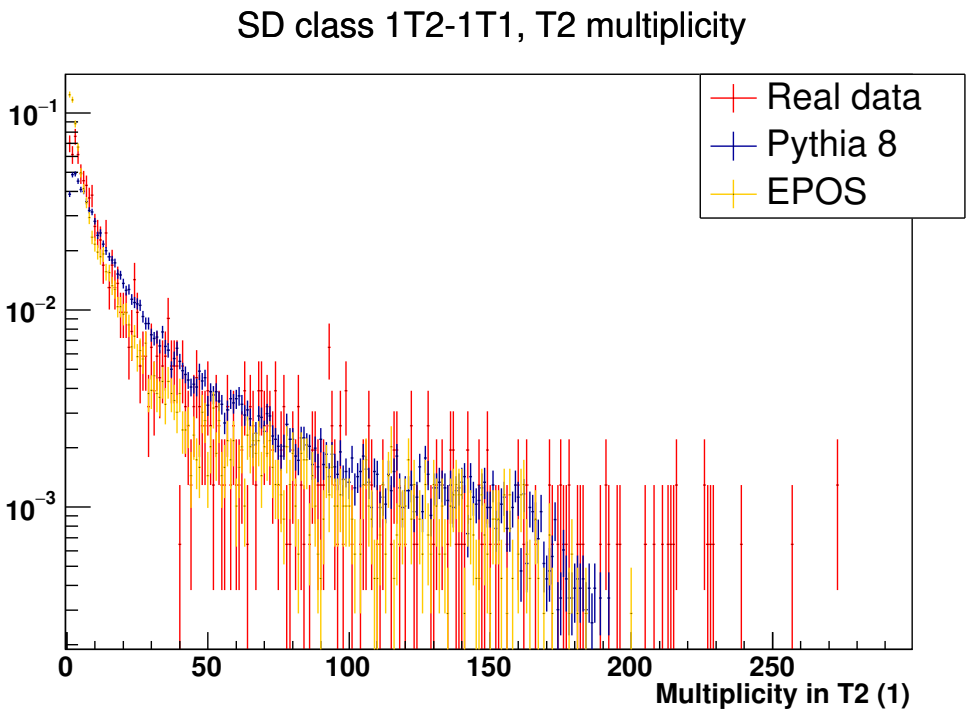

Figure L.2: Multiplicity in T2 for SD class 1T2-1T1. Histogram normalised to 1. Real Data is 1 439 000 events from Segment 1b. The Pythia 8 SD sample has 540 000 events, while the EPOS inclusive sample was 250 000 events, with 27 000 SD events.

less [1] for the 1T2 SD classes where an extra rapidity gap covering T2 would move the event into the 0T2 SD class that we do not trigger on. For the 2T2 SD class we could do a more precise calculation since we do trigger the 1T2-background classes.

[1] Correction from data, assuming all of the wrong-side 1T2 events are SD 2T2 events; in actuality the DP background estimation for these 1T2 anti-SD classes seems to make the background-subtracted ratio $N(1T2\text{-wrong})/\text{N(2T2)} \approx 3\%$

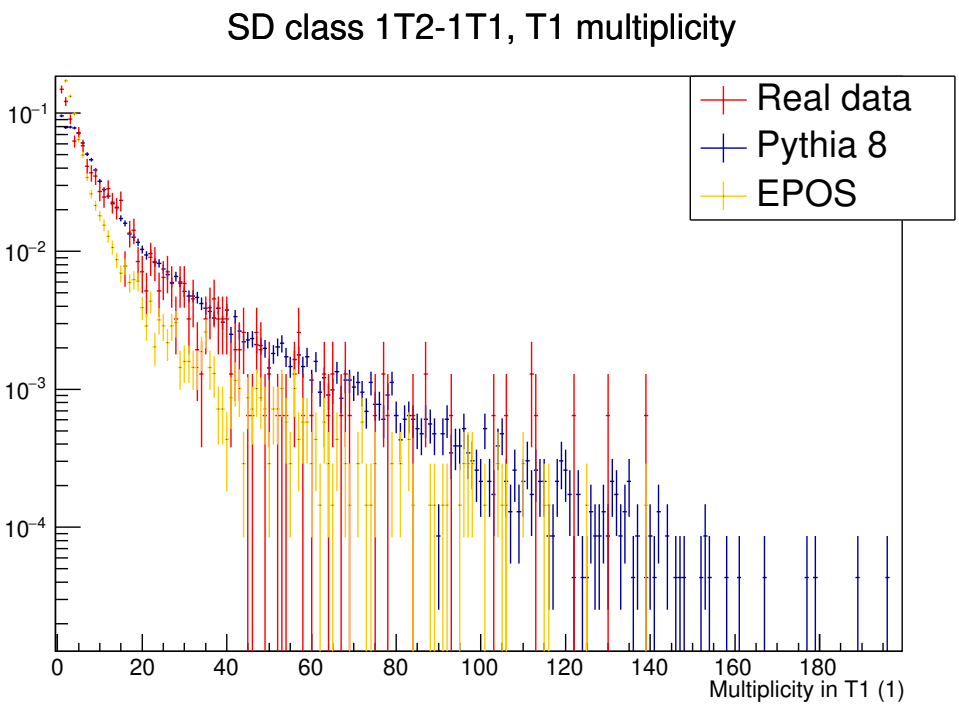

Figure L.3: Multiplicity in T1 for SD class 1T2-1T1. Histogram normalised to 1. Real Data is 1 439 000 events from Segment 1b. The Pythia 8 SD sample has 540 000 events, while the EPOS inclusive sample was 250 000 events, with 27 000 SD events.

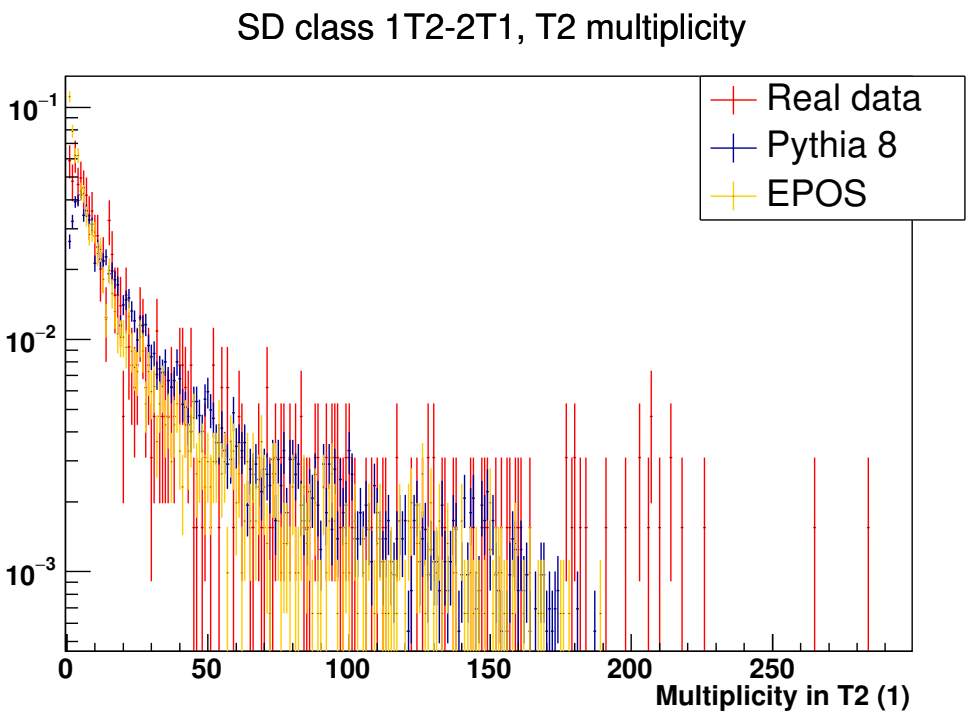

Figure L.4: Multiplicity in T2 for SD class 1T2-2T1. Histogram normalised to 1. Real Data is 1 439 000 events from Segment 1b. The Pythia 8 SD sample has 540 000 events, while the EPOS inclusive sample was 250 000 events, with 27 000 SD events.

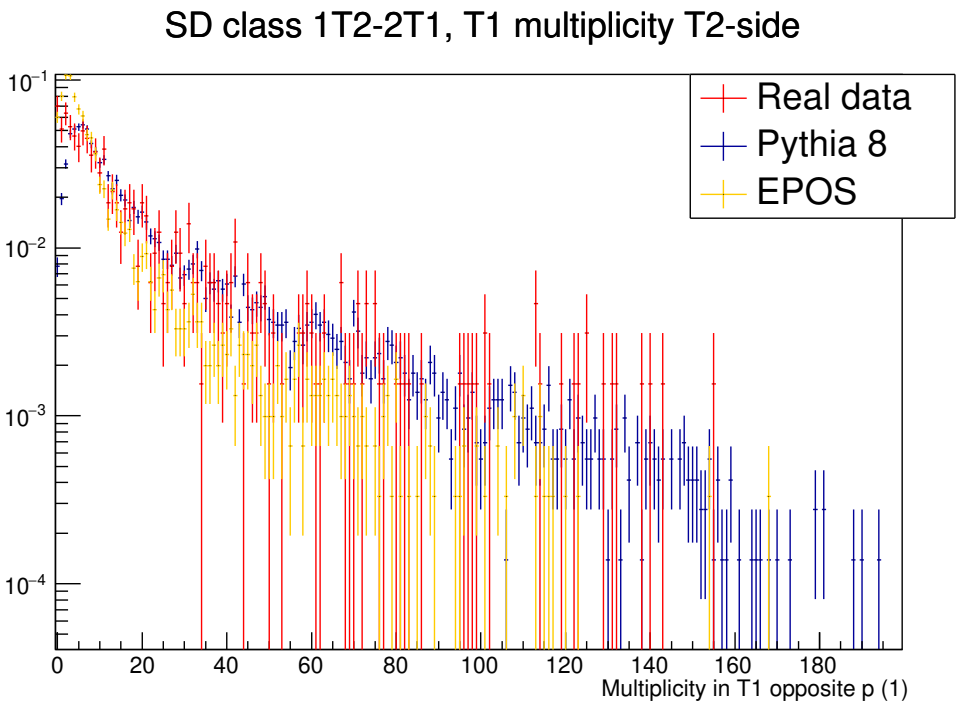

Figure L.5: Multiplicity in T1 arm in the middle for SD class 1T2-2T1. Histogram normalised to 1. Real Data is 1 439 000 events from Segment 1b. The Pythia 8 SD sample has 540 000 events, while the EPOS inclusive sample was 250 000 events, with 27 000 SD events.

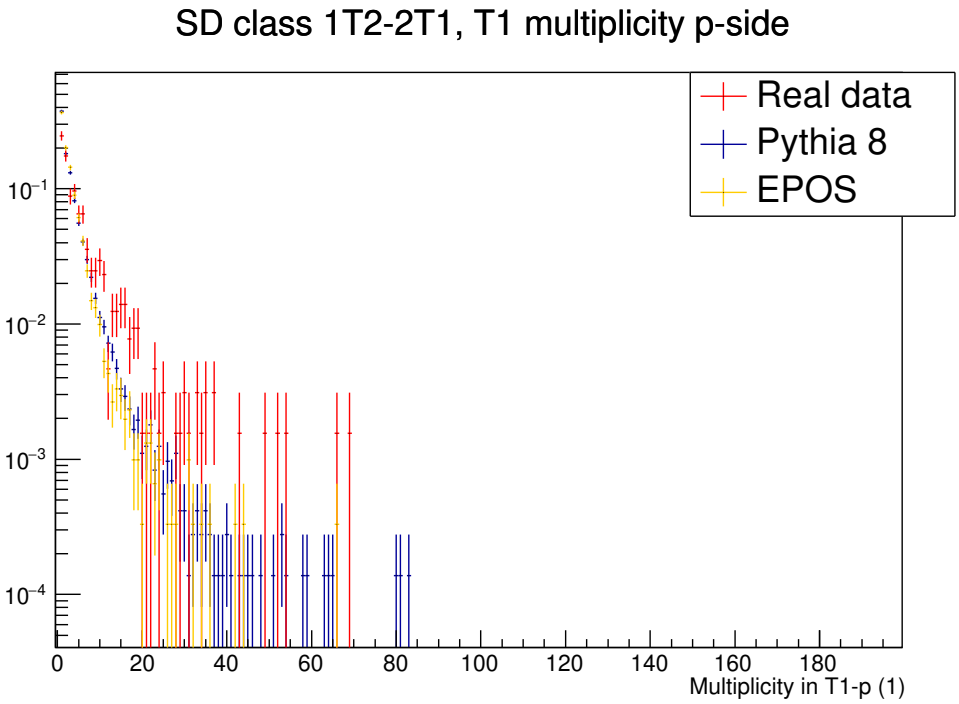

Figure L.6: Multiplicity in T1 (same arm as proton) for SD class 1T2-2T1. Histogram normalised to 1. Real Data is 1 439 000 events from Segment 1b. The Pythia 8 SD sample has 540 000 events, while the EPOS inclusive sample was 250 000 events, with 27 000 SD events.

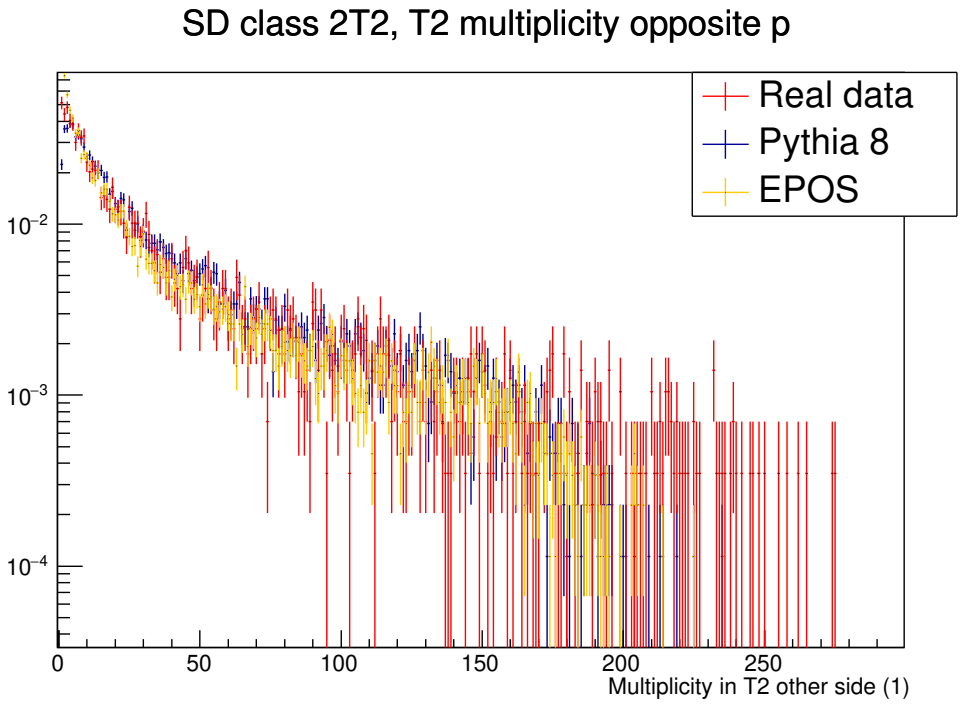

Figure L.7: Multiplicity in T2, in opposite arm from proton for SD class 2T2. Histogram normalised to 1. Real Data is 1 439 000 events from Segment 1b. The Pythia 8 SD sample has 540 000 events, while the EPOS inclusive sample was 250 000 events, with 27 000 SD events.

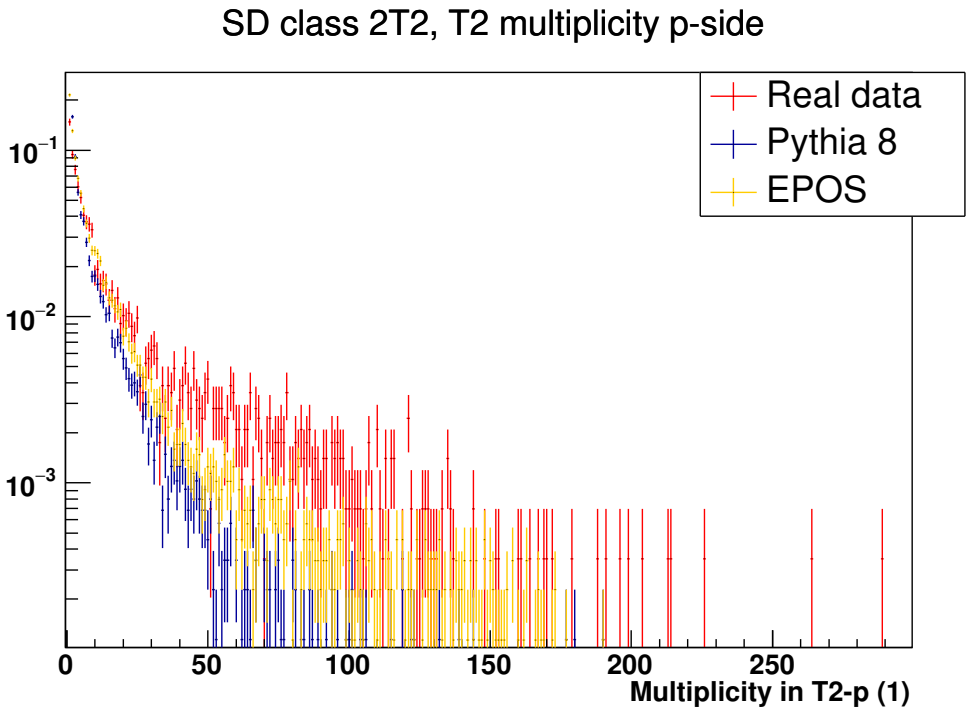

Figure L.8: Multiplicity in T2, in same arm as proton for SD class 2T2. Histogram normalised to 1. Real Data is 1 439 000 events from Segment 1b. The Pythia 8 SD sample has 540 000 events, while the EPOS inclusive sample was 250 000 events, with 27 000 SD events.

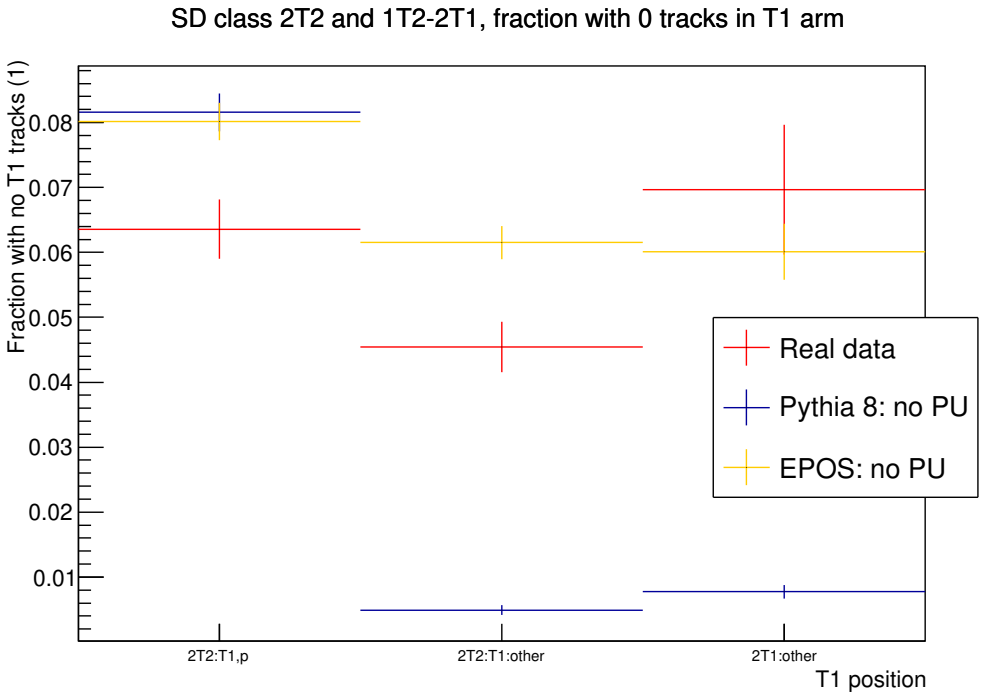

Figure L.9: Fraction of events with zero multiplicity in T1, for SD classes 2T2 and 1T2-2T1. Only T1 arms not used for classification, i.e. the arm between T2 opposite the proton and T1 or T2 on the proton side. Real Data is 100 000 events from Segment 1b. The Pythia 8 SD sample has 100 000 events, as does the EPOS inclusive sample, with approximately 11 000 SD events. No PU is mixed into the MC samples, and no fiducial cuts are applied on the proton, see Section L.1.

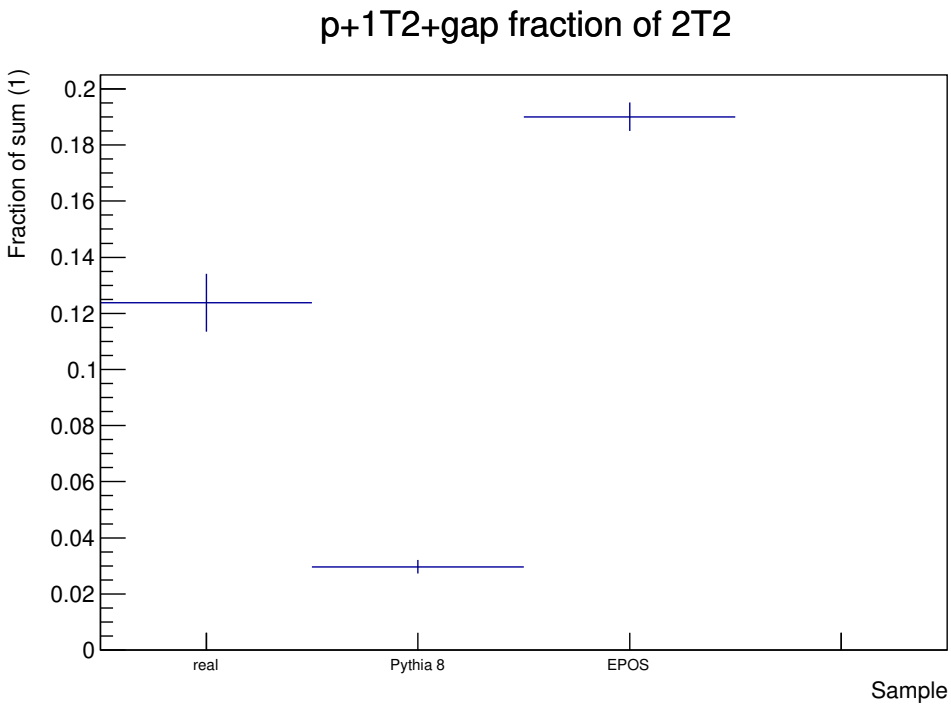

Figure L.10: Out of events in SD classes 2T2 and 1T2-wrong-side, plot of fraction in the latter class. Real Data is 100 000 events from Segment 1b. The Pythia 8 SD sample has 100 000 events, as does the EPOS inclusive sample, with approximately 11 000 SD events. No PU is mixed into the MC samples, but all fiducial cuts, including BH, are applied on the proton, see Section L.1.

Appendix M

SD class coverage in comparisons to other experiments

In Section 7.4.1, we computed the weighted cross sections for comparison with the ATLAS SD measurement [29], among others. The weights expected based on our rapidity coverage [1], and that based on the MC differential cross sections in $\log_{10}\xi$ are shown in Tables M.1 – M.3.

Table M.1: SD class weights for events within the ATLAS acceptance region ξ =0.01% – 2.5%. Rap. = based on rapidity coverage for our detectors. Pythia and EPOS, based on fraction of events in each class that fall in the ATLAS ξ region. See Appendix M.

SD class	Rap.	Pythia 8	EPOS
0T2	0	0.043	0.109
1T2-0T1	0	0	0
1T2-1T1	0.435	0.514	0.345
1T2-2T1	0.965	0.692	0.659
2T2	0	0.088	0.064

[1] See Table 5.1

Table M.2: SD class weights for events within the CMS acceptance region $\log_{10}\xi$= -5.5 – -2.5. Rap. = based on rapidity coverage for our detectors. Pythia and EPOS, based on fraction of events in each class that fall in the CMS ξ region. See Appendix M.

SD class	Rap.	Pythia 8	EPOS
0T2	0	0.044	0.143
1T2-0T1	0	0.020	0.007
1T2-1T1	0.883	0.842	0.755
1T2-2T1	0	0.073	0.119
2T2	0	0.001	0.001

Table M.3: SD class weights for events within the ALICE acceptance region M_X <200 GeV. Rap. = based on rapidity coverage for our detectors. Pythia and EPOS, based on fraction of events in each class that fall in the ATLAS ξ region. See Appendix M.

SD class	Rap.	Pythia 8	EPOS
0T2	1	0.965	0.797
1T2-0T1	1	1.000	0.957
1T2-1T1	0.834	0.762	0.810
1T2-2T1	0	0.005	0.012
2T2	0	0.000	0.000

Appendix N

QGSJet $|t|$- and ξ-spectra

Since we see a double exponential in the EPOS MC $|t|$-spectra for all 1T2 SD classes, we were interested in finding out if other MCs also predicted this type of behaviour. Therefore we asked the author of QGSJet for representative $|t|$-spectra covering the diffractive mass ranges of our 1T2 SD classes. In Figures N.1 – N.4 we tried to do a double exponential fit

$$f(|t|) = exp(A_1 + B_1 * |t|) + exp(A_2 + B_2 * |t|) \tag{N.1}$$

with the slopes constrained to the regions $B_1 < -18$ and $-18 < B_2 < -2$. Uncertainties were not given, so we assumed a Poisson distribution with a global per-histogram scaling constant, and that the bin with the smallest value corresponded to 10 entries. This was an underestimate, as you can see from the very small $\chi^2/d.o.f.$ in Figure N.2. Comparing the two Figures, you see that the 1T2-1T1 class may give a good fit, but the 1T2-0T1 class certainly does not, since a double exponential only has one inflection point, whereas the QGSJet distribution has two. The classes 1T2-2T1 and 2T2, on the other hand, seem to be described by a single exponential only (reported uncertainties are overestimated, as described above). For the class 2T2 we would expect a turnoff at finite $|t_{min}|$, as described in Chapter 6.3.3, and seen in Figure 6.24. This absence may be due to exclusion from these "SD" spectra of Reggeon processes that dominate at $\xi < -10\%$.

The SD mass spectrum, containing both high mass (HMD) and low mass diffraction (LMD), is presented in Figure N.13. The dip seen in the class 1T2-0T1 $|t|$-spectrum may come from the LMD component having a slope and a minimum in analogy with the corresponding elastic scattering process[1]. To check this, we also present

[1] Priv.comm. from the author of QGSJet

two tunes of QGSJet with deemphasized LMD; one called "+" with more HMD and the same amount of LMD as the default tune, while the tune called "-" has less LMD, and the same amount of HMD. The $|t|$-fits for these tunes are given in Figures N.5 – N.12, and the fitted slopes are given in Table N.1.

Table N.1: For QGSJet MC default tune and two tunes with relatively less LMD, the fitted $|t|$-slopes for generated protons in true SD events, with a sum of two exponentials. SD classes divided according to diffractive mass, not topology. Fit range is $0< |t| <0.4$ GeV^2. Wrongly fitted parameters in parentheses. Single = one exponential, for comparison with real data and other MCs. See section N.

Category	Larger slope	Smaller slope	Single Exp.
QGSJet	default	tune	
1T2-0T1	-32.09 ± 0.13	(-2.43 ± 0.06)	(-11.78 ± 0.08)
1T2-1T1	-27.3 ± 0.7	-5.56 ± 0.12	-8.25 ± 0.08
1T2-2T1	(-18 ± 11)	-5.33 ± 0.17	-5.91 ± 0.15
2T2	(-18 ± 11)	-4.67 ± 0.23	-5.06 ± 0.25
QGSJet	tune	'+'	
1T2-0T1	-29.11 ± 0.23	(-4.71 ± 0.08)	(-10.61 ± 0.07)
1T2-1T1	-25.5 ± 1.0	-6.38 ± 0.13	-8.47 ± 0.07
1T2-2T1	(-18.0 ± 7.8)	-5.77 ± 0.15	-6.28 ± 0.12
2T2	(-18 ± 12)	-4.96 ± 0.22	-5.30 ± 0.23
QGSJet	tune	'-'	
1T2-0T1	-31.91 ± 0.24	(-4.01 ± 0.08)	(-9.49 ± 0.08)
1T2-1T1	-26.3 ± 1.1	-6.11 ± 0.14	-8.09 ± 0.09
1T2-2T1	(-18.0 ± 7.6)	-5.38 ± 0.17	-5.94 ± 0.15
2T2	(-18 ± 13)	-4.62 ± 0.25	-4.97 ± 0.27

The cross sections given in Table 7.10 were provided by the QGSJet author, where SD-like means "True SD" plus non-SD events that have one proton with ξ less than 20%.

The cross sections for the different tunes of QGSJet are given in Table N.2. They are numerically integrated from the table of values used to produce among others Fig-

ure N.13; using different interpolations (linear or Simpson's), we estimate an uncertainty around 6%, since no error bars were given for this table, either. Note the very low cross section for SD in 2T2, compared with both EPOS and Pythia. This is contrary to the finding in Chapter 4.1.2 that QGSJet has more high-ξ protons than Pythia 8, and is explained by most such events not being considered "true" SD, and instead being either DD or nondiffractive with a randomly produced rapidity gap during hadronisation (priv.comm. from QGSJet author).

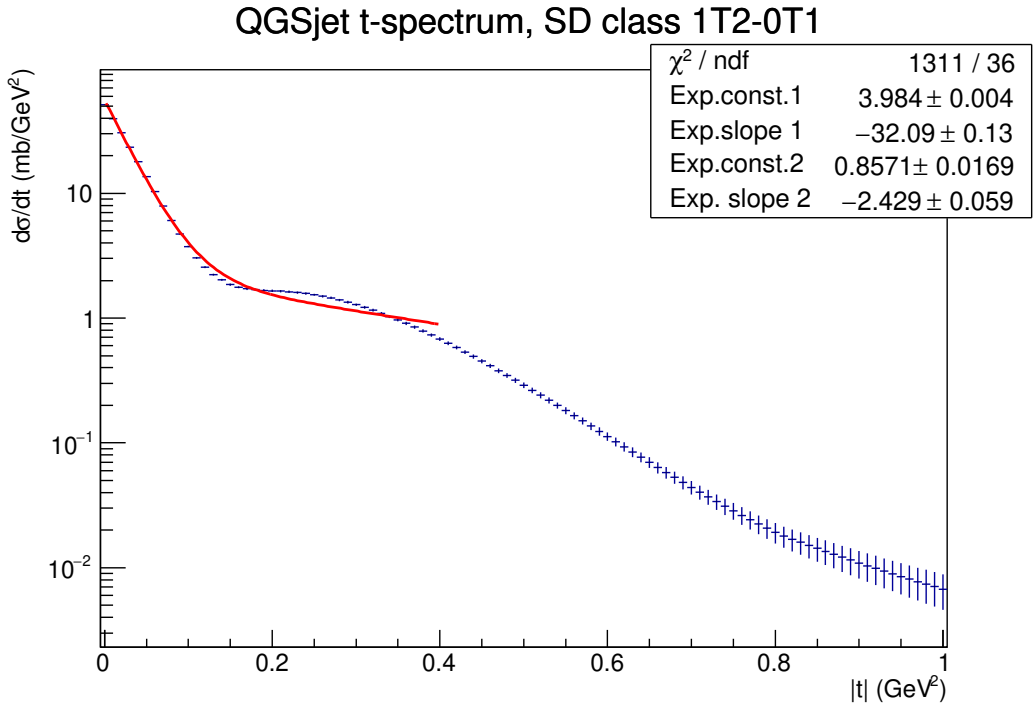

Figure N.1: Double exponential fit of QGSJet predicted $|t|$-spectrum for the 1T2-0T1 SD class. Histogram provided by the author of QGSJet (priv.comm.), see also [78,115]

N.1 QGSJet T2-trigger SD selection on inclusive sample

In the previous section we showed QGSJet predictions for true SD events, including very small predictions for the SD cross section in high mass SD classes 1T2-2T1 and 2T2. To better compare the QGSJet prediction with our data, we asked Ostapchenko for cross sections based on our SD trigger topology, evaluated for inclusively produced

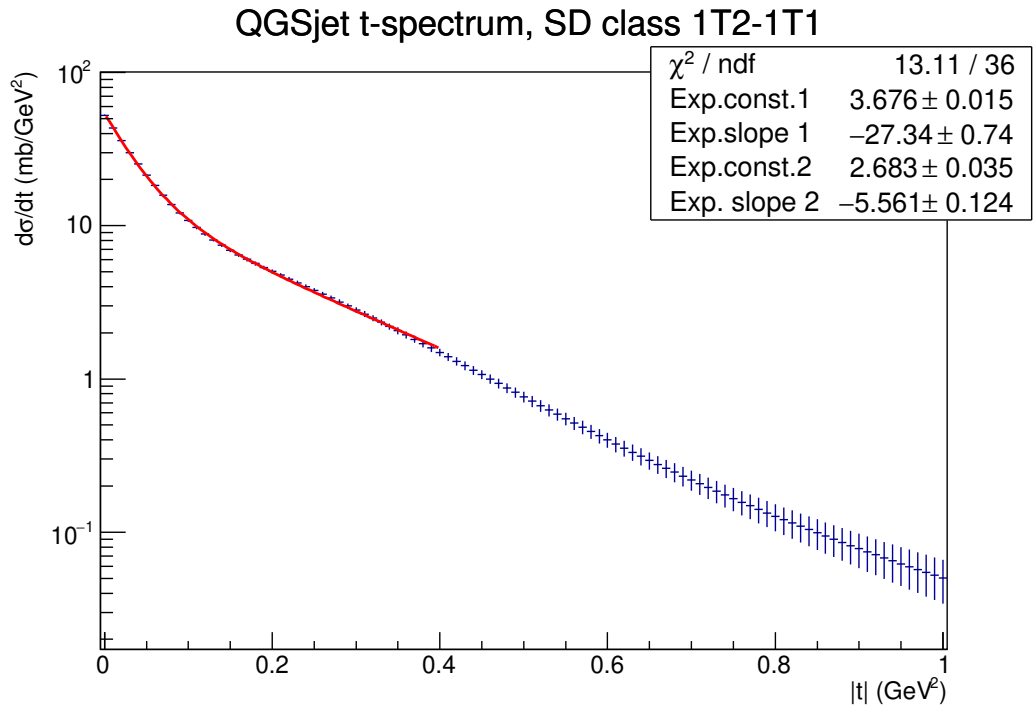

Figure N.2: Double exponential fit of QGSJet predicted $|t|$-spectrum for the 1T2-1T1 SD class. Histogram provided by the author of QGSJet (priv.comm.), see also [78,115]

SD, DD and nondiffractive ND events. Central diffraction (CD) also played a small role.

The trigger demand was for some generated particles in the T2 acceptance region $5.3 < |\eta| < 6.5$ in the arm opposite the proton, and no tracks in the T2 region in the proton-side arm. We also asked for one proton with less than $\xi = 20\%$ momentum loss, and for diffractive masses above 1.15 TeV, tracks in the T2 acceptance in both arms. This 1T2 demand suppressed most of the lowest SD class that nominally corresponds to the 0T2 topology. The cross sections per class are shown in Table N.3, and as a mass spectrum in Figure N.21. As you can see, "True SD" dominates up to the class 1T2-1T1, so we show one differential t-spectrum (of triggered true SD) for these SD classes in Figures N.14 – N.16, while for the highest two classes we show both the total triggered and true SD only spectra, in Figures N.17 – N.20. In these plots the two slopes were constrained to the regions $B_1 < -18$ and $-18 < B_2 < -2$, except for the highest two classes where the dividing line was put at $B_1 = -12$. Because of the small-$|t|$ turnoff visible in 2T2, we raised the lower limit of the fit to $|t|$=0.05 GeV^2; note that this turnoff was not visible in Figures N.4, N.11 – N.12, which may indicate

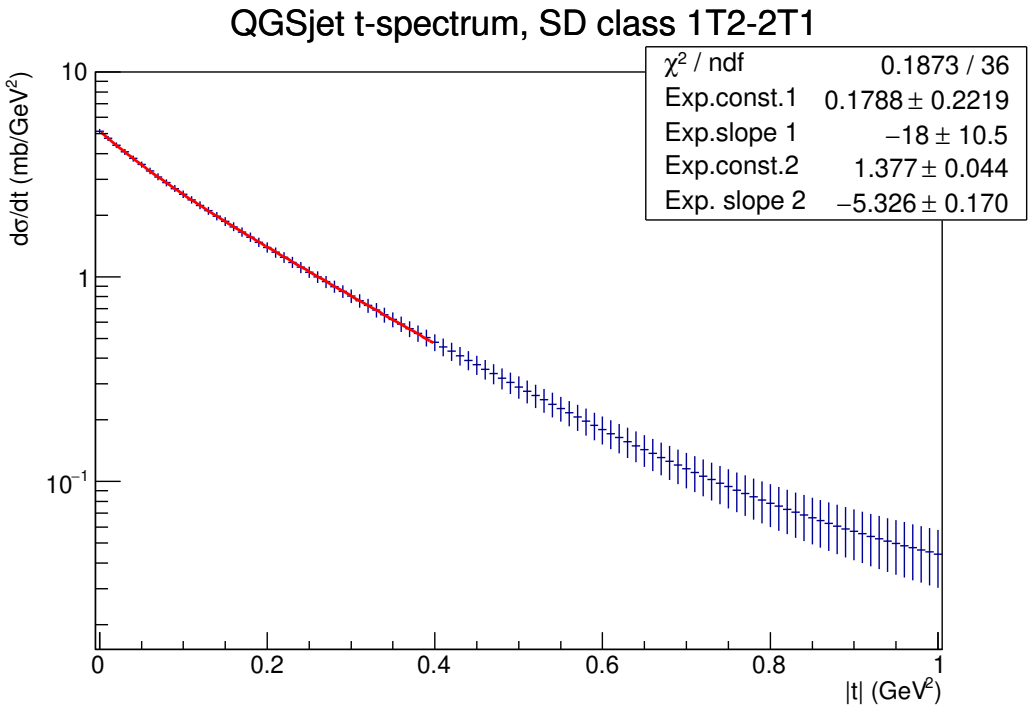

Figure N.3: Double exponential fit of QGSJet predicted $|t|$-spectrum for the 1T2-2T1 SD class. Histogram provided by the author of QGSJet (priv.comm.), see also [78,115]

changes in the MC between the two, since we expect the turnoff due to non-zero ξ, as explained in Chapter 6.3.3. Looking at all these fits, it seems a double exponential improves the fit over a single exponential for all classes expect 2T2, since the latter has a higher slope at small $|t|$ only for the ND-dominated Figure N.19, while fitting the true SD 2T2 we hit the slope constraint at $B_1 = -12$.

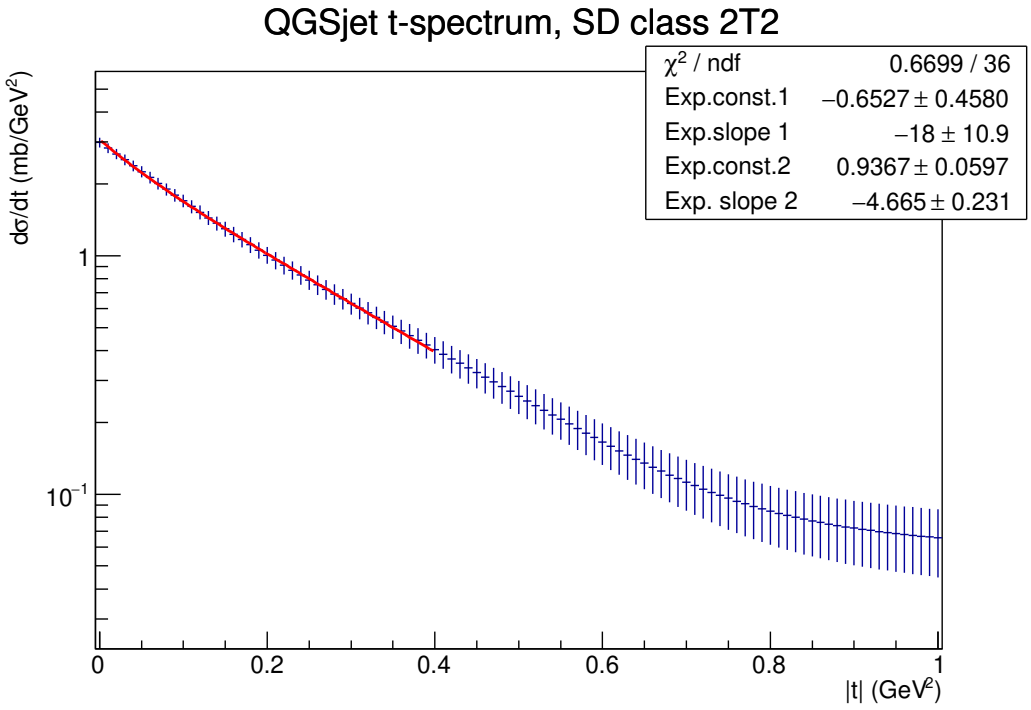

Figure N.4: Double exponential fit of QGSJet predicted $|t|$-spectrum for the 2T2 SD class. Histogram provided by the author of QGSJet (priv.comm.), see also [78, 115]

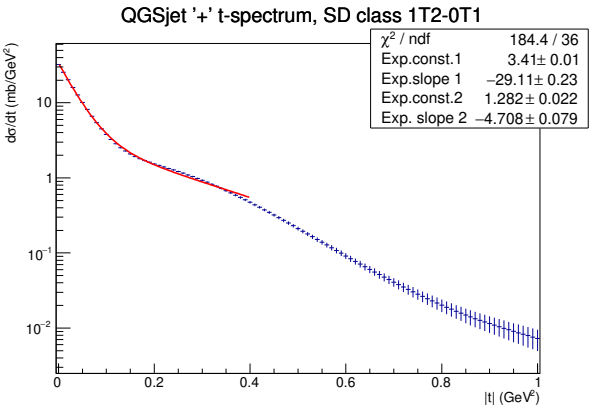

Figure N.5: Double exponential fit of QGSJet predicted $|t|$-spectrum for the 1T2-0T1 SD class, Tune '+'. Histogram provided by the author of QGSJet (priv.comm.), see also [78, 115]

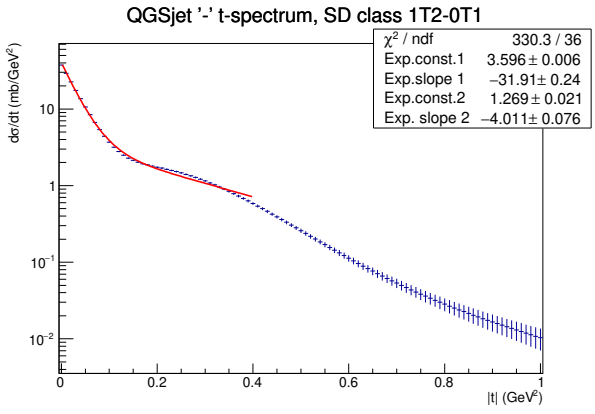

Figure N.6: Double exponential fit of QGSJet predicted $|t|$-spectrum for the 1T2-0T1 SD class, Tune '-'. Histogram provided by the author of QGSJet (priv.comm.), see also [78, 115]

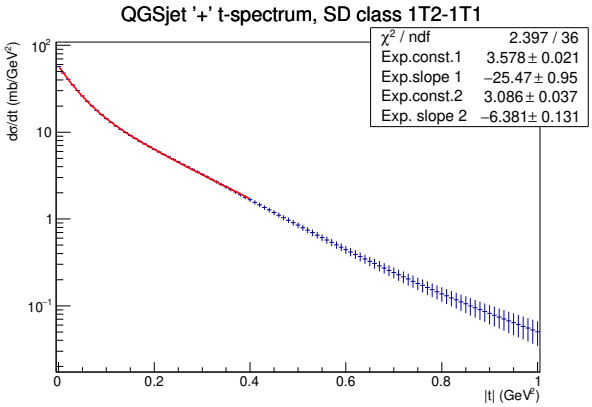

Figure N.7: Double exponential fit of QGSJet predicted $|t|$-spectrum for the 1T2-1T1 SD class, Tune '+'. Histogram provided by the author of QGSJet (priv.comm.), see also [78, 115]

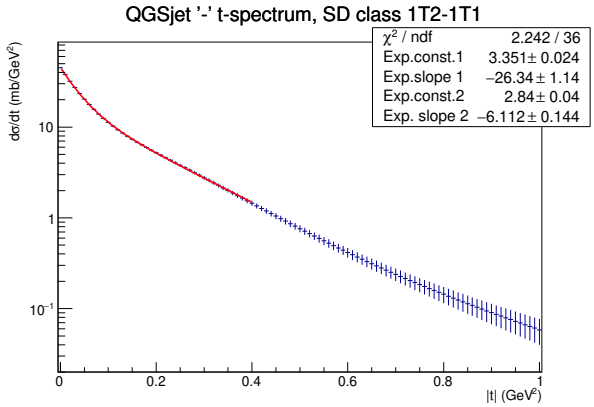

Figure N.8: Double exponential fit of QGSJet predicted $|t|$-spectrum for the 1T2-1T1 SD class, Tune '-'. Histogram provided by the author of QGSJet (priv.comm.), see also [78, 115]

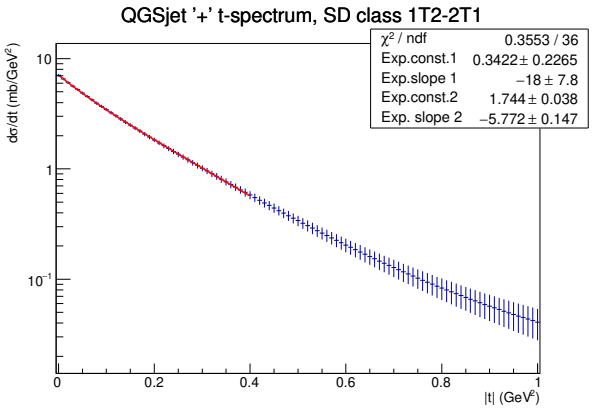

Figure N.9: Double exponential fit of QGSJet predicted $|t|$-spectrum for the 1T2-2T1 SD class, Tune '+'. Histogram provided by the author of QGSJet (priv.comm.), see also [78, 115]

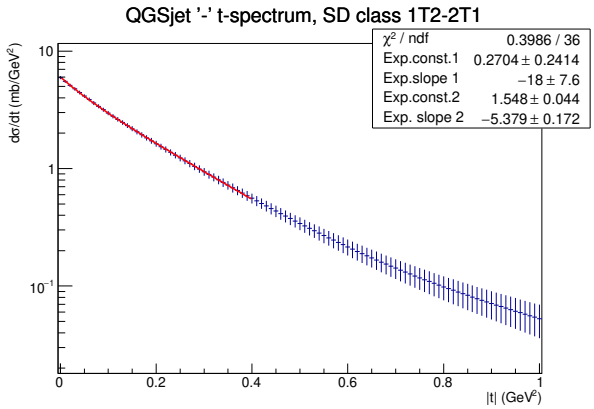

Figure N.10: Double exponential fit of QGSJet predicted $|t|$-spectrum for the 1T2-2T1 SD class, Tune '-'. Histogram provided by the author of QGSJet (priv.comm.), see also [78, 115]

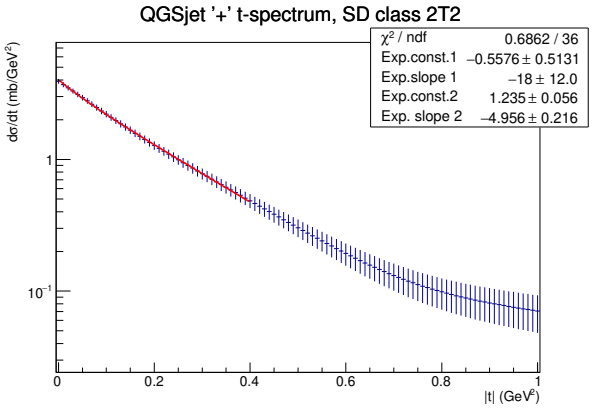

Figure N.11: Double exponential fit of QGSJet predicted $|t|$-spectrum for the 2T2 SD class, Tune '+'. Histogram provided by the author of QGSJet (priv.comm.), see also [78, 115]

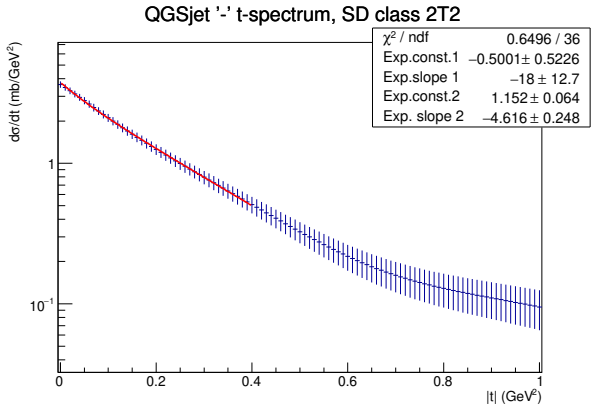

Figure N.12: Double exponential fit of QGSJet predicted $|t|$-spectrum for the 2T2 SD class, Tune '-'. Histogram provided by the author of QGSJet (priv.comm.), see also [78, 115]

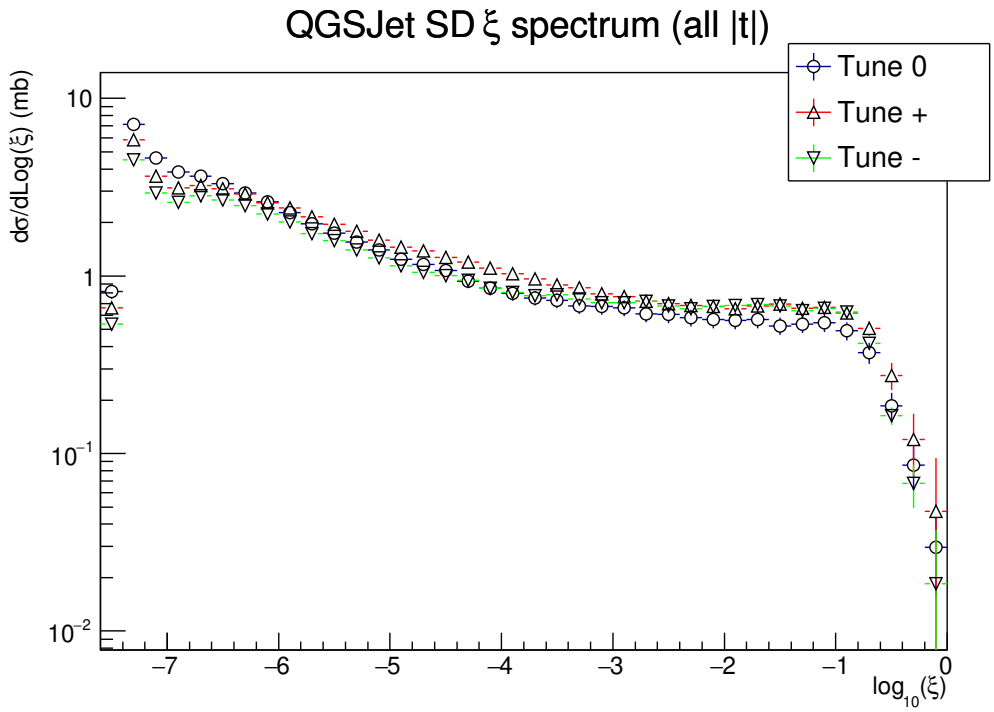

Figure N.13: QGSJet predicted diffractive mass spectrum for SD (sum of high mass and low mass diffraction components, for all $|t|$ values). Histogram provided by the author of QGSJet (priv.comm.), see also [78, 115]. Tunes '+' and '-' have relatively smaller low mass component, see Section N.

Table N.2: Cross sections for SD, three tunes of QGSJet; from [115] and numerical tables (priv.comm. from author). Tunes '+' and '-' have relatively less low mass diffraction, see Section N. "SD-like" is the additional contribution from non-SD events that have exactly one proton with ξ less than 20%, see also Table 7.10.

SD class diffractive mass range (GeV)	QGSJet II-04 default tune true SD (mb)	'+' tune (mb)	'-' tune (mb)	SD-like (default tune) (mb)
<3.1	3.89	3.18	2.54	+0
3.1 – 7.7	2.36	2.28	1.96	+0
7.7 – 380	3.64	4.29	3.50	+0.13
380 – 1150	0.57	0.68	0.68	+0.70
1150 – 3130	0.41	0.51	0.50	+5.86
$\xi < -20\%$	0.10	0.14	0.09	$\pm$0
Total SD	10.97	11.06	9.27	

Table N.3: Cross sections for SD-like topologies with tracks in one of the T2 η acceptance regions, and one proton with $\xi > -20\%$ for QGSJet MC. Class 2T2 demand tracks in both T2 acceptance arms. Priv.comm from author of QGSJet, see also [78, 115]. SD classes divided according to SD mass, not event topology. DD=Double diffractive, CD=central diff., ND=non-diff. See Section N.1 for further explanation of MC particle selections used here.

SD class	SD mass range (GeV)	Trig. (All) (mb)	True SD (mb)	DD (mb)	CD (mb)	ND (mb)
0T2	< 3.1	0.22	0.22	-	-	-
1T2-0T1	3.1 – 7.7	1.3	1.3	-	-	-
1T2-1T1	7.7 – 380	2.80	2.73	0.008	0.012	0.047
1T2-2T1	380 – 1150	0.74	0.37	0.07	0.003	0.30
2T2	1150 – 3130	4.26	0.29	0.48	0.003	3.48
Total triggered		9.32	4.91	0.56	0.02	3.83

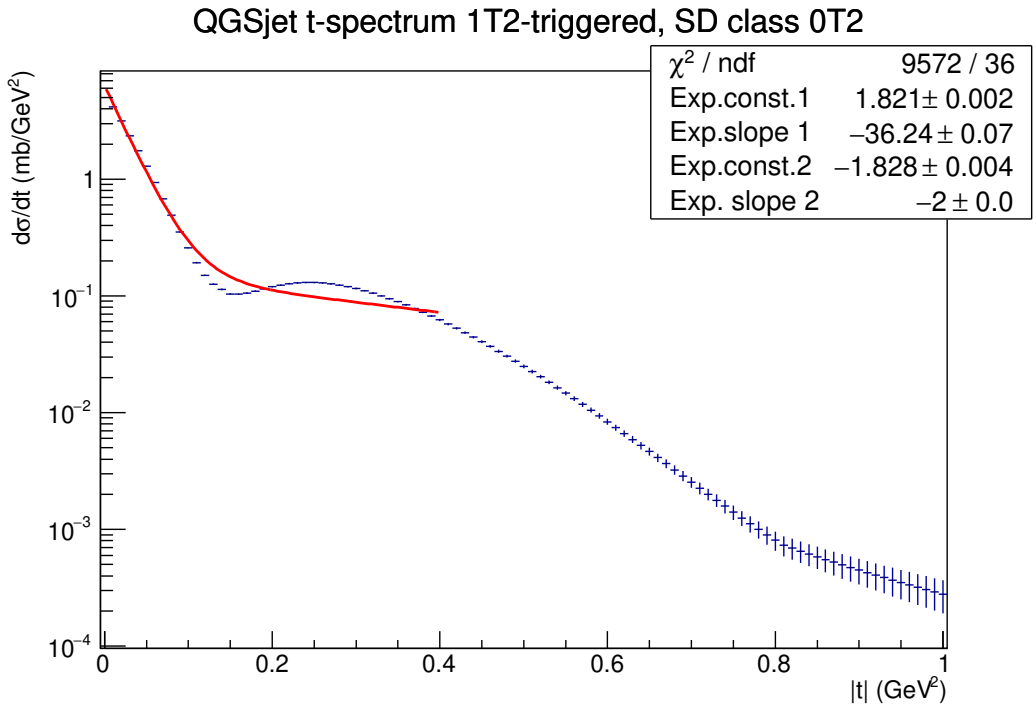

Figure N.14: Double exponential fit of QGSJet predicted $|t|$-spectrum for the 0T2 SD class triggered by 1T2. Histogram provided by the author of QGSJet (priv.comm.), see also [78, 115]

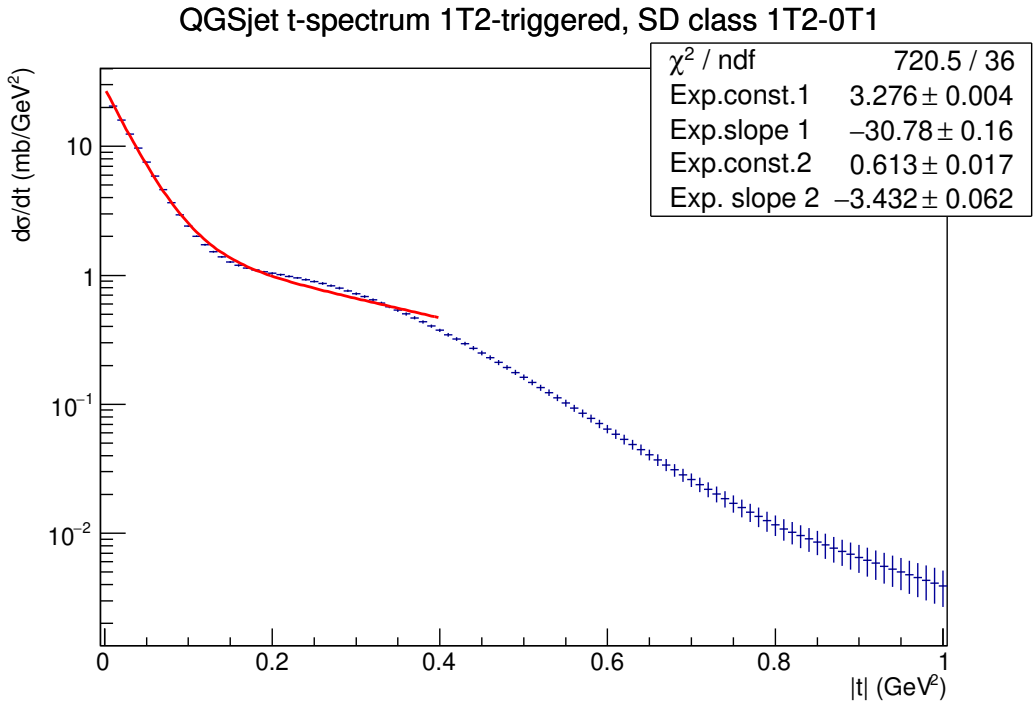

Figure N.15: Double exponential fit of QGSJet predicted $|t|$-spectrum for the 1T2-0T1 SD class. Histogram provided by the author of QGSJet (priv.comm.), see also [78,115]

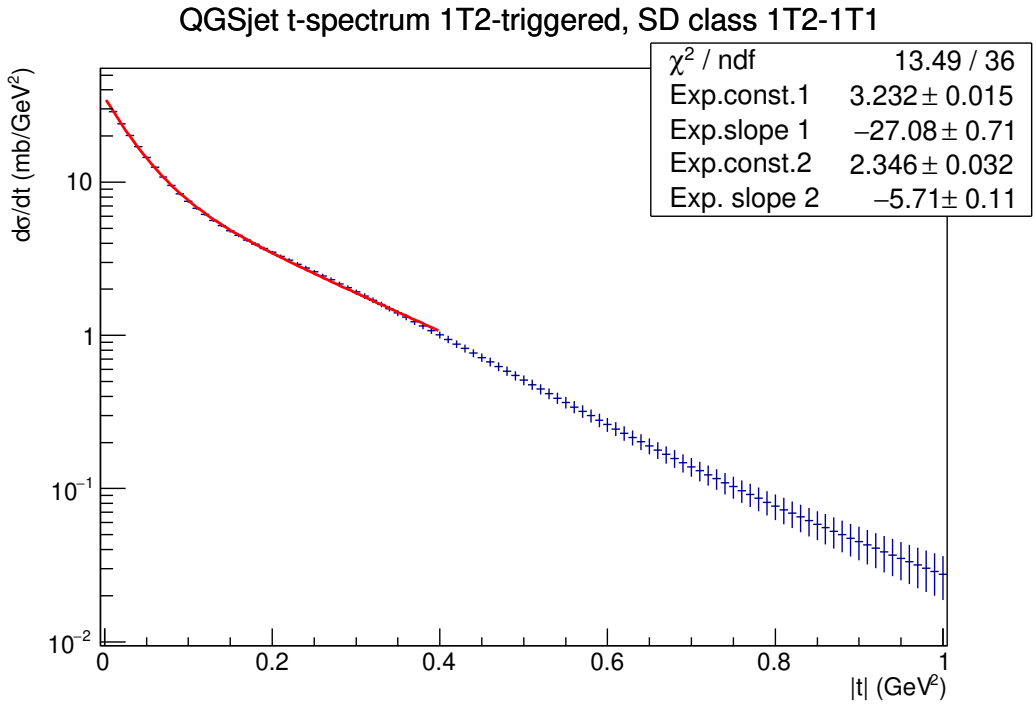

Figure N.16: Double exponential fit of QGSJet predicted $|t|$-spectrum for the 1T2-1T1 SD class. Histogram provided by the author of QGSJet (priv.comm.), see also [78,115]

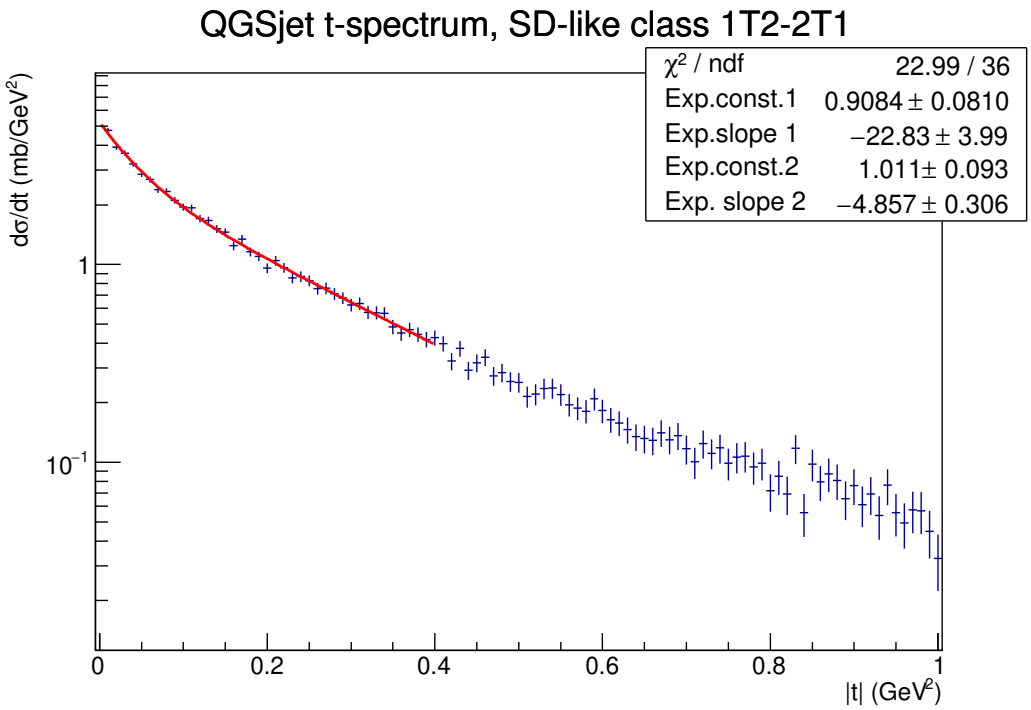

Figure N.17: Double exponential fit of QGSJet predicted $|t|$-spectrum for the triggered 1T2-2T1 SD-like class. Histogram provided by the author of QGSJet (priv.comm.), see also [78, 115]

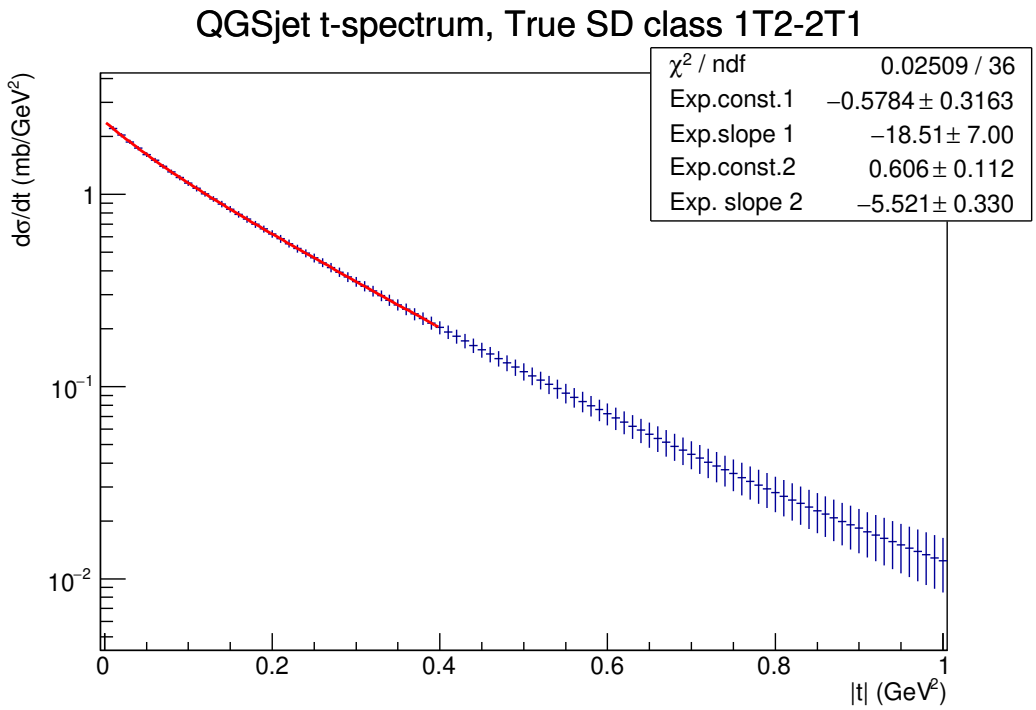

Figure N.18: Double exponential fit of QGSJet predicted $|t|$-spectrum for the 1T2-2T1 true SD class. Histogram provided by the author of QGSJet (priv.comm.), see also [78, 115]

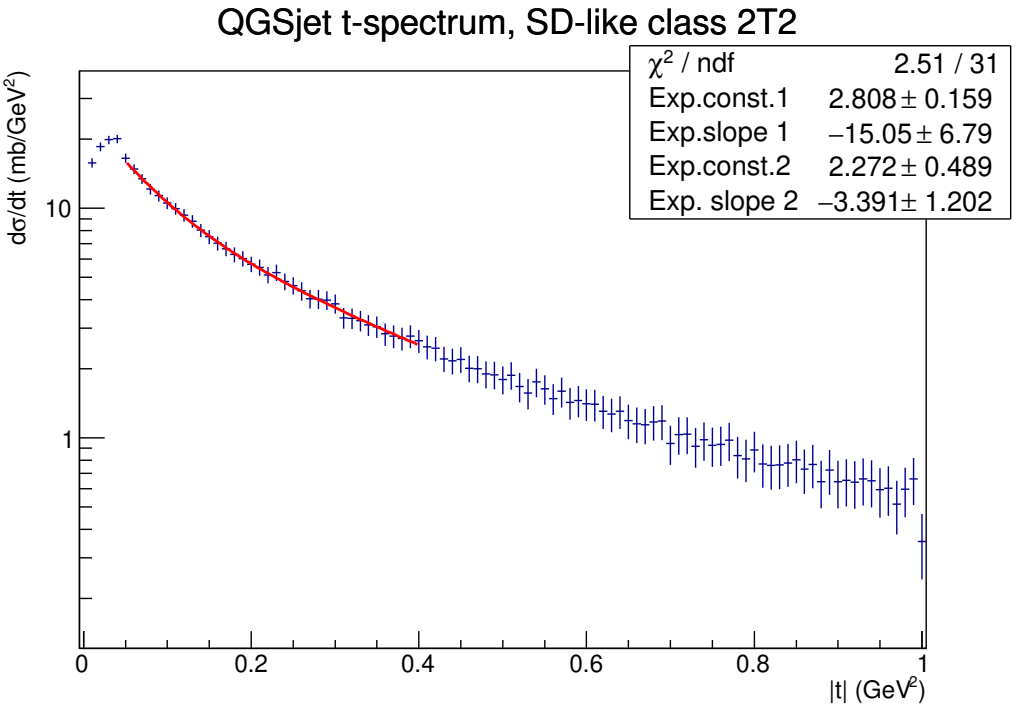

Figure N.19: Double exponential fit of QGSJet predicted $|t|$-spectrum for the 2T2-triggered SD-like class. Histogram provided by the author of QGSJet (priv.comm.), see also [78, 115]

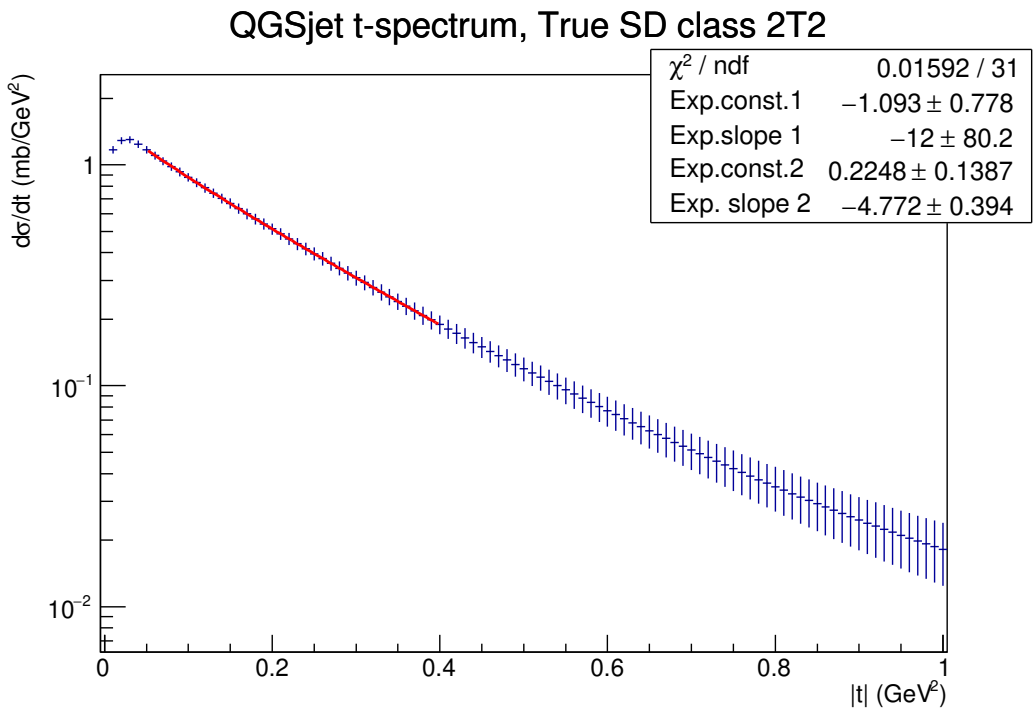

Figure N.20: Double exponential fit of QGSJet predicted $|t|$-spectrum for the 2T2-triggered true SD class. Histogram provided by the author of QGSJet (priv.comm.), see also [78, 115]. Note the downturn at small $|t|$, see Section N.1.

Table N.4: Fitted $|t|$-slopes of two-exponential sum for SD-like topologies with tracks in one of the T2 η acceptance regions, and one proton with $\xi > -20\%$ for QGSJet MC. Class 2T2 demand tracks in both T2 acceptance arms. Priv.comm from author of QGSJet, see also [78, 115]. SD classes divided according to SD mass, not event topology. Fit range is $0< |t| <0.4$ GeV^2, except for 2T2 $|t| >0.05$ GeV^2. Wrongly fitted parameters in parentheses. Single = one exponential, for comparison with real data and other MCs, same fit range as in Table 6.10. See Section N.1 for further explanation of fitting functions.

SD class	SD mass range (GeV)	Slope 1 B_1 (GeV^{-2})	Slope 2 B_2 (GeV^{-2})	Single B (GeV^{-2})
0T2(trig.)	< 3.1	-36.24 ± 0.07	(-2.0 ± 0.0)	(-19.53 ± 0.12)
1T2-0T1(trig.)	3.1 – 7.7	-30.78 ± 0.16	(-3.43 ± 0.06)	(-10.85 ± 0.07)
1T2-1T1(trig.)	7.7 – 380	-27.1 ± 0.7	-5.71 ± 0.11	(-8.24 ± 0.07)
1T2-2T1 (trig.,all)	380 – 1150	-22.8 ± 4.0	-4.9 ± 0.3	-5.98 ± 0.17
1T2-2T1 (trig.,SD)	380 – 1150	-18.5 ± 7.0	-5.5 ± 0.3	-5.98 ± 0.14
2T2 (trig.,all)	1150 – 3130	-15.1 ± 6.8	-3.4 ± 1.2	-5.50 ± 0.25
2T2 (trig.,SD)	1150 – 3130	(-12 ± 80)	-4.8 ± 0.4	-5.30 ± 0.18

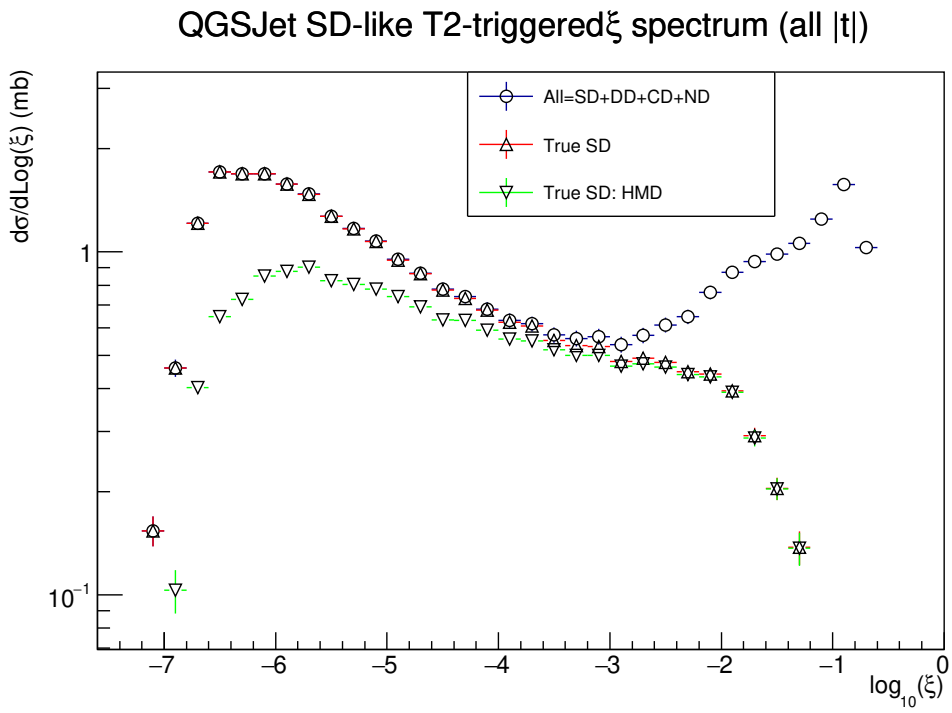

Figure N.21: QGSJet predicted diffractive mass spectrum for T2-triggered SD-like events. "All" contains SD and non-SD events with rapidity gap in one T2 arm, and with one proton. True SD is sum of high mass and low mass diffraction components, for all $|t|$ values. Histogram provided by the author of QGSJet (priv.comm.), see also [78, 115]. See Section N.1 for a description of the MC trigger selection.

Appendix O

Benchmarking weighted unfolding methods

Previously, the unfolding learning histograms[1] used for unfolding real data and MC histograms in this thesis were filled with no weighting, only for events with an SD-like track topology both for the reconstructed tracks, and the generator-level particles. As explained in Section 6.4.3, the restriction to reconstructed events only was done so as not to introduce a scaling factor, but of course the the real data and MC reconstructed histograms were filled with our best estimate of the acceptance correction as a weight. Since this weighting information was not passed to the RooUnfold unfolding module, the loss of information led to suboptimal unfolding when the acceptance varied over the histogram range. This discrepancy led to problems especially in the 2T2 SD class where the BH-cut led to a very different acceptance shape, and also in the case of non-constant (logarithmic) binning for the t-spectra.

The unweighted Bayesian unfolding was used with the default i=4 iterations, except in cases where the unfolded histogram had some or all bins filled with a very large uncertainty that grew with each iteration, in which case i=2 was selected.

To use the same weights for the learning sample 1-D reconstructed and 2-D response matrix histograms as for the corresponding histograms to be unfolded, without introducting spurious scaling factors, we fill the learning sample 1-D truth histograms for any events with a generator-level topology matching one of the SD classes, independent of the reconstructed track content of that event, while filling the 1-D reconstructed and 2-D response histograms only for events with RECO-level SD topology

[1] Simu truth, Reconstructed, and 2D response matrix

events.

To do more detailed benchmarking on the optimal unfolding parameter values, we calculated a simple χ^2 histogram, with $\chi^2 = \sum_{i=signal}(R_i - s_i)^2/s_i$, where R_i is the contents of bin i in the histogram of the reconstructed quantity R, and s is the simulated truth distribution. This was calculated for a simple five-bin histogram of the five SD categories from 0T2 to 2T2, and for the closure plots which also contain various SD background categories, but still only summing the χ^2 over the five SD signal bins.

The minimum value for the SVD parameter k was was found by doing a cross-MC unfolding, comparing the ratio of the unfolded histogram to the real simulated truth distribution with the ratio of unfolded to learning sample truth distribution. The latter was much flatter in the MC-biased small k range. This can be seen in Figure O.1, where the SVD points for k=2 unfolding depart very significantly from a closure ratio near one, while the ratio to the learning sample is nearly flat, in the Figure O.2. This bias has vanished by k=4, seen in Figures O.3 – O.4.

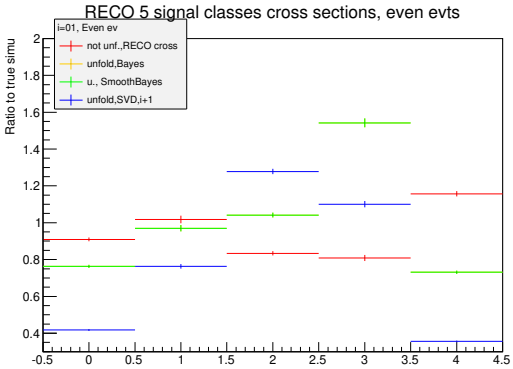

Figure O.1: Five-bin unfolding closure ratio with simu truth, Bayes 1-iteration and SVD k=2 unfolding. SVD is biased to learning sample, see text. Learning sample is Pythia 8 SD with 103 000 events, unfolding an EPOS sample with 550 000 events. Even half of the events shown.

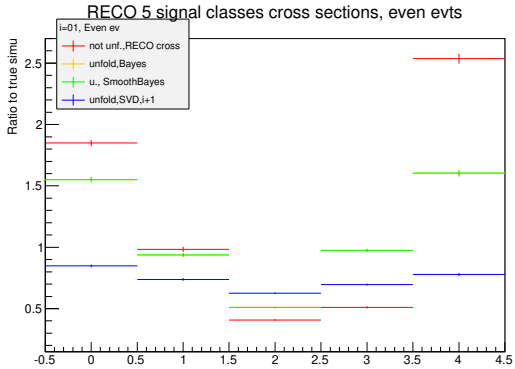

Figure O.2: Five-bin unfolding closure ratio with learning simu, Bayes 1-iteration and SVD k=2 unfolding. SVD unfolding biased to learning sample, see text. Pythia 8 SD with 103 000 events learning sample, unfolding an EPOS sample with 550 000 events. Even half of the events shown.

This minimum was also visible in the χ^2 plots for the MC biased closure unfolding, which is shown unfolded by EPOS by Pythia and vice versa, in Figures O.5 – O.6. The minimum position varies somewhat between k=5 and k=7, being larger when using the inclusive EPOS sample for learning – note that the k-value $k = 5$ is filled in the x-axis

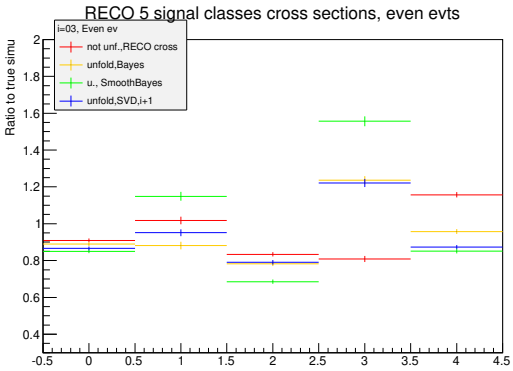

Figure O.3: Five-bin unfolding closure ratio with simu truth, Bayes 3-iteration and SVD k=4 unfolding. SVD not biased to learning sample, see text. Learning sample is Pythia 8 SD with 103 000 events, unfolding an EPOS sample with 550 000 events. Even half of the events shown.

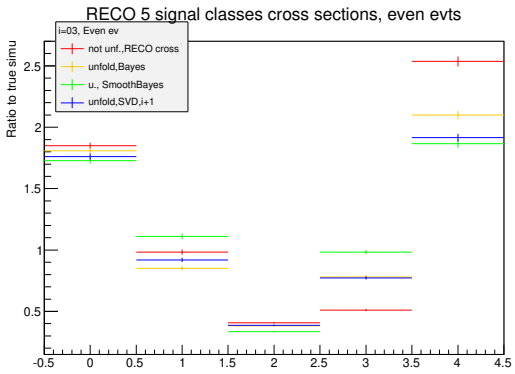

Figure O.4: Five-bin unfolding closure ratio with learning simu, Bayes 3-iteration and SVD k=4 unfolding. SVD unfolding not biased to learning sample, see text. Pythia 8 SD with 103 000 events learning sample, unfolding an EPOS sample with 550 000 events. Even half of the events shown.

at the bin numbered $i = 4$, since Bayesian unfolding accepts the parameter may be as small as one, while the minimum k for SVD is k=2. Also note that Bayesian unfolding did not significantly improve the χ^2 values after 2 iterations; at iteration 1 Smoothed and Unsmoothed Bayesian overlap.

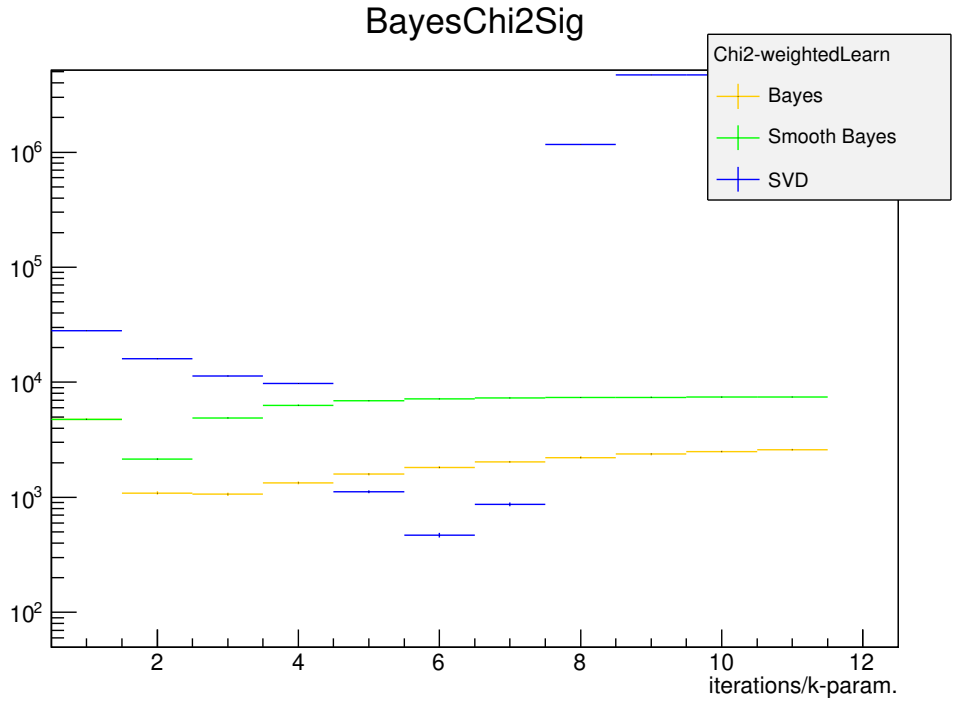

Figure O.5: χ^2 for various unfolding methods when unfolding a 103 000 Pythia 8 SD event sample, with an EPOS 550 000 event sample for learning.

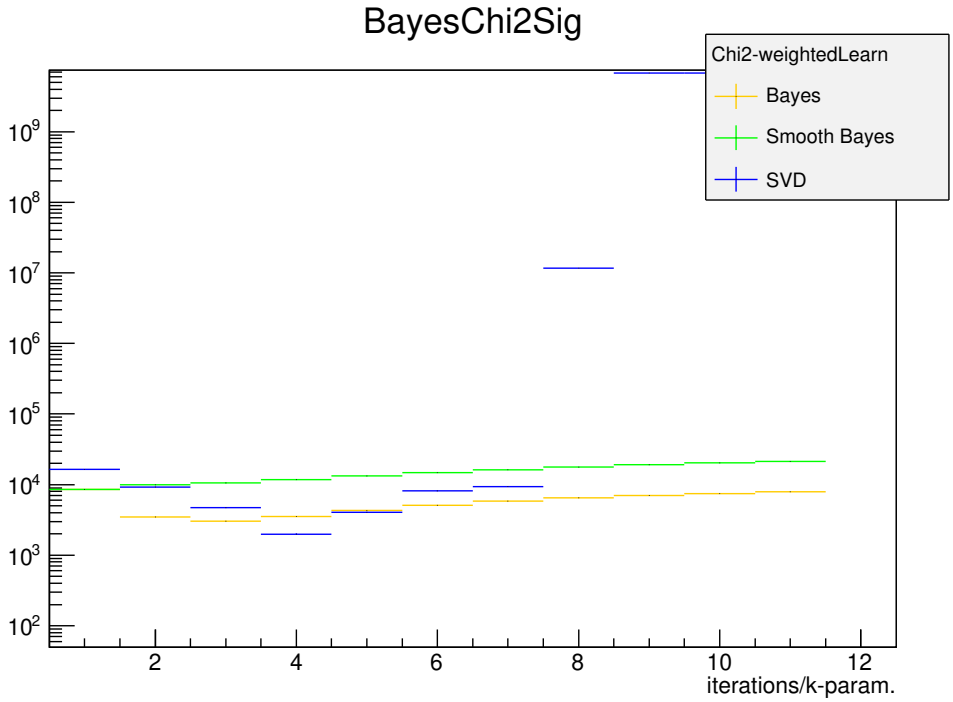

Figure O.6: χ^2 for various unfolding methods when unfolding an EPOS 550 000 event sample, with a 103 000 Pythia 8 SD event sample for learning.